NUREG/CR-0344

ANL-77-31

NUREG/CR-0344

ANL-77-31

DEFORMATION CHARACTERISTICS OF ZIRCALOY CLADDING IN VACUUM AND STEAM UNDER TRANSIENT-HEATING CONDITIONS: SUMMARY REPORT

by

H. M. Chung and T. F. Kassner

U of C-AUA-USDOE

ARGONNE NATIONAL LABORATORY, ARGONNE, ILLINOIS

Prepared for the U. S. NUCLEAR REGULATORY COMMISSION
under Interagency Agreement DOE 40-550-75

7904100075

The facilities of Argonne National Laboratory are owned by the United States Government. Under the terms of a contract (W-31-109-Eng-38) between the U. S. Department of Energy, Argonne Universities Association and The University of Chicago, the University employs the staff and operates the Laboratory in accordance with policies and programs formulated, approved and reviewed by the Association.

Available from
National Technical Information Service
Springfield, Virginia 22161

NUREG/CR-0344
ANL-77-31

Distribution Code: R3

ARGONNE NATIONAL LABORATORY
9700 South Cass Avenue
Argonne, Illinois 60439

DEFORMATION CHARACTERISTICS OF ZIRCALOY CLADDING IN VACUUM AND STEAM UNDER TRANSIENT-HEATING CONDITIONS: SUMMARY REPORT

by

H. M. Chung and T. F. Kassner

Materials Science Division

July 1978

Prepared for the Division of Reactor Safety Research
U. S. Nuclear Regulatory Commission
Washington, D.C. 20555
Under Interagency Agreement DOE 40-550-75

NRC FIN No. A2017

TABLE OF CONTENTS

TABLE OF CONTENTS

LIST OF FIGURES

LIST OF FIGURES

LIST OF FIGURES

LIST OF FIGURES

LIST OF FIGURES

LIST OF FIGURES

LIST OF FIGURES

LIST OF FIGURES

LIST OF FIGURES

LIST OF FIGURES

LIST OF FIGURES

LIST OF FIGURES

LIST OF FIGURES

LIST OF TABLES

LIST OF TABLES

LIST OF TABLES

LIST OF TABLES

DEFORMATION CHARACTERISTICS OF ZIRCALOY CLADDING IN VACUUM AND STEAM UNDER TRANSIENT-HEATING CONDITIONS: SUMMARY REPORT

by

H. M. Chung and T. F. Kassner

ABSTRACT

The high-temperature diametral expansion and rupture behavior of Zircaloy-4 fuel-cladding tubes have been investigated in vacuum and steam environments under transient-heating conditions that are of interest in hypothetical loss-of-coolant-accident (LOCA) situations in light-water reactors (LWR's). The effects of internal pressure, heating rate, axial constraint, and localized temperature nonuniformities in the cladding on the maximum circumferential strain have been determined for burst temperatures between ~650 and 1350°C. Oxidation of the cladding during transient heating in steam greatly suppresses the circumferential strain maxima that occur at burst temperatures of ~1050 and 1240°C in the β-phase region. The strain maximum at ~800°C in the α-phase region does not decrease relative to results obtained in vacuum, and, under certain conditions, oxidation enhances the circumferential strain at rupture. However, axial constraint and temperature nonuniformity in the cladding decrease the circumferential strain for rupture temperatures in the α- or predominantly α-phase region ($T \lesssim 830$°C). A good correlation was obtained between the maximum circumferential strain and the magnitude of the circumferential temperature variation in the cladding for burst temperatures near 800°C in steam. Therefore, the ballooning strain in LWR fuel cladding can be reliably estimated from the present results and a knowledge of the temperature variations in the cladding for various hypothetical LOCA transients.

I. INTRODUCTION

This report is a compilation of data and an analysis of results from Zircaloy-4 tube-burst experiments reported in Light-water-reactor Safety Research Program quarterly progress reports[1-8] for July 1975 to June 1977. The information represents part of the mechanical-property data on Zircaloy and Zircaloy-oxygen alloys generated in a U. S. Nuclear Regulatory Commission-sponsored program to determine the effect of oxygen on the uniaxial tensile, biaxial tube-burst, drop-weight impact, and thermal-shock properties of Zircaloy.

The objectives of the program are to (a) obtain information on the ballooning characteristics of Zircaloy cladding and (b) establish a quantitative cladding-embrittlement criterion applicable to postulated loss-of-coolant-accident (LOCA) situations in light-water reactors (LWR's). The mechanical-property information will be incorporated into fuel-element modeling codes that will provide a quantitative basis for evaluating cladding deformation over a wide range of LOCA and power-coolant-mismatch (PCM) conditions.

A better understanding of the high-temperature deformation and rupture behavior of Zircaloy cladding under LOCA situations is essential in evaluating the extent of coolant flow blockage and the performance of emergency-core-cooling systems (ECCS's). The present investigation identifies and quantifies the effects of critical parameters on the diametral expansion and rupture behavior of Zircaloy cladding over a wide range of test conditions. The results were evaluated in relation to the degree of oxidation of the material and the deformation mechanisms applicable to anisotropic Zircaloy cladding.

II. PHILOSOPHY OF INVESTIGATION

The complex nature of the diametral expansion and rupture behavior of Zircaloy cladding under isothermal and transient heating conditions is evidenced by the numerous investigations undertaken in recent years.[9-31] Synergistic effects that result from geometric variables (e.g., pellet-cladding axial- and diametral-gap distances, specimen length), test methods (e.g., direct or indirect heating of the tube, mechanical interactions between an internal heater and the cladding), and test conditions (i.e., heating rate, internal pressure, vacuum or steam environment) influence the temperature distribution, stress state, and mechanical properties of the cladding during deformation. Consequently, maximum circumferential strains at failure[9-31] range from 0.28 (Ref. 13) to 1.3 (Ref. 9) for a narrow range of burst temperatures between ~750 and 850°C.

To provide a basis for interpreting cladding-deformation results from in-reactor nuclear-heated fuel rods and electrically heated multirod-bundle tests, we systematically investigated the effects of internal pressure, heating rate, axial constraint of the tube, environment (vacuum/steam), temperature nonuniformity, and specimen length on the transient-heating tube-burst properties of Zircaloy-4 cladding. The present results, obtained under idealized conditions, coupled with less extensive data from in-reactor and multirod tests, should provide a quantitative basis for predicting cladding deformation and the extent of flow blockage under hypothetical LOCA situations in LWR's.

III. MATERIAL, APPARATUS, AND EXPERIMENTAL PROCEDURES

A. Material

The Zircaloy-4 cladding used in this investigation was obtained from two lots of Sandwik tubing purchased by Oak Ridge National Laboratory for

Water-Reactor Safety Research Programs.[32] The 10.9-mm outside-diameter (OD) by 0.635-mm wall-thickness material, from lots 7FD11 and 7FD12, was 80% cold-worked and stress-relieved at 500°C for 4 h. The ingot analyses of the Zircaloy-4 material are given in Table I. Maximum measured variations of the OD, inside diameter (ID), and wall thickness were 0.063, 0.061, and 0.038 mm, respectively. The only difference between the two lots of material was that lot 7FD12 received an additional straightening pass. Figure 1 shows microstructures of the as-received stress-relieved tubing.

TABLE I. Chemical Compositions of Zircaloy-4 Cladding Lots 7FD11 and 7FD12

	Ingot Analysis Composition in wt %			
	Spec.[a]	Top	Middle	Bottom
Sn	1.20-1.70	1.52	1.50	1.39
Fe	0.18-0.24	0.20	0.22	0.19
Cr	0.07-0.13	0.12	0.12	0.11
Fe + Cr	0.28-0.37	0.32	0.34	0.30
Zr		BALANCE		
	Impurities in PPM			
Al	75	38	39	<35
B	0.5	0.2	0.2	0.2
Cd	0.5	<0.2	<0.2	<0.2
Ca	30	<10	<10	<10
C	80-270	110	110	120
Cl	20	<5	<5	<5
Co	20	<10	<10	<10
Cu	50	17	17	17
Hf	100	44	39	44
H	25	7	<5	<5
Pb	130	<50	<50	<50
Mg	20	<10	<10	<10
Mn	50	<25	<25	<25
Ni	70	<35	<35	<35
N	80	33	29	34
Si	50-120	81	86	69
Ti	50	<25	<25	<25
W	100	<25	<25	<25
U	3.5	1.0	1.5	0.9
O	900-1400	1260	1180	1270
Cb	120	<50	<50	<50
Mo	50	<25	<25	<25
Ta	200	<100	<100	<100
V	50	<25	<25	<25
Na	20	<10	<10	<10

[a]Composition in purchase order specification.

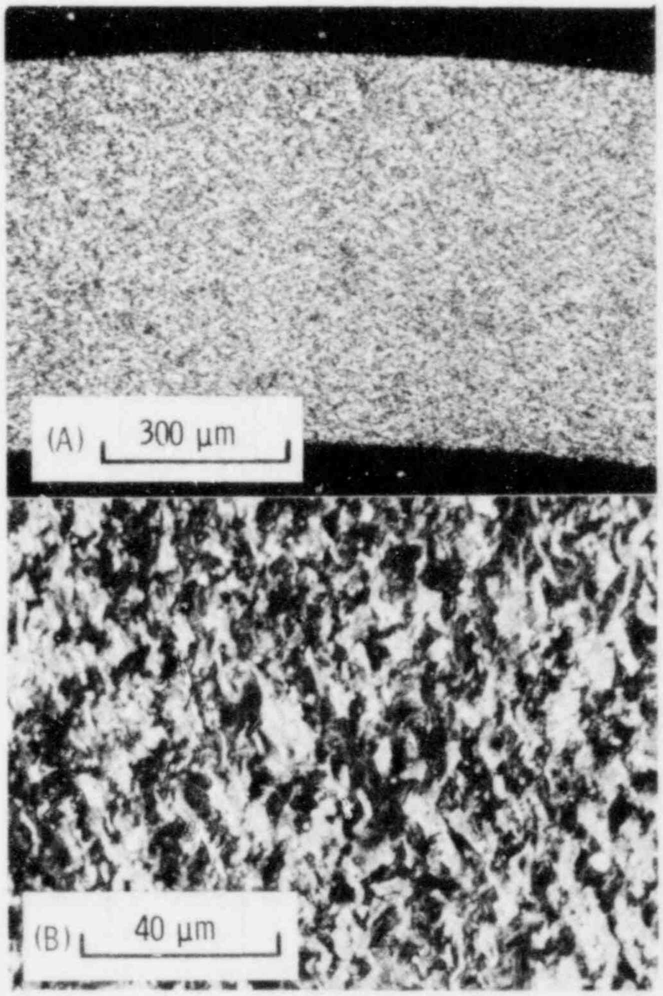

Fig. 1. Microstructure of As-received Stress-relieved Zircaloy-4 Cladding. Etched and anodized, polarized light. ANL Neg. No. 306-76-79.

B. Texture

The texture was typical of tubing fabricated for commercial fuel cladding; i.e., the basal {0002} pole figure showed intensity peaks distributed ~30° on each side of the radial direction toward the tangential direction. Figure 2 is a schematic illustration of the preferred orientation of the unit cell relative to the radial, tangential, and axial directions of the tube. A typical basal pole figure has been reported for lot 7FD12 by Chapman.[32]

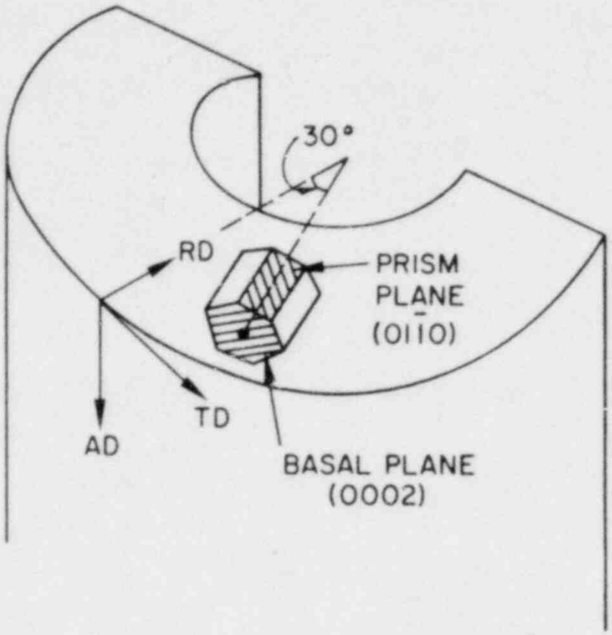

Fig. 2. Schematic Illustration of Preferred Crystallographic Orientation of Textured Zircaloy Tubing Used in Present Investigation. ANL Neg. No. 306-77-454.

C. Zircaloy-Oxygen Phase Diagram

A separate investigation was undertaken to determine the pseudobinary Zircaloy-oxygen phase diagram by resistometric measurements[3,33] and metallographic analyses[34] of quenched specimens. Figure 3 shows that the α- and β-phase boundaries for Zircaloy-oxygen alloys are considerably different than those of the zirconium-oxygen system. For the as-received cladding with ~0.12 wt % oxygen, the α and β phase boundary temperatures are 810-815 and 975-980°C, respectively.

D. Specimen Geometry

Most of the specimens were 153 mm long; however, 300-mm-long tubes were also used to investigate the effect of specimen length on the tube-burst properties. The tube length in each test is given in Appendix A along with the burst-test results.

An alumina (Al_2O_3) mandrel or a stack of alumina pellets was used to simulate the fuel column in a fuel element. Unconstrained, i.e., empty, tubes were also tested. A schematic of the 153-mm-long tube-burst specimen is shown in Fig. 4. The internal mandrel was machined from a high-purity recrystallized alumina rod. The clearances between the ID of the Zircaloy-4 tubing and the OD of the alumina mandrel were 1.3 mm over the central 114-mm portion of the specimen and 0.7 mm at the ends. In most of the experiments, the combined axial-gap distance between the end plugs and alumina mandrel was 2.5 mm; however, a gap distance of 5.9 mm also was investigated over a limited range of burst temperatures at a heating rate of 115°C/s. The gas volumes of the pressurization system and the specimen with and without the mandrel were 11.5, 3.4, and 12.5 cm^3, respectively.

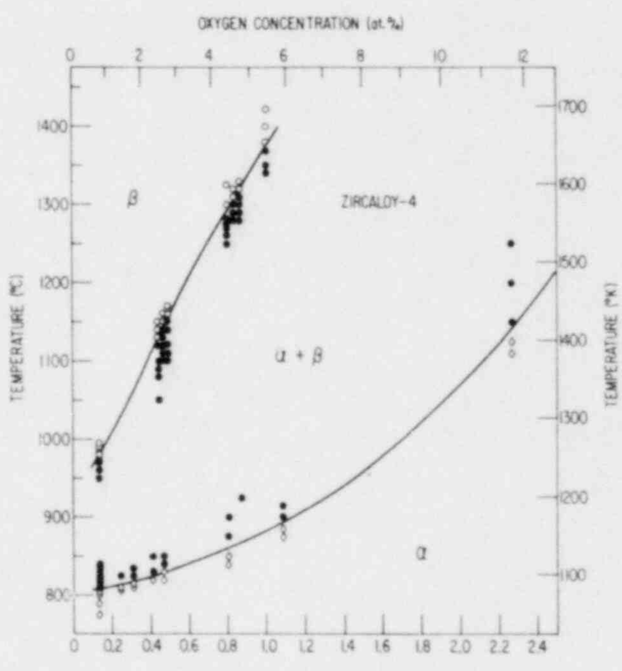

Fig. 3

Pseudobinary Zircaloy-Oxygen Phase Diagram[34] Determined from Metallographic Measurements on Oil-Quenched Specimens. ANL Neg. No. 306-78-839.

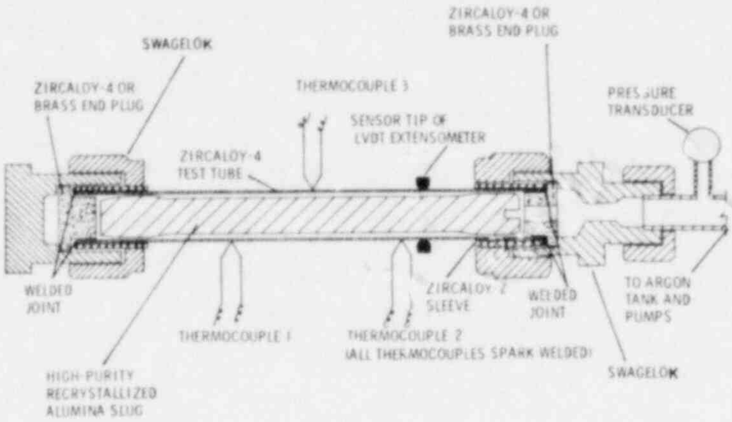

Fig. 4

Schematic of Zircaloy Tube-burst Specimen Constrained with an Alumina Mandrel. ANL Neg. No. 306-75-205.

To investigate the effect of circumferential temperature variations in the cladding on the deformation behavior, the alumina rod was replaced by a stack of 10-mm-long high-purity recrystallized alumina pellets. The average diametral gap between the cladding and pellets was varied from 0.07 to 0.5 mm. The axial gap between the top of the pellet stack and the end plug was 2.5 mm, as was the case for most of the tests with the alumina mandrel.

The specimen assembly was positioned vertically, and the top end was allowed to move freely. Typically, three or four Pt-Pt 10% Rh thermocouples (0.025-mm-dia wire), which were calibrated against a standard thermocouple, were spark-welded directly to the tube ~25 mm apart. Because of the extremely small cross section of the thermocouple wire, the error of temperature measurement under rapid transient-heating conditions, as a result of thermal shunting and slow response of the thermocouple, could be minimized. Sensor tips of the linear-variable-differential-transducer (LVDT) extensometer were positioned within the central 75-mm portion of the tubing. The Pt-Pt 10% Rh thermocouples were used exclusively for high-temperature bursts (≥900°C); however, Chromel-Alumel thermocouples were also used at lower temperatures.

E. Tube-burst Apparatus and Instrumentation

The tube-burst apparatus consisted of a bell-jar vacuum chamber, a gas-handling system to pressurize the specimen, and a programmable ac power supply for direct electrical heating of the tube. Argon was used to pressurize the specimen internally. Figure 5 shows the burst apparatus and readout instruments. A high-speed camera, a laser illuminator, and a high-speed fiber-optics recorder are visible in the foreground. Figure 6 is a schematic of the specimen, power supply, gas-handling system, and instrumentation.

A high-speed (up to 1000 frames/s) camera was used to record the diametral and axial changes of the tube during the burst test. An argon-ion or helium-neon laser was used to illuminate the central 75-mm portion of the specimen. Both the direct and shadow images of the specimen length were monitored on the high-speed camera frames. In some cases, multiple direct images were monitored by means of mirrors positioned at several angles. The burst frame could be located precisely from either the appearance of the rupture or the sudden vibration of the images at the time of the burst. Figure 7 shows the deformation sequence for a preoxidized Zircaloy tube over the time interval of 0.08 s.

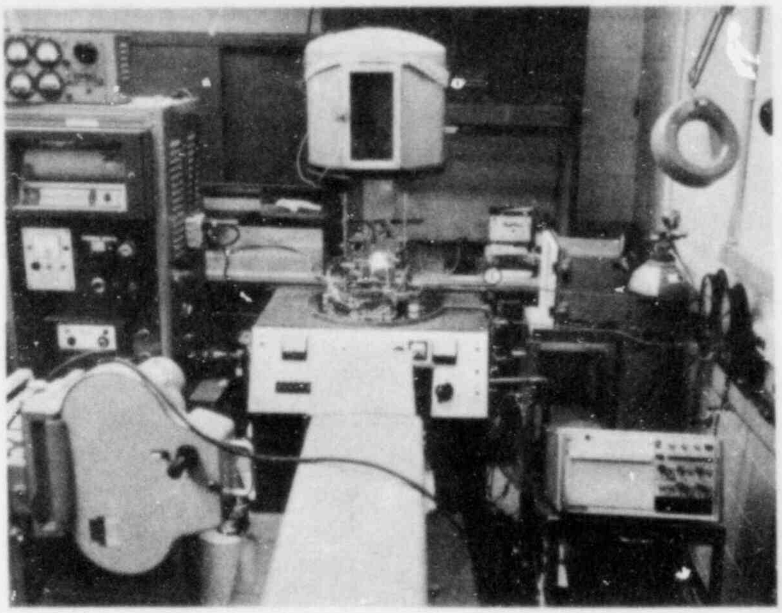

Fig. 5. Tube-burst Apparatus with High-speed Camera and Laser Illumination System. ANL Neg. No. 306-77-480.

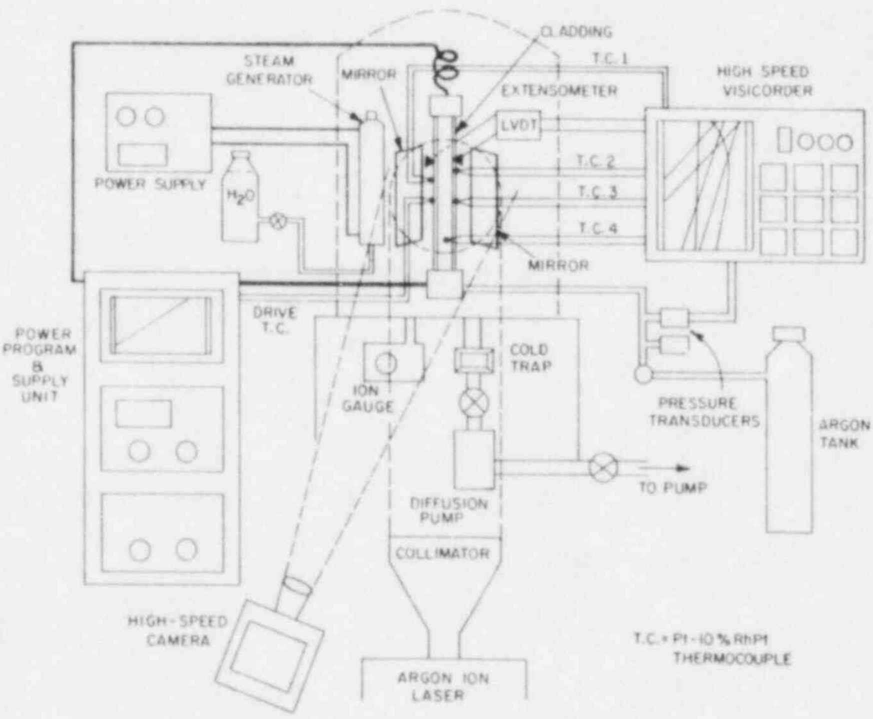

Fig. 6. Schematic of Tube-burst Apparatus and Instrumentation. ANL Neg. No. 306-77-460.

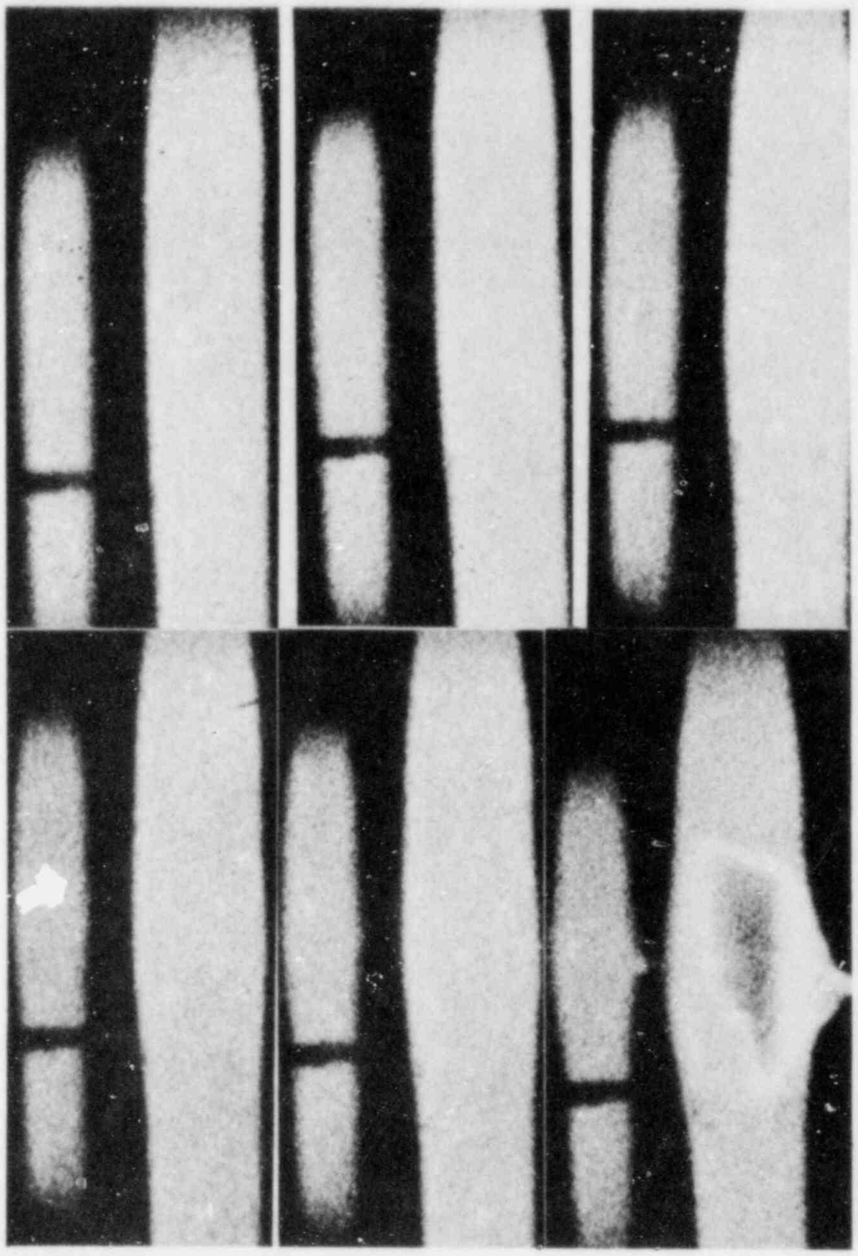

Fig. 7. High-speed-movie Frames Taken during Deformation of Oxidized and Homogenized (0.37 wt % Oxygen) Zircaloy-4 Tube. The time interval between frames was 0.004 s. The photographs, from upper left to lower right, are 20, 10, 3, 2, 1, and 0 frames before rupture. Smaller tubes are mirror images at ~160° with respect to the main image. ANL Neg. No. 306-75-226.

The specimen chamber was evacuated to ~0.1 Pa for tests in vacuum. A static vacuum pressure of ≤2.6 Pa was maintained in the bell-jar chamber during a burst test in vacuum. For bursts in a steam environment, the steam pressure was maintained at 5-8 x 10^4 Pa. Distilled water was used for steam generation. A steam-generation rate of ~5 g/s resulted in uniform oxidation of the cladding surfaces and exceeded the minimum rate for steam starvation by a considerable margin. Steam condensation on the chamber was minimized by warming the surface before admitting the vapor.

The signals from the extensometer, thermocouples, and pressure transducer were recorded on a multichannel high-speed Visicorder. The high-speed-camera frames and multichannel records were matched at the moment of burst. Camera frames were magnified 32-40 times larger in an optical microscope. Then the microscope photographs were used to calculate the diametral strains. Extensometer data were used to check the diametral strain obtained from the high-speed-camera frames over the region of uniform diametral expansion. Figure 8 shows typical profiles of temperature and pressure versus time obtained from the multichannel Visicorder. Figure 8 also shows the diametral strain and ballooning profiles determined from high-speed-camera frames.

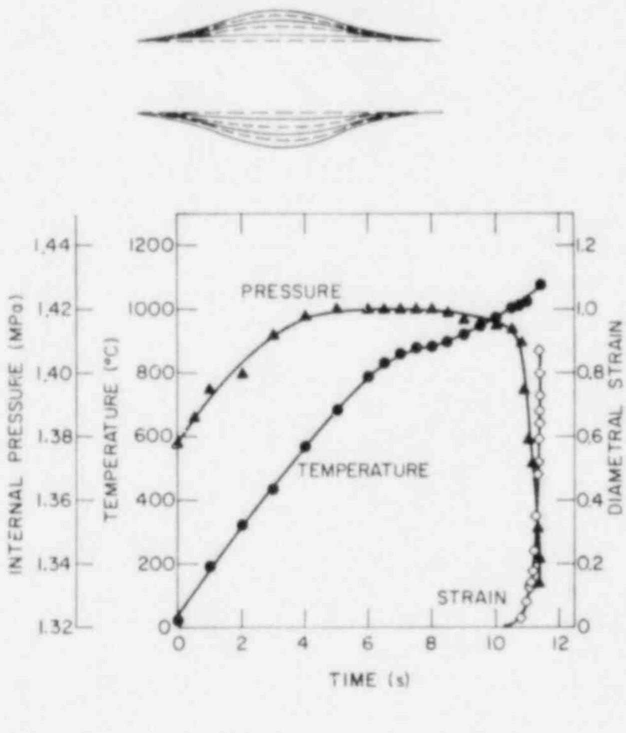

Fig. 8

Temperature, Internal Pressure, Diametral Strain, and Ballooning Profiles as a Function of Time during Rupture Test of Zircaloy Cladding. ANL Neg. No. 306-78-405.

IV. ANALYSIS OF DIAMETRAL EXPANSION AND BALLOONING BEHAVIOR

A. Diametral Expansion and Plastic Instability

Uniform diametral expansion of the tube is followed by rapid localized ballooning at an axial position of least strength. An understanding of the deformation process near the onset of plastic instability, i.e., the transition from uniform tube expansion to localized ballooning, is essential to the development of a failure criterion for internally pressurized cladding. The commonly accepted instability criterion of $dP = 0$, where P is the internal pressure, was found to occur significantly in advance of the initiation of localized ballooning. Hardy[12] came to the same conclusion. For example, we found that, for a rupture test on oxidized-homogenized (acicular α'-phase) Zircaloy-4 that contained 0.37 wt % oxygen at a heating rate of 115°C/s and an initial pressure of 3.92 MPa, the pressure maximum occurred 2.5 s before the rupture. However, examination of individual frames from the high-speed-camera film revealed that the localized ballooning does not take place until ~0.04 s before rupture. The deformation and ballooning data given in Appendix B provide additional evidence for the fact that plastic instability occurs after the point of maximum pressure.

Franklin[35] derived an instability relation for internally pressurized tubes, based upon the more accepted criterion

$$\frac{\delta \dot{A}}{\delta A} = 0, \tag{1}$$

where A is the cross-sectional area of the tube at any instant during deformation, $\dot{A}$ is the rate of decrease of the cross-sectional area A, and the operator δ refers to the difference between the parameters in the "thinned" and "unthinned" regions of the specimen at the same small time increment. The biaxial stability relation is

$$\frac{\delta \dot{\epsilon}_\theta + \delta \dot{\epsilon}_z}{\delta \epsilon_\theta + \delta \epsilon_z} < \dot{\epsilon}_\theta + \dot{\epsilon}_z \text{ (plastically stable)}, \tag{2}$$

where ϵ_θ, $\dot{\epsilon}_\theta$, and ϵ_z, $\dot{\epsilon}_z$ are the tangential (hoop) and axial strains and strain rates, respectively.

The axial strain and strain rate can be neglected safely in contrast to the tangential strain and strain rate within the limit of uniform or nearly uniform expansion. Then the stability relation can be written as

$$\frac{\delta \dot{\epsilon}_\theta}{\delta \epsilon_\theta} \leq \dot{\epsilon}_\theta, \tag{3}$$

and, in terms of radial displacements, Eq. 3 becomes

$$\frac{\delta \dot{r}}{\dot{r}} \le 2\frac{\delta r}{r}. \tag{4}$$

We can apply this criterion to examine a deformation and ballooning sequence such as shown in Fig. 7. Figure 9 is a plot of the normalized tube diameter D/D_0, as a function of time, for the region of maximum local ballooning. Also shown is the diametral strain rate, approximated from the slope of the diametral-strain-versus-time curve. The latter curve indicates that the strain rate is very high near the onset of instability. To apply the stability criterion to the curves in Fig. 9, we can define a normalized diametral-strain parameter as

$$\epsilon_d = \frac{D}{D_0} = \frac{r}{r_0}, \tag{5}$$

and, combining Eqs. 4 and 5, we obtain

$$\delta \ln \dot{\epsilon}_d \le 2\delta \ln \epsilon_d. \tag{6}$$

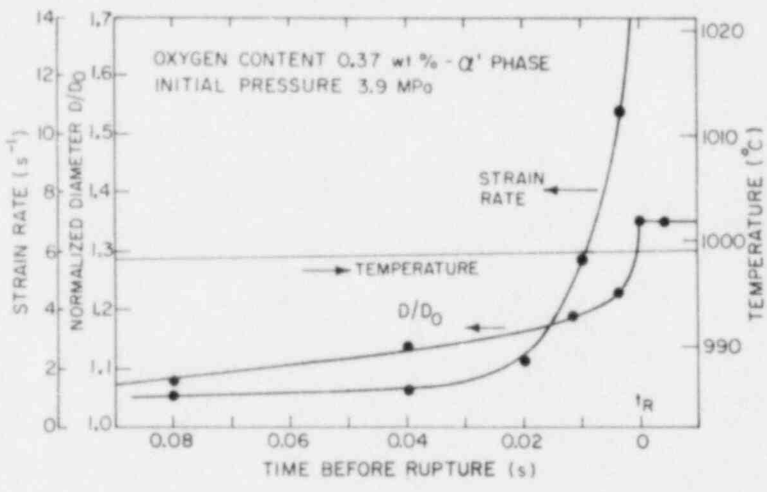

Fig. 9. Diametral Strain, Strain Rate, and Temperature at Burst Region of Zircaloy-4 Specimen Shown in Fig. 7 as a Function of Time near Onset of Plastic Instability. ANL Neg. No. 306-75-204 Rev.

If we compare two axial locations on the tube separated by an infinitesimally small distance during the time increment dt, Eq. 6 can be written as an approximation

$$\frac{d \ln \dot{\epsilon}_d}{dt} \le 2\frac{d \ln \dot{\epsilon}_d}{dt}, \tag{7}$$

and numerical values of both quantities can be computed from the curves in Fig. 9. Either term in Eq. 7 will be referred to hereafter as the stability

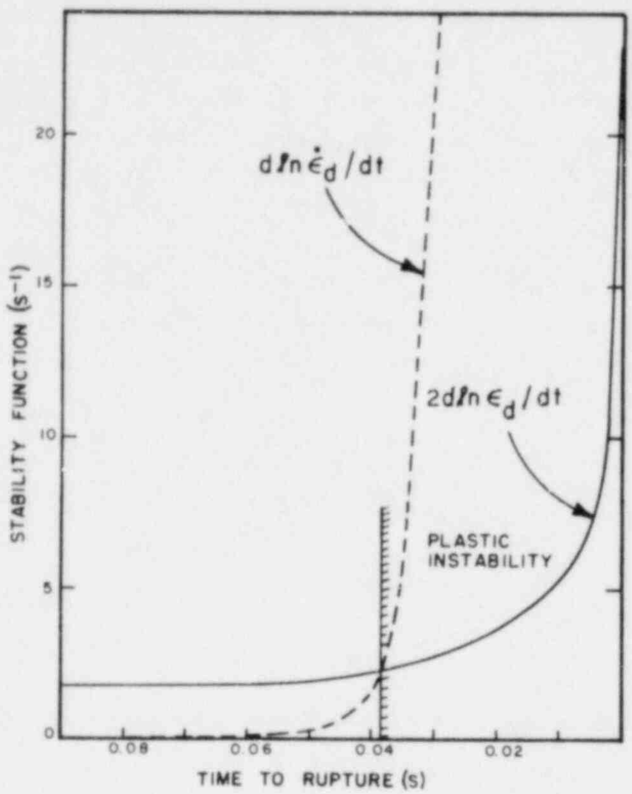

Fig. 10

Stability Functions Calculated from Eq. 7 and Deformation Data Obtained at Heating Rate of 115°C/s on Oxidized-Homogenized Zircaloy-4 Specimen Containing 0.37 wt % Oxygen. ANL Neg. No. 306-75-225 Rev.

function. Figure 10 shows a plot of the two terms in Eq. 7 obtained from the data in Fig. 9. The calculated time for the onset of plastic instability is in good agreement with the high-speed-camera frames, which show that the onset of localized ballooning occurred at ~0.04 s before rupture. on the basis of numerous observations of this type, it is concluded that the criterion, Eq. 6 or 7, provides a quantitative means of accurately determining the onset of plastic instability in the Zircaloy-4 cladding in the tube-burst experiments. Although multiple instabilities can occur in the tube, they result in rupture at one location. A computer program was used to analyze the data from the high-speed-camera frames and Visicorder records and to determine the onset of plastic instability in the tube-burst experiments. The plastic-stability condition, Eq. 7, can be written as

$$D\frac{d^2D}{dR^2} \Big/ 2\left(\frac{dD}{dR}\right)^2 \leq 1 \text{ (plastically stable)}, \qquad (8)$$

where D is the diameter and R is the high-speed-camera frame number before rupture, either an integer or an interpolated noninteger value.

The burst-test results are summarized in Appendix A. In Appendix B, a selected number of tests is described in greater detail; i.e., the temperature, internal-pressure, and diametral-strain values are listed as a function of time from the start of the temperature ramp until rupture occurs. Also, values at the onset of plastic instability, determined from Eq. 8, are indicated for each test.

B. Effective Stress and Strain

For multiaxial stress situations, a simple representation of the work and strain-rate hardening, analogous to uniaxial stress situations,[36] is no longer feasible. Three principal plastic strains must be considered. The functional relationship between the principal plastic strains and strain rates that accurately incorporate work and strain-rate hardening have not been established for isothermal biaxial deformation under a simple hydrostatic pressure loading, let alone the complex anisotropic behavior of Zircaloy tubes. However, some form of an approximate expression for the "equivalent" stress and strain would be more meaningful than using only engineering quantities such as an engineering hoop stress[9,15] determined from the geometry of the undeformed cladding and maximum internal pressure.

In this investigation, a practical and reasonable approximation that takes account of transient-heating deformation will be adopted for the equivalent stress and strain. An effective stress $\bar{\sigma}$ and strain $\bar{\epsilon}$ have been defined in terms of the principal stresses and strains by

$$\bar{\sigma} = \frac{1}{\sqrt{2}}\left[(\sigma_z - \sigma_\theta)^2 + (\sigma_\theta - \sigma_r)^2 + (\sigma_r - \sigma_z)^2\right]^{1/2} \tag{9}$$

and

$$\bar{\epsilon} = \frac{\sqrt{2}}{3}\left[(\epsilon_z - \epsilon_\theta)^2 + (\epsilon_\theta - \epsilon_r)^2 + (\epsilon_r - \epsilon_z)^2\right]^{1/2}, \tag{10}$$

where the subscripts z, θ, and r refer to the axial, tangential, and radial components, respectively. In calculating effective strain up to the onset of plastic instability, we assumed that the tangential strain was equal to diametral strain and the axial strain was negligible. Beyond the point of onset of local ballooning, the assumption is no longer valid; therefore, the effective strain value is, at best, a crude approximation. The radial-strain value was obtained from the incompressibility equation

$$(1 + \epsilon_\theta)(1 + \epsilon_r)(1 + \epsilon_z) = 1 \tag{11}$$

and the condition that $\epsilon_z \simeq 0$.

For the purpose of calculating the effective stress up to the onset of plastic instability, the tangential stress is given by

$$\sigma_\theta = \frac{P(t)D(t)}{2h(t)}, \tag{12}$$

where P(t) is the internal pressure and h(t) is the wall thickness. We assumed that the biaxiality b is

$$b = \sigma_\theta/\sigma_z \simeq 2.0 \tag{13}$$

and the radial stress component $\sigma_r \simeq 0$. The wall thickness h(t) was calculated from

$$\left(\frac{D}{2}\right)^2 - \left(\frac{D}{2} - h\right)^2 = \left(\frac{D_0}{2}\right)^2 - \left(\frac{D_0}{2} - h_0\right)^2, \tag{14}$$

where D_0 and h_0 are the initial diameter and wall thickness of the tube, respectively.

The effective stress is plotted as a function of temperature in Fig. 11 at several isostrain values up to the strain at the onset of plastic instability. These results were obtained from burst tests at a heating rate of ~115°C/s in vacuum. Similar results for lower heating rates are discussed in Sec. V and VI.

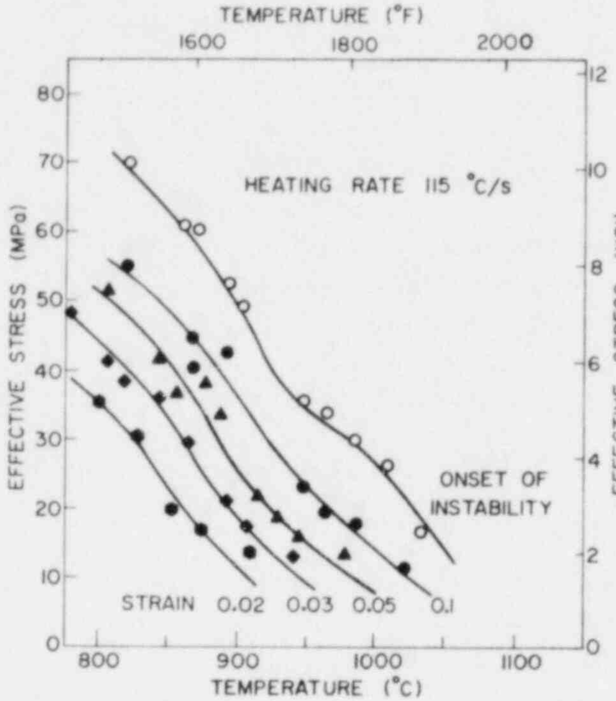

Fig. 11. Effective Stress vs Temperature at Constant Effective Strain Values Obtained from Zircaloy Tube-burst Tests at Initial Heating Rate of 115°C/s. Effective stress and temperature at onset of plastic instability are also shown. ANL Neg. No. 306-76-28.

C. Circumferential, Axial and Radial Strains at Rupture

The maximum circumferential strain was calculated from the circumference of the ruptured tube minus the width of the rupture. A nonstretchable cellophane tape was used to measure the circumference. When the cladding was burst in the α- or predominantly α-phase region, i.e., at T $\lesssim$ 840°C, the measured circumferential strain was not necessarily equal to the diametral strain determined from the high-speed-camera frames, because of significant asymmetry of the ballooned and ruptured cross section with respect to the center of axis. At higher temperatures, the ballooning is more symmetric, and a pinhole-type rupture usually occurs. Consequently, the measured circumferential strains were in good agreement with the values obtained from diametral-strain measurements.

The axial strains were determined from direct measurement of the change in cladding length after burst. The axial contraction was assumed to be limited to only the 75-mm-long portion of the cladding, which contained the ballooned region. This is a reasonable approximation for tubes with a single balloon; however, in some cases, multiple balloons form in tubes with a long heated length ($\gtrsim$ 300 mm) or with large temperature nonuniformity produced by a stack of pellets. In a later case, meaningful axial strains cannot be computed solely from a length measurement. Also, for tubes that rupture in the α- or predominantly α-phase temperature range, the effect of bending of the tube on the length measurement must also be considered.

Radial strains in the region of maximum circumferential expansion were determined from measurements of the wall thickness from polished cross sections of the tube. Care was taken to ensure that the tube axis was perpendicular to the cross section.

D. Other Physical Parameters of Importance

In addition to circumferential, axial, and radial strains in the rupture location, the maximum uniform diametral expansion of the tube and the area of the burst opening are important considerations relative to the reduction in water flow rate and fission-product release from the fuel rod, respectively, during the reflood stage of a LOCA. The magnitude of the uniform diametral expansion of a tube is determined by a number of parameters, e.g., internal pressure, heating rate, temperature of the onset of plastic instability, steam oxidation, and local temperature nonuniformity during transient heating. The uniform diametral strain was determined from the high-speed-camera frames for individual burst tests. For unconstrained and mandrel-constrained cladding, the maximum uniform diametral expansion in a steam environment did not exceed ~0.17 for heating rates between 5 and 120°C/s. The uniform diametral strain was somewhat lower for pellet-constrained cladding because of the large local temperature nonuniformity in the tube; however, multiple ballooned regions formed at different axial locations.

The area of the burst opening can influence the ingress of steam and the amount of oxidation of the inner surface of the cladding as well as the egress of fission products (and possibly fuel fragments) to the coolant. The burst opening of the tubes was photographed at a magnification of ~1.75X and the projected opening area was measured by a planimeter. For rupture temperature $\gtrsim 900°C$, the burst opening is quite small, i.e., $\leq 8\ mm^2$, whereas at lower temperatures, the burst openings range between ~5 and 130 mm^2. The results are given in Appendix C.

V. DEFORMATION CHARACTERISTICS IN VACUUM ENVIRONMENT

A. Effect of Burst Temperature on Circumferential Strain

The information obtained on the circumferential strain at failure as a function of burst temperature (Fig. 12) for tests without a mandrel (unconstrained) is in good agreement with the results of other investigators.[9,11-12] The results in Fig. 12 represent the simplest type of burst behavior; i.e., the biaxiality is ~2.0 up to the moment of rupture. Heating rate has a significant effect on the circumferential strain for bursts in an α-phase region ($\leq$810°C); however, the strain is not dependent on this variable when rupture occurs at temperatures in the ($\alpha + \beta$)- or β-phase ranges ($\geq$840°C).

The rupture-strain-versus temperature plot, which is a failure criterion based on strain, shows two superplastic strain maxima at ~815 and ~1050°C. Figure 12 also shows a prominent third strain maximum at ~1220°C, which was not observed in the previous investigations. The uniaxial-tension-test results[36] on recrystallized Zircaloy-4 indicate strain maxima at 1200 and 1300°C, in addition to those at 850 and 1000°C, for strain rates of 3.3×10^{-4} and 3.3×10^{-3} s^{-1}, respectively. However, β-phase grain growth was significant in the uniaxial tension tests, and this influences the height and location of the strain maxima at temperatures above 1200°C.

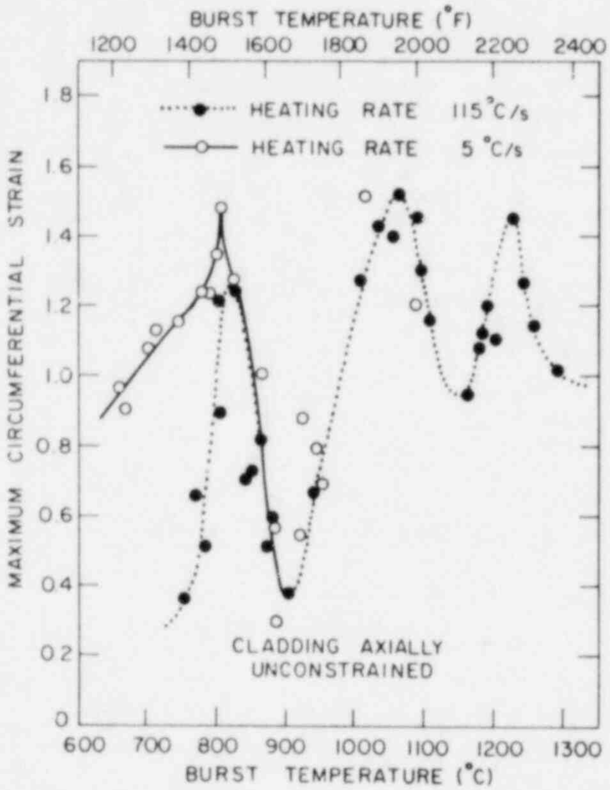

Fig. 12. Maximum Circumferential Strain at Rupture vs Burst Temperature for Unconstrained Zircaloy-4 Cladding at Heating Rates of 115 and 5°C/s in Vacuum. ANL Neg. No. 306-76-255 Rev.

The sharp decrease in the circumferential strain for burst temperatures between 1050 and 1150°C has been verified by Brzoska et al.[27] in similar experiments. Figure 12 illustrates the extreme sensitivity of the maximum circumferential strain on the burst temperature.

B. Effect of Burst Temperature on Failure Mode

The failure mode of the cladding is also strongly dependent on the burst temperature. Three distinct failure modes were observed over different temperature ranges. For ruptures in the α- or predominantly α-phase region (≤840°C), the burst is violent and the opening is square-shape, as shown in Fig. 13A. For bursts in the two-phase region (840-980°C), the burst opening is narrow and characterized by the V-shape splits at both ends, as shown in Fig. 13B. In the β-phase region (>980°C), pinhole ruptures occur and the cladding surface exhibits the characteristic "orange-peel" appearance (Fig. 13C). The deformation mechanisms associated with the different failure modes are discussed in Sec. V.G in conjunction with microstructural analyses of the material in the burst area.

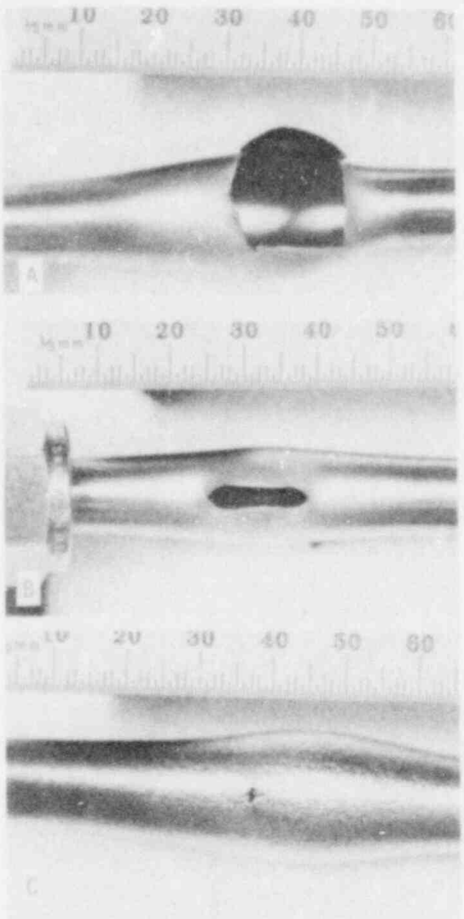

Fig. 13

Typical Failure Modes for Zircaloy Cladding in (A) α- or Predominantly α-phase Region, (B) (α + β)-phase Region, and (C) β-phase Region, Showing Pinhole Opening and "Orange-peel" Surface Appearance. ANL Neg. No. 306-78-397.

C Axial Contraction of Tube during Rupture

Axial strains, for tubes in which the circumferential strains are shown in Fig. 12, were measured and plotted against burst temperature. The results are shown in Fig. 14. The tubes exhibited significant contraction at burst temperatures ≤840°C and negligible length changes at higher burst temperatures (T ≥870°C). No increases in tube length were observed.

As the heating rate decreases from 115 to 5°C/s, the circumferential and axial strain maxima in Fig. 14 shift from ~825 to 810°C. For a given heating rate, the maxima in the axial contraction and circumferential strain occur at the same temperature. In the α-phase region (T ≤ 810°C), large axial contraction is associated with large circumferential expansion. However, in the two-phase region (810 ≤ T ≤ 980°C), in which the circumferential strains are of similar magnitude, axial contraction is larger for the higher heating rate, i.e., 115°C/s. As the material is heated through the $\alpha \rightarrow \beta$ phase transformation, the ratio of the amount of α to β phase is greater, at a given temperature, for the higher heating rate. Consequently, the anisotropy of the tube is more pronounced for the high-heating rate deformation.

The pronounced mechanical anisotropy of the α-phase cladding results from the tube texture (see Fig. 2) and the limited slip systems that operate in the hexagonal-close-packed (hcp) material. Since most of the total circumferential strain occurs after the onset of plastic instability, i.e., during the ballooning stage, the deformation process involves high strain rates (0.1-10 s^{-1}),

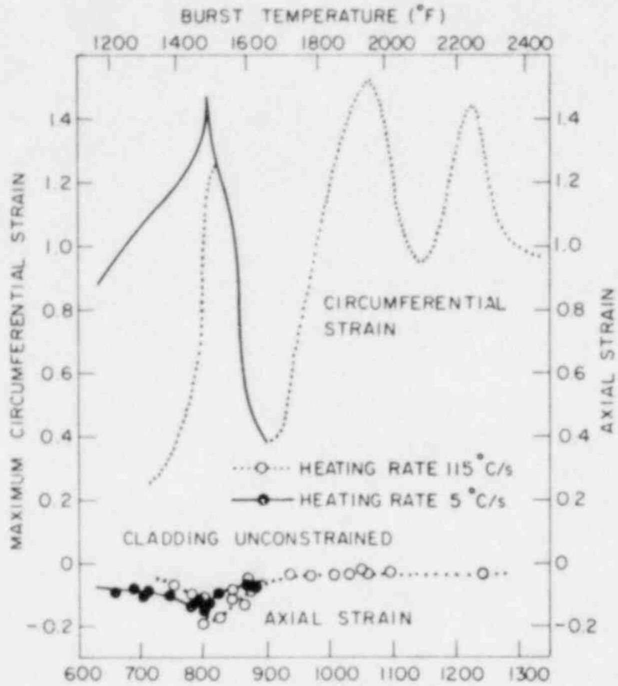

Fig. 14. Axial and Circumferential Strains vs Burst Temperature for Unconstrained Zircaloy Cladding at Heating Rates of 5 and 115°C/s in Vacuum. ANL Neg. No. 306-76-258 Rev.

and dislocation slip is the predominant mechanism. Slip on prism and basal planes has been reported in α-phase Zircaloy.[37] Since the Burgers vector in either case is parallel to the basal plane, deformation in the radial direction (i.e., wall thinning) is difficult for cladding with the texture shown in Fig. 2. Since accommodation of tangential expansion solely by wall thinning is difficult in an incompressible material, significant axial contraction occurs in α-phase cladding.

Figure 15 shows an example of a ballooning and cladding contraction sequence for a preoxidized specimen isothermally deformed at 751°C. When an internal mandrel or pellet stack is present inside the tube, the cladding can contract axially to a limited extent, and further ballooning from that point on must be accommodated by radial wall thinning only. Under these circumstances, the circumferential strain of the axially constrained tube will be significantly less than for unconstrained cladding.

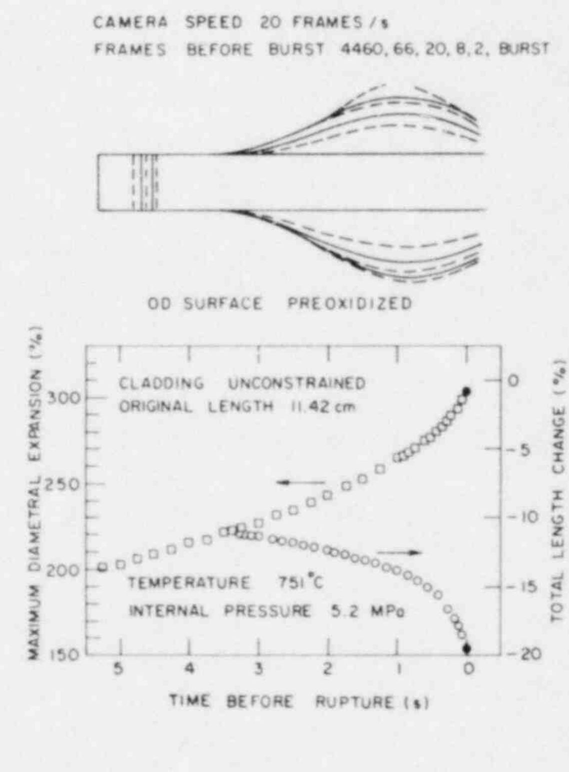

Fig. 15

Localized Ballooning Characteristics and Diametral and Axial Strains during an Isothermal Stress-rupture Test on Preoxidized Zircaloy-4 Cladding in Vacuum at 751°C and Internal Pressure of 5.2 MPa. ANL Neg. No. 306-76-254.

D. Mechanism of Tube Bending during Rupture under Transient-heating Conditions

Bending of the tube during rupture can occur because of two independent effects: jet blast and nonuniform axial contraction. During rapid heating, a circumferential temperature variation may develop during uniform expansion and ballooning of the tube. If the cladding ruptures in the α- or predominantly α-phase region under this situation, asymmetric axial contraction occurs. Circumferential expansion accompanied by axial contraction is greater on the high-temperature side of the tube. Consequently, the tube bends toward the side of ballooning (high-temperature side) and eventually ruptures. Figure 16 shows a sequence of high-speed-camera frames of a tube that ruptured in steam at 740°C (initial pressure 13.8 MPa, heating rate 55°C/s). At 0.5 s before rupture, the tube expansion was uniform; however, during localized ballooning, the specimen bent in the direction of the rupture, i.e., ~15°, immediately before rupture occurred.

In contrast to bending before rupture, as shown in Fig. 16, the bending caused by jet blast takes place at the moment of rupture. As the stored gas volume and internal pressure increase, the rupture becomes more violent and bending occurs to a greater extent. Therefore, for rupture in the α-phase region, i.e., $\leq$840°C, the combined jet blast and the nonuniform axial-contraction effects cause significant bending of the tubes. Because of lower internal pressures, thinning of the tube wall, and different failure modes, tube bending becomes negligible at temperatures $\geq$840°C.

E. Effect of Axial Constraint on Deformation

Information on maximum circumferential strain versus burst temperature, similar to the data in Fig. 12, was obtained for cladding tubes that contained an alumina mandrel (Fig. 4). The internal mandrel acts as a constraint against either axial contraction or bending of the tube. Figure 17 compares circumferential strain and burst temperature for constrained and unconstrained cladding at a heating rate of 5°C/s in vacuum. A similar comparison at a heating rate of 115°C is shown in Fig. 18. The circumferential strain for constrained cladding is considerably lower at both heating rates; however, the difference is more pronounced for bursts in α- or predominantly α-phase region.

Figure 19 is a plot of diametral strain versus temperature for unconstrained Zircaloy-4 cladding for different internal pressures and a heating rate of 115°C/s. Similar information for mandrel-constrained cladding is shown in Fig. 20. The effective stress and strain, obtained from the data in Figs. 19 and 20 and Eqs. 9 and 10, are shown as a function of temperature in Figs. 21 and 22 for the unconstrained and mandrel-constrained cladding, respectively. The transient-deformation results in Figs. 19-22 provide a possible explanation for the large decrease in the circumferential expansion

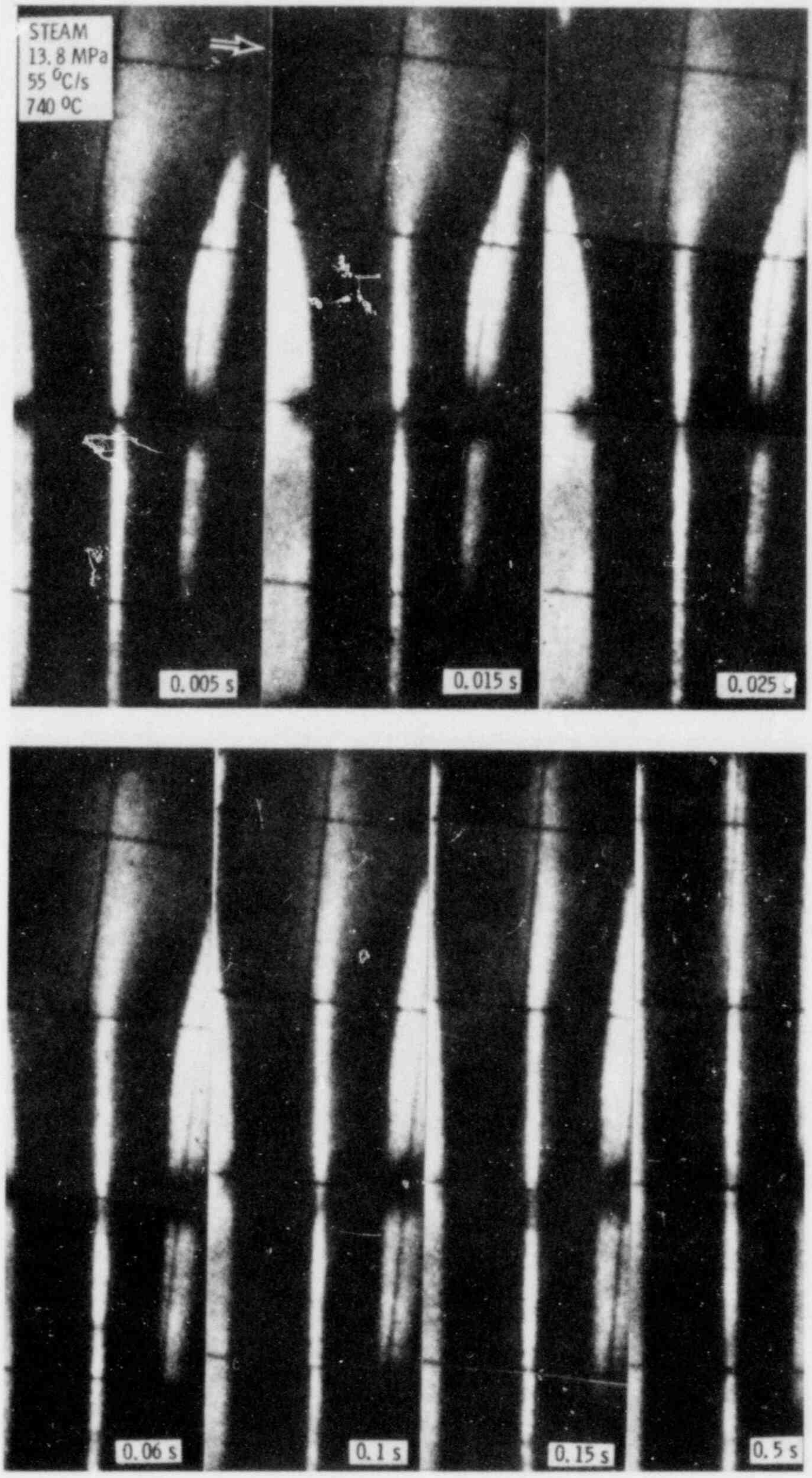

Fig. 16. High-speed-camera Frames of Ballooning Deformation of Zircaloy-4 Cladding Ruptured in Steam at 740°C at Heating Rate of 55°C/s and Initial Internal Pressure of 13.8 MPa. Note the extent of specimen bending toward the rupture location (arrow) as ballooning progresses. ANL Neg. No. 306-76-158.

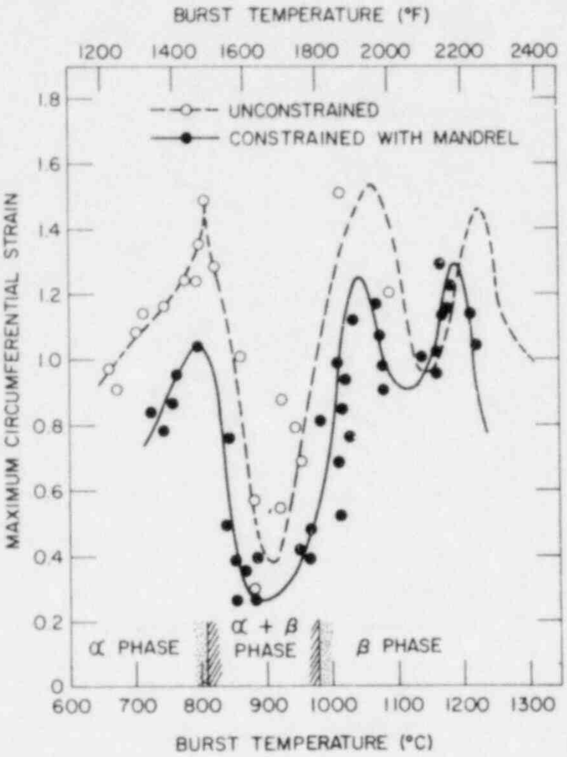

Fig. 17. Maximum Circumferential Strain at Rupture vs Burst Temperature for Unconstrained and Mandrel-constrained Zircaloy-4 Cladding at Heating Rate of 5°C/s in Vacuum. ANL Neg. No. 306-77-469.

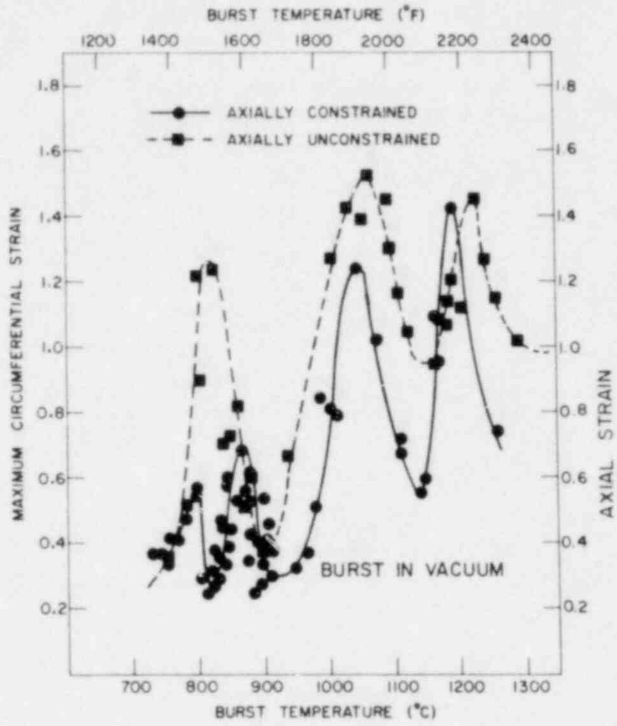

Fig. 18. Maximum Circumferential Strain at Rupture vs Burst Temperature for Unconstrained and Mandrel-constrained Zircaloy-4 Cladding at Heating Rate of 115°C/s in Vacuum. ANL Neg. No. 306-76-98 Rev.

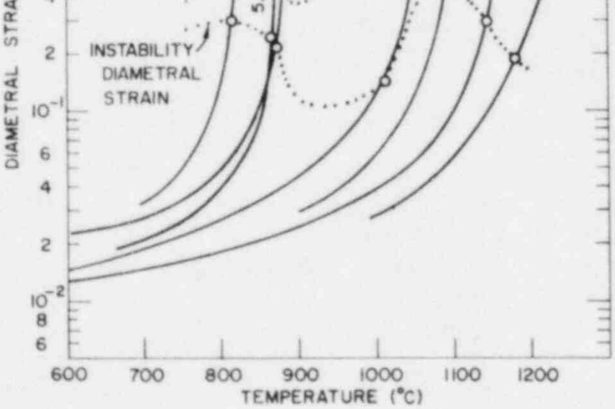

Fig. 19

Diametral Strain vs Temperature for Unconstrained Zircaloy-4 Cladding for Different Internal Pressures at Heating Rate of 115°C/s in Vacuum. ANL Neg. No. 306-76-84 Rev.

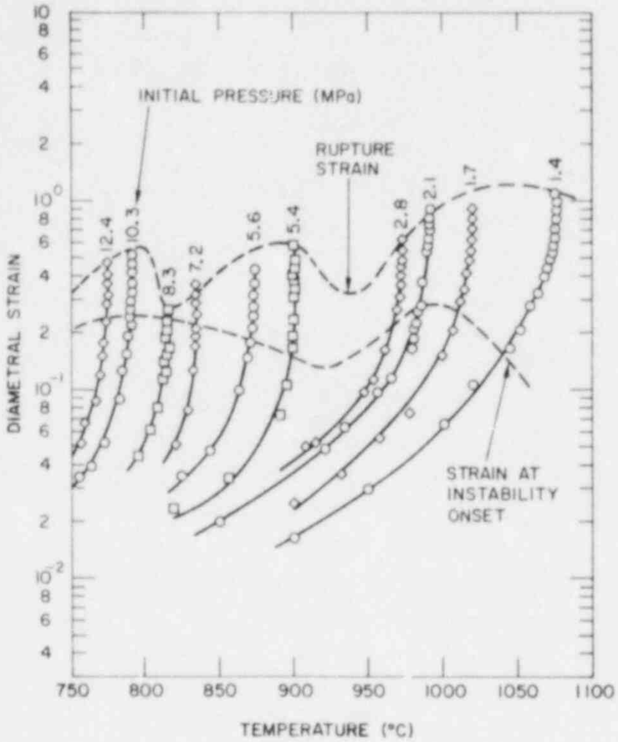

Fig. 20. Diametral Strain vs Temperature for Mandrel-constrained Zircaloy-4 Cladding for Different Internal Pressures at Heating Rate of 115°C/s in Vacuum. ANL Neg. No. 306-77-463 Rev.

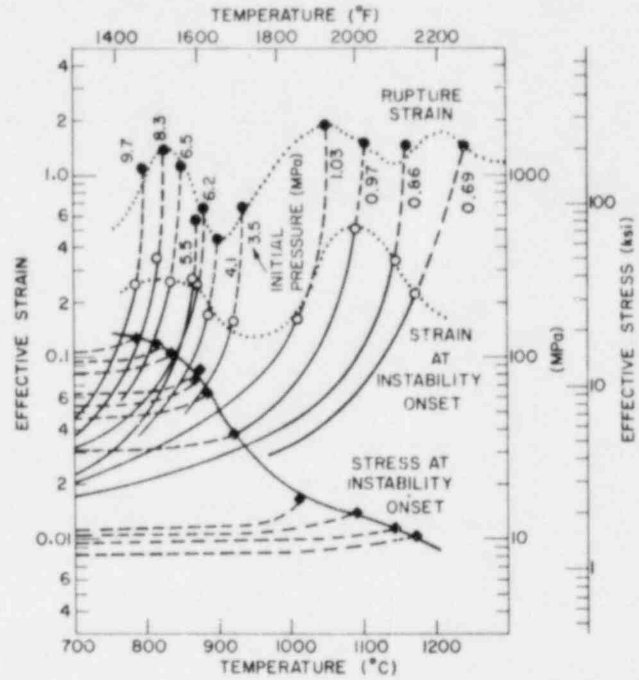

Fig. 21. Effective Stress and Strain as a Function of Temperature up to Onset of Plastic Instability for Unconstrained Zircaloy-4 Cladding at Heating Rate of 115°C/s in Vacuum. ANL Neg. No. 306-76-83 Rev.

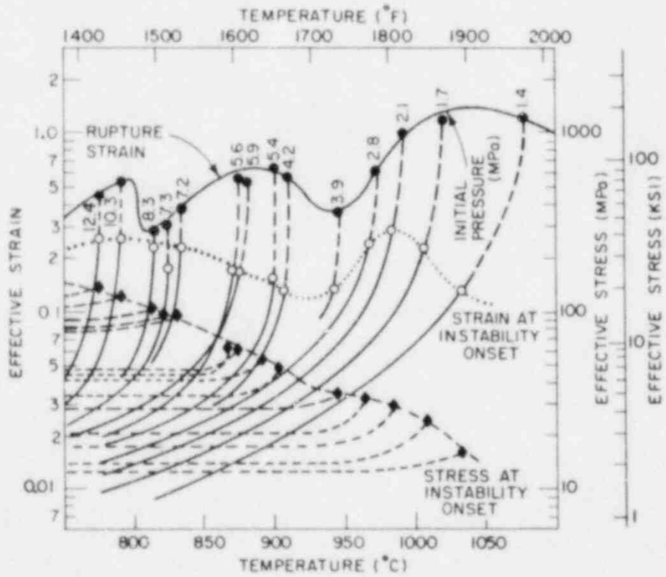

Fig. 22

Effective Stress and Strain as a Function of Temperature up to Onset of Plastic Instability for Mandrel-constrained Zircaloy-4 Cladding at Heating Rate of 115°C/s in Vacuum. ANL Neg. No. 306-76-24 Rev.

of axially constrained tubes (Fig. 18), particularly for burst temperatures ≤870°C. Since the deformation behavior of the constrained and unconstrained tubes (Figs. 22 and 21, respectively) is nearly identical up to the onset of plastic instability, the large difference in the circumferential strain at failure for temperatures between 750 and 850°C occurs during the ballooning stage. In both cases, the cladding remains in the α phase up to ~840°C during the high-heating-rate tests, although this temperature is slightly higher than the equilibrium α-phase boundary for Zircaloy that contains ~0.1 wt % oxygen, i.e., ~810°C.[34] Large tangential strain, uniform wall thinning, and axial contraction of the unconstrained tube occur in the α-phase material near the superplastic maximum at ~820°C.

When the axial contraction becomes equal to the gap clearance between the end plugs and mandrel, the cladding-ballooning deformation is constrained and no additional contraction is possible. From this point to rupture, the biaxiality, i.e., $b \equiv \sigma_\theta/\sigma_z$, changes during ballooning because of the induced reaction force exerted by the axial constraint. The biaxiality condition depends on the ballooning mode and the axial gap clearance between the mandrel and the cladding end plugs. If the gap distance is quite small, the biaxiality condition changes immediately after the onset of plastic instability. To examine conditions that lie between the totally constrained and unconstrained cases, an "axial-constraint parameter" γ can be defined as

$$\gamma = \frac{1}{\epsilon_z^0}\left(\frac{L}{L_0} - 1\right), \tag{15}$$

where

L_0 = original length of the cladding,

L = length of the cladding minus the gap clearance (i.e., length of insert rod plus end plugs), and

ϵ_z^0 = axial strain at the same rupture temperature as for an unconstrained tube, e.g., the data from the lower curves in Fig. 14.

The effect of biaxiality on tangential strain is illustrated schematically in Fig. 23 for several axial constraint conditions: unconstrained ($\gamma \geq 1$), partially constrained ($1 > \gamma > 0$), and totally constrained ($\gamma = 0$).

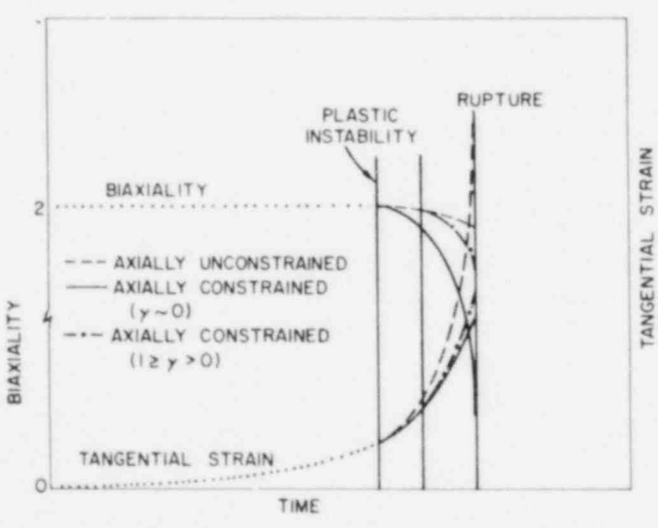

Fig. 23

Schematic Representation of Effect of Different Axial-constraint Parameters on Biaxiality and Circumferential Strain in Plastic-instability Region during Tube-burst Test. ANL Neg. No. 306-76-97.

Bending of the tube during localized ballooning prior to burst, discussed previously, was minimal for the mandrel-constrained cladding, even for bursts at ≤840°C. However, as Källström[38] indicated, if the bending is significant, the state of biaxiality will be more complicated than the situation just mentioned. Then the combined effects of biaxiality and symmetry during ballooning deformation should be considered.

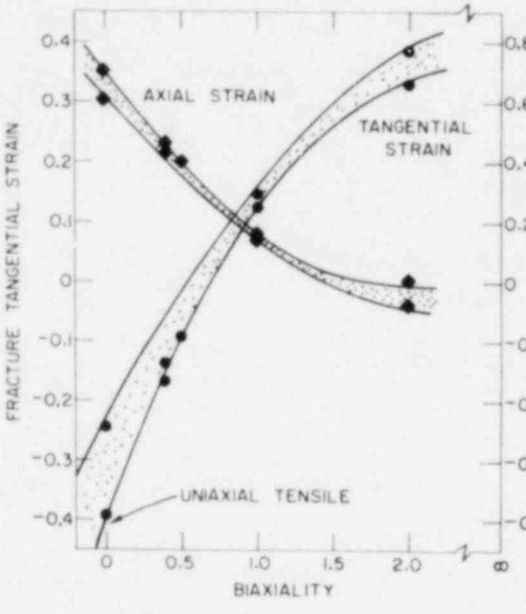

Fig. 24. Effect of Biaxiality on Room-temperature Tangential and Axial Fracture Strains of Zircaloy-2 Tubing. Constructed from data of Mehan.[39] ANL Neg. No. 306-76-85.

Mehan,[39] Maki and Ooyama,[40] and Miyamoto et al.[41] have investigated the effect of biaxiality on the plastic-flow and fracture behavior of Zircaloy-2 at room temperature. Their data show a large decrease in fracture tangential strain as the biaxiality decreases. This is illustrated in Fig. 24, constructed from Mehan's data.[39] Similar behavior has been reported by Dressler and Matucha[42] for Zircaloy-4 at 400°C. Although we are not aware of isothermal data of this type for Zircaloy-4 at high temperatures, we would expect similar behavior for burst temperatures in the α-phase region below ~850°C. Figure 25 shows diametral-strain/time curves for partially constrained specimens (γ = 0.20 and 0.49) tested under otherwise identical conditions. The lower circumferential strain associated with the smaller γ value at a burst temperature of ~830°C and the deformation data in Fig. 22 (axially constrained) and Fig. 21 (axially unconstrained) are consistent with the variation of tangential strain with time shown schematically in Fig. 23 for different axial-constraint conditions. Figure 26 shows the circumferential strain at failure as a function of burst temperature for different degrees of axial constraint, i.e., axial-gap distances of 2.5, 5.9, and 112 mm. The circumferential-strain peak decreases and moves to higher temperatures as the axial-gap distance decreases.

Fig. 25

Effect of Degree of Axial Constraint on Maximum Diametral Strain during Ballooning Deformation of Zircaloy-4 Cladding in Vacuum at Heating Rate of 115°C/s. ANL Neg. No. 306-76-162.

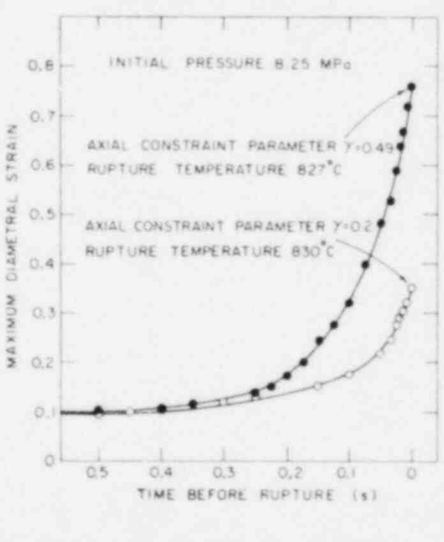

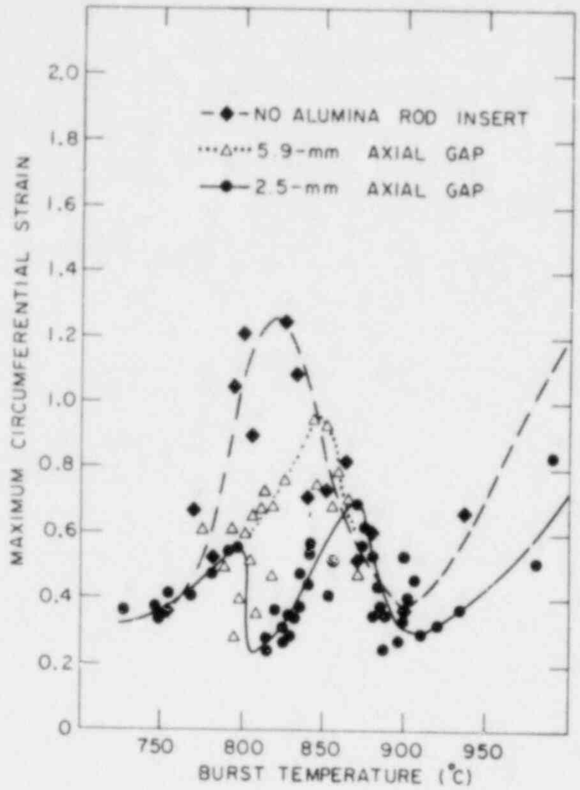

Fig. 26. Maximum Circumferential Strain at Failure vs Burst Temperature for Three Axial-constraint Conditions for Zircaloy-4 Cladding at Heating Rate of 115°C/s in Vacuum. ANL Neg. No. 306-76-161 Rev.

The presence of strain maximum and minimum at 790 and 820°C, respectively, for the high-heating-rate (115°C/s) tests was unexpected, but the evidence is conclusive (see also Fig. 18). The maximum and minimum were observed only for tightly constrained tubes burst in vacuum at this heating rate. The strain peak was not observed for burst tests in steam under analogous conditions. These results are explained in Sec. VI.D in conjunction with the effect of steam oxidation on the deformation behavior.

F. Effect of Heating Rate on Deformation

The effect of heating rate on the deformation and rupture behavior of Zircaloy cladding has been examined at ~5, 55, and 115°C/s. Figure 27 shows the circumferential strain at failure as a function of the burst temperature for axially constrained tubes at the three heating rates. A constant gap distance of 2.5 mm between the end plugs and the alumina mandrel was maintained in these tests, and the L/L_0 value was 0.983. The failure strains are not dependent on the heating rate for burst temperatures >920°C; however, the first strain maximum increases and shifts to lower temperatures as the heating rate decreases. The strain maximum decreases ~70°C for the range of heating rates.

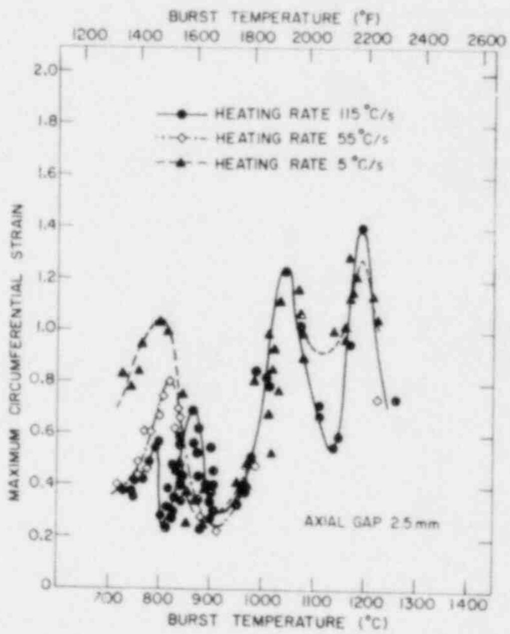

Fig. 27

Effect of Heating Rate on Rupture Temperature and Maximum Circumferential Strain of Axially Constrained Zircaloy-4 Cladding Burst in Vacuum. ANL Neg. No. 306-76-92.

The dependence of the temperature of the strain maximum near 825°C and the height of the strain peak on heating rate can be explained on the basis of strain-rate and microstructural considerations. Strain-rate hardening of the material increases as the heating rate increases; i.e., less time is available for annealing and relaxation of the cladding. Therefore, a higher temperature is required to achieve the same amount of effective strain without failure. Also, the fraction of α phase that exists at a given temperature above the equilibrium α-phase boundary is greater for the higher-heating-rate tests. As a result, the microstructure most favorable for large deformation will occur at higher temperatures for higher heating rates. The variation of the height of the strain peak with heating rate is believed due primarily to the strain rate. Similar observations have been made for the heating-rate dependence of the circumferential strain maxima for 20% cold-worked Type 316 stainless steel cladding.[43]

Figure 28 shows the effect of initial pressure on the rupture temperature for the axially constrained cladding at heating rates of 5, 55, and 115°C/s and the unconstrained cladding at 115°C/s. The faster strain rate associated with the 115°C/s heating rate results in higher burst temperatures, which are not a function of the axial restraint. The nearly horizontal pressure-insensitive portion of the 5°C/s curve at ~850°C is in the temperature range in which the Zircaloy cladding exhibits a relatively large strength decrease as the temperature increases. The burst-temperature dependence on heating rate is shown in Fig. 29 for internal pressures between 0.7 and 14 MPa. For high internal pressure, i.e., ≥3.5 MPa, the heating-rate effect is small. However, the effect is significant for low internal pressures which result in bursts in the β-phase region.

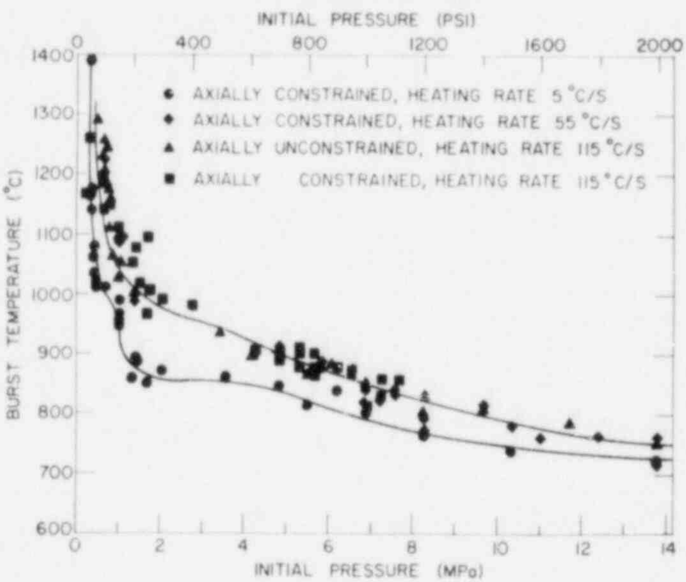

Fig. 28. Dependence of Rupture Temperature on Initial Internal Pressure for Zircaloy-4 Cladding Burst in Vacuum at Different Heating-rate and Axial-constraint Conditions. ANL Neg. No. 306-76-86 Rev.

The effect of heating rate on the cladding strength is also evident from Fig. 30, in which the effective stress at the onset of plastic instability is plotted against temperature. The high-heating-rate experiments result in a higher instability stress at any temperature, which can be attributed to the increase in the flow stress at the higher strain rates. These results are consistent with the data in Fig. 28, which show that the burst strength is higher for a higher heating rate. As expected, axial constraint does not have a significant effect on the instability stress at the 115°C/s heating rate. Figure 31 compares reported values for engineering hoop stress at rupture,[9,11,12] obtained from tests at different heating rates, with the effective stress at instability from Fig. 30. The literature data fall between the low- and high-heating-rate results of the present investigation. The increase in the instability stress, by as much as a factor of three for heating rates between 5 and 115°C/s, indicates the importance of heating rate on the instability and failure stresses of Zircaloy cladding.

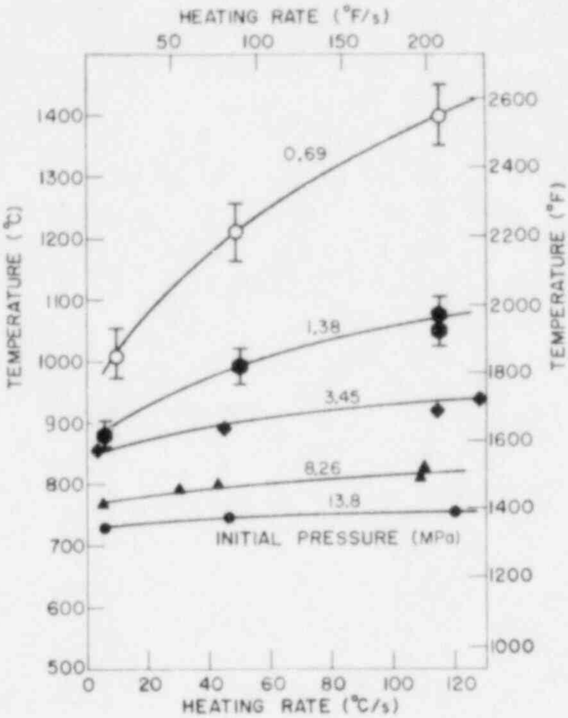

Fig. 29. Effect of Heating Rate on Rupture Temperature of Axially Constrained Zircaloy-4 Cladding Burst in Vacuum at Various Initial Internal Pressures. ANL Neg. No. 306-76-94 Rev.

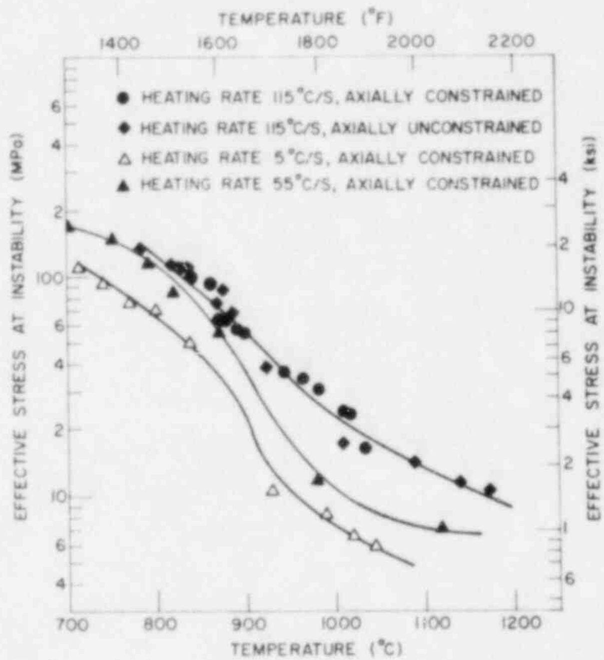

Fig. 30. Effective Stress at Onset of Plastic Instability vs Temperature for Zircaloy-4 Cladding Deformed under Different Axial-constraint and Heating-rate Conditions in Vacuum. ANL Neg. No. 306-76-88 Rev.

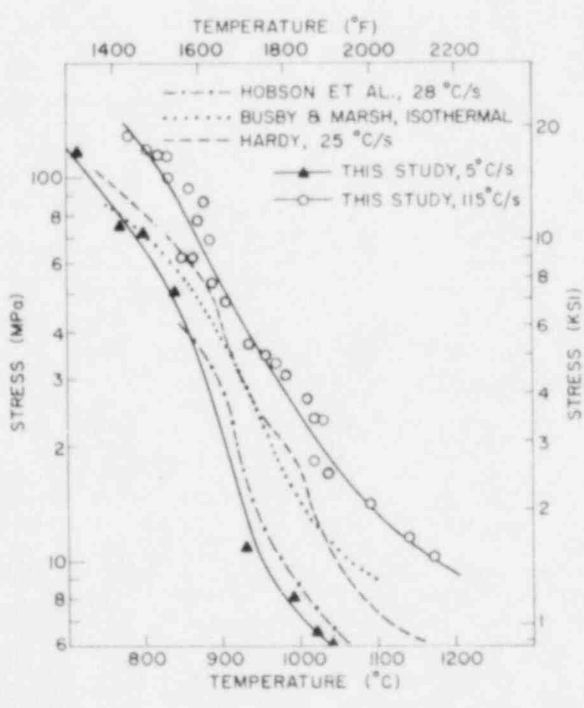

Fig. 31

Comparison of Effective Stress at Instability and Engineering Hoop Stress at Rupture for Zircaloy-4 Cladding at Different Temperatures. ANL Neg. No. 306-76-33 Rev.

Diametral-strain-versus-temperature curves for mandrel-constrained cladding at a heating rate of 115°C/s were shown in Fig. 20. Similar information at heating rates of 55 and 5°C/s are shown in Figs. 32 and 33, respectively. The corresponding effective stress and strain data up to the onset of plastic instability are plotted as a function of temperature in Figs. 34 and 35 for heating rates of 55 and 5°C/s, respectively. From a comparison of the data in Figs. 22, 34, and 35, the strains at the onset of plastic instability at temperatures in the α- or predominantly α-phase region are of similar magnitude (0.2-0.3) at the three heating rates. Consequently, the comparatively high circumferential strain at the 5°C/s heating rate can be attributed tc the greater localized ballooning.

Figure 36 is a three-dimensional plot of the circumferential strain at failure for as-received mandrel-constrained tubing as a function of two critical LOCA-related parameters, i.e., the initial pressure in the cladding and the heating rate.

G. Microstructural Observations

The microstructure of a tube burst in the α-phase region shows either partially recrystallized and elongated grains (Fig. 37A) or fully recrystallized equiaxed α grains (Fig. 37B). No evidence of dynamic recrystallization was

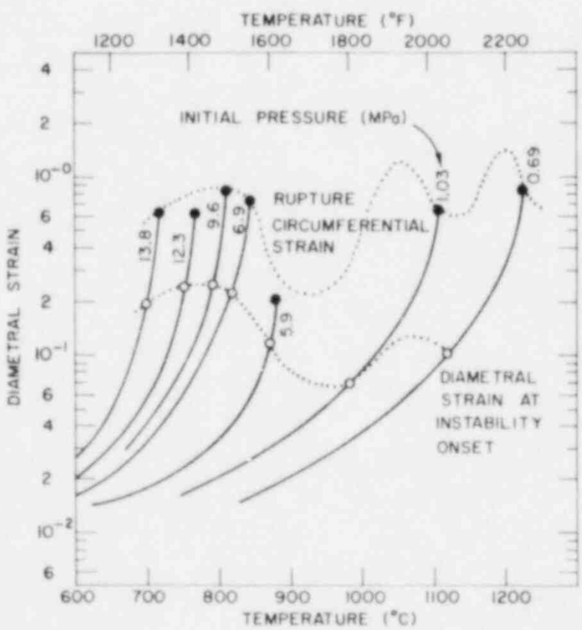

Fig. 32. Diametral Strain vs Temperature for Axially Constrained Zircaloy-4 Cladding Burst in Vacuum for Different Internal Pressures at Heating Rate of 55°C/s. ANL Neg. No. 306-76-126 Rev.

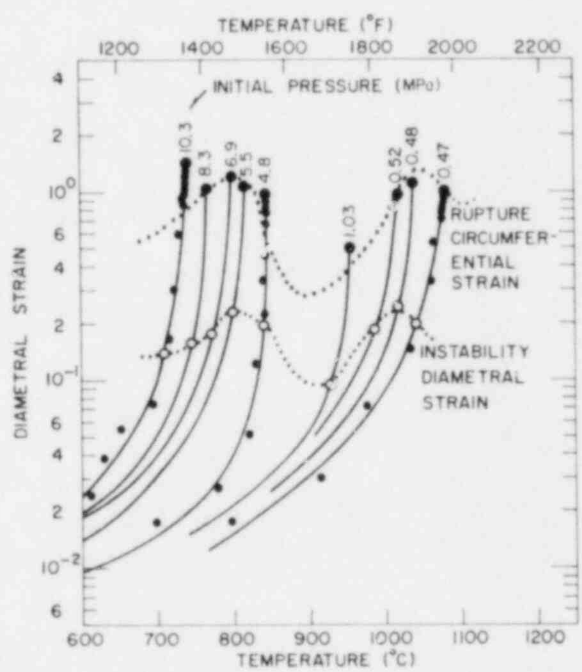

Fig. 33. Diametral Strain vs Temperature for Axially Constrained Zircaloy-4 Cladding Burst in Vacuum for Different Internal Pressures at Heating Rate of 5°C/s. ANL Neg. No. 306-76-96 Rev.

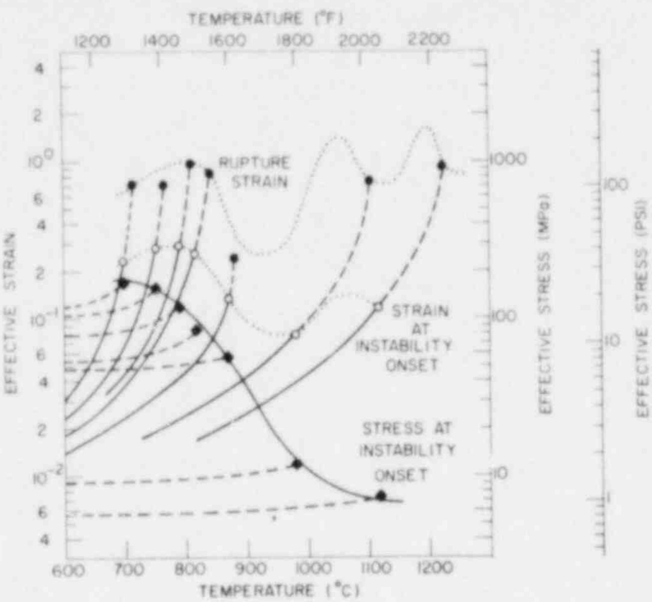

Fig. 34. Effective Stress and Strain as a Function of Temperature up to Onset of Plastic Instability for Mandrel-constrained Zircaloy-4 Cladding Burst at Heating Rate of 55°C/s in Vacuum. ANL Neg. No. 306-76-128.

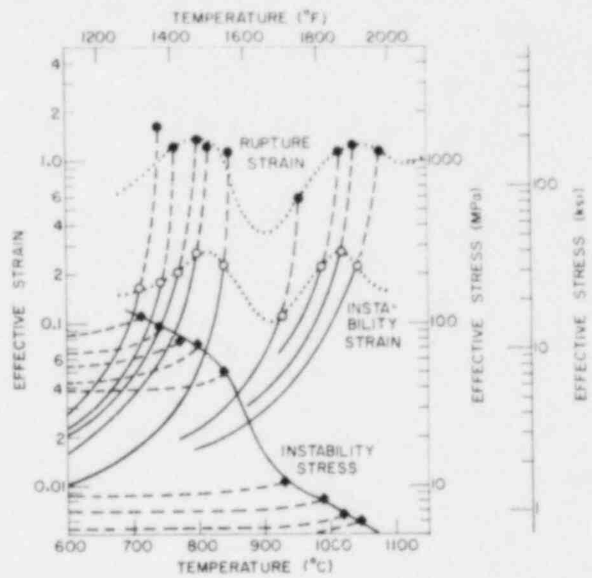

Fig. 35. Effective Stress and Strain as a Function of Temperature up to Onset of Plastic Instability for Mandrel-constrained Zircaloy-4 Cladding Burst at Heating Rate of 5°C/s in Vacuum. ANL Neg. No. 306-76-93.

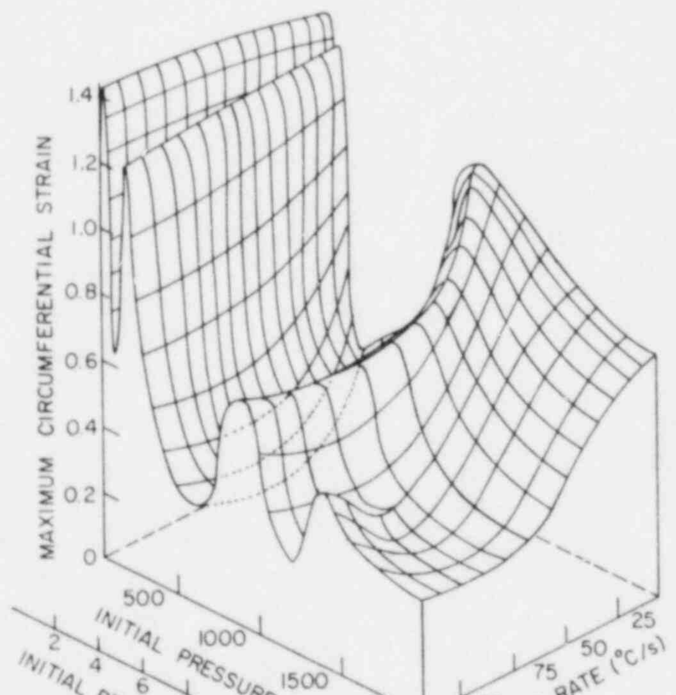

Fig. 36

Effect of Initial Internal Pressure and Heating Rate on Maximum Circumferential Strain for Axially Constrained Zircaloy-4 Cladding Burst in Vacuum. ANL Neg. No. 306-76-129 Rev.

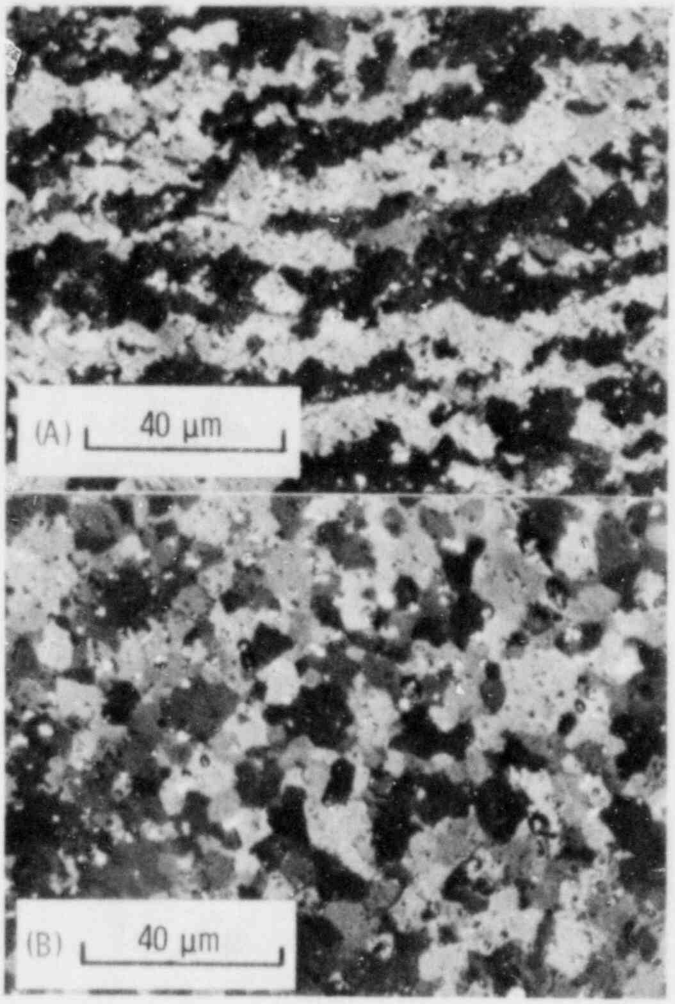

Fig. 37

Microstructures of Zircaloy-4 Cladding That Ruptured at Temperatures near Superplastic Deformation Maximum at 820°C. Etched and anodized, polarized light. (A) Heating rate of 5°C/s, axially constrained. Maximum circumferential expansion of 103% for rupture at 800°C. (B) Heating rate of 115°C/s, axially unconstrained, maximum circumferential expansion of 124% for rupture at 826°C. ANL Neg. No. 306-76-78.

observed. The extent of recrystallization appears to be sensitive to burst temperature. The more complete recrystallization in Fig. 37B is probably a result of the higher burst temperature. The exact mechanism responsible for the large circumferential strain peak near 820°C (Fig. 27) is not clearly understood. Grain-boundary sliding of equiaxed α grains may play a significant role in addition to deformation by dislocation glide. If the grain-boundary-sliding contribution is significant, for instance at a low heating rate of 5°C/s, the effect of axial constraint would be smaller (Fig. 17) than for the high-heating-rate bursts (Fig. 18).

Several observations have been made concerning the size and distribution of second-phase particles after deformation at temperatures in an α-phase region. In the fracture-tip region of specimens ruptured at a low heating rate, second-phase particles are larger and more densely populated (see Fig. 38) than in the as-received material, i.e., >4-5 μm, compared with 0.5-1 μm. Figure 39 shows SEM fractographs of a specimen burst at 816°C at a heating rate of 5°C/s in vacuum. A typical ductile fracture surface with shear dimples is shown in Fig. 39A. The arrows identify the coarse second-phase particles, one of which is magnified in Fig. 39B. Normal second-phase particles in the

Zircaloy-4 have a composition of $Zr_xFe_5Cr_2$, obtained from the dispersive X-ray spectrum analysis in Fig. 40. The aluminum and copper signals in the spectrum originate from the specimen mount.

Similar results for Zircaloy-4 have been reported by Van der Sande and Bement.[44] In contrast to the as-received material, the second-phase particles shown in Fig. 39 exhibit a higher concentration of chromium, as evidenced in Fig. 41. The above observations concerning the size and distribution of second-phase particles suggest that, at low heating rates, the effect of precipitation hardening by the second-phase particles on deformation at temperatures in the α-phase region may be significant.

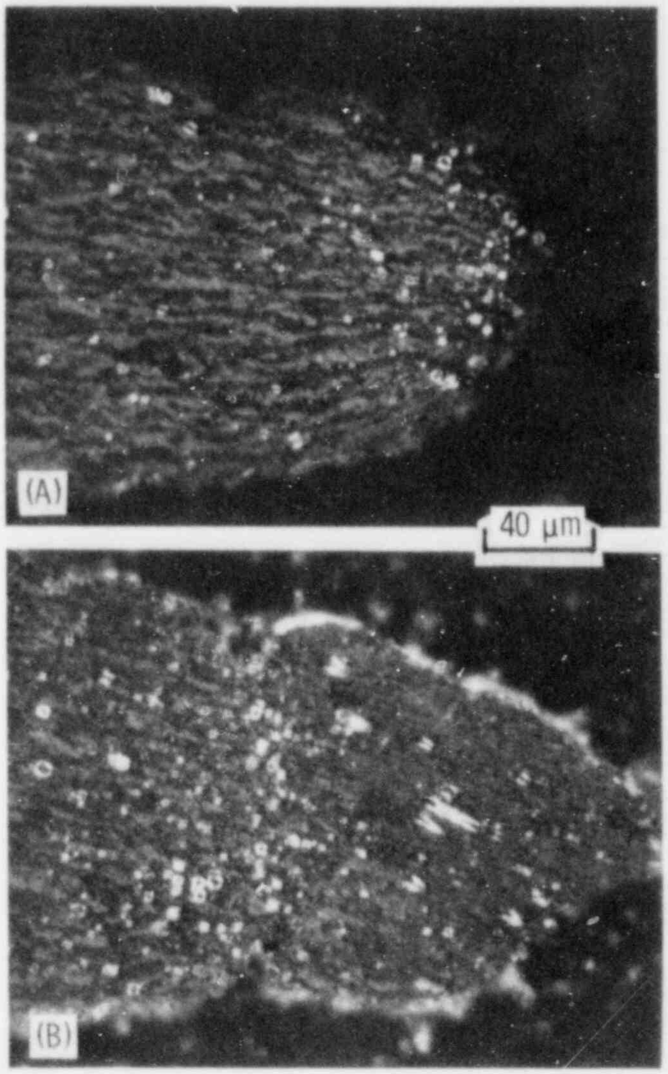

Fig. 38

Second-phase Particle Precipitation near Fracture Tip of Zircaloy-4 Cladding Burst in Vacuum at Heating Rate of 7°C/s. Burst Temperature (A) 741°C, (B) 690°C. ANL Neg. No. 306-77-479.

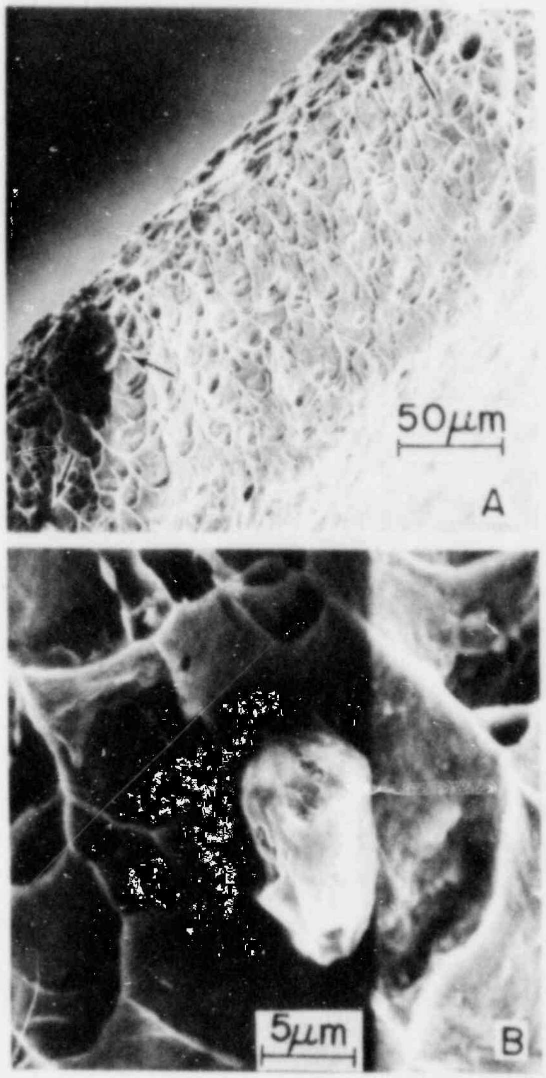

Fig. 39

Scanning-electron Micrographs of Large Second-phase Particles Precipitated in Fracture-tip Region of Zircaloy-4 Cladding Burst at 816°C in Vacuum at Heating Rate of ~5°C/s. (A) Fractograph showing shear dimples and particles; (B) larger magnification of a particle. ANL Neg. No. 306-77-41.

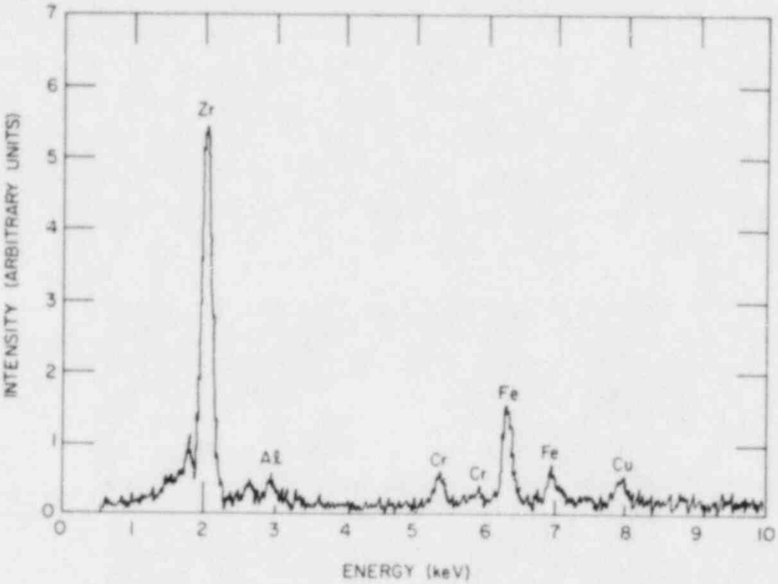

Fig. 40. X-ray Energy Spectrum of Normal Second-phase Particles in As-received Zircaloy-4. ANL Neg. No. 306-77-474.

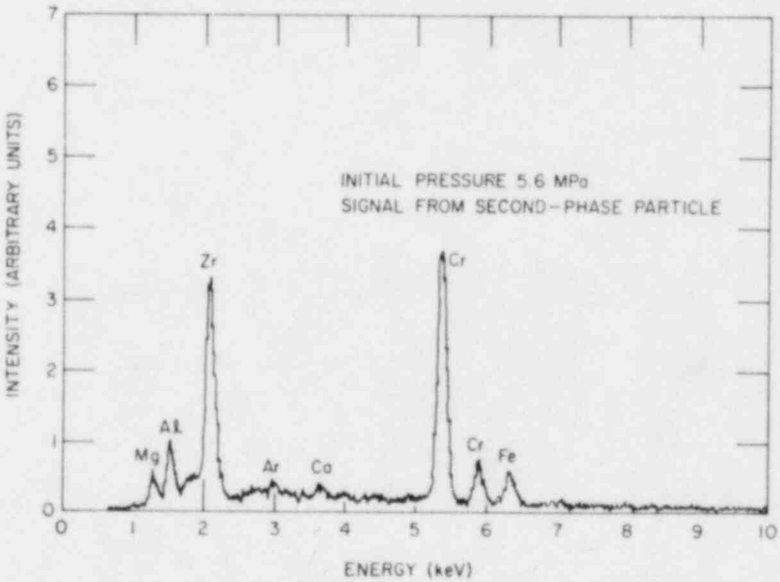

Fig. 41. X-ray Energy Spectrum of Second-phase Particles in Fracture-tip Region of Zircaloy-4 Cladding Burst at 816°C in Vacuum at Heating Rate of 5°C/s. The spectrum was obtained from the particle in Fig. 39B. ANL Neg. No. 306-77-461.

Rupture of Zircaloy-4 cladding in the β-phase region is characterized by a pinhole failure (Fig. 13C) and an "orange-peel" surface appearance. The "orange-peel" surface irregularities, present on both the inner and outer surfaces of the tube, are comparable to the grain size of the β-phase cladding. When the cladding deforms under a small internal pressure (≤0.5 MPa), rupture occurs at high temperature after a relatively long heating period. In this situation, β-phase grain growth is significant; hence the "orange-peel" surface irregularities are much larger. Figure 42 shows a scanning-electron micrograph of the surface of a tube heated to 1255°C/s, at 115°C/s, deformed for 38 s under an internal pressure of 0.29 MPa to a circumferential strain of 0.26, and cooled to room temperature without rupture occurring. Grain-boundary sliding in the β-phase material is evident from the micrograph.

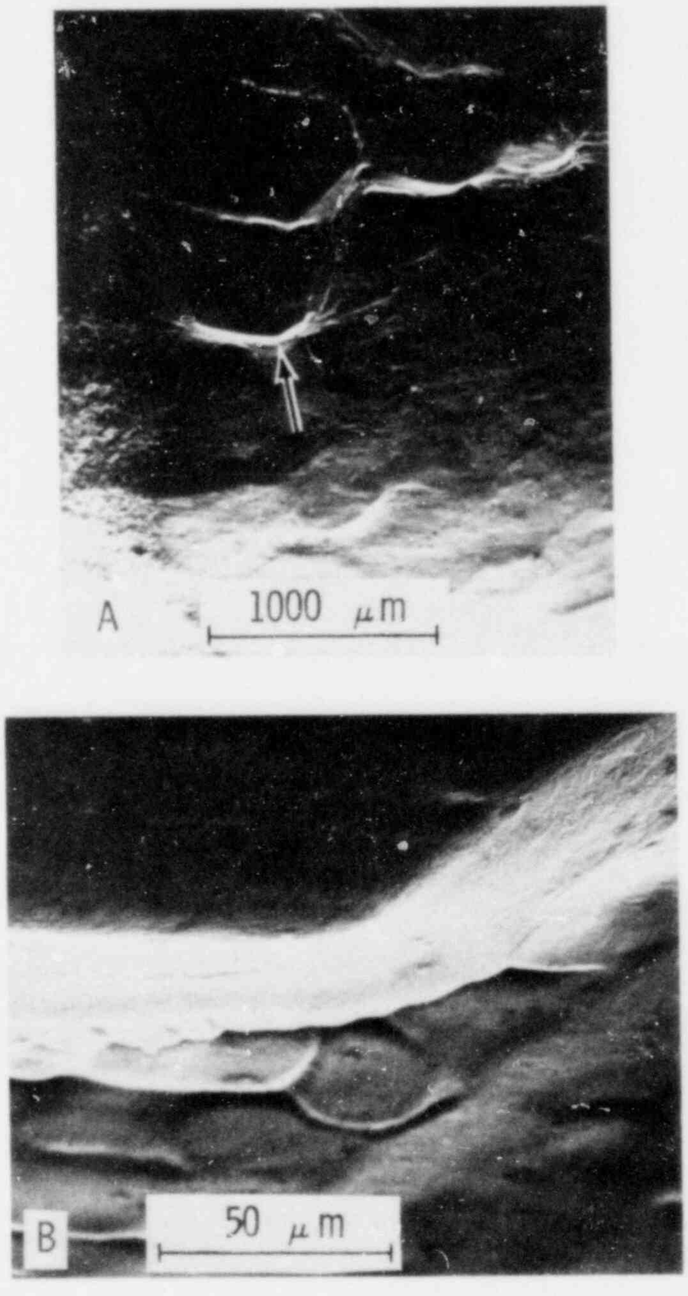

Fig. 42. Low- and High-magnification Scanning-electron Micrographs of Zircaloy-4 Cladding Tube Showing Surface Irregularities Formed by β-phase Grain-boundary Sliding. The tube was deformed in vacuum at 1255°C for 38 s under an internal pressure of 0.29 MPa to a circumferential strain of 0.26. ANL Neg. No. 306-76-133.

Figure 43 shows the cross section of another tube, which ruptured at 1050°C at a heating rate of 115°C/s (maximum circumferential strain 1.25). Both the inside and outside surfaces show irregularities that result in the "orange-peel" appearance. In this specimen, the rim-α structure[6] was formed at the grain boundaries of the previous β phase; thus the β-phase grain structure can be clearly identified. As indicated by the arrows in Fig. 43, the troughs of the surface irregularities coincide with the β-phase grain boundaries. This indicates that grain-boundary sliding is the mechanism responsible for the "orange-peel" surface appearance and for the significant portion of the total deformation of a tube ruptured at $T \geq 1000°C$.

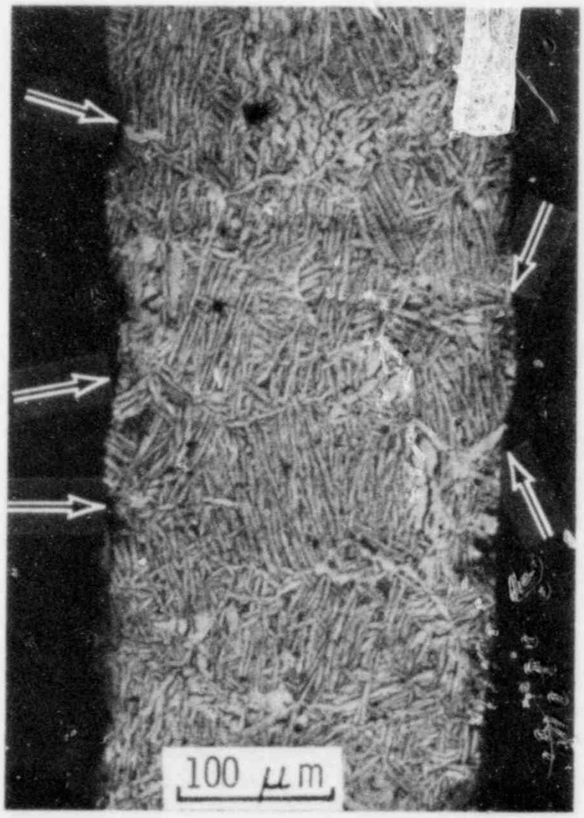

Fig. 43

Micrograph of Cross Section in Ballooned Region of Zircaloy-4 Tube Ruptured at 1050°C in Vacuum at Heating Rate of 115°C/s, Showing Inside- and Outside-surface Irregularities Formed by Grain-boundary Sliding. Arrows indicate troughs at the surface, which are responsible for the "orange-peel" effect. The underlying β-phase grain boundaries are made evident by the rim-α structure formed during the $\beta \rightarrow \alpha'$ transformation. ANL Neg. No. 306-77-37.

VI. DEFORMATION CHARACTERISTICS IN STEAM ENVIRONMENT

To investigate the effect of oxidation on the deformation characteristics, burst tests similar to those in vacuum were performed in steam at heating rates of 5, 55, and 115°C during which simultaneous oxidation and deformation occurred as the specimen temperature increased. Under these conditions, the load-bearing fraction of the cladding wall, i.e., either α phase or α/β composite, contains dissolved oxygen with a sharp concentration gradient near the surface. The dissolved oxygen increases the strength of the metallic region of the cladding. However, the oxide layer reduces the metal thickness and introduces additional tangential stress because of volume expansion, which thereby weakens the cladding. These factors work against each other and complicate the deformation and burst behavior of the cladding. Furthermore, the dissolved oxygen may modify the concentration of the second-phase particles normally present in the cladding and thereby affect the cladding strength. This section presents the tube-burst results and deformation characteristics of Zircaloy-4 cladding in steam environment.

A. Effect of Heating Rate on Deformation

In Sec. V.F, the heating rate was shown to influence the deformation behavior of Zircaloy-4 cladding at temperatures in the α- and $(\alpha + \beta)$-phase regions via a strain-rate hardening mechanism and the morphology (ratio of α- to β-phase material) of the material as it is heated through the $\alpha \rightarrow \beta$ transformation at different rates. In addition to these effects, the extent of oxidation of the cladding in steam increases as the heating rate decreases, and it is well known that oxygen influences the strength and ductility of Zircaloy.[36]

Figure 44 shows the effect of initial internal pressure on the burst temperature of unconstrained Zircaloy-4 cladding in steam at heating rates of 5 and 115°C/s. Figure 45 shows the relationship between the maximum

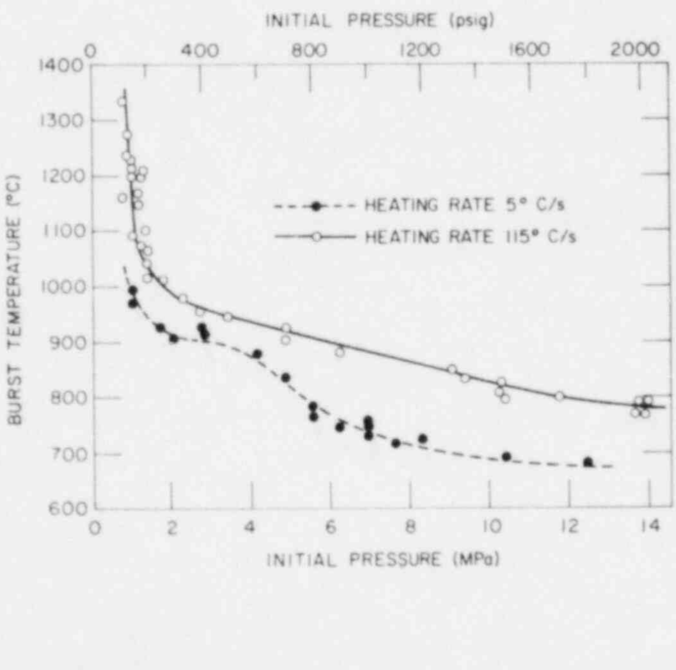

Fig. 44

Burst Temperature vs Initial Internal Pressure for Unconstrained Zircaloy-4 Cladding Tubes Ruptured in Steam at Heating Rates of 5 and 115°C/s. ANL Neg. No. 306-78-411.

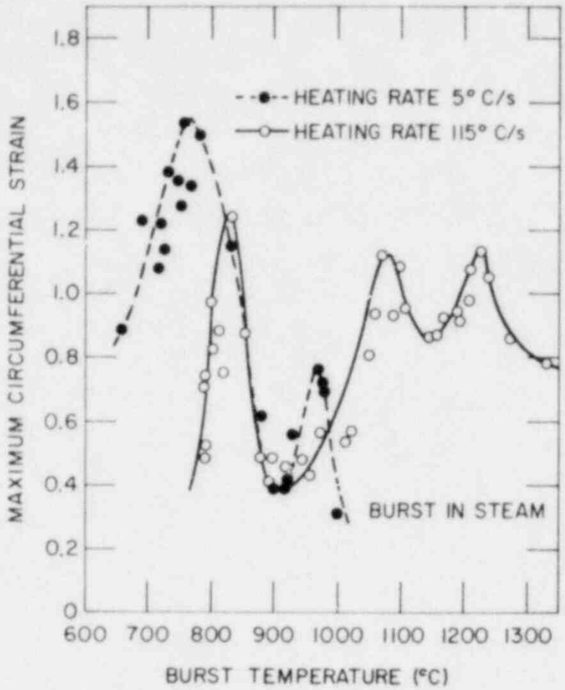

Fig. 45

Maximum Circumferential Strain at Rupture as a Function of Burst Temperature for Unconstrained Zircaloy-4 Cladding Burst in Steam at Heating Rates of 5 and 115°C/s. ANL Neg. No. 306-77-23 Rev.

circumferential strain and the burst temperature at the two heating rates. The effect of heating rate on the burst strain at temperatures ≤840°C is similar to that in a vacuum environment (Fig. 12), since the oxidation kinetics for α-phase Zircaloy are quite slow. However, because of the relatively fast oxidation kinetics at temperatures in the β-phase region, heating rate has a large effect on the burst-strain temperatures at ≥950°C. At a high heating rate (115°C/s), the time-to-rupture is quite short, and consequently, the results for circumferential strain versus rupture temperature are similar to those in a vacuum environment (Fig. 12). At the low heating rate (5°C/s), a small peak in the curve for circumferential strain versus burst temperature is observed at ~980°C. At higher burst temperatures, the circumferential expansion decreases sharply as a result of the significant amount of oxidation associated with the low heating rate. At even lower heating rates, i.e., ≲3°C/s, we expect the strain peak at ~980°C would diminish or disappear entirely.

The deformation and rupture behavior of mandrel-constrained cladding was investigated at heating rates of 5, 55, and 115°C/s in steam. Figure 46 shows the relationships of burst temperature to initial pressure for the three heating rates. Compared to the similar results in a vacuum environment (Fig. 28), the heating-rate effect is more pronounced in steam, particularly for burst temperatures ≤850°C (initial internal pressures ≥5 MPa). As the heating rate decreases from ~115 to 5°C/s, the rupture temperatures exhibit a larger decrease in the steam environment compared to tests in vacuum. This can also be seen from a comparison of the slopes of the curves for burst temperature versus heating rate in Figs. 47 and 29 for the steam and vacuum environments, respectively. Since Zircaloy is a strain-rate-sensitive material between 700 and 1350°C,[36] it is reasonable that the burst temperature increases with an increase in the heating rate. The comparatively large heating-rate dependence of the burst temperature at low internal pressures (<2 MPa) results from the combined effects of strain-rate sensitivity and steam oxidation.

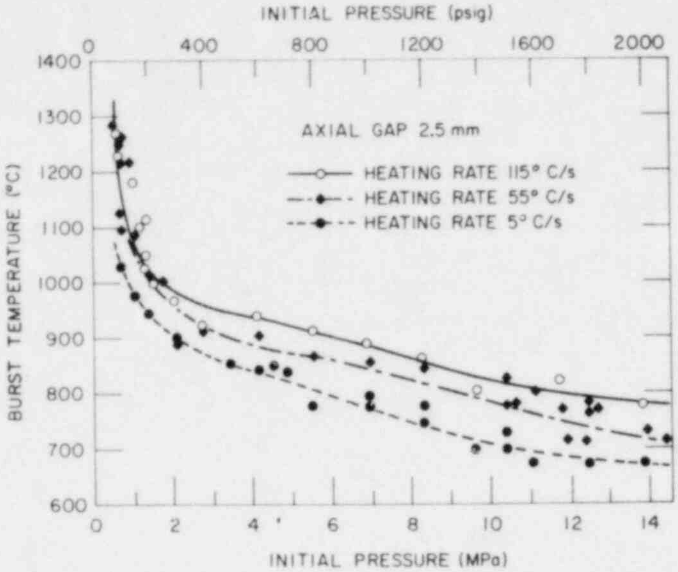

Fig. 46

Burst Temperature vs Initial Pressure for Mandrel-constrained Zircaloy-4 Cladding in Steam at Heating Rates of 5, 55, and 115°C/s. ANL Neg. No. 306-78-398.

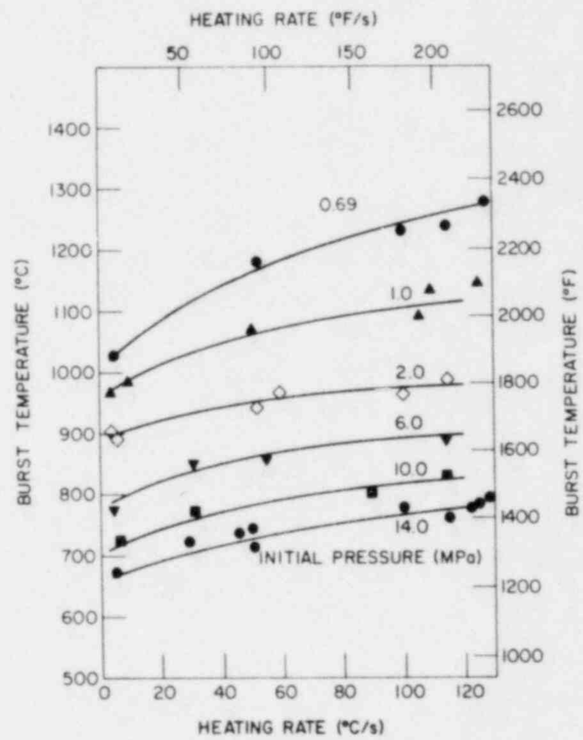

Fig. 47

Effect of Heating Rate on Burst Temperature of Mandrel-constrained Zircaloy-4 Cladding in Steam at Various Initial Internal Pressures. ANL Neg. No. 306-78-408.

In view of the conclusive evidence (Figs. 29 and 47) for the pronounced effect of heating rate on the burst temperature, particularly in a steam environment, this variable should be incorporated into the fuel-element modeling codes to obtain more accurate predictions of burst temperature.

Figure 48 shows the effect of heating rate on the circumferential strain at failure. The results for burst temperatures in the α-phase region ($\leq$840°C) are similar to those obtained in a vacuum environment (Fig. 27); i.e., the magnitudes of the circumferential strain maxima are equivalent at the respective heating rates. However, the strain maxima shift ~25°C to lower temperatures.

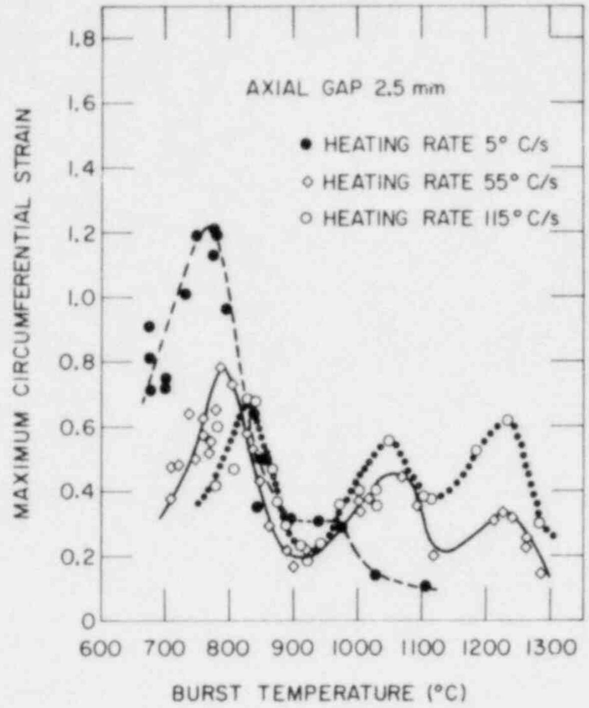

Fig. 48

Maximum Circumferential Strain vs Burst Temperature for Mandrel-constrained Zircaloy-4 Cladding in Steam at Heating Rates of 5, 55, and 115°C/s. ANL Neg. No. 306-78-414.

In contrast to the deformation results in the α-phase region, the maximum circumferential strains for rupture temperatures in the β-phase region (≳980°C) are lower in steam than in vacuum, and the values decrease as the heating rate decreases. Because of severe oxidation of β-phase cladding at a heating rate of ~5°C/s, the strain maximum at ~1050°C is no longer observed.

Figure 49 is a three-dimensional plot showing the effects of heating rate and initial internal pressure on the maximum circumferential strain of the mandrel-constrained cladding burst in steam. Compared to similar results obtained in a vacuum environment (Fig. 36), the prominent strain peaks observed for the lower pressures (≲4 MPa) have nearly disappeared. However, the circumferential expansion of the cladding for internal pressures ≳8 MPa is virtually the same in the two environments. This occurs because the amount of oxidation is insignificant for tubes that rupture in the α-phase region under transient-heating conditions.

Fig. 49

Effect of Initial Pressure and Heating Rate in Steam on Maximum Circumferential Strain of Mandrel-constrained Zircaloy-4 Cladding. ANL Neg. No. 306-76-151 Rev.

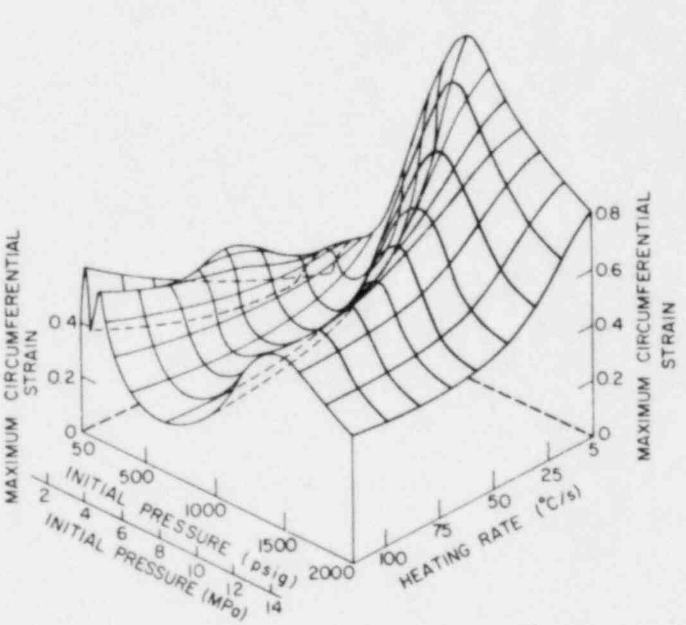

Figures 50-52 show the diametral strain as a function of temperature for the axially constrained cladding at heating rates of 115, 55, and 5°C/s, respectively. The diametral strain at the onset of plastic instability and the circumferential strain at failure are also indicated on the figures. Compared with the results obtained in vacuum (Figs. 20, 32, and 33), the extent of ballooning deformation after the onset of plastic instability decreases significantly at temperatures in the β-phase region.

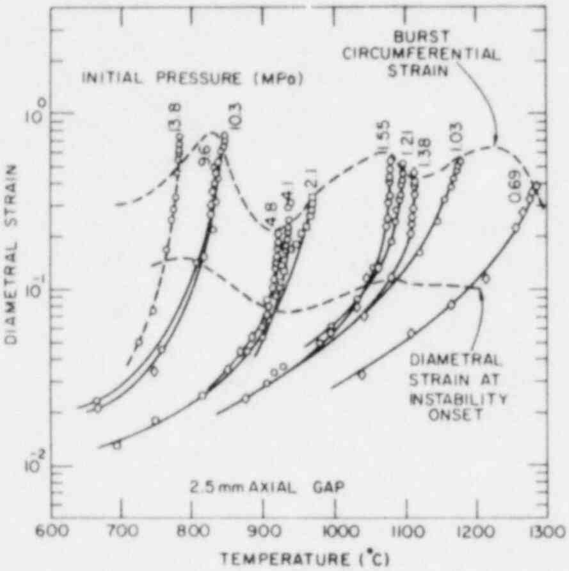

Fig. 50

Diametral Strain vs Temperature for Axially Constrained Zircaloy-4 Cladding at Different Internal Pressures at Heating Rate of 115°C/s in Steam. ANL Neg. No. 306-76-246.

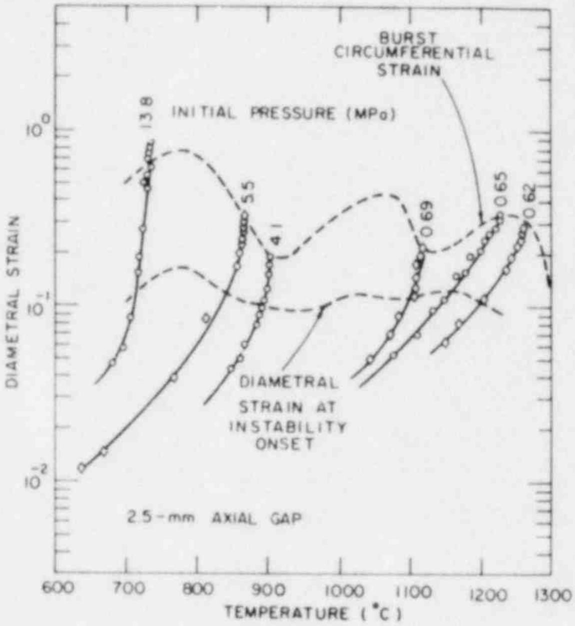

Fig. 51

Diametral Strain vs Temperature for Axially Constrained Zircaloy-4 Cladding at Different Internal Pressures at Heating Rate of 55°C/s in Steam. ANL Neg. No. 306-76-245.

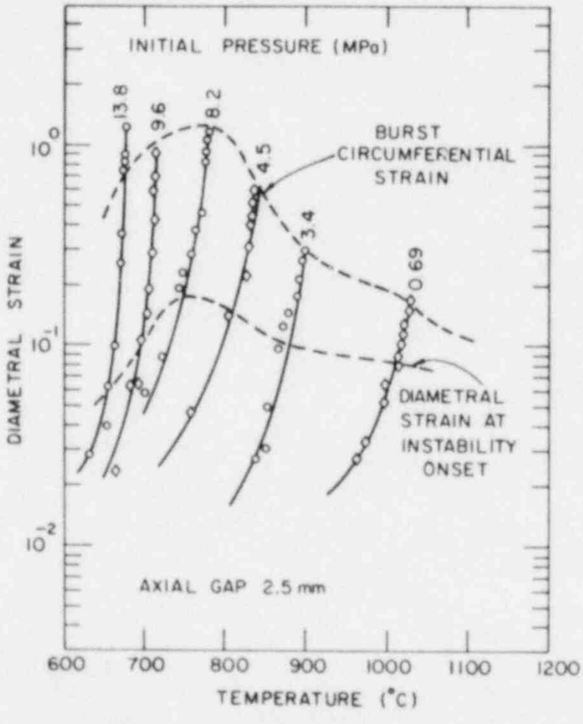

Fig. 52

Diametral Strain vs Temperature for Axially Constrained Zircaloy-4 Cladding at Different Internal Pressures at Heating Rate of 5°C/s in Steam. ANL Neg. No. 306-76-252.

The difference between the diametral and circumferential strains at failure for burst temperatures in the α-phase region results from a greater degree of asymmetric ballooning at the lower temperatures. A comparison of the diametral-strain-time curves in steam and vacuum for similar burst temperatures and heating rates in the β-phase region reveals that oxidation decreases the diametral strain at failure more than the strain at instability; i.e., ballooning deformation in the β-phase region is severely limited. This indicates that different deformation mechanisms for ballooning operate in vacuum and steam in the β-phase region.

B. Comparison of Burst Strength and Strain in Vacuum and Steam

This section discusses the effects of steam oxidation on the burst strength and strain of Zircaloy cladding in greater detail and compares the data obtained in vacuum and steam environments at each heating rate.

Figures 53-55 compare the burst temperature as a function of the initial pressure for mandrel-constrained cladding ruptured in vacuum and steam environments at heating rates of 115, 55, and 5°C/s, respectively. For internal pressures ≳5 MPa, the cladding bursts in the α- or predominantly α-phase region; and for a given internal pressure, the burst temperature increases as the heating rate increases. The increase in the burst temperature in a steam environment compared to vacuum, for internal pressures ≳5 MPa and at a heating rate of 115°C/s (Fig. 53), suggests that oxygen-solute strengthening of the α-phase material is greater than the weakening effect caused by the thin oxide layer at the surface. This situation is reversed for the low heating rate of 5°C/s (Fig. 55). As the heating rate decreases, and

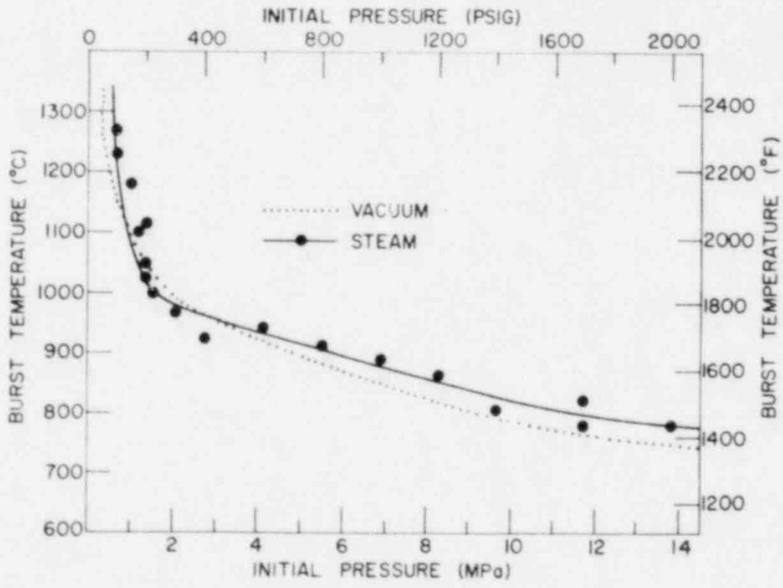

Fig. 53. Burst Temperature as a Function of Initial Internal Pressure for Axially Constrained Zircaloy-4 Cladding in Steam and Vacuum at Heating Rate of 115°C/s. ANL Neg. No. 306-76-127 Rev.

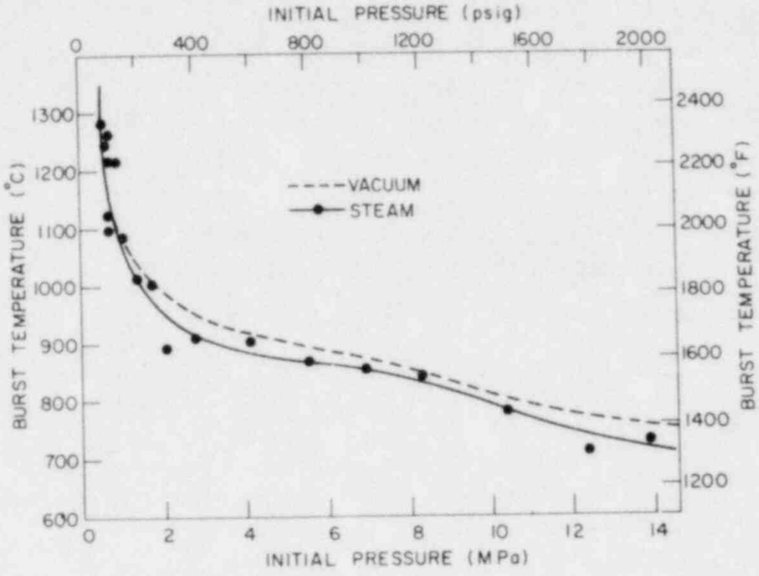

Fig. 54. Rupture Temperature as a Function of Initial Internal Pressure for Axially Constrained Zircaloy-4 Cladding in Steam and Vacuum Environments at Heating Rate of 55°C/s. ANL Neg. No. 306-76-157.

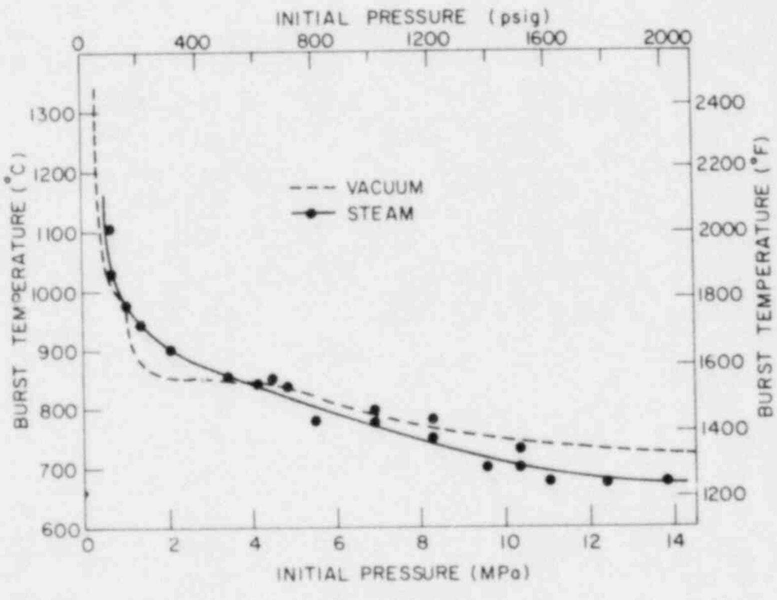

Fig. 55. Rupture Temperature as a Function of Initial Internal Pressure for Axially Constrained Zircaloy-4 Cladding in Steam and Vacuum Environments at Heating Rate of 5°C/s. ANL Neg. No. 306-76-153.

hence the amount of oxidation increases, the load-bearing wall thickness becomes smaller and additional tangential stress is imposed on the cladding by volume expansion of the oxide layer, which lowers the burst temperature.

In the β-phase region above ~980°C, the situation is not as simple as for α-phase material. Solute strengthening of the β phase occurs to a greater extent because of the higher oxygen diffusivity; however, as is discussed in Sec. VI.E, additional weakening of the cladding results from oxide cracking and accelerated oxidation, which lead to localized section thinning.

Figures 56 and 57 show similar comparisons of burst temperature as a function of initial internal pressure for unconstrained Zircaloy-4 cladding at heating rates of 115 and 5°C/s, respectively. For initial pressure ≳5 MPa, the burst temperatures of constrained and unconstrained cladding are virtually the same in each environment. However, at the high heating rate, the burst temperatures in a steam environment (Fig. 56) are higher than those in vacuum, whereas at the lower heating rate, the situation is opposite.

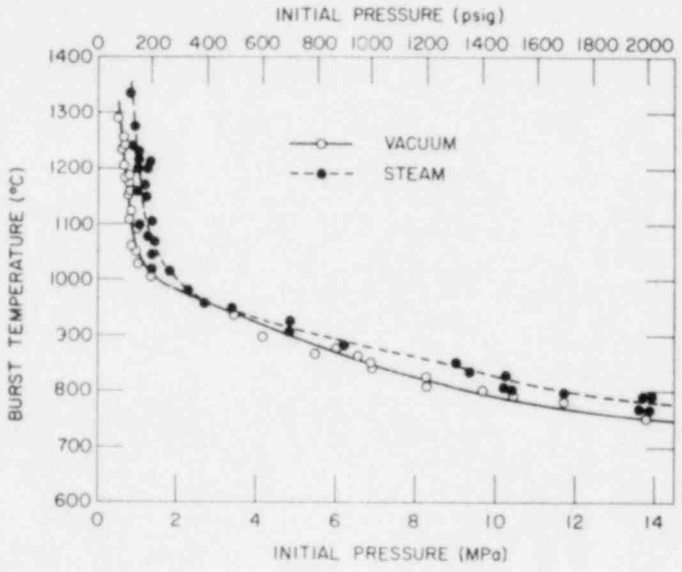

Fig. 56

Burst Temperature as a Function of Initial Internal Pressure for Unconstrained Zircaloy-4 Cladding in Steam and Vacuum at Heating Rate of 115°C/s. ANL Neg. No. 306-78-409.

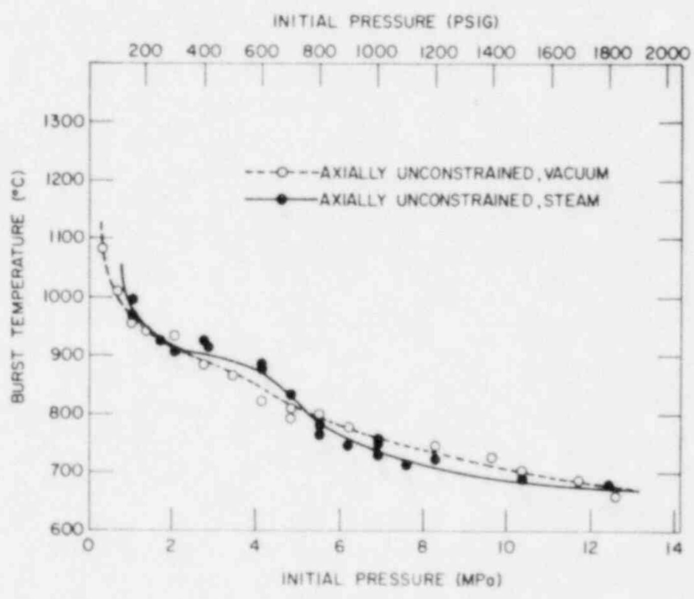

Fig. 57

Burst Temperature as a Function of Initial Internal Pressure for Unconstrained Zircaloy-4 Cladding in Steam and Vacuum at Heating Rate of 5°C/s. ANL Neg. No. 306-77-477.

Figures 58 and 59 compare maximum circumferential strains at failure as a function of burst temperature for unconstrained cladding in steam and vacuum environments for heating rates of 115 and 5°C/s, respectively. At high heating rates in the β-phase region, i.e., ≥980°C, the shape of the strain-versus-burst-temperature curves in the steam and vacuum environments is similar. However, the strain values are somewhat lower for the tests in steam. Because of the severe oxidation during the relatively long test duration associated with the 5°C/s heating rate, the superplastic strain maxima are largely suppressed. The strains corresponding to burst temperatures in the two-phase region are nearly equal in the vacuum and steam environments at both heating rates.

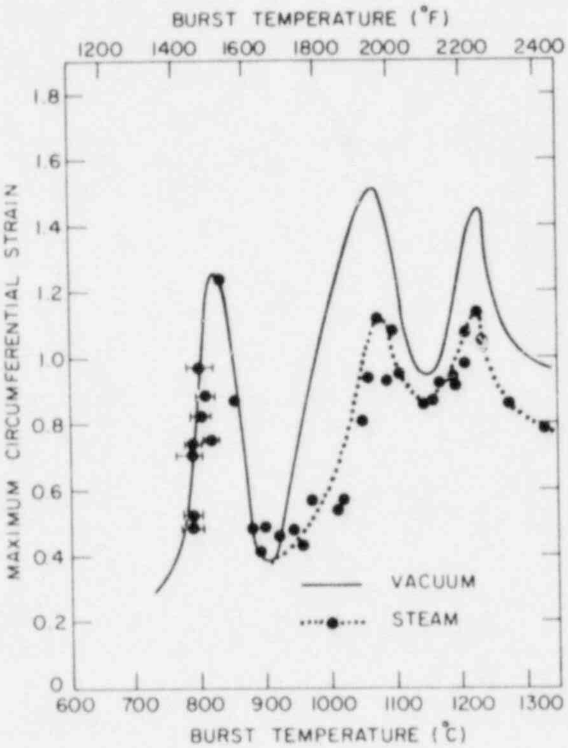

Fig. 58

Maximum Circumferential Strain vs Burst Temperature in Vacuum and Steam Environments for Unconstrained Cladding Burst at Heating Rate of 115°C/s. ANL Neg. No. 306-76-?49 Rev.

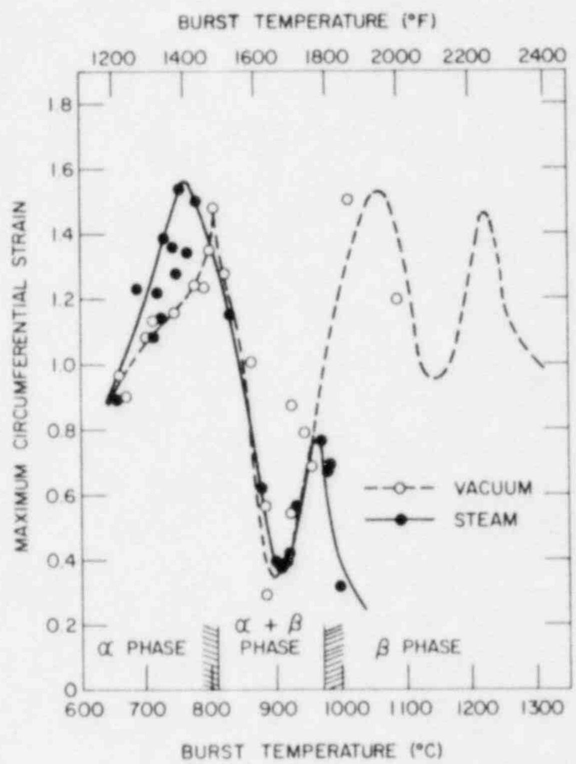

Fig. 59

Maximum Circumferential Strain vs Burst Temperature in Vacuum and Steam Environments for Unconstrained Cladding at Heating Rate of 5°C/s. ANL Neg. No. 306-77-468.

For bursts in the α- or predominantly α-phase region, i.e., ≤840°C, the effect of steam oxidation on the circumferential strain at failure is negligible at the high heating rate (Fig. 58). This result is interesting because, at this heating rate, the burst temperature in steam is definitely higher than in vacuum (Fig. 56). At the low heating rate (5°C/s), the maximum circumferential strains at failure are larger in a steam environment than in vacuum for burst temperatures between 730 and 800°C. Although the increment is not large, the difference is greater than the uncertainty in the strain and temperature measurements. As is described later, similar results were obtained for mandrel-constrained cladding burst at a similar heating rate. The shift in the strain maximum from ~810 to 770°C (Fig. 59) is accompanied by a corresponding shift of the temperature of maximum axial contraction, as shown in Fig. 60. This suggests that the deformation mechanisms operating during diametral expansion and rupture in the α-phase region are similar in vacuum and steam environments, although the circumferential expansion is somewhat greater in steam. A possible explanation for the small strain increment appears in Sec. VI.C.

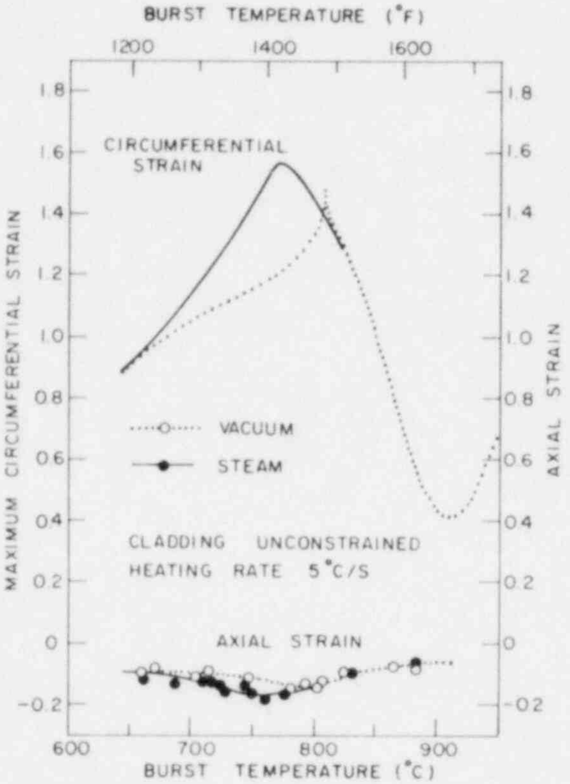

Fig. 60

Average Axial Strain vs Burst Temperature for Unconstrained Zircaloy-4 Cladding in Vacuum and Steam at Heating Rate of 5°C/s. ANL Neg. No. 306-76-247.

Figures 61-63 compare circumferential strain at failure as a function of burst temperature for mandrel-constrained cladding in vacuum and steam environments for heating rates of 115, 55, and 5°C/s, respectively. The rupture strains at temperatures in the β-phase region decrease as the heating rate decreases. For bursts in the α- or predominantly α-phase region, the rupture strains in steam are larger than in vacuum for heating rates ≤50°C/s. These observations are similar to those for the unconstrained cladding.

In contrast to the results for unconstrained cladding at a heating rate of 115°C/s, which showed no effect of steam oxidation on the rupture strains at temperatures ≤840°C (Fig. 58), the results for the constrained cladding (Fig. 61) show a peculiar strain minimum and maximum at burst temperatures of 820 and 790°C, respectively, in vacuum (Fig. 18) that are not observed in a steam environment. In effect, the circumferential strain for tightly constrained tubes at a heating rate of 115°C/s in steam is greater than in vacuum for a narrow range of burst temperatures between 790 and 850°C. Nowhere has such a result been reported previously. A possible mechanism for this behavior is discussed in Sec. VI.D.

An accurate prediction of the circumferential strain at rupture as a function of LOCA-related parameters, e.g., cladding internal pressure and heating rate, is of practical importance in assessing the extent of flow-channel blockage. From the data in Figs. 53-55 and 61-63, the rupture circumferential strains can be plotted as a function of initial pressure for each heating rate. Figures 64-66 show plots of this type for heating rates of 115, 55, and 5°C/s, respectively. Similar results obtained in vacuum are shown for comparison.

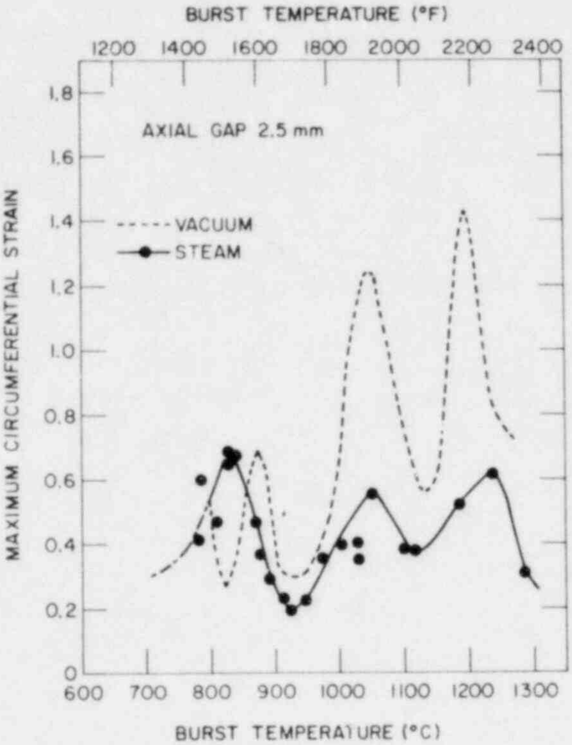

Fig. 61

Maximum Circumferential Strain as a Function of Burst Temperature for Axially Constrained Zircaloy-4 Cladding in Steam and Vacuum Environments at Heating Rate of 115°C/s. ANL Neg. No. 306-78-415.

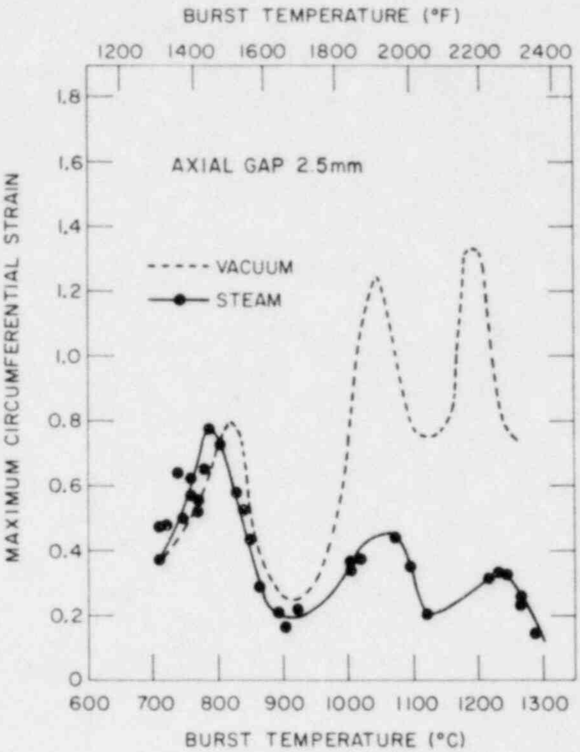

Fig. 62

Maximum Circumferential Strain as a Function of Burst Temperature for Axially Constrained Zircaloy-4 Cladding in Steam and Vacuum Environments at Heating Rate of 55°C/s. ANL Neg. No. 306-77-20 Rev.

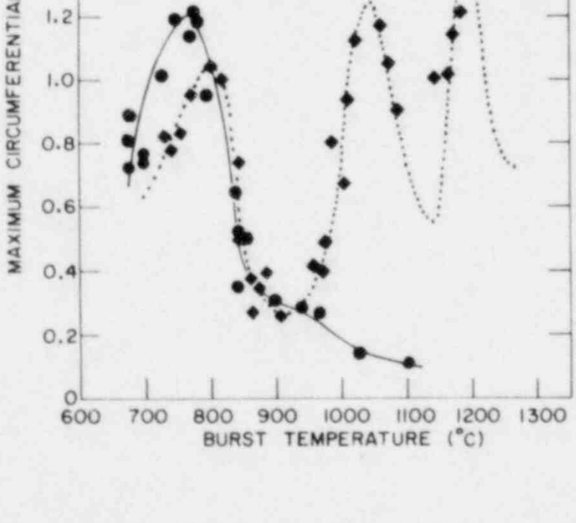

Fig. 63

Maximum Circumferential Strain as a Function of Burst Temperature for Axially Constrained Zircaloy-4 Cladding in Steam and Vacuum Environments at Heating Rate of 5°C/s. ANL Neg. No. 306-76-130 Rev.

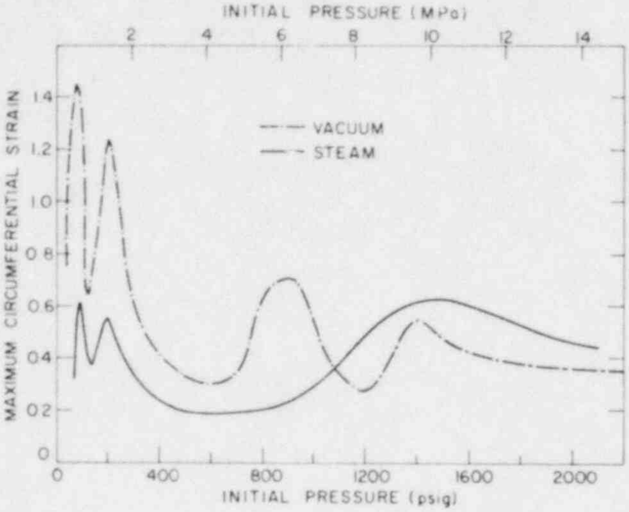

Fig. 64

Maximum Rupture Circumferential Strain as a Function of Initial Internal Pressure for Axially Constrained Zircaloy-4 Cladding in Steam and Vacuum Environments at Heating Rate of 115°C/s. ANL Neg. No. 306-76-156 Rev.

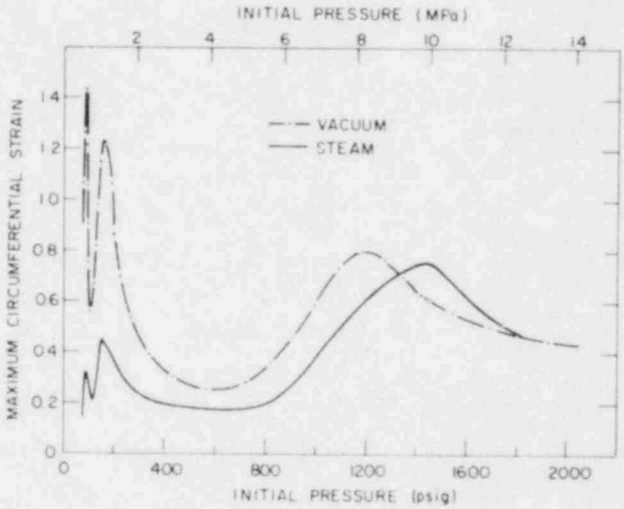

Fig. 65

Maximum Rupture Circumferential Strain as a Function of Initial Internal Pressure for Axially Constrained Zircaloy-4 Cladding in Steam and Vacuum Environments at Heating Rate of 55°C/s. ANL Neg. No. 306-76-152 Rev.

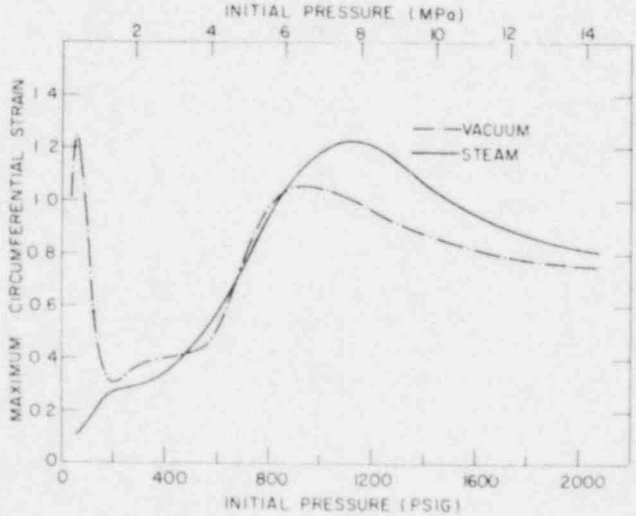

Fig. 66

Maximum Rupture Circumferential Strain as a Function of Initial Internal Pressure for Axially Constrained Zircaloy-4 Cladding in Steam and Vacuum Environments at Heating Rate of 5°C/s. ANL Neg. No. 306-76-154.

Maximum circumferential expansion in steam occurs at initial pressures of 11, 10, and 8 MPa for heating rates 115, 55, and 5°C/s, respectively. For cladding internal pressures ≥7 MPa, the circumferential expansion does not decrease appreciably relative to results obtained in vacuum, and under certain conditions, oxidation enhances the circumferential strain at rupture.

C. Deformation Mechanism of α-phase Zircaloy in Steam at Low Heating Rates

The significant enhancement of the circumferential expansion in steam, compared to that in a vacuum environment, for both constrained and unconstrained cladding at burst temperatures between 700 and 800°C at low heating rates can be explained as follows. Since the ZrO_2 layer on the cladding surface does not exhibit local cracking during transient heating (~5°C/s), the volume expansion of the ZrO_2 layer will exert additional tangential stress on the underlying metallic α-phase cladding. The additional tangential stress introduced by the oxide layer can decrease the burst temperature, as mentioned above, and increase the diametral strain as a result of a change in the biaxiality. During simultaneous oxidation and deformation, the tangential stress σ_θ can be written as

$$\sigma_\theta(t) = \frac{P(t)D(t)}{2h(t)} + \sigma_s(t), \qquad (16)$$

where P, D, h, and σ_s are the time-dependent pressure differential across the tube wall, tube diameter, tube thickness, and stress induced by the oxide layer, respectively. The biaxiality $b = \sigma_\theta(t)/\sigma_z(t)$, where σ_z is the axial stress component, can be written as

$$b = \frac{P(t)D(t)}{2h(t)\sigma_z(t)} + \frac{\sigma_s(t)}{\sigma_z(t)} = b_V(t) + \frac{\sigma_s(t)}{\sigma_z(t)}, \qquad (17)$$

where $b_V(t)$ is the biaxiality condition in a vacuum environment.

The variation of the biaxiality and tangential strain with time for constrained and unconstrained tubes in vacuum and steam is shown schematically in Fig. 67. The effect of axial constraint on these parameters was discussed in Sec. V.E for tubes that were burst in vacuum. In this case, the larger tangential strain for an unconstrained tube was associated with a smaller decrease in the biaxiality after the onset of plastic instability in the material. A similar situation exists for deformation in steam; however, an increase in biaxiality (i.e., $b > 2$), as a result of the oxidation, occurs before the onset of plastic instability; consequently, the biaxiality and the tangential strain at rupture are larger in steam than in vacuum.

Figure 68 shows the diametral-strain-versus-time curves obtained at a low heating rate of 5°C/s for two runs in steam and one in vacuum, with approximately the same burst temperature. The curves indicate that the diametral strains are nearly the same for the initial stages of deformation and that the enhanced ballooning in steam occurs immediately before rupture. The experimental observation in Fig. 68 is a predictable result if the model shown schematically in Fig. 67 is a valid representation of the steam-oxidation effect.

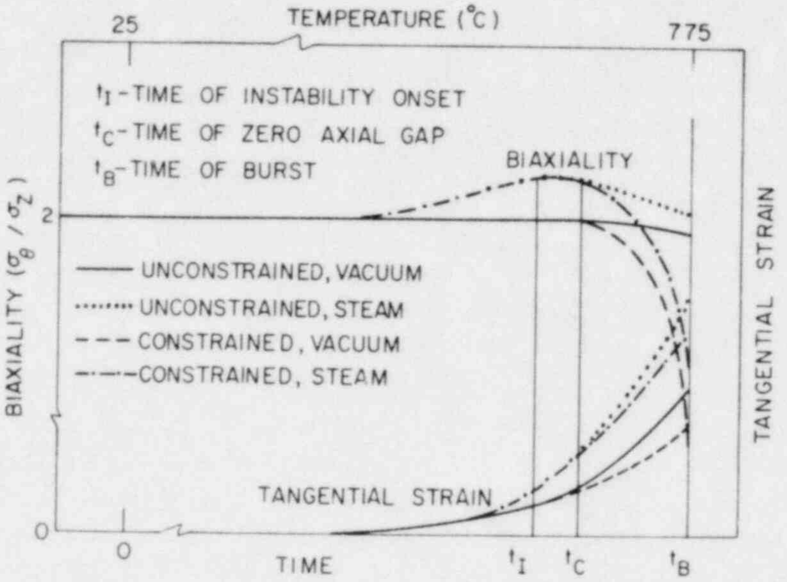

Fig. 67. Schematic Representation of Effect of Axial Constraint on Biaxiality and Tangential Strain in Plastic-instability Region of Zircaloy Tube Burst in Vacuum and Steam Environments. ANL Neg. No. 306-76-260.

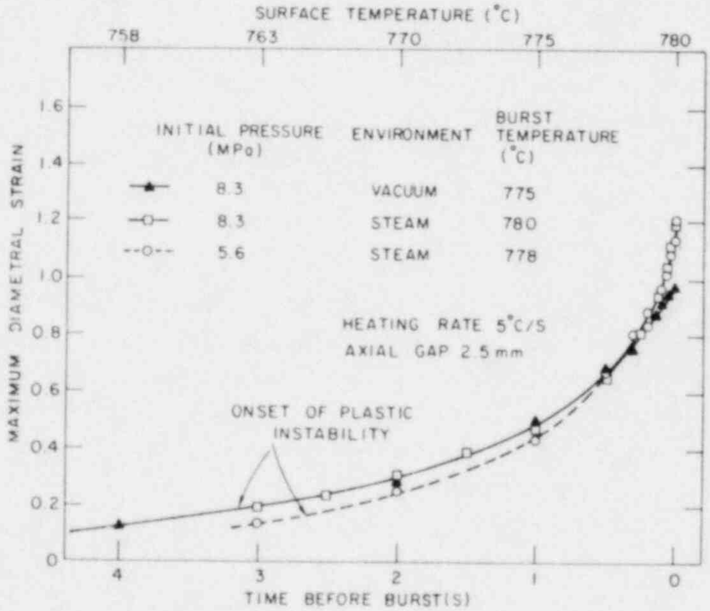

Fig. 68

Maximum Diametral Strain as a Function of Time before Rupture for Axially Constrained Zircaloy-4 Cladding in Steam and Vacuum at Heating Rate of 5°C/s. ANL Neg. No. 306-76-263.

The stress induced by the oxide layer σ_s can be estimated from the expression given by Southwell[45]

$$\sigma_s = \frac{E(R - 1)\zeta_o}{RD}, \tag{18}$$

where E, R, and ζ_o are Young's modulus, the Pilling-Bedworth ratio, and the thickness of the oxide layer, respectively. The tangential stress that results from the oxide layer produced on a tube that ruptured at 760°C in a 5°C/s heating-rate experiment was computed from Eq. 18. A value of 4.9 MPa was obtained from the measured oxide-layer thickness of 1.05×10^{-3} mm, a tube diameter of 13.4 mm at the onset of plastic instability, and a Pilling-Bedworth ratio of 1.56. A value of Young's modulus of 1.8×10^{5} MPa for an oxide layer of zero porosity at 700°C, obtained from the data of Smith and Crandal,[46] was used.

For the unconstrained tube, the axial and tangential stresses due to an internal pressure of 5.6 MPa at the onset of instability are ~46.5 and 93 MPa, respectively. Therefore, the biaxiality at the onset of instability increases ~5% (i.e., from 2.0 to 2.1) as a result of oxidation under the above conditions. Since the tangential strain at failure is strongly dependent on the biaxiality, this magnitude of biaxiality increase could be sufficient to enhance the circumferential expansion in steam to the extent shown in Fig. 59 or 63. As the heating rate increases or the burst temperature decreases below ~700°C, ζ_o becomes smaller, and hence, the oxidation effect on the circumferential strain becomes insignificant.

Several isothermal stress-rupture experiments were conducted on as-received and preoxidized Zircaloy-4 cladding in vacuum and steam to verify the observations in Figs. 59 and 63, and the hypothesis relative to Fig. 67, that concern enhanced circumferential strain during transient-heating experiments in steam. In the stress-rupture tests, uncertainties were virtually eliminated in the burst-temperature measurement caused by thermal shunting of the thermocouples in steam and local temperature variations that can occur during transient heating. The nonpressurized specimens were preoxidized at a given heating rate in steam to ~800°C and quenched to produce oxide-layer thicknesses equivalent to those formed in the transient-heating burst experiments in steam.

Four thermocouples (one control and three monitoring) were spark-welded to thin tantalum foils (0.178 mm thick) that had been spot-welded to the cladding tube. The thermocouple locations did not result in preferential burst sites. The specimens were heated to the test temperature in vacuum, steam was admitted to the chamber, the temperature was readjusted, and the specimen was rapidly pressurized by opening a needle valve. For the rupture tests in vacuum, the specimens were pressurized after the test temperature was attained. The pressure and temperature were recorded by the Visicorder, and the diametral strain was monitored by the high-speed camera and laser-light system used in the transient-heating experiments.

Figure 69 shows the diametral strain as a function of time for an unconstrained as-received and a preoxidized (100°C/s in steam to 800°C and quench) specimen ruptured in vacuum at 750°C at an internal pressure of 4.2 MPa. The calculated oxygen distribution in the ZrO_2/α composite specimen is shown in the inset of the figure. The larger diametral strain associated with the preoxidized specimen is attributed to the increase in the biaxiality of the specimen due to the oxide layer. The larger degree of oxidation and oxygen dissolution in α-phase Zircaloy during the test in steam resulted in a smaller strain at rupture compared with that of either the as-received or the preoxidized specimen tested in vacuum. This result indicates that, under these conditions, oxygen dissolution in the material had a greater effect on the ductility than the increase in biaxiality due to the oxide layer. Figure 70 shows similar results for an as-received and a preoxidized specimen ruptured in vacuum at 750°C and an internal pressure of 5.2 MPa. Again, the modified cladding with a preoxidized oxide layer results in a larger expansion than the as-received specimen, in agreement with the prediction based on the model depicted in Fig. 67.

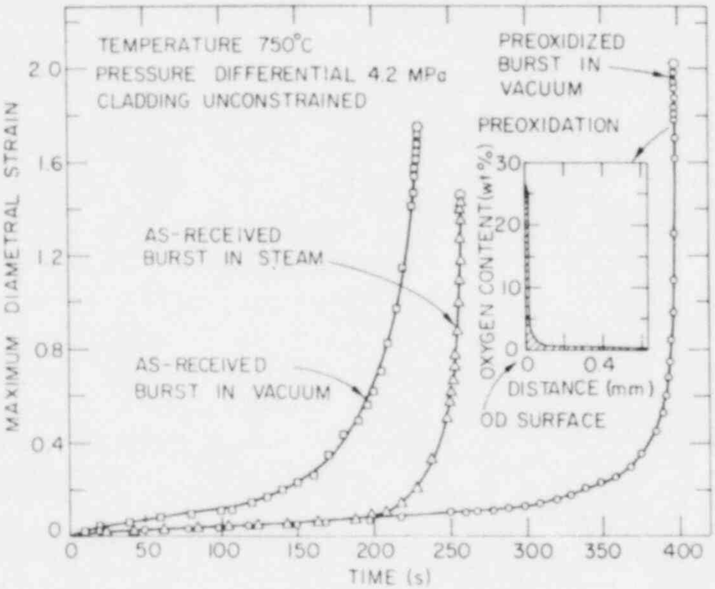

Fig. 69

Maximum Diametral Strain as a Function of Time in Isothermal Stress-rupture Tests on Unconstrained As-received Zircaloy-4 Cladding in Steam and Vacuum and Preoxidized Cladding in Vacuum at 750°C and Internal Pressure of 4.2 MPa. ANL Neg. No. 306-76-237.

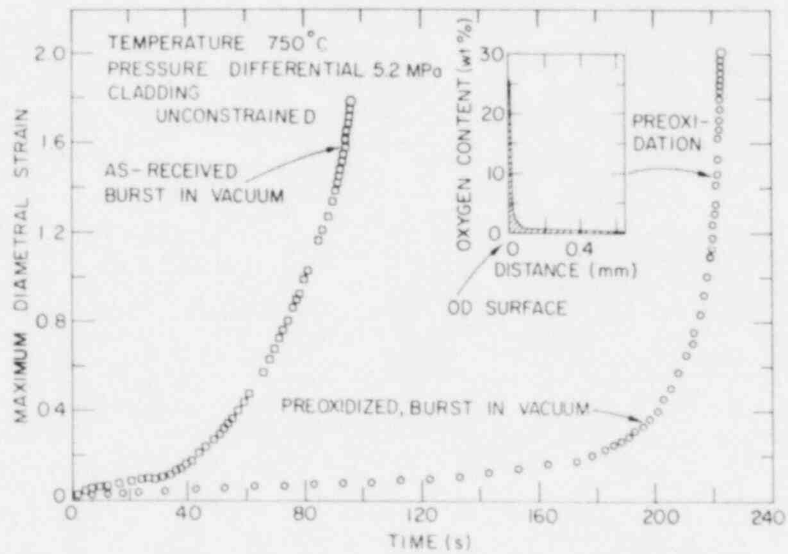

Fig. 70. Maximum Diametral Strain as a Function of Time in Isothermal Stress-rupture Tests on Unconstrained As-received and Preoxidized Zircaloy-4 Cladding in Vacuum at 750°C and Internal Pressure of 5.2 MPa. ANL Neg. No. 306-76-241.

D. Deformation Mechanism of α-phase Zircaloy in Steam at High Heating Rates

Because of the thin oxide layers formed at heating rates $\gtrsim 50°C/s$, the strain-enhancing effect of the steam environment, described above for low heating rates, is not observed. Thus, an optimum heating rate probably exists that maximizes the strain-enhancing effect. However, for constrained cladding, abnormally small circumferential strains were observed at high heating rates $\gtrsim 100°C/s$ in vacuum, as evidenced by the additional strain maximum and minimum for burst temperatures of ~800 and 825°C, respectively. The strain maximum and minimum in the α-phase region was not observed in a steam environment (Fig. 61), nor was the anomaly observed for unconstrained cladding burst in vacuum at a similar heating rate.

Additional tube-rupture experiments on axially constrained cladding have been performed at the 115°C/s heating rate to confirm the observations relative to the effect of steam oxidation on the deformation behavior at temperatures in the α-phase region. To explore the possibility that thermal shunting and/or in situ oxidation of the thermocouples in steam can result in uncertainties in the burst-temperature measurements, specimens were preoxidized in steam under transient-heating conditions (i.e., 115°C/s heating rate to ~800°C and rapidly cool to room temperature) and then burst in vacuum at the same heating rate. Furthermore, the Pt-Pt 10% Rh thermocouples were spark-welded to the specimens before and after the preoxidation treatment.

Figure 71 shows the maximum circumferential strain for the preoxidized specimens burst in vacuum along with data for as-received specimens

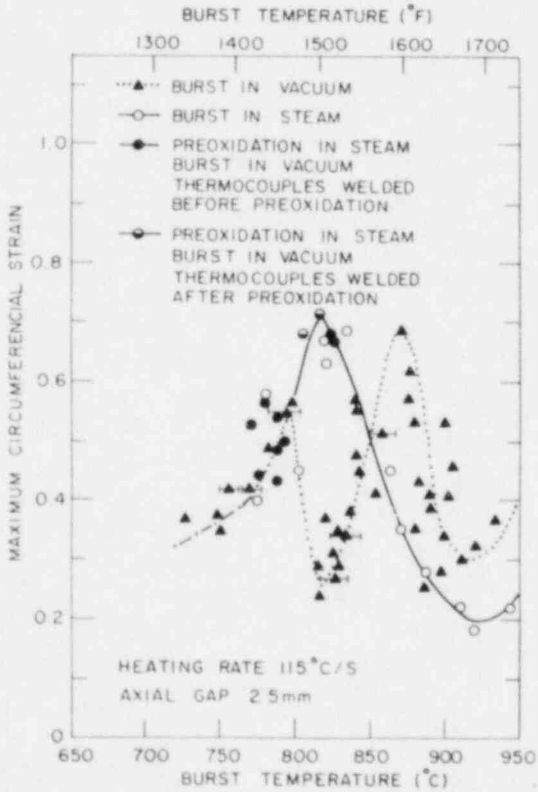

Fig. 71

Maximum Circumferential Strain vs Burst Temperature for Axially Constrained As-received Cladding in Steam and Vacuum and Preoxidized Cladding Ruptured in Vacuum at Heating Rate of 115°C/s. ANL Neg. No. 306-76-264.

burst in vacuum and in steam. The results indicate that there is no difference in circumferential-strain characteristics for the specimens burst in the two environments at temperatures ≤800°C and that the values for the preoxidized specimens ruptured in vacuum are in good agreement with the in situ burst data in steam at temperatures between ~780 and 830°C. These results indicate that errors in the temperature measurement due to thermal shunting and oxidation of the thermocouples are negligible.

To further minimize the uncertainty of the burst-temperature measurement, several isothermal stress-rupture tests were performed on constrained as-received cladding in steam and vacuum at temperatures between ~720 and 840°C. The internal pressure in these tests was adjusted so that the deformation time (viz., 5-8 s) was much shorter than for the tests at the 4.2- and 5.2-MPa stress levels at 750°C, in Figs. 69 and 70. Consequently, as shown in Fig. 72, the circumferential-strain data are in good agreement with the results from the 115°C/s heating-rate experiments on constrained cladding in steam and vacuum (i.e., Fig. 71).

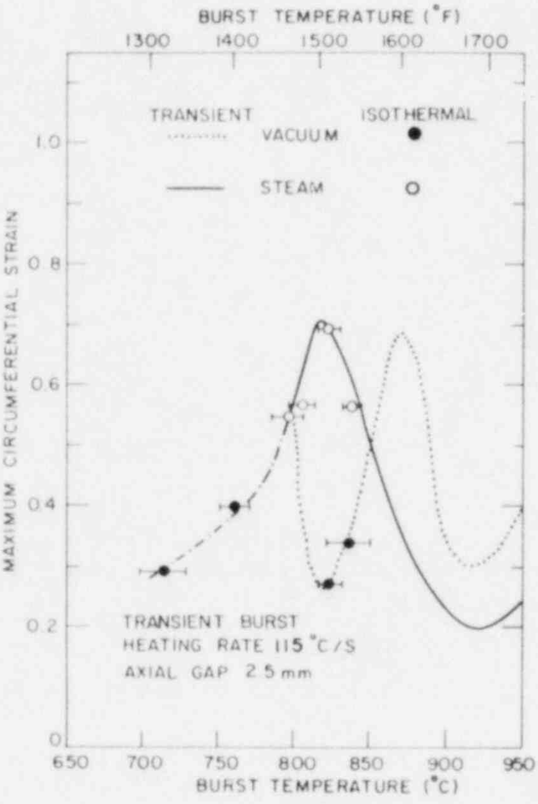

Fig. 72

Comparison of Maximum Circumferential Strain vs Burst-temperature Data Obtained from Short-term Isothermal Stress-rupture Tests on Constrained Zircaloy-4 Cladding in Steam and Vacuum with Similar Data (i.e., the curves) from Transient-heating Experiments at 115°C/s in the Two Environments. ANL Neg. No. 306-76-243.

Microstructural examinations revealed significant differences in the rupture region of specimens burst in steam and vacuum at temperatures between ~800 and 850°C. Figure 73 shows typical cross sections of the failure location of tubes burst in vacuum and steam in this temperature range. The large reduction in the wall thickness of the specimen burst in vacuum (Fig. 73A) is characteristic of a rupture-type failure, whereas the fracture edge of the specimen burst in steam (Fig. 73B) is similar to that produced by a shear process. Elongated as well as equiaxed (recrystallized) α grains are evident in both specimens. Figure 74 shows the corresponding scanning-electron micrographs of the failure locations of the specimens burst in vacuum and steam. The single row of coalesced voids in Fig. 74A is characteristic of a tensile failure, whereas typical shear dimples and ridges that result from the coalescence of microvoids are evident in Fig. 74B (where the shear direction is from the lower right to the upper left).

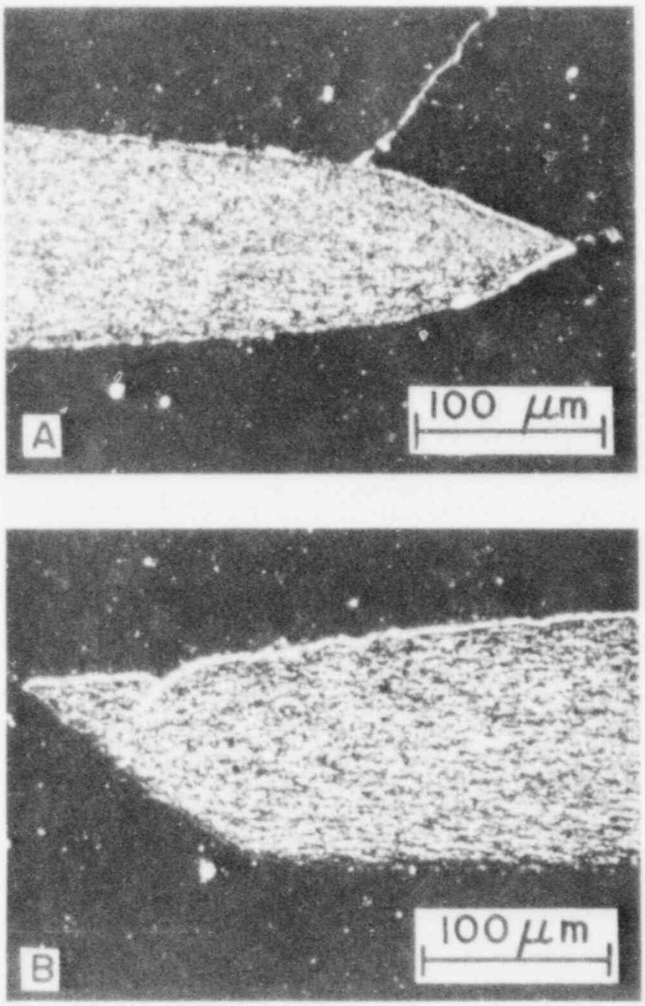

Fig. 73

Cross Section of Fracture Location of Axially Constrained Zircaloy-4 Cladding That Burst at 825°C (A) in Vacuum and (B) in Steam at Heating Rate of 115°C/s. ANL Neg. No. 306-76-239.

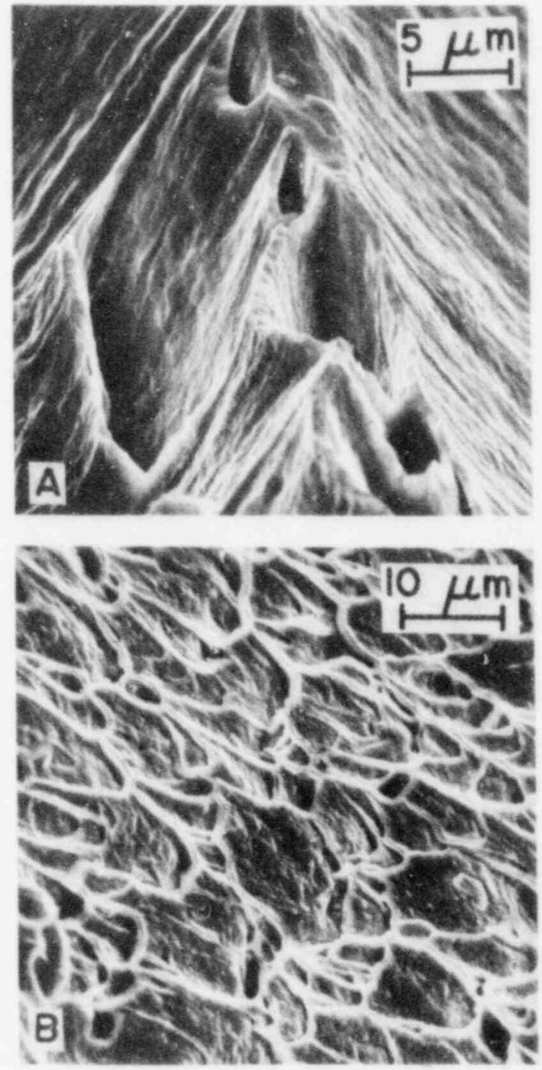

Fig. 74

Scanning-electron Micrographs of Fracture Edge of Zircaloy-4 Cladding Shown in Fig. 73 That Burst at 825°C (A) in Vacuum and (B) in Steam at Heating Rate of 115°C/s. ANL Neg. No. 306-76-238.

The photomicrographs in Figs. 73 and 74 suggest that, near 825°C, the deformation-slip systems operative during the ballooning stage of tightly constrained cladding are different in the two environments. From an examination of the burst location on the tubes, the failure mode for the specimens in Fig. 71 has been classified in terms of either a rupture- or fracture-type failure in Fig. 75. Below ~800°C, fracture occurs by a shear process for the specimens burst in vacuum and steam. Fracture-type failures also occur in the preoxidized specimens burst in vacuum and for specimens burst in steam at temperatures to ~830°C. Rupture failures occur in vacuum and steam above ~810 and 830°C, respectively.

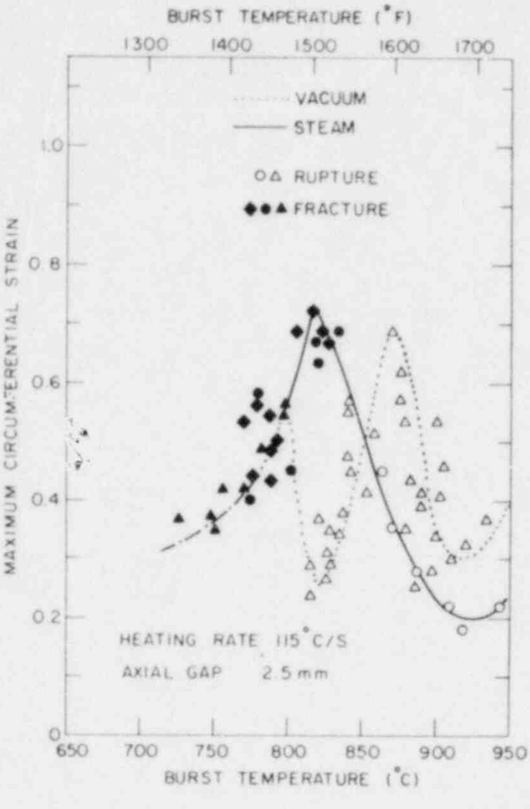

Fig. 75

"Rupture" and "Fracture" Failure-mode Classifications for Deformation Data in Fig. 71 on Axially Constrained Zircaloy-4 Cladding. ANL Neg. No. 306-76-261.

In contrast to the behavior of constrained cladding, a fracture-type failure mode was observed for unconstrained tubing near 825°C (maximum circumferential strain, 1.24) in both environments. These observations indicate that a fundamental transition in the deformation mechanism of α-phase Zircaloy occurs in the constrained cladding in vacuum that is responsible for the anomalously low strain between ~800 and 850°C. The diametral-strain/time curves for axially constrained cladding at a heating rate of 115°C/s shown in Figs. 76 and 77 indicate that this transition occurs after the onset of plastic instability in the material and just before burst. In general, the anomalous rupture-type failure and small circumferential strain of α-phase material (Figs. 71, 72, and 75) occur when the cladding is severely constrained and the local strain rate is quite high. The deformation process under these limited conditions may involve pyramidal slip with $(\vec{c} + \vec{a})$-type Burgers vectors.

As discussed in Sec. V.C, because of the texture of the cladding and the limited slip systems in α-phase Zircaloy (i.e., either prism or basal slip), deformation in the radial direction (i.e., wall thinning) is difficult. As a result, fracture-type surfaces such as those shown in Figs. 73B and 74B are normally observed for bursts in the α- or predominantly α-phase regions. In contrast, however, the multiple-slip systems for β or two-phase material result in a large wall thinning and rupture surfaces characterized by Figs. 73A and 74A. Prism and/or basal slip alone could probably not lead to the amount of wall thinning observed (Fig. 73A) under the present conditions of material texture, temperature, and strain rate. Also, twinning is unlikely between 750 and 840°C. No twinning was observed in the specimens after rapid cooling from the burst temperature (~55°C/s from ~825 to ~400°C). Therefore, slip systems with $(\vec{c} + \vec{a})$-type Burgers vectors are probably responsible for the wall thinning at the rupture area.

Pyramidal slip with a $(\vec{c} + \vec{a})$ Burgers vector has been reported for zirconium[47,48] and titanium[49] single crystals and polycrystalline Zircaloy-4 (Ref. 50) at elevated temperatures under a constrained condition. If oxygen dissolution in Zircaloy in the steam environment suppresses $(\vec{c} + \vec{a})$ slip, at least for a fraction of the cross section, the amount of wall thinning would decrease near the fracture tip, as was observed.

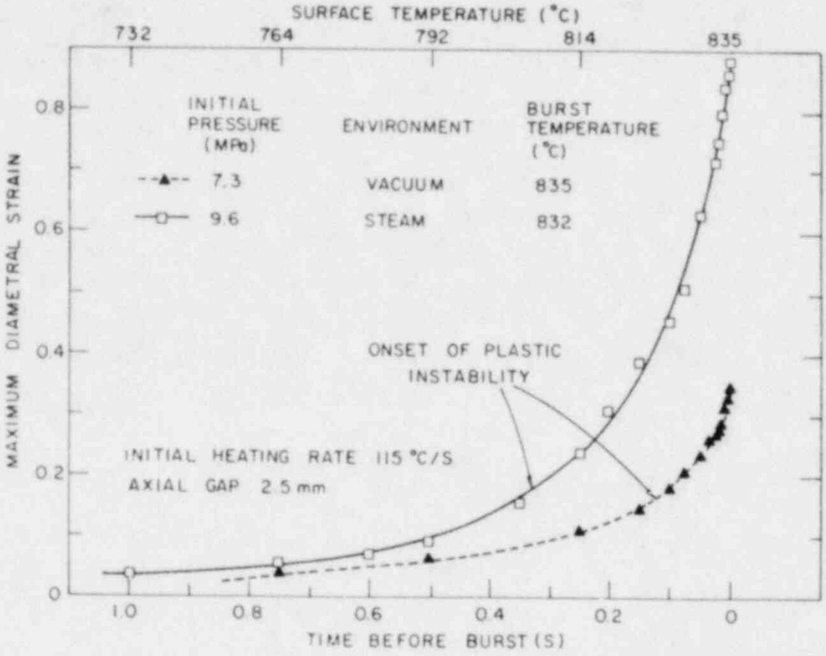

Fig. 76. Maximum Diametral Strain as a Function of Time before Rupture for Axially Constrained Zircaloy-4 Cladding in Steam and Vacuum at Heating Rate of 115°C/s. ANL Neg. No. 306-76-262.

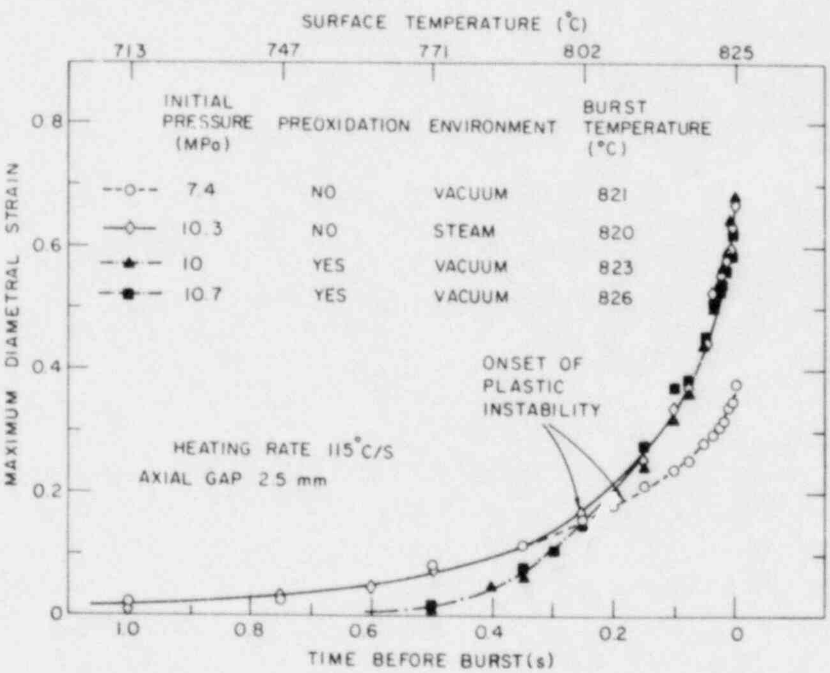

Fig. 77. Maximum Diametral Strain as a Function of Time before Rupture for Axially Constrained As-received Zircaloy-4 Cladding in Steam and Vacuum and Preoxidized Cladding in Vacuum at Heating Rate of 115°C/s. ANL Neg. No. 306-76-244.

A possible explanation for the larger circumferential strain for the high-heating-rate tests on severely constrained cladding in steam, compared with those in vacuum, for burst temperatures between 800 and 850°C (Fig. 71) involves the following. The smaller degree of wall thinning in the steam environment, due to the postulated suppression of $(\vec{c} + \vec{a})$ slip, amounts to an inherent "necking resistance." Hence, the failure is further delayed in the steam environment, and a larger circumferential expansion is expected. The lesser extent of wall thinning in addition, leads to significant axial contraction and, consequently bending of the tube, particularly when temperature nonuniformities exist along the circumference. Bending decreases the axial stress in the region of the specimen that is undergoing ballooning, i.e., the future rupture area; therefore, the biaxiality decreases less rapidly than for an axially constrained tube burst in vacuum, where bending is negligible at 800-850°C.

Tube bending, which takes place during ballooning but before burst, is more pronounced for tests in steam or for preoxidized specimens than for as-received tubes burst in vacuum under otherwise identical conditions. As discussed previously, higher tangential strains at burst are associated with larger values of biaxiality during ballooning; hence, the strain in steam is larger than in vacuum.

The anomalous deformation and burst behavior shown in Fig. 71 was not observed for a less severely constrained cladding (a 5.9- versus a 2.5-mm axial gap) under otherwise identical conditions. Apparently the anomaly and, hence, the strain-enhancing effect of steam, are observed only under limited conditions of severe constraint, ballooning temperatures near 825°C, and high heating rates.

E. Deformation Mechanism of β-phase Zircaloy in Steam

In a steam environment, the "orange-peel" surface appearance, characteristic of tubes that rupture in vacuum at temperatures in the β-phase region (Sec. V.G), is observed only on the inside surface of the cladding. The outside surface has axial cracks in the oxide, and the cracks extend into the central β-phase region of the tube wall. Whenever the cracks develop into extended grooves, the material at the inside surface opposite the cracks undergoes localized thinning or necking. These regions of localized radial strain in the tube wall (e.g., Fig. 78) are larger than the irregularities responsible for the "orange-peel" appearance shown in Fig. 43. The well-defined, smoothly shaped grooves on the outside surface accommodate most of the circumferential expansion of the cladding, and one of them eventually proceeds to rupture. The cross section in Fig. 78 contains 51 such grooves, and an enlarged micrograph of one groove is shown in Fig. 79.

Fig. 78

Typical Cross Section of Zircaloy-4 Tube That Burst at a Temperature in the β-phase Region in a Steam Environment. The inner surface shows large irregularities, but the outer surface is relatively smooth with small grooves initiated by oxide cracking. ANL Neg. No. 306-77-28.

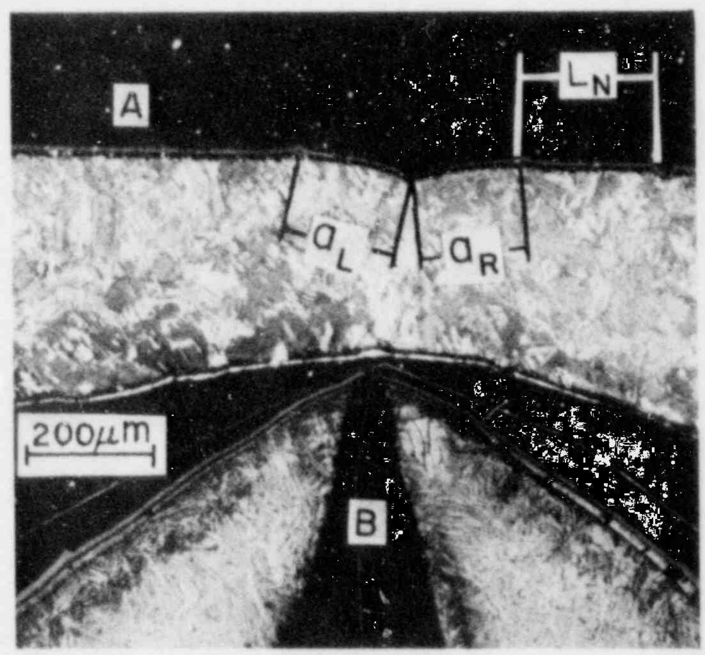

Fig. 79

Magnified Cross Section of Specimen in Fig. 78 Showing (A) Symmetry of Cusp at Outer Surface, Length L_N between Cracks in Oxide, and Thinning of Tube Wall Opposite Cusp, and (B) Rupture Area. ANL Neg. No. 306-77-39.

If we define the distance between two adjacent axial cracks in the oxide layer as L_N (Fig. 79), the circumferential strain ϵ_θ^{ox} at which initial cracking of the oxide occurs can be calculated from

$$\epsilon_\theta^{ox} = \frac{\sum_{N=1}^{N=N_{ox}} L_N}{\pi D_0} - 1, \tag{19}$$

where N_{OX} is the total number of axial cracks around the circumference and D_0 is the initial cladding diameter. The circumferential strain at rupture from the cross section in Fig. 78 is 0.21. The value of ϵ_{θ}^{OX} for this specimen, obtained from Eq. 19 and measurements of L_N from micrographs similar to Fig. 79, is 0.025. Since this quantity is quite small, i.e., ~10% of the strain at failure, most of the circumferential expansion occurs in the groove regions. Therefore, the mechanism of β-phase deformation in steam can be explained if the mechanism of groove development is understood.

Tearing is a frequently favored failure mechanism when small unbroken areas remain behind the main crack front as in Fig. 79A. The left and right sides of the well-defined cusp are of same length, i.e., $a_L = a_R$ in Fig. 79A, and the fracture tip is also symmetrical (Fig. 79B). The thicknesses of the oxide and α layers at both sides of a groove decrease as the cusp is approached; this indicates that the exposure time to steam was identical for both sides of the cusp. On the basis of these observations, a groove is believed to advance by slow tearing of the β-phase material at the location of a crack in the oxide and α layers. A β-phase grain boundary is frequently observed (with the aid of the rim-α structure formed during the $\beta \rightarrow \alpha'$ transformation) at the location of the cusp of an advancing groove, e.g., Fig. 80 for cladding tubes that ruptured at 1280 and 1265°C. The formation of the rim-α structure

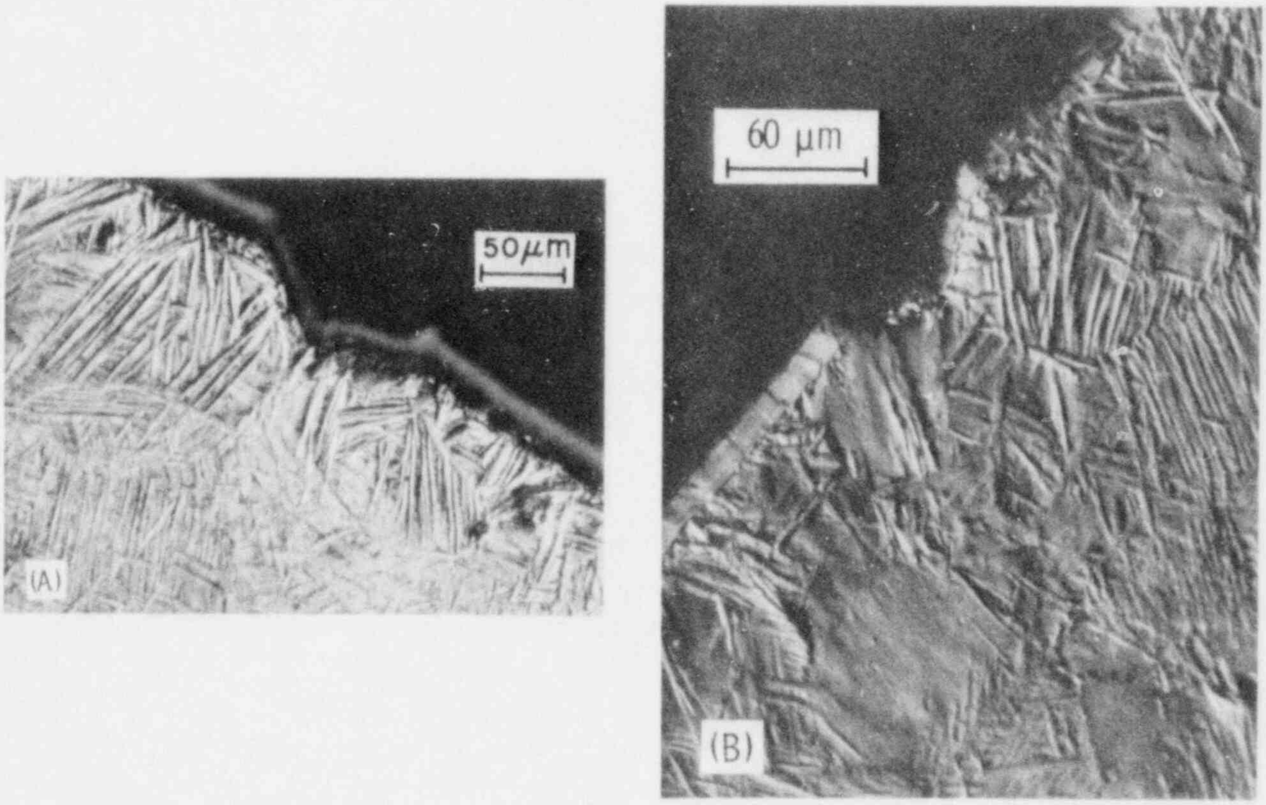

Fig. 80. Optical Micrographs Showing β-phase Grain Boundary Located at Moving Front of Cusp Similar to That in Fig. 79A. (A) Rupture temperature 1280°C; (B) rupture temperature 1265°C. The observation suggests that the groove advances by β-phase grain-boundary tearing. ANL Neg. Nos. 306-77-31 and -481.

is dependent on the cooling rate and is limited to a narrow range of cooling rates at the β phase-boundary temperature.[6] If the specimen is cooled too fast, the Widmanstätten structure is predominant[6] and the previous β-phase grain boundary cannot be distinguished.

It is not clear why a grain boundary is the preferential path for tearing. Apparently a β-phase grain boundary is weak and susceptible either to separation or to sliding. One possible explanation is that a crack in the oxide and α layers above the underlying grain boundary provides a preferential route for oxygen diffusion. Thus, stress concentration and enhanced diffusion along the β-phase grain boundary can weaken the area and induce an intergranular tear.

According to this model, an intergranular tear will not be favored if the strain rate is rapid and less time is allowed for oxygen diffusion. Figure 81 shows the cross section of a Zircaloy tube that was oxidized in steam for 48 s at 1154°C, without internal pressurization, and suddenly pressurized and ruptured at this temperature in 0.25 s. During high-strain-rate deformation and rupture, a well-defined cusp similar to that in Fig. 79 was not observed; i.e., the crack opening is rough and irregularly shaped. Similar observations have been reported by Bradhurst and Heuer[51] for Zircaloy-2 cladding rapidly deformed in steam at 1060°C.

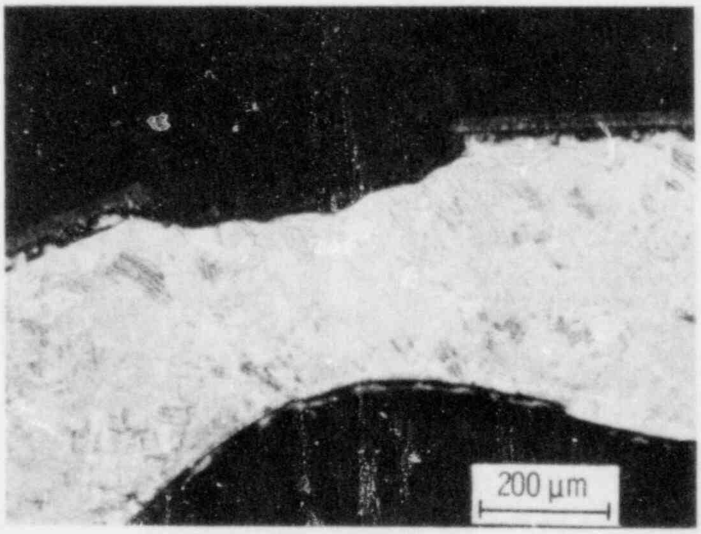

Fig. 81

Cross Section of Zircaloy-4 Tube Oxidized in Steam for 48 s at 1154°C without Internal Pressure and Ruptured at This Temperature in 0.25 s. Irregular local deformation occurs at the outer surface as a result of the high strain rate. The pattern is in contrast to the smooth cusp that forms at low strain rates (e.g., Fig. 79A). ANL Neg. No. 306-77-29.

Figure 82 is a scanning-electron micrograph of the fracture surface of the specimen described in Fig. 81. The ZrO_2, stabilized α, and transformed β phases are clearly visible. The transformed β cross section is irregular, as indicated by Fig. 81. However, a detailed examination of the transformed β fracture surface is hampered because of the rapid oxidation of the β phase during cooling. The stabilized α layer clearly shows an intergranular fracture at this temperature. Although no evidence was actually obtained for the fracture behavior of the α layer during transient deformation and rupture, intergranular failure is expected because of the brittle nature of the layer.

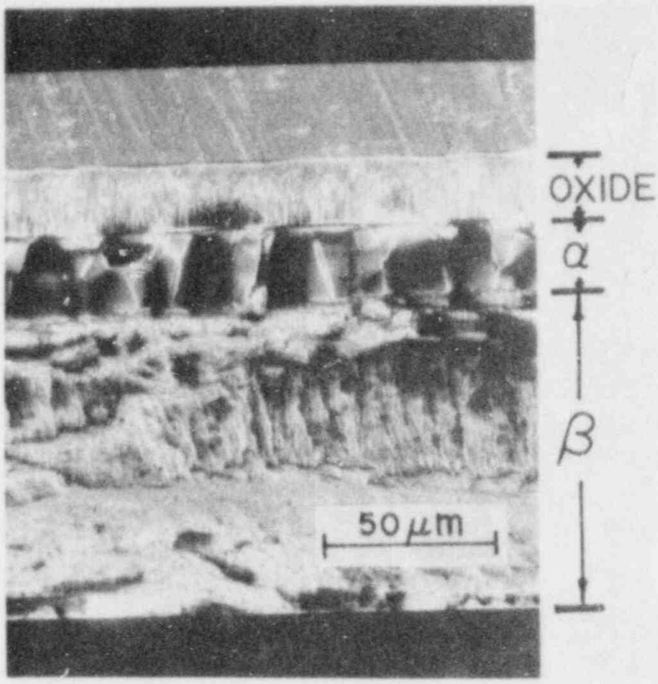

Fig. 82

Scanning-electron Micrograph of Fracture Surface of Specimen Described in Fig. 81. Intergranular fracture of the stabilized α phase and an irregular fracture surface of the β phase are evident. ANL Neg. No. 306-77-27.

On the basis of the above observations and hypothesis, a deformation and rupture mechanism for Zircaloy cladding at temperatures ≳1000°C in steam is shown schematically in Fig. 83. Actual micrographs that correspond

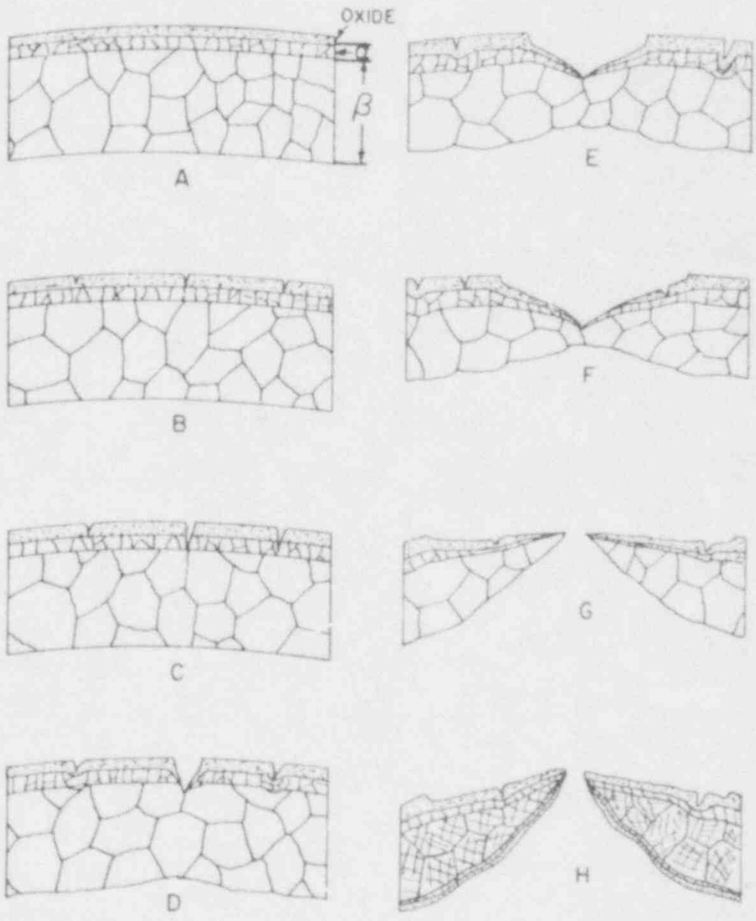

Fig. 83

Schematic Representation of Deformation and Rupture Sequence for Zircaloy Cladding in Steam Environment at Temperatures ≳1000°C. Figure 83H illustrates the cross section after cooling through the β → α' transformation. ANL Neg. No. 306-77-25.

to Figs. 83E and 83H are shown in Figs. 79A and 79B, respectively. Figure 83H is the final microstructure expected after rupture of the cladding in steam and cooling through the $\beta \rightarrow \alpha'$ phase transformation.

According to this model, at low strain rates, localized intergranular tearing will be the preferred deformation mode for β-phase cladding in a steam environment, and at high strain rates, localized plastic deformation by dislocation glide at the crack area will be dominant. If the extent of oxidation, i.e., the thicknesses of the oxide and α layers, is identical, more cracks in the oxide and α layers will be formed at higher strain rates. However, the situation is not as simple under transient-heating conditions, since a higher heating rate imposes a higher strain rate but a smaller oxidation. If the oxidation is small enough, e.g., a high-heating-rate burst at $\gtrsim$1000°C, the effect of localized deformation, such as shown in Figs. 79 and 83, will be quite small and the nonlocalized plastic deformation between the oxide cracks will be significant. In this case, the deformation characteristics in steam are similar to those in vacuum.

F. Effect of Specimen Length on Rupture Characteristics

Results in previous sections of this report were obtained on 153-mm-long Zircaloy tubes. To determine whether the specimen length had any effect on the deformation characteristics, several tube-burst experiments were performed on 300-mm-long tubes in vacuum and steam at heating rates of 5, 45, and 115°C/s. Figures 84 and 85 compare the circumferential strains as a function of burst temperature in vacuum and steam, respectively, for several of the 300-mm-long tubes with curves based on numerous tests with the 153-mm sample length. These results confirm the generally accepted criterion that, under otherwise identical conditions, the specimen length has no significant effect[52] on the tube-burst properties if the length-to-diameter ratio of the tube is >10.

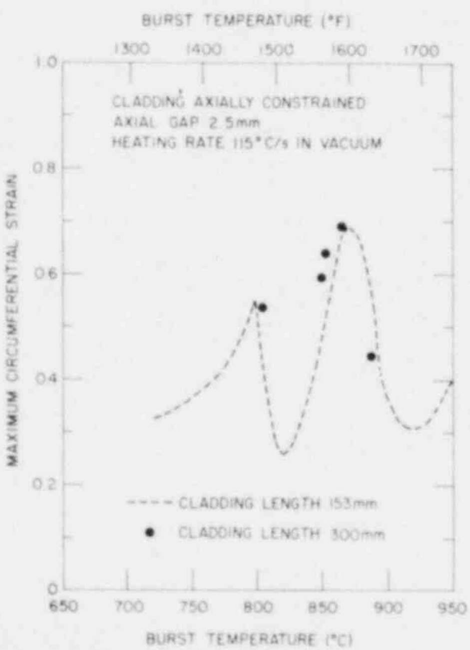

Fig. 84

Maximum Circumferential Strain vs Burst Temperature for 153- and 300-mm-long Axially Constrained Cladding at Heating Rate of 115°C/s in Vacuum. ANL Neg. No. 306-77-145.

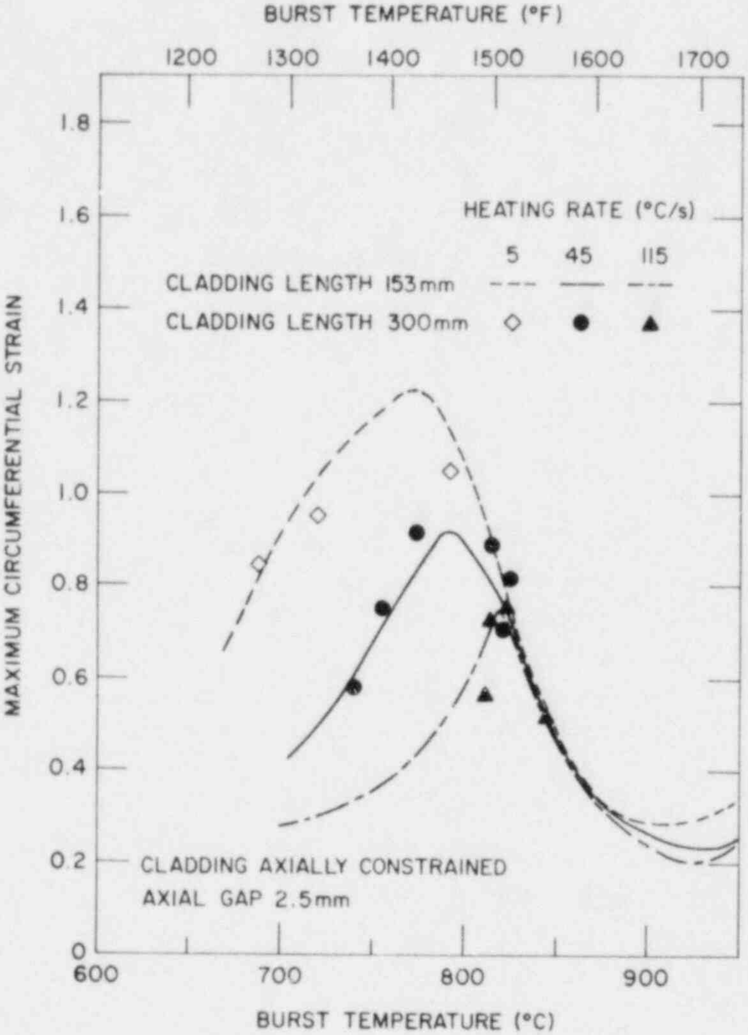

Fig. 85

Maximum Circumferential Strain vs Burst Temperature for 153- and 300-mm-long Axially Constrained Cladding at Three Heating Rates in Steam. ANL Neg. No. 306-77-149.

VII. DEFORMATION CHARACTERISTICS OF PELLET-CONSTRAINED ZIRCALOY CLADDING

Although the circumferential rupture strain of α-phase Zircaloy cladding does not decrease as a result of oxidation in a steam environment under transient-heating conditions, temperature nonuniformities in the cladding, particularly around the circumference, markedly reduce the ballooning at initial pressures ≥ 5 MPa. Temperature nonuniformities in the cladding are inevitable during transient heating of a fuel rod because of offset of UO_2 pellets from the centerline position, pellet geometry changes, and nonuniform pellet enrichment. These variations result in local hot spots during deformation of the cladding. Because of the large temperature sensitivity of Zircaloy deformation, as evidenced in Fig. 12, temperature nonuniformities during ballooning may have a pronounced effect on the overall failure strain.

A. Measurements of Local Temperature Nonuniformities in Zircaloy Cladding

To investigate the effect of circumferential temperature variations in the cladding on the deformation behavior, we replaced the alumina rod, which was used to simulate the fuel column, by a stack of 10-mm-long, high-purity, recrystallized alumina pellets. The average diametral gap between the cladding and the pellets was varied from 0.07 to 0.5 mm, and the axial gap between the top of the pellet stack and the end plug was 2.5 mm, as was the case for most of the tests with the alumina rod. As a result of the asymmetrical position of the pellets with respect to the inner surface of the cladding (Fig. 86), large local temperature variations in the circumferential and axial directions developed in the cladding during the transient-heating tube-burst experiments.[7]

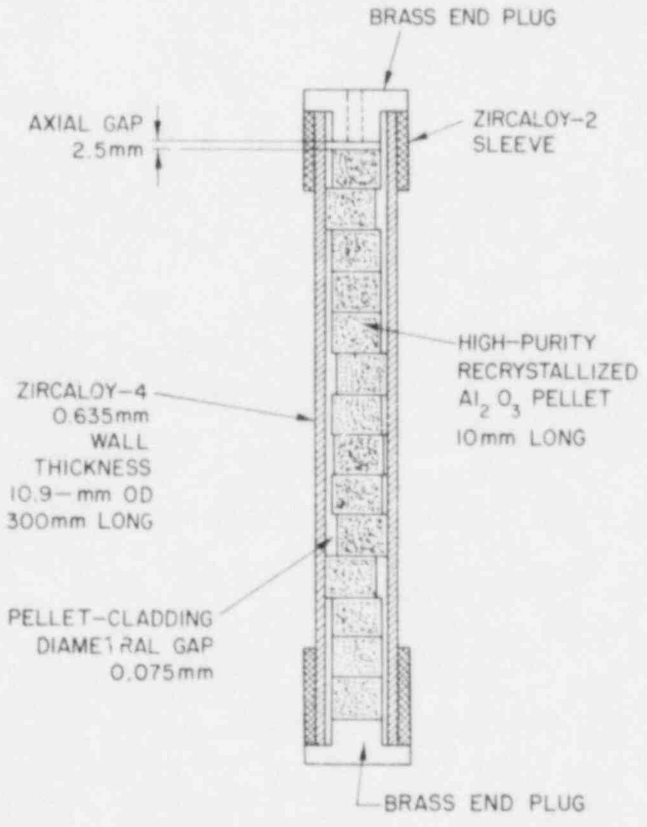

Fig. 86

Schematic Diagram of Cladding Tube Containing Alumina Pellets. ANL Neg. No. 306-77-150.

Figure 87 shows typical localized "hot" and "cold" spots on a cladding tube during the later stages of a burst test, along with thermocouple locations in the vicinity of the burst region. Figure 88 shows the temperature- and pressure-time information from this test as well as the point at which the photograph in Fig. 87 was taken. The maximum temperature difference between thermocouples 7 and 11 at the moment of burst was ~150°C. Because of the temperature nonuniformity, highly nonsymmetric ballooning and bending were commonly observed in specimens that contained alumina pellets (Fig. 89). Also, multiple ballooned regions on the cladding were frequently observed, particularly for high-heating-rate experiments. Infrared scans of internal heating elements have indicated temperature nonuniformities which result in localized ballooning, similar to Fig. 89, at multiple axial positions.[13]

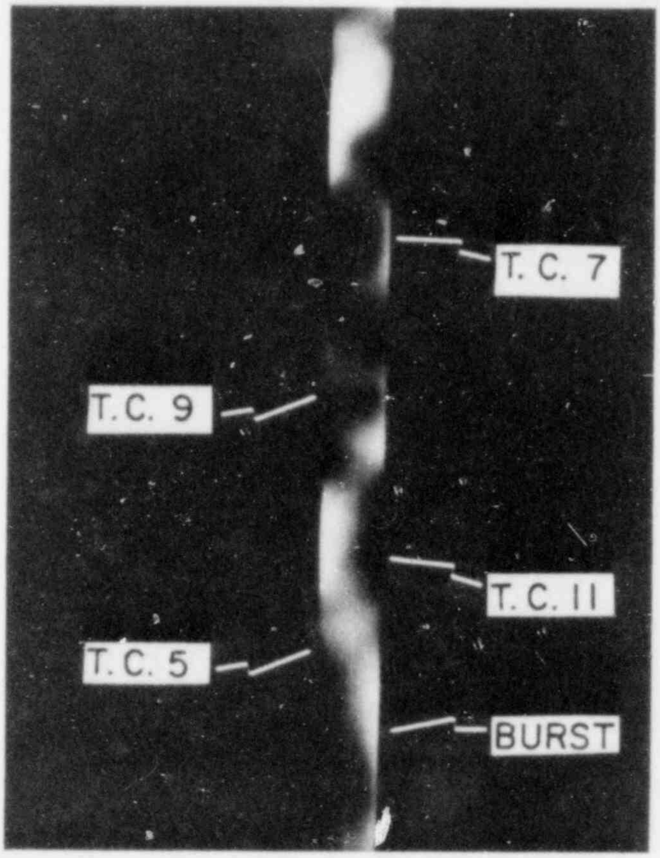

Fig. 87

Nonuniform Brightness of Cladding Specimen Containing Alumina Pellets due to Axial and Circumferential Temperature Variations during Heating at 45°C/s. ANL Neg. No. 306-77-135.

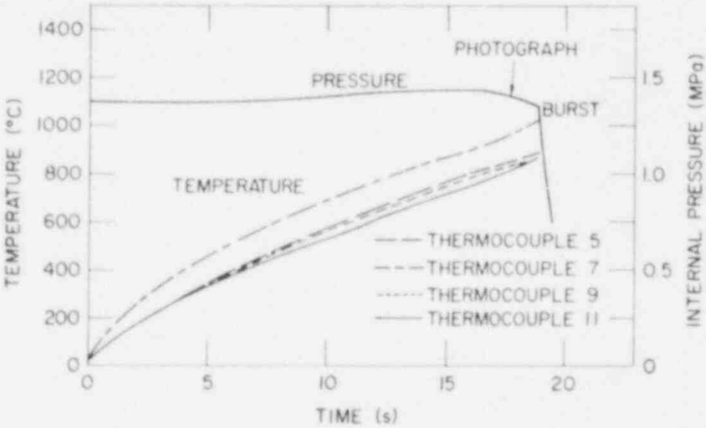

Fig. 88

Temperature and Internal Pressure as a Function of Time for Cladding Specimen Described in Fig. 87. ANL Neg. No. 306-77-141.

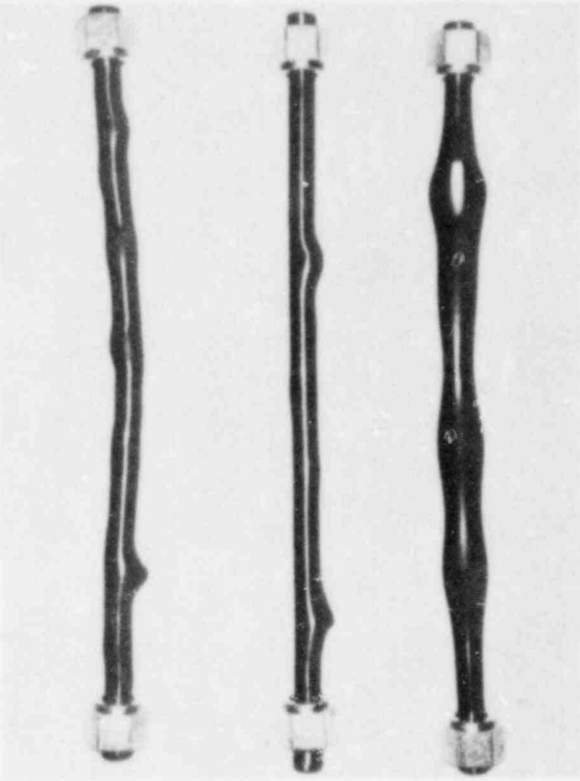

Fig. 89

Cladding Constrained by Pellets after Burst. Multiple ballooning regions and irregular bends are a result of temperature nonuniformity. ANL Neg. No. 306-77-134.

In general, the burst opening in the cladding is in the axial direction, since the tangential stress is higher than the axial stress during the final stages of ballooning. However, for pellet-constrained cladding that ruptures at temperatures in the α- or predominantly α-phase region, tangential rupture orientations, as shown in Fig. 90, were occasionally observed. The internal pressures and heating rates for the specimens shown in Fig. 90 were 11.2 and 9.7 MPa and 51 and 11°C/s, respectively. The tangential failure orientation results from a large circumferential temperature gradient in the ballooning region in which the higher temperature was opposite the burst opening.

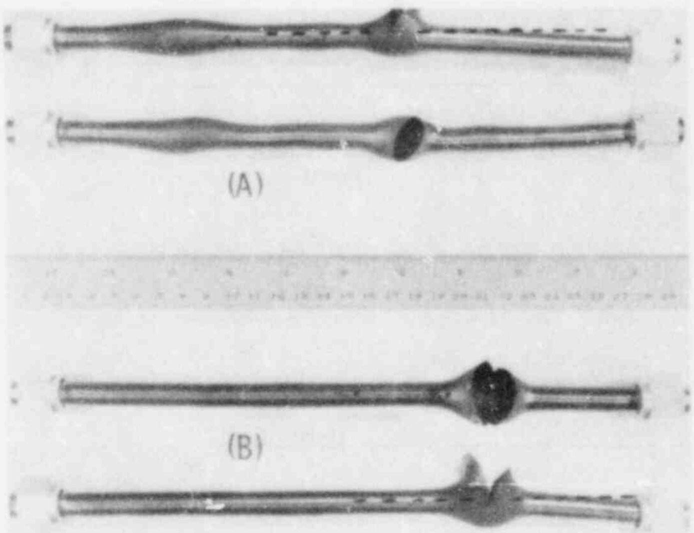

Fig. 90

Pellet-constrained Zircaloy-4 Cladding with 0.5-mm Diametral Gap after Rupture in Steam Showing Tangential Rather Than Typical Axial Burst Openings. The initial pressures and heating rates are (A) 11.2 MPa and 51°C/s, and (B) 9.7 MPa and 11°C/s. ANL Neg. No. 306-77-329.

The ballooning sequence that leads to this type of failure is as follows. Initially, as the hotter side of the tube begins to balloon, the material undergoes tangential expansion as well as axial contraction, because wall thinning is not favorable during the deformation of α-phase cladding. At this stage, axial contraction of the cooler side of the tube is negligible and the tube bends in the direction of the ballooning region (Fig. 90B). As a result of the bending moment on the tube, the cooler side also deforms and the axial stress in this region can exceed the tangential stress, particularly when tight contact between the pellet edge and the cladding causes a local stress concentration.

B. Effect of Temperature Nonuniformities on Circumferential Strain at Rupture

Since oxidation of the Zircaloy is not an important parameter in the deformation behavior of cladding that bursts in the α- or predominantly α-phase region ($\leq$840°C), the temperature nonuniformity becomes the major factor in the localization of the strain. In comparison with previous results for either unconstrained or mandrel-constrained cladding, in which nearly uniform heating was achieved, plastic instability occurred at an earlier stage of deformation and the circumferential strain was considerably smaller for pellet-constrained cladding. Figure 91 compares the diametral expansion of mandrel- and pellet-constrained cladding tubes, which both ruptured at a maximum temperature of ~825°C at a heating rate 115°C/s in steam. The initial pressure of both cladding tubes was 8.9 MPa. The nonuniform local temperatures of the pellet-constrained tube (Fig. 91B) are indicated by the dark-bright pattern of the tube surface recorded by a high-speed camera ~1.5 s before the burst.

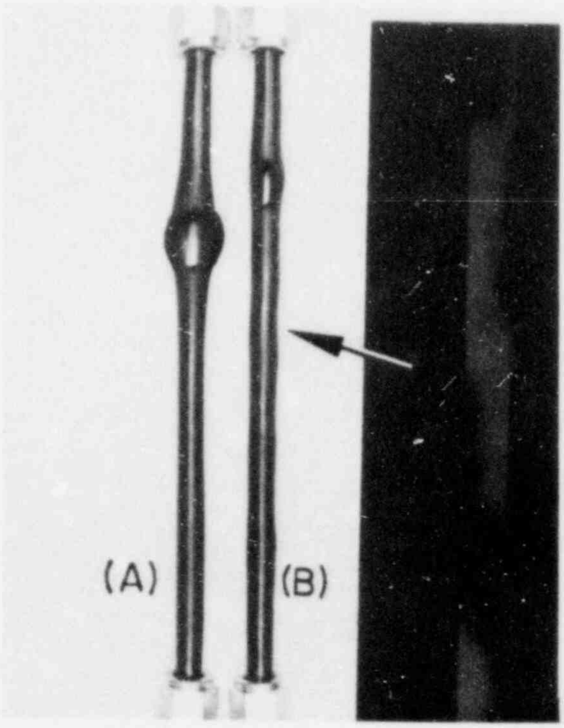

Fig. 91

Comparison of Circumferential Expansion of (A) Mandrel-constrained and (B) Pellet-constrained Cladding Tubes Burst at Nearly Identical Maximum Temperature of ~825°C. Nonuniform local temperature pattern of (B) ~1.5 s before burst is also shown. Initial internal pressure 8.9 MPa and heating rate 115°C/s for both tubes burst in steam. ANL Neg. No. 306-77-422.

Nonuniform heating of the cladding, caused by the larger heat transfer between the "hot" cladding and the relatively "cold" offset alumina pellets during the transient heating, greatly decreases the burst strain. In a nuclear-heated fuel rod, the heat-transfer situation is reversed; viz., the hot UO_2 pellets heat the cold Zircaloy cladding. However, the nonuniform heating pattern can be simulated effectively in our tests on pellet-constrained cladding with direct-resistance heating.

Since local temperature nonuniformity was identified as a critical parameter in relation to the ballooning strain, the parameter was investigated systematically by varying the heating rate and pellet-cladding diametral gap size. We believe that the ballooning strain in nuclear-heated Zircaloy fuel cladding can be predicted with reasonable accuracy from (1) a well-established correlation of the rupture strain and the degree of temperature nonuniformity in the cladding (obtained from out-of-reactor tests) and (2) a knowledge of the temperature nonuniformity in LWR fuel cladding under typical LOCA situations. Information on the deformation characteristics of pellet-constrained cladding obtained from a high-speed camera revealed that the rupture always occurs in the region of highest temperature (brightest surface area in the tube). Therefore, the maximum temperature and maximum local temperature difference, in the short length of the cladding that undergoes ballooning and eventual rupture, become important parameters in relation to the rupture behavior of pellet-constrained cladding. A simple correlation between the maximum circumferential strain and burst temperatures, e.g., Figs. 27 and 48, is no longer meaningful.

The maximum circumferential strain for pellet-constrained cladding (pellet-cladding diametral gap, 0.07 mm; axial gap, 2.5 mm) are shown in Figs. 92-94 for average heating rates of 115, 45, and 5°C/s in steam, respectively. The data points in these figures correspond to the maximum cladding temperature, and the bars associated with each point represent the range of temperatures obtained from the four or five thermocouples in each test.

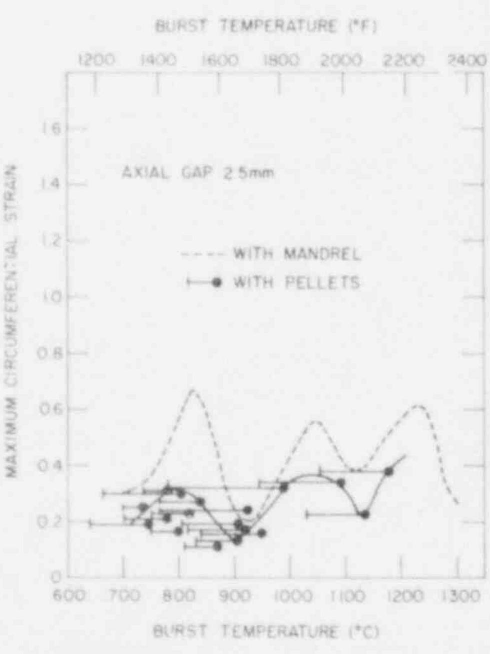

Fig. 92

Maximum Circumferential Strain vs Maximum Burst Temperature in Steam at Heating Rate of 115°C/s for Cladding Constrained by Pellets. Maximum recorded temperature differences are shown by bars. Similar results for mandrel-constrained cladding are also shown for comparison. ANL Neg. No. 306-77-151.

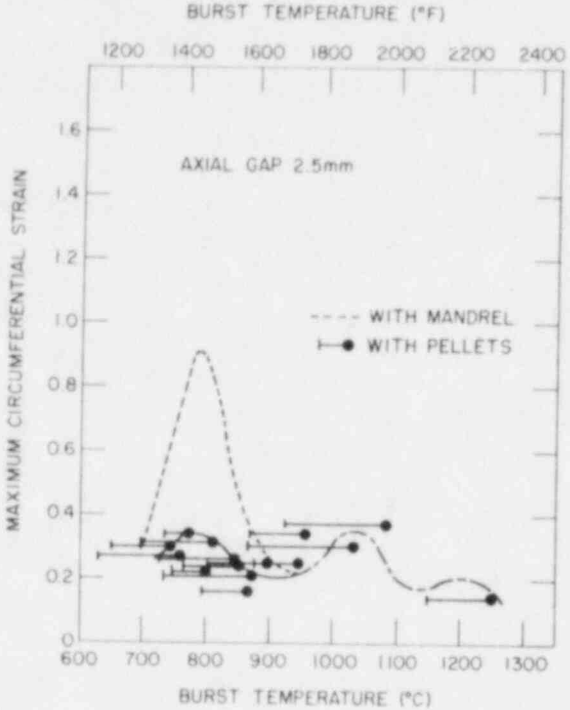

Fig. 93. Maximum Circumferential Strain vs Maximum Burst Temperature in Steam at Heating Rate of 45°C/s for Cladding Constrained by Pellets. Maximum recorded temperature differences are shown by bars. Similar results for mandrel-constrained cladding are also shown for comparison. ANL Neg. No. 306-77-155.

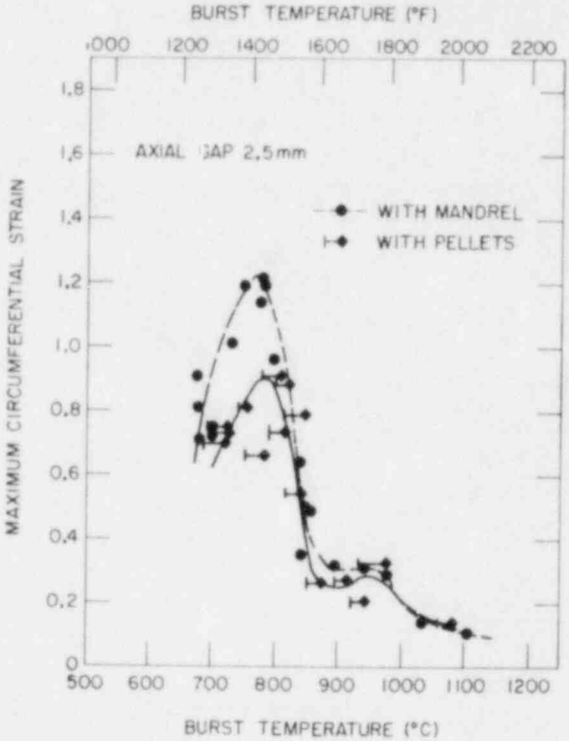

Fig. 94. Maximum Circumferential Strain vs Maximum Burst Temperature in Steam at Heating Rate of 5°C/s for Cladding Constrained by Pellets. Maximum recorded temperature differences are shown by bars. Similar results for mandrel-constrained cladding are also shown for comparison. ANL Neg. No. 306-77-152.

Except for the 5°C/s heating-rate data in Fig. 94, the circumferential strain at failure is significantly lower for the tubes constrained by pellets at burst temperatures ≤850°C; i.e., the strain does not exceed a value of 0.4 for all cases. Within the uncertainty of the temperature measurements in these experiments, the general features of the strain-burst-temperature relationships obtained with the mandrel-constrained tubes are evident at the three heating rates. An examination of Figs. 92-94 reveals that (a) the temperature nonuniformity increases as the average heating rate increases, (b) the circumferential strain for burst temperatures ≤850°C decreases as the temperature nonuniformity increases, and (c) the temperature nonuniformity has a minimal effect on circumferential strain for rupture in the two-phase and β-phase regions, except at a heating rate of 115°C/s. Therefore, temperature nonuniformity, caused by the offset pellets, is not expected to have a significant effect on the circumferential strain at failure for rupture temperatures ≥900°C and heating rates ≤50°C/s.

C. Effect of Pellet-Cladding Diametral-gap Distance on Temperature Nonuniformity and Circumferential Strain

The magnitude of the local circumferential and axial temperature variation in Zircaloy fuel cladding under hypothetical LOCA situations is not well known and thus cannot be simulated directly in out-of-reactor experiments. Factors such as offset pellets, cladding ovality due to creep-collapse, pellet cracking, and variations in pellet enrichment generally increase the probability of hot-spot development. Alternatively, heat generation in adjacent fuel rods reduces temperature nonuniformity in the cladding.

To investigate the effect of temperature nonuniformity on the maximum circumferential expansion of Zircaloy cladding, we conducted a series of transient-heating burst experiments with pellet-cladding diametral-gap distances of 0.2 and 0.5 mm for comparison with previous results (Figs. 92-94) obtained with a smaller diametral gap of 0.07 mm. Other variables such as the length of each pellet (i.e., 10 mm) and maximum variation in the pellet diameter (i.e., ~0.04 mm) remained constant.

Figure 95 shows a qualitative comparison of the temperature distribution, as evidenced by the "hot" and "cold" spots, produced in two tubes with diametral-gap distances of 0.07 and 0.5 mm for heating rate of 45°C/s and an internal pressure of 9.65 MPa. The tube with the smaller diametral-gap distance (Fig. 95A) exhibits a higher density of "cold" spots that are smaller in size than those obtained with a 0.5-mm gap (Fig. 95B). The probability of developing a relatively large uniform-temperature zone, as shown by the arrow in Fig. 95B, is greater for a larger diametral gap. The magnitude of the temperature nonuniformity in the cladding with 0.2- and 0.5-mm diametral gaps was similar under similar heating-rate conditions.

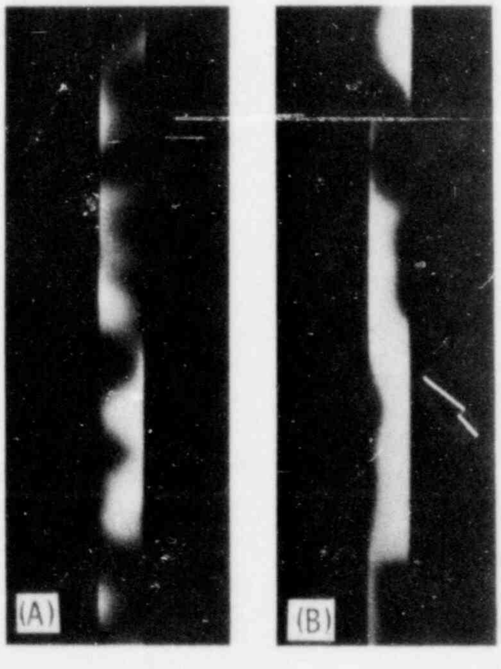

Fig. 95

Comparison of Temperature Distributions in Zircaloy, as Evidenced by "Hot" and "Cold" Regions, at Heating Rate of 45°C/s and Internal Pressure of 9.7 MPa for Pellet-Cladding Diametral-gap Distances of (A) 0.07 and (B) 0.5 mm. ANL Neg. No. 306-77-330.

Figure 96 shows the maximum recorded local temperature difference for cladding temperatures between ~750 and 800°C as a function of the heating rate for diametral-gap distances of 0.07, 0.2, and 0.5 mm. At low heating rates (≤20°C/s), the temperature variations in the cladding are small (~40-60°C) and relatively insensitive to the diametral-gap distance, whereas at higher heating rates, the temperature non-uniformity increases as the diametral-gap distance decreases.

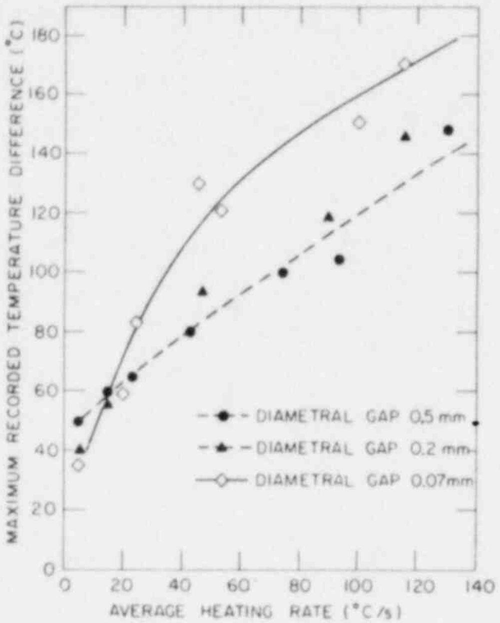

Fig. 96

Relationship between Maximum Local Temperature Difference at Temperatures near 800°C and Heating Rate for Pellet-Cladding Diametral-gap Distances of 0.07, 0.2, and 0.5 mm. ANL Neg. No. 306-77-331 Rev.

The relationships between the maximum circumferential strain and the burst temperature for the different diametral-gap distances are shown in Figs. 97-99 for heating rates of 115, 45, and 5-10°C/s, respectively. At the lowest heating rate, the diametral-gap distance does not strongly affect the circumferential strain; however, as the heating rate increases (≳45°C/s), the circumferential strain for burst temperatures near 800°C is approximately a factor of two higher for the larger gap distances. No significant difference was observed in the circumferential strains at failure for cladding with 0.2- and 0.5-mm diametral-gap distances. This is consistent with the results in Fig. 96 for the variation of the maximum temperature difference with heating rate for the two gap sizes.

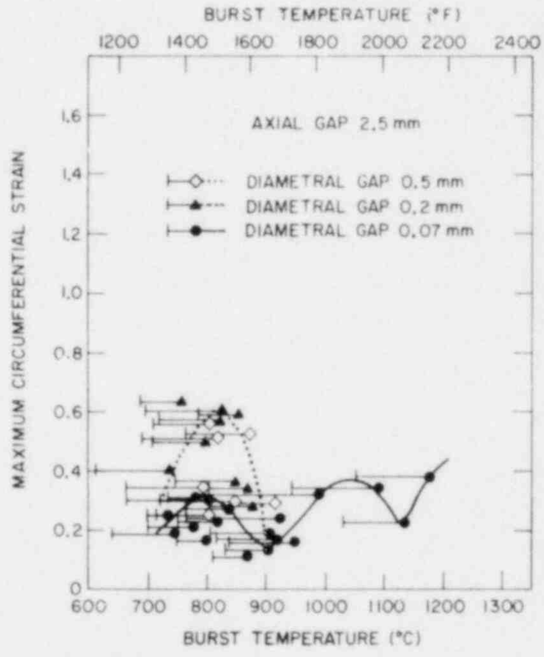

Fig. 97

Maximum Circumferential Strain vs Burst Temperature for Axially Constrained Zircaloy-4 Cladding with Pellet-Cladding Diametral-gap Distances of 0.07, 0.2, and 0.5 mm at Heating Rate of 115°C/s in Steam. ANL Neg. No. 306-77-342.

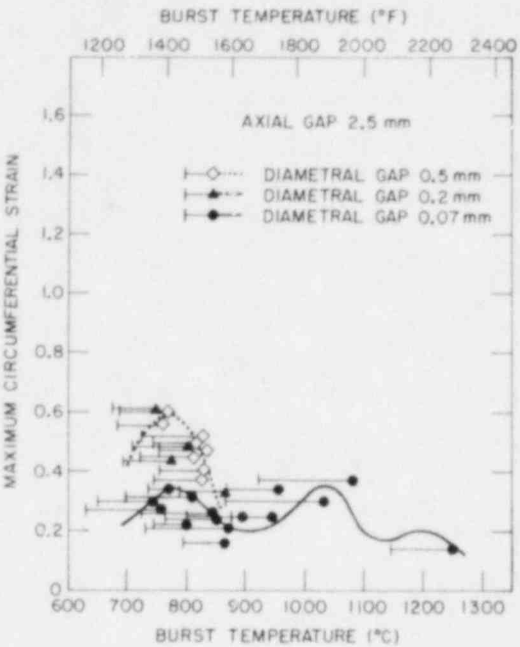

Fig. 98

Maximum Circumferential Strain vs Burst Temperature for Axially Constrained Zircaloy-4 Cladding with Pellet-Cladding Diametral-gap Distances of 0.07, 0.2, and 0.5 mm at Heating Rate of 45°C/s in Steam. ANL Neg. No. 306-77-352.

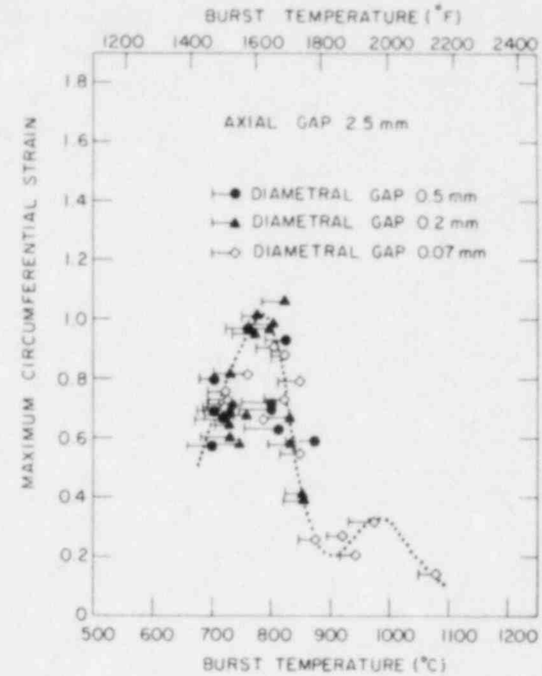

Fig. 99

Maximum Circumferential Strain vs Burst Temperature for Axially Constrained Zircaloy-4 Cladding with Pellet-Cladding Diametral-gap Distances of 0.07, 0.2, and 0.5 mm at Heating Rate of 5-10°C/s in Steam. ANL Neg. No. 306-77-340.

The increase in the circumferential strain from ~30 to 60% for gap distances of 0.07 to 0.2-0.5 mm, respectively, at heating rates of 115 and 45°C/s is due to the larger regions of more uniform temperature in the case of the larger diametral-gap distances (e.g., Fig. 95B), although the maximum local temperature variations, as evidenced by the bars in Figs. 97-99, are not strongly dependent on the gap size for burst temperatures near 800°C. Based upon the relatively small differences between the circumferential strain behavior of pellet- and mandrel-constrained cladding (0.07-mm diametral gap) for burst temperatures in the $(\alpha + \beta)$- or β-phase regions, the effect of diametral-gap distance on the maximum circumferential strain will be small for burst temperatures ≥850°C.

Figures 100-102 show the effect of diametral-gap distance on the relationship between the maximum circumferential strain and the initial pressure for heating rates of 115, 45, and 5-10°C/s, respectively. At heating rates ≥45°C/s, the diametral-gap distance has a significant effect on the circumferential strain for internal pressures between 8 and 13 MPa, whereas no effect of gap distance was observed at the lowest heating rate. At low heating rates (i.e., ≤15°C/s) and internal pressures ≥5 MPa, circumferential strains between ~0.6 and 0.8 are likely, and, for a limited internal pressure range of 6-8 MPa, strains as high as 1.0 are possible in a steam environment. In a similar study, Furuta et al.[53] report a maximum circumferential strain of ~0.81 at ~800°C for pellet-constrained Zircaloy cladding (0.15-mm diametral gap) at a heating rate of ~3°C/s in steam. The result is in good agreement with the data in Fig. 99.

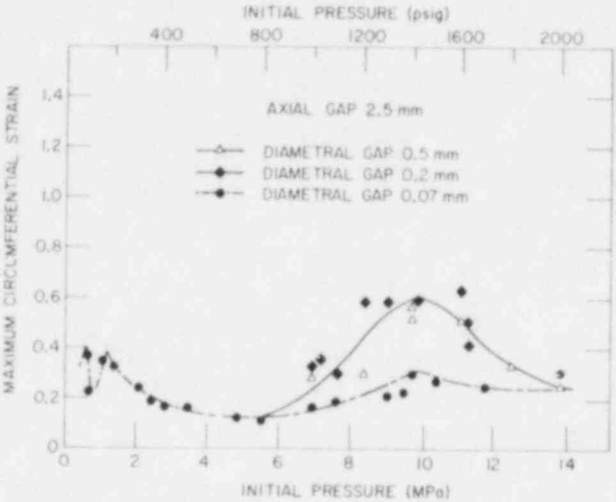

Fig. 100

Maximum Rupture Circumferential Strain as a Function of Initial Internal Pressure for Axially Constrained Zircaloy-4 Cladding with Pellet-Cladding Diametral-gap Distances of 0.07, 0.2, and 0.5 mm at Heating Rate of 115°C/s in Steam. ANL Neg. No. 306-77-347.

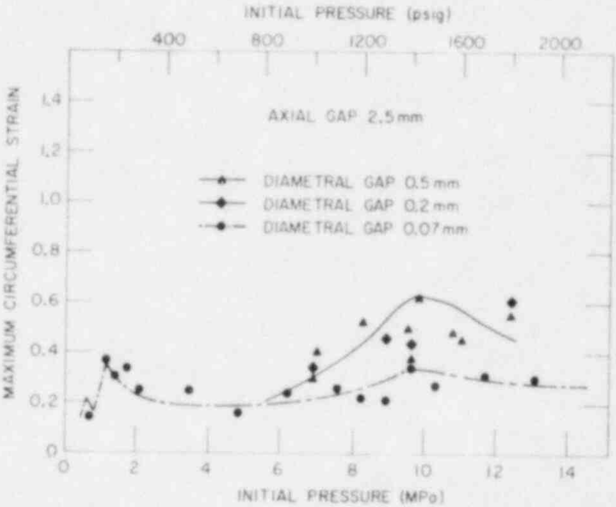

Fig. 101

Maximum Rupture Circumferential Strain as a Function of Initial Internal Pressure for Axially Constrained Zircaloy-4 Cladding with Pellet-Cladding Diametral-gap Distances of 0.07, 0.2, and 0.5 mm at Heating Rate of 45°C/s in Steam. ANL Neg. No. 306-77-346.

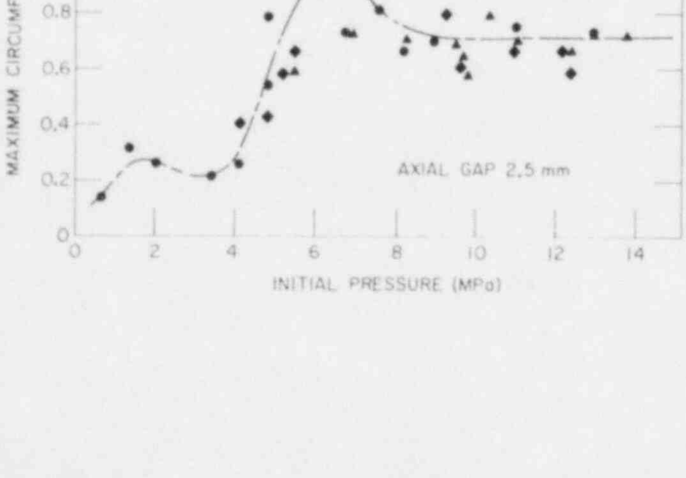

Fig. 102

Maximum Rupture Circumferential Strain as a Function of Initial Internal Pressure for Axially Constrained Zircaloy-4 Cladding with Pellet-Cladding Diametral-gap Distances of 0.07, 0.2, and 0.5 mm at Heating Rate of 5-10°C/s in Steam. ANL Neg. No. 306-77-341 Rev.

D. Comparisons of Maximum Circumferential Strain for Unconstrained and Mandrel- and Pellet-constrained Tubes in Steam

Figure 103 compares maximum circumferential strain for unconstrained and mandrel- and pellet-constrained (diametral gap, 0.07 mm) Zircaloy-4 cladding burst in steam at a heating rate of 115°C/s (e.g., the maximum circumferential strain peak near 800°C decreases from 1.24 for unconstrained cladding to 0.3 for pellet-constrained cladding). The large reduction of the burst strain is a result of the combined effects of axial constraint and circumferential temperature nonuniformity.

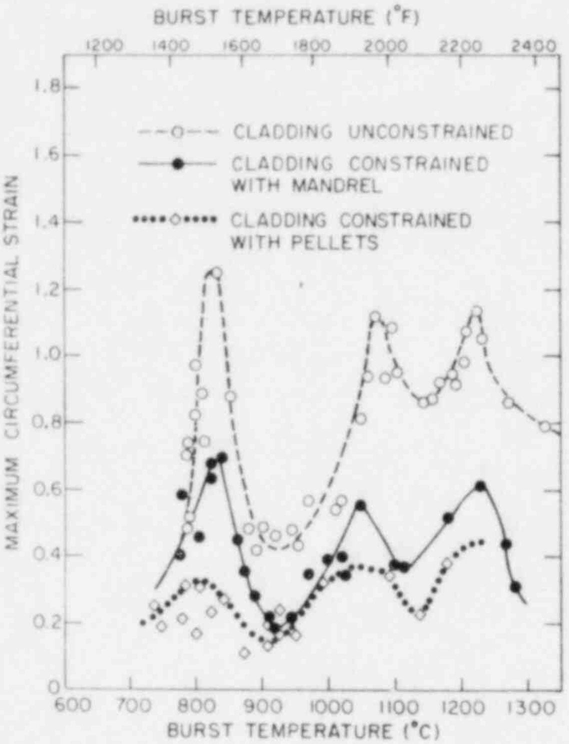

Fig. 103. Maximum Circumferential Strain vs Maximum Burst Temperature for Unconstrained and Mandrel- and Pellet-constrained Zircaloy-4 Cladding Tubes Burst in Steam at Heating Rate of 115°C/s. ANL Neg. No. 306-78-414.

A similar comparison for a heating rate of 5°C/s is shown in Fig. 104. In contrast to the results at the high-heating rate, the temperature nonuniformity is not large and the strain values are similar to those for mandrel-constrained cladding. When the local temperature nonuniformity is large, e.g., Figs. 97-99, it is more meaningful to correlate the maximum circumferential strain with initial internal pressure.

Figures 105-107 compare the dependence of maximum circumferential strain on initial internal pressure for unconstrained and mandrel- and pellet-constrained cladding at heating rates of 115, 45, and 5°C/s, respectively, in steam. The effect of temperature nonuniformity produced by the alumina pellets is quite pronounced for cladding pressures ≥5 MPa, i.e., for tubes that burst in the α- or predominantly α-phase region. The initial pressure, which results in maximum circumferential expansion, decreases from ~9.8 to 6.2 MPa as the heating rate decreases from 115 to 5°C/s.

E. Effect of Average Heating Rate on Deformation Behavior

The effects of initial internal pressure and average heating rate in steam on the maximum circumferential strain for pellet-constrained cladding (0.07-mm diametral gap) are best described in the three-dimensional plot in Fig. 108. A similar diagram for mandrel-constrained cladding was shown in Fig. 49. Figure 108 shows that circumferential strains ≥0.4 will result for internal pressures ≥6 MPa and heating rates ≤25°C/s.

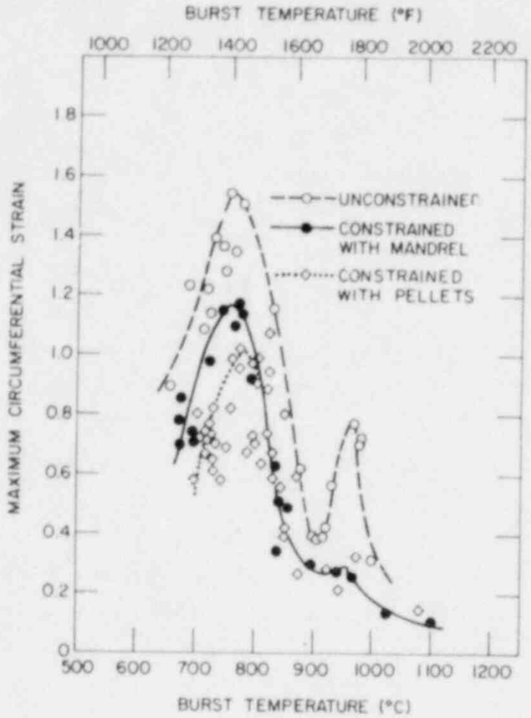

Fig. 104. Maximum Circumferential Strain vs Maximum Burst Temperature for Unconstrained and Mandrel- and Pellet-constrained Zircaloy-4 Cladding Tubes Burst in Steam at Heating Rate of 5°C/s. ANL Neg. No. 306-77-339.

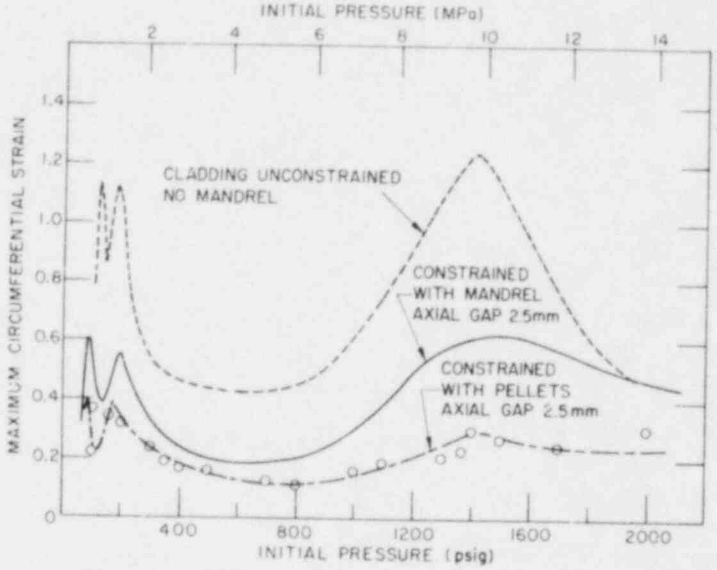

Fig. 105. Maximum Circumferential Strain vs Initial Internal Pressure for Unconstrained and Mandrel- and Pellet-constrained Cladding at Heating Rate of 115°C/s in Steam. ANL Neg. No. 306-77-153.

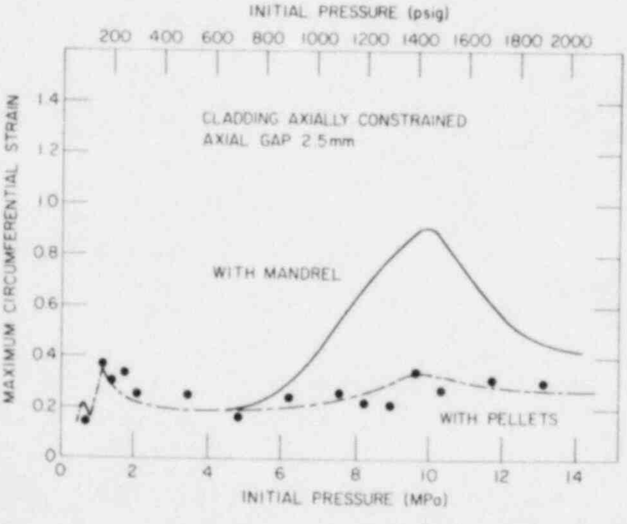

Fig. 106. Maximum Circumferential Strain vs Initial Internal Pressure for Mandrel- and Pellet-constrained Cladding at Heating Rate of 45°C/s in Steam. ANL Neg. No. 306-77-147.

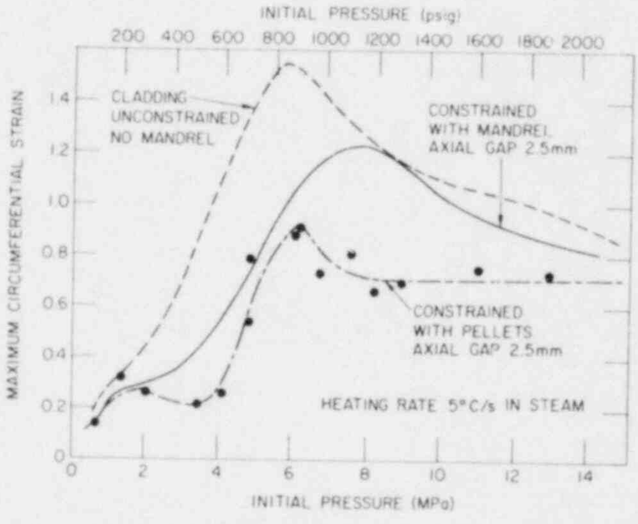

Fig. 107. Maximum Circumferential Strain vs Initial Internal Pressure for Unconstrained and Mandrel- and Pellet-constrained Cladding at Heating Rate of 5°C/s in Steam. ANL Neg. No. 306-77-157.

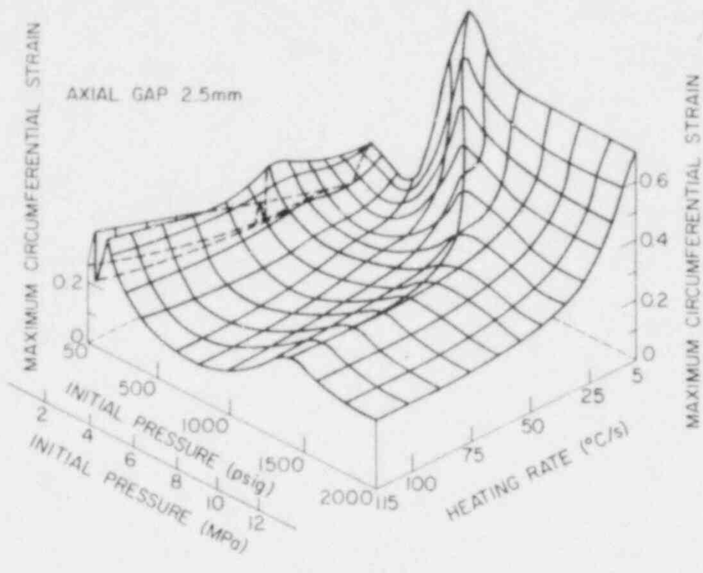

Fig. 108. Effect of Initial Internal Pressure and Heating Rate in Steam on Maximum Circumferential Strain for Zircaloy-4 Cladding Constrained by Pellets. ANL Neg. No. 306-77-139.

To compare the circumferential strains at rupture in our investigation with the results of other investigators, it is useful to plot the rupture strain as a function of pressure differential across the cladding for different heating rates (e.g., Fig. 109). Figure 109 clearly demonstrates the importance of heating rate for burst pressures ≥4 MPa; i.e., rupture strains ~0.32-0.35, 0.6, and 0.9 were obtained for heating rates of ~115, 45, 15-22, and 5-8°C/s, respectively. Figure 109 also shows results from in-reactor ballooning experiments conducted in the FR2 reactor at the Karlsruhe Nuclear Research Center, Federal Republic of Germany,[31] at heating rates of 6-19°C/s. In view of the pronounced effect of heating rate in this range on the rupture strain, a knowledge of the heating rate for each test would provide a better basis for comparison with our results.

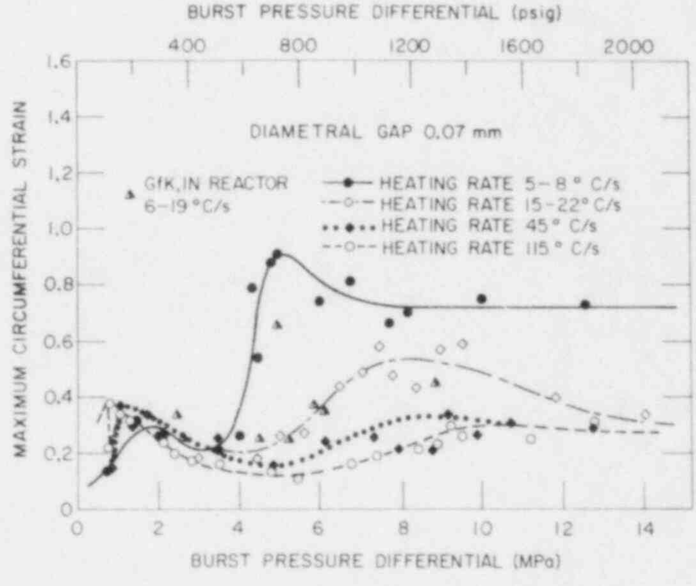

Fig. 109

Maximum Circumferential Strain vs Burst Pressure Differential for Pellet-constrained Cladding (Diametral-gap size 0.07 mm) Burst in Steam at Heating Rates of 5-8, 15-22, 45, and 115°C/s. A comparison with in-pile test results[31] (heating rate 6-19°C/s) is also shown. ANL Neg. No. 306-78-406.

Figure 110 summarizes the effect of heating rate on the maximum circumferential strain of Zircaloy-4 cladding in steam for burst temperatures near 800°C and cladding pressures ≥5 MPa. Results for unconstrained and mandrel- and pellet-constrained cladding with various diametral-gap sizes are shown. The data points were obtained from Figs. 45 (unconstrained), 48 (mandrel-constrained), 109 (pellet-constrained, diametral gap 0.07 mm),

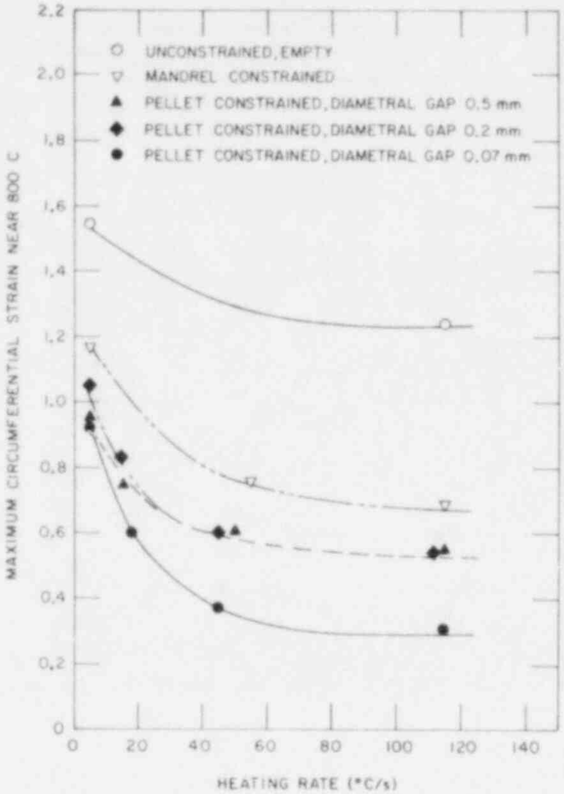

Fig. 110. Effect of Heating Rate on Maximum Circumferential Strain near 800°C for Unconstrained and Mandrel- and Pellet-constrained Zircaloy-4 Cladding in Steam. ANL Neg. No. 306-77-338 Rev.

and 97-99 (pellet-constrained, diametral gaps of 0.2 and 0.5 mm). The influence of heating rate on the rupture strain is most pronounced for pellet-constrained cladding with a small diametral gap at rates between ~5 and 50°C/s. The range of circumferential strains between ~0.3 and 1.5 for burst temperatures near 800°C indicated in this figure results from the synergistic effects of several variables, e.g., the diametral- and axial-gap sizes and the circumferential temperature variations in the cladding. To the extent that is possible, the effects of these parameters have been quantified in this investigation.

F. Relationship between Initial Internal Pressure of Cladding and Differential Burst Pressure

At the end of the blowdown phase, several seconds after the initiation of a hypothetical LOCA transient, the external pressure exerted on the cladding decreases to a low value (~0.4 MPa) that is insignificant compared to the internal pressures in typical prepressurized PWR fuel rods. Therefore, for heating rates ≤150°C/s, the internal pressure and pressure differential across the cladding are nearly equal during the critical period when significant diametral expansion and ballooning of the cladding occur. Consequently, pressurization of the cladding in in-reactor blowdown experiments is comparable to the conditions in the present investigation.

The initial internal pressure of cladding can be unambiguously defined in both in-reactor or out-of-reactor experiments. However, the burst-pressure differential in a fuel rod is a function of several parameters such as plenum volume, gas conductance in the annulus between the pellet and cladding, and cladding diametral expansion and ballooning, which are most important. Although the burst-pressure differential may be a more rigorous parameter than the initial internal pressure for establishing a correlation between the burst temperature and cladding pressure, the differential pressure at rupture is difficult to predict in most instances.

Figure 111 shows the burst-pressure differential for pellet-constrained cladding tubes as a function of the initial internal pressure of the cladding at room temperature for the relatively simple specimen geometry in our investigation. Regardless of diametral-gap size and heating rate, a good correlation exists. Figure 112 shows the burst temperature of pellet-constrained cladding (diametral gap 0.07 mm) as a function of burst-pressure differential. The results agree with similar data for mandrel-constrained cladding tubes (Fig. 46); i.e., for burst-pressure differentials ≥5 MPa, the maximum burst temperatures are higher at the higher heating rates. Figure 112 also includes data points from the in-reactor tests reported by Karb.[31] Within the uncertainty in the measurements of burst temperature in the in-reactor tests, the agreement with our out-of-reactor results is good.

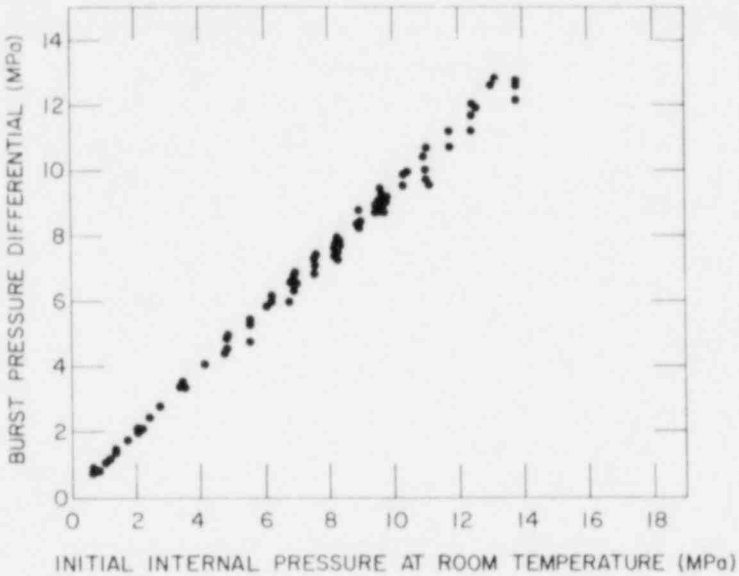

Fig. 111

Burst Pressure Differential vs Initial Internal Pressure at Room Temperature for Pellet-constrained Zircaloy-4 Cladding Ruptured in Steam. ANL Neg. No. 306-78-402.

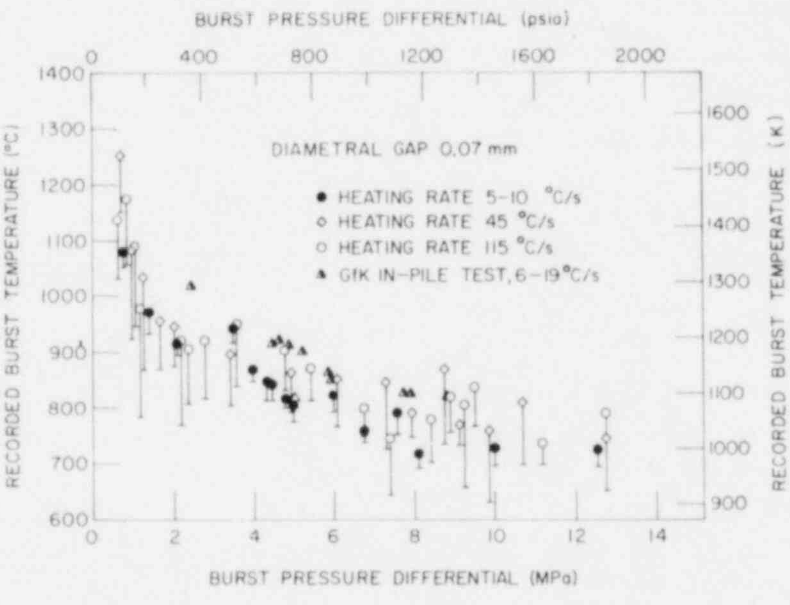

Fig. 112. Recorded Burst Temperature of Pellet-constrained (0.07-mm diametral gap) Zircaloy-4 Cladding as a Function of Burst Pressure Differential for Heating Rates of 115, 45, and 5-10°C/s. Results[31] from in-reactor tests are shown for comparison. ANL Neg. No. 306-78-407.

VIII. ANALYSIS OF LOCALIZED DEFORMATION OF ZIRCALOY-4 CLADDING AT TEMPERATURES IN α-PHASE REGION

The complex nature of Zircaloy deformation at temperatures in the α- or predominantly α-phase region (≤840°C) is evident from the results in prior sections of this report. Localized deformation in Zircaloy tubes that ruptured in the narrow temperature range of ~700-840°C was analyzed in detail to rationalize the large variation in rupture strain shown in Fig. 113 for different conditions, e.g., environment, heating rate, specimen length, preoxidation, pellet-cladding diametral- and axial-gap size, and internal pressure. Data of other investigators [9-31,53] result in a plot similar to Fig. 113 for this range of burst temperatures.

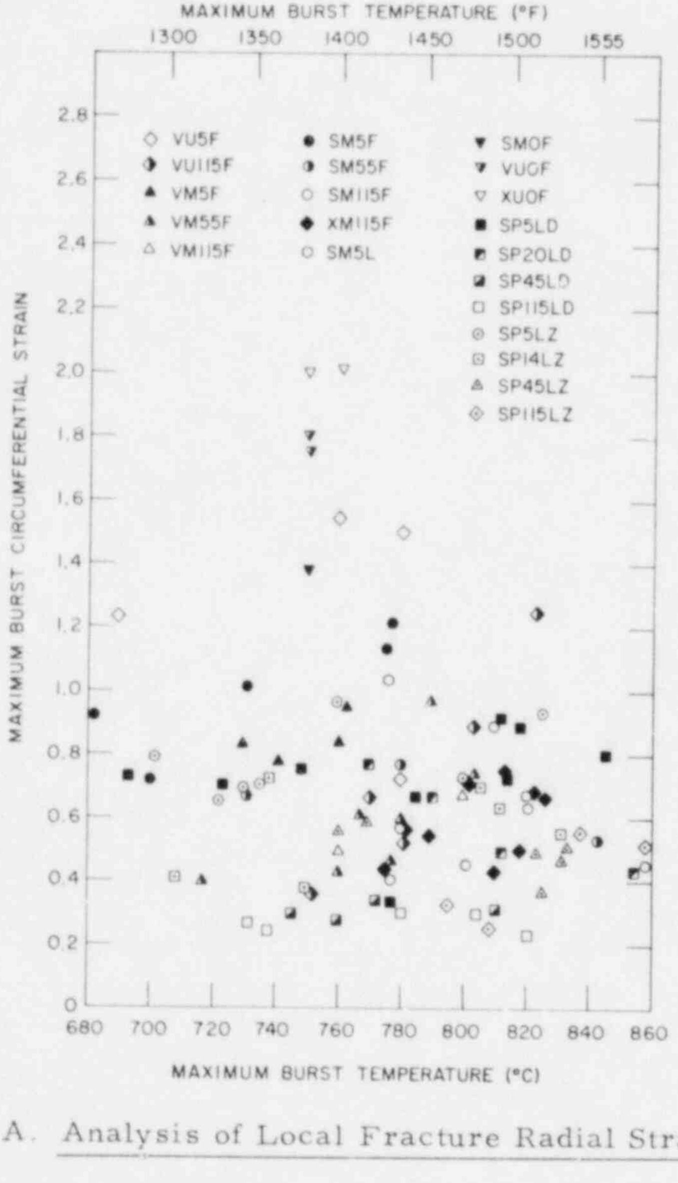

Fig. 113

Maximum Circumferential Strain vs Maximum Burst Temperature for Zircaloy-4 Cladding Tubes Burst in α- or Predominantly α-phase Region under Various Conditions. Test conditions can be identified from the following code abbreviations: V = vacuum environment, S = steam environment, X = preoxidized cladding in steam at a transient-heating rate of 115°C/s for 7 s and burst in vacuum, U = unconstrained cladding, M = mandrel-constrained cladding with a 2.5-mm axial gap, P = pellet-constrained cladding with a 2.5-mm axial gap, F = specimen length of 153 mm, L = specimen length of 300 mm, D = pellet-cladding diametral gap of 0.07 mm, Z = pellet-cladding diametral gap of 0.5 mm, numerals denote the heating rate in °C/s, and O represents isothermal stress-rupture tests. ANL Neg. No. 306-77-459.

A. Analysis of Local Fracture Radial Strain

In Sec. VI.D, the failure mode of Zircaloy cladding was classified in terms of a "rupture"- or "fracture"-type failure. The fracture edge of the former was sharp as a result of considerable thinning of the tube wall, whereas in the latter case, blunt edges characteristic of a shear process were typically observed. In a steam environment, "fracture"-type failures occurred invariably in α-phase material at temperatures ≤810°C, and "rupture"-type failures were found at higher temperatures. Because of the blunt fracture edge, the local radial strain can be measured unambiguously in specimens that burst at the lower temperatures. The cross section at the location of maximum circumferential strain was examined for tubes that burst at temperatures ≤830°C under different combinations of heating rate, initial internal pressure, degree of axial constraint, cladding length, circumferential temperature nonuniformity, preoxidation, and test environment (i.e., vacuum or steam). The true local radial fracture strains were determined from thickness measurements at the fracture tips and the relation

$$e_r^0 = \ln(h_F/h_0), \tag{20}$$

where

e_r^0 = true fracture radial strain,

h_F = thickness of the fracture tip measured perpendicular to a centerline at the midwall position,

and

h_0 = initial undeformed cladding thickness.

The true fracture radial strain is plotted in Fig. 114 as a function of the maximum temperature at burst for unconstrained and mandrel-constrained

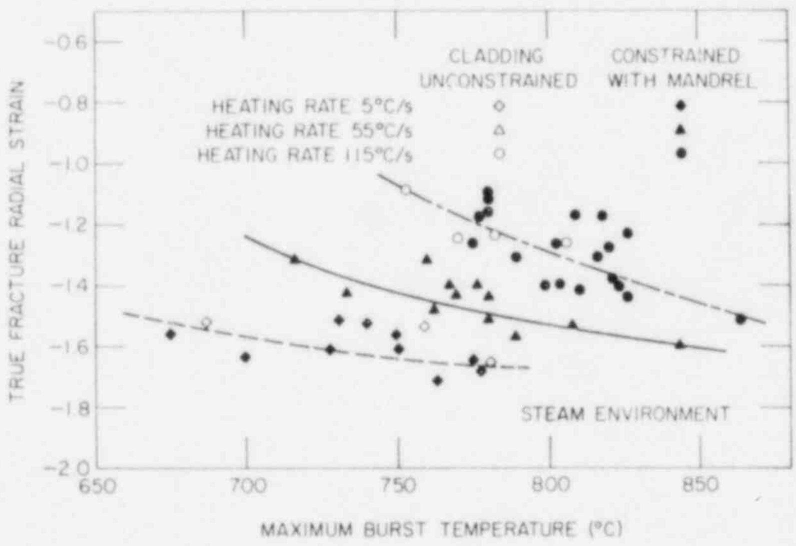

Fig. 114. True Fracture Radial Strain vs Maximum Burst Temperature for Unconstrained and Mandrel-constrained Zircaloy-4 Cladding Burst in Steam at Heating Rates of 5, 55, and 115°C/s. For burst temperatures below ~850°C, the cladding is entirely or predominantly in the α phase. ANL Neg. No. 306-77-142.

cladding at three heating rates in a steam environment. The results indicate that the radial strain decreases as the burst temperature increases (i.e., more wall thinning at the higher temperatures) and increases with heating rate. Figures 115 and 116 compare the fracture radial strain as a function of burst temperature for Zircaloy cladding constrained by the mandrel and the pellet stack at heating rates of ~55 and ~5°C/s, respectively. At both heating rates, the radial strains for the pellet-constrained cladding are higher (less thinning); this is a direct consequence of the more localized ballooning that occurs when

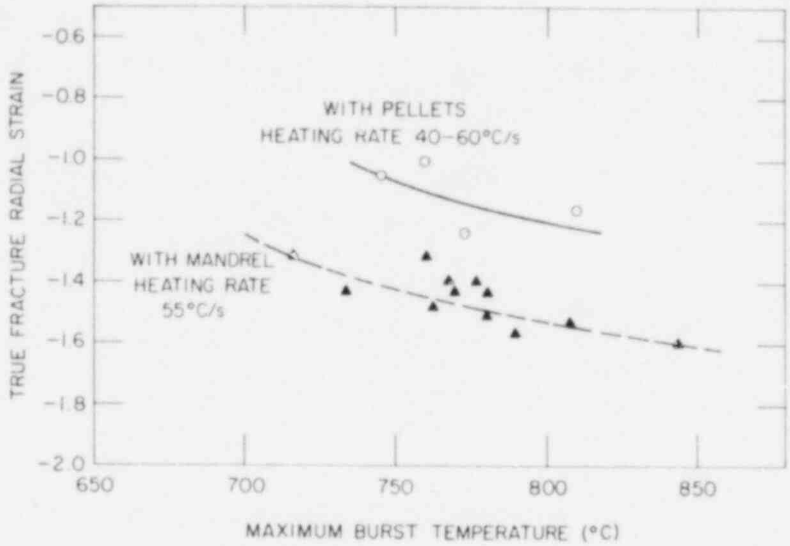

Fig. 115. True Fracture Radial Strain vs Maximum Burst Temperature for Unconstrained and Mandrel- and Pellet-constrained Cladding Burst in Steam at Heating Rate of 40–60°C/s. ANL Neg. No. 306-77-146.

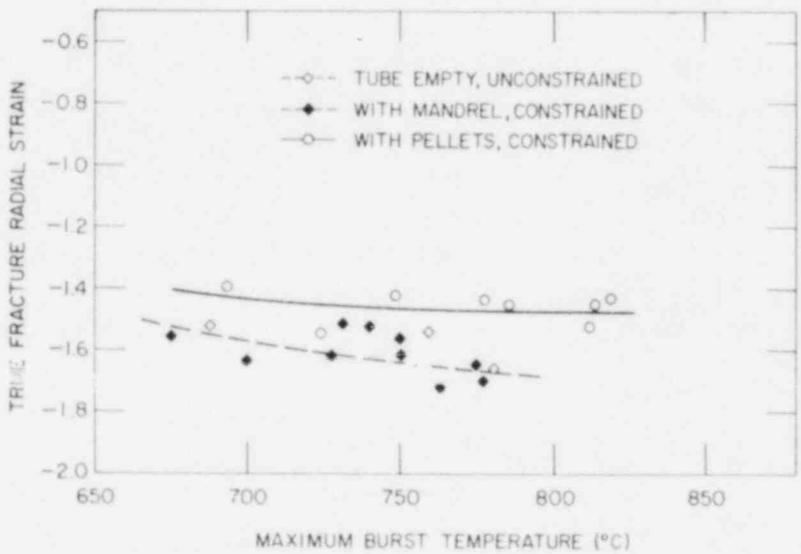

Fig. 116. True Fracture Radial Strain vs Maximum Burst Temperature for Unconstrained and Mandrel- and Pellet-constrained Cladding Burst in Steam at Heating Rate of 5°C/s. ANL Neg. No. 306-77-156 Rev.

the circumferential temperature variation is quite large. Since deformation is highly localized, the effective strain rate at the fracture tip is also greater than for the mandrel-constrained cladding.

B. Radial-strain Localization Parameter

Based on the results in Figs. 97-99 and 114-116, the radial strain at fracture can be correlated with the heating rate and the maximum circumferential temperature variation for the cladding at burst temperatures $\lesssim 830°C$. Oxidation of the cladding is small at these temperatures during the transient-heating tests, and differences in the amount of oxidation due to temperature variations are also quite small. It should therefore be possible to correlate the maximum circumferential strain with a quantitative measure of the extent of radial strain localization, such that the circumferential strain decreases as the radial strain becomes more localized.

For this purpose, a radial-strain-localization parameter W can be defined by

$$W = 1 - \frac{1}{2\pi}\int_0^{2\pi} \frac{e_r(\theta)}{e_r^0} d\theta, \qquad (21)$$

where

θ = tangential angle from fracture tip,

$e_r(\theta)$ = $\ln(h/h_0)$, i.e., true local radial strain at different θ positions around circumference of cladding,

and

h = local thickness of cladding cross section at region of maximum circumferential strain.

Thus, the radial-strain-localization parameter can be calculated from measured values of the cladding thickness from each experiment. Figure 117 shows micrographs of a cladding cross section and lists the e_r/e_r^0 values as a function of normalized angular position $\theta/2\pi$. It was assumed that

$$\theta/2\pi = \ell/L, \qquad (22)$$

where

ℓ = distance from fracture tip along circumference of tube

and

L = outside circumference of tube determined from cross section.

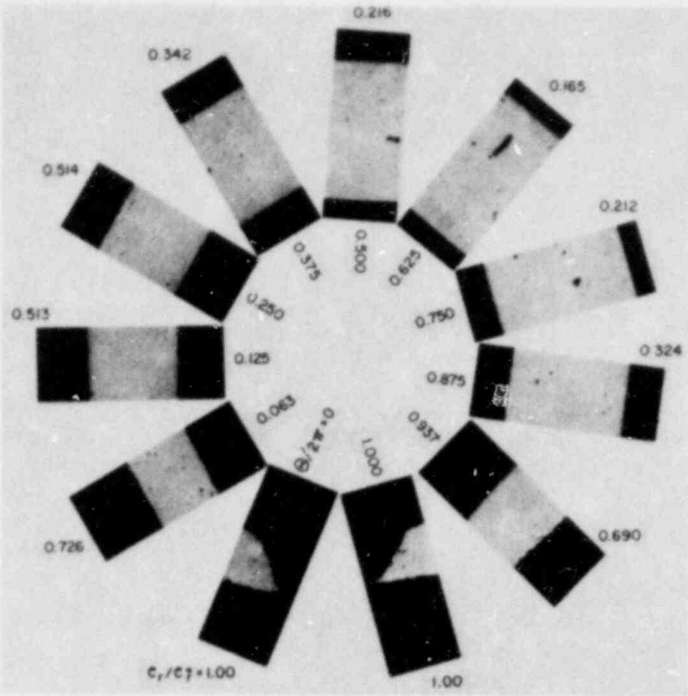

Fig. 117

Calculation of Ratio of True Local Radial Strain to True Fracture Radial Strain at Different Tangential Angles in Cross Section of Maximum Circumferential Strain. ANL Neg. No. 306-77-133.

The e_r/e_r^0 values, such as those shown in Fig. 117, were plotted against $\theta/2\pi$ and integrated according to Eq. 21 with a planimeter. The results from several tubes are shown in Fig. 118, where the shaded area for one of the experiments corresponds to the parameter W. Table II lists values for Zircaloy-4 tubes that were ruptured in vacuum and steam along with other burst parameters such as the circumferential strain, heating rate, and burst pressure.

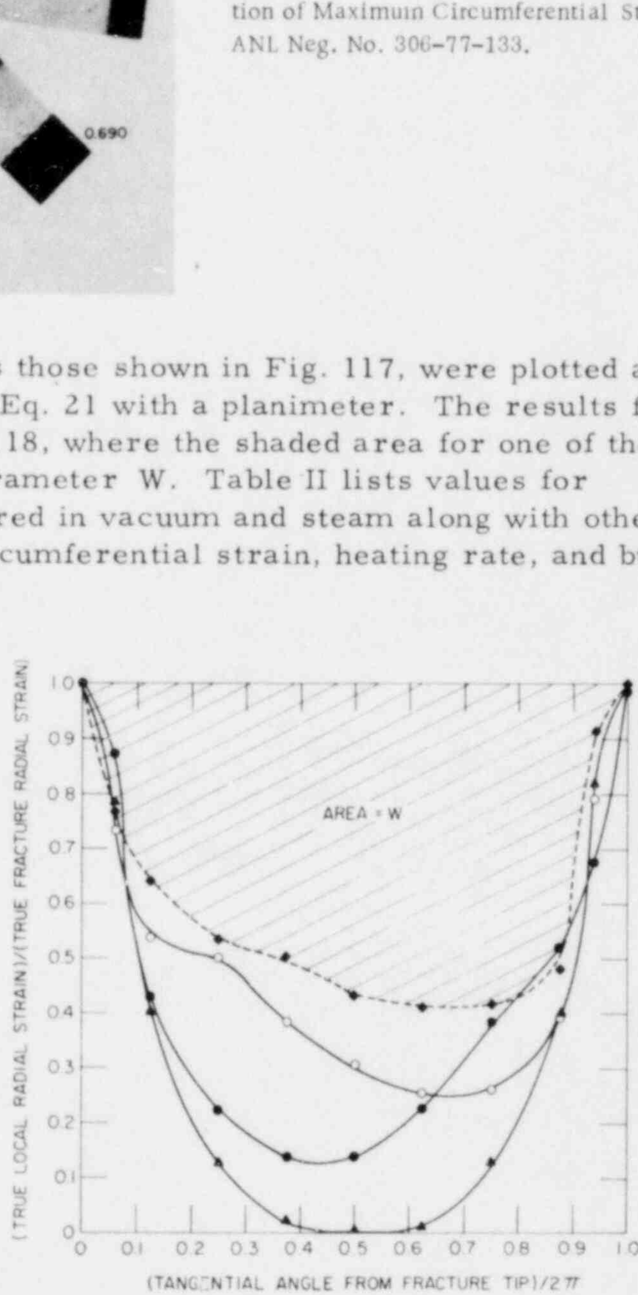

Fig. 118

Method of Determining Radial-strain-localization Parameter W from Plots of Ratio of True Local Radial Strain to True Fracture Radial Strain as a Function of Normalized Tangential Angle. ANL Neg. No. 306-77-144.

TABLE II. Radial-strain-localization (W) Parameters for Zircaloy-4 Cladding Burst under Different Test Conditions at Temperatures between ~700 and 850°C

Test Number	Test Environment	Constraint	Initial Pressure, MPa	Heating Rate, °C/s	Maximum Burst Temperature, °C	Maximum Circumferential Strain	W Parameter
AS-54	Vacuum	None	8.27	130	826	1.24	0.391
AS-55			13.8	111	753	0.36	0.702
AS-56			11.7	120	782	0.52	0.670
AS-67			8.27	115	806	0.89	0.546
AS-194		Mandrel[a]	7.96	119	801	0.66	0.629
AS-69			7.51	40	767	0.61	0.645
AS-70			7.51	70	797	0.67	0.633
AS-73			9.69	50	760	0.49	0.654
AS-75			7.51	35	780	0.60	0.662
AS-77			8.39	53	777	0.46	0.686
AS-78			9.69	39	717	0.40	0.712
AS-79			8.11	58	806	0.74	0.624
AS-80			8.66	56	760	0.43	0.732
AS-196			6.89	56	789	0.97	0.518
AS-43			7.51	5.2	765	0.95	0.546
AS-45			8.39	6.5	741	0.78	0.565
AS-46			9.69	6.1	729	0.83	0.535
AS-112			7.51	4.8	760	0.84	0.575
IS-68	Steam	None	10.3	111	809	0.89	0.488
IAS-130			10.3	7.9	689	1.23	0.411
IAS-131			6.89	4.7	759	1.54	0.381
IAS-132			5.51	4.0	781	1.50	0.392
IS-4		Mandrel[a]	8.27	115	867	0.45	0.665
IS-6			9.65	100	802	0.45	0.666
IS-10			11.7	103	777	0.40	0.667
IS-11			13.8	101	780	0.58	0.579
IS-12			11.7	126	821	0.63	0.611
IS-66			10.3	115	820	0.67	0.539
IS-65			10.3	5.9	700	0.72	0.614
IL-15			7.58	5.4	774	1.04	0.447
IS-34			8.27	54	843	0.52	0.640
IS-35			10.3	31	782	0.77	0.590
IS-37			13.8	30	732	0.64	0.605
IS-46			10.3	6	732	1.00	0.438
IS-47			11.0	5	675	0.91	0.497
IS-51			6.89	5	775	1.13	0.445
IS-52			5.48	5	777	1.21	0.424
CP-2[b]	Vacuum		10.4	118	798	0.43	0.651
CP-3[b]			13.8	121	775	0.44	0.701
CP-5[b]			9.96	107	825	0.68	0.593
CP-6[b]			10.7	115	826	0.67	0.545
CP-7[b]			12.1	114	-	0.73	0.512
CP-8[b]			12.8	113	789	0.54	0.620
CP-9[b]			10.5	118	838	0.50	0.625
CP-10[b]			11.0	110	780	0.57	0.593
CP-11[b]			11.0	107	816	0.72	0.520
CP-12[b]			12.4	116	804	0.71	0.598

TABLE II (Contd.)

Test Number	Test Environment	Constraint	Initial Pressure, MPa	Heating Rate, °C/s	Maximum Burst Temperature, °C	Maximum Circumferential Strain	W Parameter
SR-2	Vacuum	None	4.13	0	750	1.75	0.364
SR-5	"		5.17	0	750	1.79	0.403
SS-1	Steam		4.13	0	750	1.38	0.423
SCP-1[b]	Vacuum		4.13	0	750	2.01	0.389
SCP-2[b]	"		5.17	0	750	2.00	0.353
IPL-18	Steam	Pellet[c]	10.3	100	838	0.27	0.753
IPL-19			10.8	115	780	0.31	0.730
IPL-20			11.7	118	737	0.25	0.782
IPL-21			8.96	106	779	0.21	0.812
IPL-26			9.65	119	804	0.30	0.766
IPL-28			9.44	145	820	0.23	0.787
IPL-29			13.1	40	745	0.30	0.744
IPL-30			11.7	60	810	0.31	0.745
IPL-31			10.3	43	759	0.29	0.779
IPL-36			9.65	45	972	0.34	0.729
IPL-52			9.65	15.1	770	0.77	0.525
IPL-53			8.96	22.3	857	0.43	0.693
IPL-54			8.27	14.9	790	0.66	0.578
IPL-55			7.58	15.2	812	0.49	0.700
IPL-1			8.20	5.8	785	0.66	0.626
IPL-2			6.75	5.7	814	0.74	0.541
IPL-3			10.3	5.5	777	0.34	0.736
IPL-4			8.96	4.9	723	0.70	0.588
IPL-5			13.0	5	693	0.73	0.525
IPL-6			6.20	5	802	0.91	0.481
IPL-7			6.06	5	818	0.88	0.522
IPL-12			11.0	5	728	0.75	0.580
IPL-89	Steam	Pellet[d]	8.27	5.4	773	0.95	0.452
IPL-90			6.89	6.6	824	1.06	0.408
IPL-91			8.30	10	796	0.95	0.434
IPL-92			9.30	10	735	0.81	0.481
IPL-93			9.65	41	770	0.44	0.648
IPL-94			8.96	73	851	0.59	0.584
IPL-95			11.0	75	760	0.63	0.557
IPS-96			12.3	7.5	728	0.66	0.539
IPS-97			11.0	7.3	759	0.67	0.548
IPS-98			9.65	5.3	738	0.60	0.561
IPS-100			7.58	10	802	0.97	0.44[illegible]
IPS-102			7.58	6.6	779	1.02	0.503
IPS-107			12.3	10	751	0.58	0.606
IPS-108			8.96	49	812	0.46	0.663
IPS-109			12.4	45	756	0.63	0.646
IPS-111			8.27	80	834	0.60	0.605
IPS-112			9.65	112	818	0.56	0.641
IPS-113			11.2	91	809	0.51	0.663

TABLE II (Contd.)

Test Number	Test Environment	Constraint	Initial Pressure, MPa	Heating Rate, °C/s	Maximum Burst Temperature, °C	Maximum Circumferential Strain	W Parameter
IPL-65	Steam	Pellet[e]	9.65	133	875	0.52	0.640
IPL-67	↓	↓	12.4	130	795	0.33	0.736
IPL-68			13.8	139	808	0.26	0.731
IPL-84			9.65	94	807	0.56	0.659
IPL-77			9.78	54	768	0.60	0.606
IPL-78			12.4	41	760	0.56	0.655
IPL-80			9.65	47	825	0.37	0.733
IPL-81			8.27	47	833	0.52	0.664
IPL-85			9.58	50	823	0.49	0.666
IPL-86			10.9	51	832	0.48	0.706
IPL-69			6.89	20	831	0.55	0.657
IPL-74			11.0	20	708	0.41	0.709
IPL-75			12.4	14	749	0.38	0.716
IPL-56			12.5	7.0	722	0.66	0.558
IPL-57			11.1	4.2	738	0.70	0.502
IPL-58			10.4	8.1	702	0.79	0.554
IPL-59			9.55	6.5	730	0.68	0.595
IPL-60			8.27	4.6	759	0.97	0.492
IPL-61			6.89	4.5	800	0.72	0.587
IPL-62			5.56	4.5	825	0.93	0.525
IPL-71			8.27	9.8	803	0.70	0.612
IPL-73			9.65	10.1	811	0.63	0.580
IPL-76	↓	↓	13.8	10.2	739	0.72	0.583

[a]Zircaloy tube was constrained with an axisymmetric alumina mandrel in which the radial and axial-gap distances were 1.3 and 2.5 mm, respectively.

[b]Specimens were preoxidized on the outer surface during heating from 25 to 800°C in steam at ~115°C/s under zero differential pressures and ruptured in vacuum.

[c]Zircaloy tube was constrained with a column of 10-mm-long alumina pellets in which the diametral and axial-gap distances were 0.07 and 2.5 mm, respectively.

[d]Zircaloy tube was constrained with a column of 10-mm-long alumina pellets in which the diametral and axial-gap distances were 0.2 and 2.5 mm, respectively.

[e]Zircaloy tube was constrained with a column of 10-mm-long alumina pellets in which the diametral and axial-gap distances were 0.5 and 2.5 mm, respectively.

Figure 119 is a plot of the maximum circumferential strain versus the parameter W for experiments that encompass a wide range of experimental conditions. A surprisingly good correlation between the circumferential strain and the radial-strain-localization parameter was obtained. For isothermal stress-rupture tests, the circumferential strain increases markedly as the parameter W decreases. It is expected that the theoretical limits for the curve in Fig. 119 are

$$\lim_{W \to 0} \epsilon_\theta^M = \infty \tag{23}$$

and

$$\lim_{W \to 1.0} \epsilon_\theta^M = 0, \tag{24}$$

where ϵ_θ^M is the maximum circumferential strain. Results for pellet-constrained tubes with a 0.2-mm diametral gap are listed in Table II, but are not included in Fig. 119.

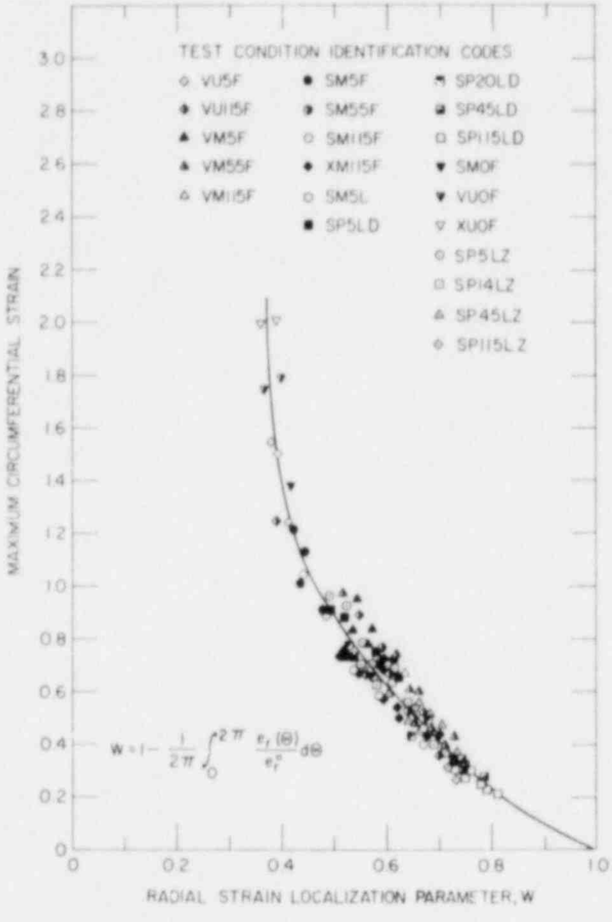

Fig. 119

Maximum Circumferential Strain vs Radial-strain-localization Parameter for α-phase Cladding Burst under Different Test Conditions at Temperatures between 700 and 850°C. Test conditions can be identified from the following code abbreviations: V = vacuum environment, S = steam environment, X = preoxidized cladding in steam at a transient-heating rate of 115°C/s for 7 s and burst in vacuum, U = unconstrained cladding, M = mandrel-constrained cladding with a 2.5-mm axial gap, P = pellet-constrained cladding with a 2.5-mm axial gap, F = specimen length of 153 mm, L = specimen length of 300 mm, D = pellet-cladding diametral gap of 0.07 mm, Z = pellet-cladding diametral gap of 0.5 mm, numerals denote the heating rate in °C/s, and O represents isothermal stress-rupture tests. ANL Neg. No. 306-77-143 Rev.

Figure 120 shows the dependence of the parameter W on the maximum circumferential temperature difference ΔT_θ^M for pellet-constrained cladding with diametral-gap distances of 0.07 and 0.5 mm at several heating rates in steam.

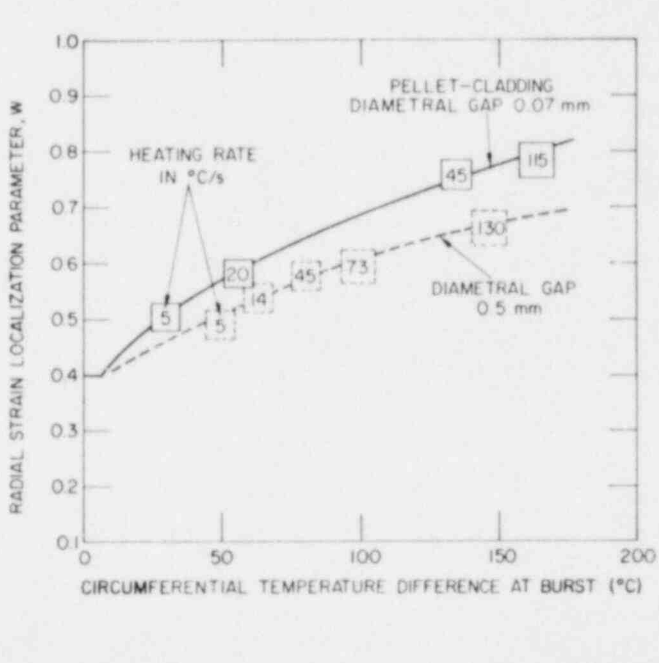

Fig. 120

Radial-strain-localization Parameter as a Function of Maximum Circumferential Temperature Difference in Zircaloy Tubes with Pellet-Cladding Diametral-gap Distances of 0.07 and 0.5 mm Ruptured in Steam at Temperatures near 800°C. ANL Neg. No. 306-77-140 Rev.

Information on the temperature difference at rupture for transient-heating burst experiments on pellet-constrained Zircaloy-4 cladding is listed in Appendix A (Tables A.17-A.21). The results in Fig. 120 are limited to experiments in which the maximum burst temperature lies within ±25°C of the ~800°C strain peak (i.e., the maximum in the curve for circumferential strain versus burst temperature near 800°C in Figs. 97-99).

If the major effect of an increase in heating rate in these experiments is to increase the magnitude of the temperature nonuniformity in the cladding, in contrast to a large increase in the effective strain rate during ballooning, the results in Figs. 119 and 120 and Tables II and A.17-A.21 can be used to directly relate the maximum circumferential strain to the maximum temperature variation in the cladding for burst temperatures near 800°C. Figure 121 shows this relationship for Zircaloy-4 cladding with diametral-gap distances of 0.07-0.5 mm. For a given temperature difference, the larger strains associated with the 0.5-mm-gap distance result from the distribution of "hot" and "cold" regions in the tube; i.e., the small diametral gap (0.07 mm) produces a higher density of "cold" spots, which are smaller than those obtained with the 0.5-mm-gap distance (Fig. 95).

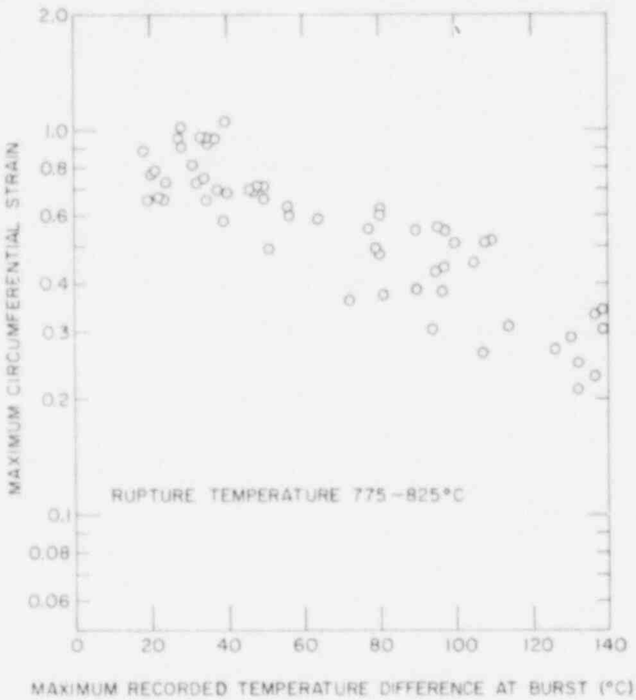

Fig. 121. Maximum Circumferential Strain as a Function of Maximum Circumferential Temperature Difference in Pellet-constrained Zircaloy Tubes Ruptured in Steam at Temperatures near 800°C. ANL Neg. No. 306-78-544.

Although the information in Fig. 121 is limited to our specimen geometry and test conditions, the essential parameters that control the deformation of Zircaloy under hypothetical LOCA situations were incorporated into the experiments in a manner as representative as in other out-of-reactor simulations of fuel-rod behavior. In this regard, our results encompass the entire range of rupture strains (~0.2 to 1.3) reported by other investigators[9-31] for burst temperatures near 800°C. Therefore, we believe the maximum circumferential strain for burst temperatures between ~775 and 825°C can be predicted with reasonable accuracy from a knowledge of the local temperature variation in the cladding.

Information from the multirod burst-test program at Oak Ridge National Laboratory and from the in-reactor ballooning experiments on Zircaloy-clad UO_2 fuel rods in the Power Burst Facility at the Idaho National Engineering

Laboratory and the FR-2 Reactor at the Karlsruhe Nuclear Research Center in the Federal Republic of Germany can be used to test the general validity of the extensive data base developed in our investigation. The combined results should eliminate the large uncertainty in fuel-element modeling codes regarding predictions of circumferential expansion of Zircaloy cladding and the extent of flow blockage during postulated LOCA situations in LWR's.

IX. SUMMARY AND CONCLUSIONS

The high-temperature deformation and rupture behavior of Zircaloy-4 cladding has been investigated in vacuum and steam environments under transient-heating conditions that are of interest in hypothetical LOCA conditions in LWR's. The effects of internal pressure, heating rate, axial constraint, and localized temperature nonuniformity in the cladding on the circumferential strain have been determined for burst temperatures between ~650 and 1350°C. Parameters that have a major influence on the deformation and burst behavior have been identified. The following conclusions can be stated based upon the results of this work.

1. In-situ steam oxidation greatly suppresses the high-temperature circumferential strain maxima at burst temperatures of ~1050 and 1240°C in the β-phase region. The circumferential strain at rupture also decreases as the heating rate decreases because of the longer oxidation period associated with low heating rates. The significant reduction in the circumferential strain in the β-phase region results from cracking of the oxide layer, accelerated oxidation of the underlying metal, and localized deformation by tearing of the β-phase material. In a vacuum environment, deformation occurs by a grain-boundary sliding mechanism, and rupture occurs by a pinhole-type failure.

2. The circumferential strain for tubes burst in steam in the α-phase regions at low heating rates (≲50°C/s) is greater than that in vacuum, because the biaxiality increases as a result of the additional tangential stress induced by the oxide layer. At higher heating rates, steam oxidation has no effect on the circumferential strain at rupture for temperatures in the α-phase region. Because of the anisotropy of α-phase Zircaloy, deformation in the radial direction (i.e., thinning of the tube wall) is difficult and axial contraction of the cladding is significant. The amount of axial contraction of the tube increases as the circumferential strain increases. Axial constraint of the cladding by an internal mandrel or pellet stack alters the stress-biaxiality condition and, as a consequence, decreases the circumferential strain.

3. Temperature nonuniformity in the ballooning region of a Zircaloy tube significantly reduces the circumferential strain at failure at temperatures in the α-phase region. Heating rate and the pellet-cladding diametral-gap distance were the most important factors that determine the extent of temperature nonuniformity in the cladding. The circumferential strain decreases as the

heating rate (and, consequently, the temperature nonuniformity) increases. Nonuniform temperatures along the circumference of the tube also cause asymmetric axial contraction and tube bending before rupture. The extent of bending increases during rupture, due to the jet-blast effect at high internal pressures.

4. For cladding tubes that rupture in the α- or predominantly α-phase region, i.e., for initial internal pressures $\gtrsim 5$ MPa, good correlation was obtained between the maximum circumferential strain and a radial-strain-localization parameter. Because of a relatively simple relationship between the temperature nonuniformity and the radial-strain-localization parameter, the maximum circumferential strain could be correlated with the degree of temperature nonuniformity at maximum rupture temperatures near 800°C.

5. Since several interdependent factors influence the maximum circumferential strain at rupture temperatures near 800°C, comparisons between the ballooning strain obtained in this investigation with similar data from multirod and in-reactor tests should be based upon the heating rate, maximum burst temperature, and magnitude of the circumferential temperature variations in the cladding. The maximum circumferential strain at failure can be reasonably estimated from the present results if the magnitude of the temperature variations in the cladding can be calculated from fuel-element modeling codes for various hypothetical LOCA transients.

APPENDIX A

Summary of Burst-test Data

This appendix presents information on the initial pressure, heating rate, maximum pressure, burst pressure, burst temperature, and circumferential and axial strains at failure. Tables A.1 and A.2 contain results obtained on unconstrained Zircaloy-4 cladding in vacuum at heating rates of ~115 and 5°C/s, respectively. Tables A.3-A.7 list burst-test results for mandrel-constrained cladding in vacuum. In addition to the heating rate, the axial-gap distance (Table A.4) and the specimen length (Table A.7) were varied.

TABLE A.1. Burst-test Results for Unconstrained Zircaloy-4 Cladding[a] at a Heating Rate of ~115°C/s in Vacuum

Test Number	Initial Pressure, MPa	Heating Rate,[b] °C/s	Maximum Pressure, MPa	Burst Pressure, MPa	Burst Temperature, °C	Maximum Circumferential Strain	Axial Strain at Rupture[c]
AS-2	0.83	100	1.0[illegible]	0.85	1122	1.04	-
AS-48	5.51	115	7.04	5.79	870	0.52	-0.052
AS-49	6.13	117	7.86	6.62	8[illegible]0	0.60	-0.085
AS-50	6.89	109	8.72	7.[illegible]7	8[illegible]5	0.70	-0.116
AS-51	6.54	115	8.34	6.76	865	0.82	-0.131
AS-52	6.89	115	8.82	7.72	846	0.73	-0.085
AS-53	9.64	120	12.5	11.4	800	1.21	-0.191
AS-54	8.27	130	10.5	9.31	826	1.24	-0.176
AS-55	13.8	111	17.6	15.2	753	0.36	-0.065
AS-56	11.7	120	15.2	13.1	782	0.52	-0.098
AS-57	1.38	100	1.79	1.38	1005	1.27	-0.041
AS-58	0.69	126	0.92	0.69	1241	1.26	-0.033
AS-59	1.03	120	1.34	0.87	1051	1.39	-0.020
AS-60	0.86	120	0.94	0.75	1060	1.52	-0.026
AS-61	0.96	117	1.34	0.92	1035	1.43	-0.033
AS-62	3.44	129	4.48	3.65	937	0.68	-0.032
AS-63	1.03	128	1.35	0.99	1096	1.29	-0.026
AS-65	4.20	120	5.41	4.83	900	0.38	-0.031
AS-67	8.27	115	10.3	7.93	806	0.89	-0.132
AS-99	0.69	143	0.84	0.69	1255	1.14	-
AS-100	0.79	109	0.93	0.83	1189	1.20	-
AS-101	0.74	123	0.92	0.79	118[illegible]	1.18	-
AS-102	0.71	119	0.88	0.74	1180	1.07	-
AS-103	0.89	124	1.10	0.98	1090	1.45	-
AS-104	0.83	140	1.02	0.85	1108	1.16	-
AS-105	0.83	117	1.01	0.85	1172	1.09	-
AS-106	0.83	115	1.03	0.86	1163	0.95	-
AS-107	0.69	113	0.86	0.85	120[illegible]	1.12	-
AS-108	0.62	120	0.77	0.61	12[illegible]0	1.45	-
AS-109	0.52	115	0.65	0.57	12[illegible]9	1.01	-
AS-148	11.4	117	14.0	13.8	790	0.66	-
AS-190	10.3	120	13.2	11.5	794	1.04	-
AS-191	7.58	108	9.24	7.79	832	1.08	-

[a]Specimen length was 153 mm.

[b]Average heating rate for the temperature range 300-810°C.

[c]Axial strain is based on a 75-mm-long uniform temperature zone.

TABLE A.2. Burst-test Results for Unconstrained Zircaloy-4 Cladding[a] at a Heating Rate of ~5°C/s in Vacuum

Test Number	Initial Pressure, MPa	Heating[b] Rate, °C/s	Maximum Pressure, MPa	Burst Pressure, MPa	Burst Temper-ature, °C	Maximum Circum-ferential Strain	Axial Strain at Rupture[c]
AS-24	1.38	4.5	1.53	1.43	869	0.57	-
AS-137	4.82	5.8	5.87	4.96	793	1.24	-0.126
AS-139	6.20	5.1	7.58	6.62	780	1.24	-0.138
AS-140	5.51	5.0	6.79	5.86	802	1.35	-0.143
AS-141	4.82	4.8	5.94	5.24	806	1.48	-0.136
AS-142	4.13	5.0	5.10	4.55	825	1.28	-0.088
AS-143	3.44	5.4	1.52	1.10	865	1.01	-0.063
AS-145	8.27	5.2	10.0	8.69	745	1.16	-0.106
AS-146	10.3	5.9	12.5	11.0	704	1.08	-0.109
AS-147	12.5	4.9	15.2	14.1	660	0.97	-0.094
AS-149	11.7	3.5	14.4	13.4	680	0.90	-0.081
AS-182	2.75	8.0	3.45	3.38	886	0.29	-0.072
AS-183	2.07	5.0	2.59	2.41	934	0.88	-
AS-184	1.38	7.4	1.76	1.69	942	0.80	-
AS-185	1.72	5.2	2.20	2.14	922	0.54	-
AS-186	1.03	4.1	1.32	1.28	957	0.69	-
AS-187	0.69	5.5	0.90	0.83	1012	1.51	-
AS-188	0.34	5.1	0.45	0.41	1085	1.20	-
AS-189	8.96	5.4	9.86	7.74	717	1.13	-0.088

[a]Specimen length was 153 mm.

[b]Average heating rate for the temperature range 300-810°C.

[c]Axial strain is based on a 75-mm-long uniform temperature zone.

TABLE A.3. Burst-test Results for Mandrel-constrained[a] Zircaloy-4 Cladding[b] in Vacuum at a Heating Rate of ~115°C/s

Test Number	Initial Pressure, MPa	Heating Rate,[c] °C/s	Maximum Pressure, MPa	Burst Pressure, MPa	Burst Temperature, °C	Maximum Circumferential Strain
AS-1	3.93	114	4.08	3.89	909	0.30
AS-3	2.06	115	2.10	1.99	992	0.84
AS-4	2.75	115	2.84	2.68	979	0.51
AS-5	1.38	110	1.42	1.34	1075	1.02
AS-6	4.27	143	-	-	912	0.38
AS-7	1.72	134	1.77	1.61	1005	0.82
AS-8	1.51	110	1.59	1.41	1013	0.79
AS-9	1.38	120	1.45	1.28	1056	1.24
AS-10	2.82	120	4.40	4.21	876	0.34
AS-11	4.82	119	-	-	901	0.34
AS-12	5.61	115	-	-	865	0.69
AS-13	6.20	114	-	-	876	0.62
AS-14	5.85	115	-	-	877	0.53
AS-15	4.82	120	-	-	891	0.41
AS-16	5.37	118	-	-	879	0.43
AS-17	5.56	108	-	-	899	0.54
AS-18	4.20	99	-	-	908	0.46
AS-19	6.54	132	-	-	871	0.56
AS-20	7.30	120	-	-	835	0.35
AS-21	7.29	114	-	-	827	0.27
AS-22	8.27	115	-	-	815	0.25
AS-23	7.65	121	-	-	856	0.43
AS-64	1.72	115	1.83	1.76	968	0.37
AS-66	5.51	118	5.95	5.72	880	0.24
AS-90	1.03	100	1.08	0.98	1105	0.71
AS-91	0.69	90	0.72	0.61	1190	1.40
AS-92	0.86	120	0.90	0.83	1147	0.59
AS-93	1.03	111	1.08	0.99	1111	0.67
AS-94	0.69	125	0.72	0.68	1140	0.55
AS-95	0.52	100	0.54	0.50	1161	1.08
AS-96	0.34	115	0.37	0.34	1172	0.95
AS-97	3.04	110	-	-	949	0.32
AS-98	0.34	119	0.36	0.34	1260	0.74
AS-113	8.39	105	10.9	8.96	770	0.46
AS-114	8.39	115	10.9	9.79	845	0.48
AS-115	7.51	115	8.65	8.00	830	0.28
AS-116	7.51	118	8.69	7.72	821	0.37
AS-117	7.51	95	8.72	7.86	858	0.41
AS-127	6.89	117	7.24	6.89	892	0.27
AS-128	7.51	120	8.62	7.86	840	0.57
AS-129	7.18	112	7.91	7.24	849	0.55
AS-150	8.39	115	12.9	12.0	795	0.58
AS-151	10.2	95	16.0	14.3	745	0.37
AS-152	9.69	102	14.5	13.0	751	0.35
AS-153	7.81	96	9.38	8.55	857	0.58
AS-154	8.11	100	10.9	10.0	791	0.55
AS-155	8.11	108	10.1	9.38	758	0.42
AS-156	9.19	108	10.2	9.31	775	0.42
AS-157	7.81	112	9.38	8.62	845	0.46
AS-158	7.81	100	9.44	8.76	727	0.37
AS-159	7.51	107	8.56	7.93	828	0.34
AS-160	7.34	115	8.22	7.65	890	0.41
AS-192	7.81	116	-	-	803	0.29
AS-193	7.51	109	-	-	822	0.31
AS-194	7.96	119	-	-	801	0.66

[a] Axial gap between the alumina mandrel and end plug was 2.5 mm; radial gap between the axisymmetric mandrel and the Zircaloy tube was 1.3 mm.

[b] Specimen length was 153 mm.

[c] Average heating rate for the temperature range 300-810°C.

TABLE A.4. Burst-test Results for Mandrel-constrained[a] Zircaloy-4 Cladding[b]--Axial gap of 5.9 mm--in Vacuum at a Heating Rate of ~115°C/s

Test Number	Initial Pressure, MPa	Heating[c] Rate, °C/s	Maximum Pressure, MPa	Burst Pressure, MPa	Burst Temperature, °C	Maximum Circumferential Strain
AS-118	7.51	121	8.73	8.07	873	0.49
AS-119	7.81	140	9.55	8.75	826	0.76
AS-120	7.81	115	9.44	8.55	820	0.48
AS-121	7.51	120	8.71	7.72	873	0.70
AS-122	7.84	117	9.51	8.27	856	0.68
AS-123	7.84	115	9.55	8.41	845	0.75
AS-124	8.11	115	10.1	8.89	845	0.94
AS-125	7.81	115	9.44	8.41	860	0.79
AS-126	7.81	115	9.44	8.13	820	0.68
AS-170	9.19	115	12.7	12.4	794	0.28
AS-171	8.93	119	12.1	11.8	808	0.36
AS-172	8.53	121	11.3	9.86	852	0.92
AS-173	8.66	87	11.5	10.5	798	0.41
AS-174	8.39	112	10.9	9.51	814	0.73
AS-175	8.11	107	10.1	8.82	805	0.54
AS-176	9.19	132	13.0	11.2	805	0.59
AS-177	9.45	107	13.7	12.0	774	0.62
AS-178	9.45	90	13.7	11.7	795	0.61
AS-179	9.45	124	13.8	12.2	788	0.50
AS-180	9.47	121	13.8	11.7	813	0.67
AS-181	9.45	130	13.8	12.1	807	0.65

[a]Radial gap between the axisymmetric alumina mandrel and the Zircaloy tube was 1.3 mm.

[b]Specimen length was 153 mm.

[c]Average heating rate for the temperature range 300-810°C.

TABLE A.5. Burst-test Results for Mandrel-constrained[a] Zircaloy-4 Cladding[b] in Vacuum at a Heating Rate of ~55°C/s

Test Number	Initial Pressure, MPa	Heating[c] Rate, °C/s	Maximum Pressure, MPa	Burst Pressure, MPa	Burst Temperature, °C	Maximum Circumferential Strain
AS-68	7.51	30	8.74	7.51	789	0.67
AS-69	7.51	40	8.72	8.13	767	0.61
AS-70	7.51	70	8.82	8.41	797	0.67
AS-71	6.89	55	7.24	6.67	843	0.66
AS-72	7.18	66	8.01	7.17	830	0.62
AS-73	9.69	50	14.5	13.2	760	0.49
AS-74	7,18	36	8.00	6.89	838	0.70
AS-75	7.51	35	8.62	8.07	780	0.60
AS-76	7.02	34	7.96	7.17	820	0.80
AS-77	8.39	53	10.5	10.2	777	0.46
AS-78	9.69	39	14.8	13.9	717	0.40
AS-79	8.11	58	10.0	9.03	806	0.74
AS-80	8.66	56	11.6	11.0	760	0.43
AS-81	5.73	70	5.01	4.96	915	0.21
AS-82	6.31	55	6.20	5.79	880	0.27
AS-83	1.38	75	1.71	1.31	990	0.47
AS-84	0.69	76	0.69	0.48	1222	0.74
AS-85	1.03	60	1.08	1.02	1080	0.74
AS-86	1.03	57	1.08	1.02	1105	0.57
AS-195	6.89	55	7.20	6.76	821	0.77
AS-196	6.89	56	7.25	6.84	789	0.97
AS-197	9.19	51	13.2	13.20	762	0.51

[a]Axial gap between the end plug and alumina mandrel was 2.5 mm; radial gap between the axisymmetric mandrel and the Zircaloy tube was 1.3 mm.

[b]Specimen length was 153 mm.

[c]Average heating rate for the temperature range 300-810°C.

TABLE A.6. Burst-test Results for Mandrel-constrained[a] Zircaloy-4 Cladding[b] in Vacuum at a Heating Rate of ~5°C/s

Test Number	Initial Pressure, MPa	Heating Rate,[c] °C/s	Maximum Pressure, MPa	Burst Pressure, MPa	Burst Temperature, °C	Maximum Circumferential Strain
AS-25	1.38	2.5	1.66	1.61	892	0.39
AS-26	1.07	3.0	1.12	1.03	990	0.82
AS-27	0.69	5.6	0.79	0.72	1010	0.68
AS-28	0.35	3.5	0.39	0.30	1220	1.14
AS-29	0.55	8.0	0.63	0.56	1012	0.94
AS-30	0.45	5.5	0.51	0.44	1063	1.16
AS-31	0.35	6.0	0.39	0.34	1164	1.01
AS-32	0.48	6.1	0.54	0.49	1020	0.93
AS-33	1.03	5.5	1.10	1.03	955	0.41
AS-34	0.47	5.5	0.51	0.47	1072	1.07
AS-35	0.47	5.4	0.53	0.48	1080	0.90
AS-36	0.52	7.0	0.61	0.56	1037	1.11
AS-37	1.72	6.1	1.89	1.86	857	0.25
AS-38	2.05	5.2	2.28	2.23	870	0.34
AS-39	3.58	4.0	3.81	3.70	857	0.37
AS-40	5.55	5.1	5.96	5.31	816	1.01
AS-41	4.83	4.5	5.27	4.96	843	0.49
AS-42	6.21	6.7	6.69	6.10	840	0.75
AS-43	7.51	5.2	8.86	8.24	765	0.95
AS-44	6.89	5.5	8.03	6.96	800	1.03
AS-45	8.39	6.5	11.0	9.93	741	0.78
AS-46	8.69	6.1	14.8	13.5	729	0.83
AS-47	1.38	4.5	1.52	1.50	890	0.26
AS-87	1.03	5.6	1.02	1.01	970	0.48
AS-88	1.03	5.5	1.09	1.08	968	0.39
AS-89	0.35	5.6	0.39	0.34	1139	1.01
AS-110	0.41	5.4	0.46	0.37	1180	1.21
AS-111	0.38	5.3	0.43	0.37	1170	1.12
AS-112	7.51	4.8	8.86	8.07	760	0.84
AS-161	0.69	5.0	0.75	0.68	1010	0.98
AS-162	0.70	5.0	0.76	0.69	1021	0.92
AS-163	0.65	5.0	0.70	0.68	1033	0.76
AS-164	0.71	5.0	0.79	0.76	1020	0.84
AS-165	0.41	7.0	0.43	0.43	1081	0.98
AS-166	0.35	5.0	0.40	0.36	1174	1.14
AS-167	0.35	5.0	0.38	0.34	1160	0.96
AS-168	0.36	5.0	0.40	0.34	1220	1.04
AS-169	0.36	5.0	0.34	0.29	1170	1.28

[a] Axial gap between the end plug and alumina mandrel was 2.5 mm; radial gap between the axisymmetric mandrel and Zircaloy tube was 1.3 mm.

[b] Specimen length was 153 mm.

[c] Average heating rate for the temperature range 300-810°C.

TABLE A.7. Burst-test Results for 300-mm-long Mandrel-constrained[a] Zircaloy-4 Cladding in Vacuum at a Heating Rate of ~115°C/s

Test Number	Initial Pressure, MPa	Heating Rate,[b] °C/s	Maximum Pressure, MPa	Burst Pressure, MPa	Burst Temperature, °C	Maximum Circumferential Strain
AL-1	9.64	129	10.5	8.62	804	0.53
AL-2	11.0	118	12.0	10.2	864	0.68
AL-3	8.27	116	9.03	7.58	848	0.60
AL-4	7.58	114	8.27	6.62	883	0.44
AL-5	8.96	113	9.82	7.86	846	0.64

[a] Axial gap between the alumina mandrel and end plug was 2.5 mm; radial gap between the axisymmetric alumina mandrel and Zircaloy tube was 1.3 mm.

[b] Average heating rate for the temperature range 300-810°C.

Burst-test results for unconstrained Zircaloy-4 cladding in steam are reported in Tables A.8 and A.9 for heating rates of ~115 and 5°C/s, respectively. Tables A.10-A.12 contain results for mandrel-constrained cladding in steam at heating rates of ~115, 55, and 5°C/s, respectively. Similar results obtained with 300-mm-long tubes are given in Table A.13.

TABLE A.8. Burst-test Results for Unconstrained Zircaloy-4 Cladding[a] at a Heating Rate of ~115°C/s in Steam

Test Number	Initial Pressure, MPa	Heating Rate,[b] °C/s	Maximum Pressure, MPa	Burst Pressure, MPa	Burst Temperature, °C	Maximum Circumferential Strain
IS-3	6.89	121	7.23	6.67	896	0.40
IS-68	10.3	111	-	10.3	809	0.89
IS-73	11.7	107	14.1	11.3	800	0.96
IS-74	13.8	116	16.9	14.1	778	0.70
IS-75	13.8	129	17.0	14.5	790	0.88
IS-76	13.8	223	-	15.4	797	0.52
IS-77	13.8	124	16.6	13.6	789	0.73
IS-87	1.38	119	1.69	1.38	1020	0.97
IS-88	1.38	115	1.72	1.45	1051	0.81
IS-89	1.38	116	1.72	1.38	1059	0.94
IS-90	1.76	101	2.20	2.00	1010	0.54
IS-91	2.12	124	2.63	2.41	972	0.57
IS-92	2.71	115	3.34	3.10	957	0.43
IS-93	3.45	104	4.31	3.79	943	0.48
IS-94	4.86	114	5.99	5.44	920	0.47
IS-95	4.82	121	6.06	5.48	901	0.49
IS-96	6.20	118	7.72	6.55	878	0.48
IS-97	10.33	108	13.0	10.6	828	0.75
IS-98	10.33	98	12.9	11.4	801	0.82
IS-99	1.03	122	1.31	0.83	1087	0.93
IS-100	0.69	120	0.90	0.76	1155	0.87
IS-101	0.69	121	0.86	0.76	-	0.59
IS-102	0.69	115	0.74	0.74	-	-
IS-103	0.83	117	1.03	0.89	1330	0.79
IS-104	0.93	108	1.19	1.02	1235	1.06
IS-105	0.93	109	1.17	1.00	1272	0.86
IS-106	0.97	110	1.29	1.07	1227	1.14
IS-107	1.00	119	1.28	1.10	1206	0.98
IS-108	1.03	105	1.30	1.03	1189	0.95
IS-109	1.17	107	1.45	1.14	1193	0.92
IS-110	1.28	115	1.59	1.24	1096	1.08
IS-111	1.23	121	1.52	1.27	1105	0.94
IS-112	1.27	104	1.32	1.27	1205	1.08
IS-113	1.25	103	1.58	1.03	1070	1.12
IS-114	1.14	118	1.41	1.10	1164	0.95
IS-115	1.14	119	1.41	1.10	1143	0.87
IS-116	8.99	116	11.1	8.82	845	0.87
IS-117	9.34	118	11.4	8.96	830	1.24

[a]Specimen length was 153 mm.

[b]Average heating rate for the temperature range 300-810°C.

TABLE A.9. Burst-test Results for Unconstrained Zircaloy-4 Cladding at a Heating Rate of ~5°C/s in Steam

Test Number	Initial Pressure, MPa	Heating Rate,[a] °C/s	Maximum Pressure, MPa	Burst Pressure, MPa	Burst Temperature, °C	Maximum Circumferential Strain	Axial Strain at Rupture[b]
IS-69	7.57	5.0	9.16	7.92	715	1.08	-
IS-70	6.89	5.0	8.34	6.89	730	1.39	-
IS-71	6.20	5.2	7.58	6.27	745	1.36	-
IS-72	5.51	5.8	6.75	5.51	766	1.34	-
IS-118	2.79	6.3	2.86	2.76	916	0.40	-
IS-119	2.75	7.5	3.34	3.24	922	0.41	-
IS-120	2.06	4.2	2.54	2.41	905	0.39	-
IS-121	1.74	5.1	2.14	2.05	925	0.59	-
IS-122	0.96	9.0	1.30	1.05	995	0.32	-
IS-123	1.03	6.3	1.31	1.17	970	0.77	-
IS-124	1.03	4.5	1.30	1.17	978	0.72	-
IL-5[c]	4.82	6.5	5.99	4.86	829	1.14	-
IL-8[c]	3.10	4.7	3.43	3.07	900	0.39	-
IL-12[c]	1.03	4.9	1.14	0.98	980	0.70	-
IAS-130	10.3	7.9	12.5	11.6	689	1.23	-0.123
IAS-131	6.89	4.7	7.79	6.06	759	1.54	-0.185
IAS-132	5.51	4.0	6.76	5.31	781	1.50	-0.158
IAS-133	4.13	5.2	5.17	4.69	883	0.58	-0.080
IAS-134	12.4	5.0	13.0	12.5	660	0.88	-0.101
IAS-135	8.27	5.0	10.2	8.68	724	1.22	-0.136
IAS-136	4.82	8.2	5.96	5.37	875	0.61	-0.083
IAS-138	6.89	5.3	8.34	7.30	749	1.28	-0.155
IAS-144	10.2	5.3	12.5	10.9	708	1.14	-0.126

[a]Average heating rate for the temperature range 300-810°C.

[b]Axial strain is based on a 75-mm-long uniform zone.

[c]Specimen length was 300 mm; other tubes were 153 mm long.

TABLE A.10. Burst-test Results for Mandrel-constrained[a] Zircaloy-4 Cladding[b] in Steam at a Heating Rate of ~115°C/s

Test Number	Initial Pressure, MPa	Heating Rate,[c] °C/s	Maximum Pressure, MPa	Burst Pressure, MPa	Burst Temperature, °C	Maximum Circumferential Strain
IS-1	7.58	120	7.89	7.30	870	0.36
IS-2	0.69	111	0.73	0.70	1265	0.43
IS-4	8.27	115	8.58	7.51	867	0.45
IS-5	6.89	110	7.25	6.61	882	0.28
IS-6	9.65	100	10.0	9.23	802	0.45
IS-7	5.51	108	5.75	5.58	910	0.22
IS-8	4.13	115	4.31	4.18	940	0.22
IS-9	2.75	100	2.89	2.83	920	0.18
IS-10	11.7	103	12.2	11.3	777	0.40
IS-11	13.8	101	14.4	13.1	780	0.58
IS-12	11.7	126	12.1	10.7	821	0.63
IS-13	1.38	104	1.44	1.39	1025	0.34
IS-14	0.69	110	0.77	0.67	1231	0.61
IS-15	0.69	130	0.72	0.70	1281	0.32
IS-16	1.03	105	1.09	0.99	1180	0.52
IS-17	1.21	85	1.27	1.21	1097	0.37
IS-18	1.38	118	1.45	1.24	1113	0.37
IS-19	2.06	100	2.48	2.07	968	0.35
IS-20	1.55	114	1.62	1.52	1000	0.39
IS-21	1.38	117	1.39	1.32	1048	0.55
IS-22	1.38	85	1.43	1.36	1024	0.40
IS-66	10.3	115	10.8	9.36	820	0.67
IS-67	9.65	117	10.1	8.61	834	0.69

[a]Axial gap between the alumina mandrel and end plug was 2.5 mm; radial gap between the axisymmetric mandrel and Zircaloy tube was 1.3 mm.

[b]Specimen length was 153 mm.

[c]Average heating rate for the temperature range 300-810°C.

TABLE A.11. Burst-test Results for Mandrel-constrained[a] Zircaloy-4 Cladding[b] in Steam at a Heating Rate of ~55°C/s

Test Number	Initial Pressure, MPa	Heating Rate[c], °C/s	Maximum Pressure, MPa	Burst Pressure, MPa	Burst Temperature, °C	Maximum Circumferential Strain
IS-23	1.03	50	1.08	1.03	1071	0.44
IS-24	0.69	52	0.72	0.70	1097	0.35
IS-25	0.41	50	0.46	-	-	-
IS-26	1.38	54	1.43	1.39	1022	0.36
IS-27	1.72	56	1.78	1.67	1003	0.34
IS-28	2.06	55	2.13	2.10	843	0.21
IS-29	2.75	55	2.88	2.83	924	0.22
IS-30	1.55	55	1.63	1.55	1004	0.37
IS-31	4.13	51	4.34	4.28	902	0.16
IS-32	5.51	60	5.79	5.58	866	0.28
IS-33	6.89	49	7.20	6.68	856	0.44
IS-34	8.27	54	8.61	8.10	843	0.52
IS-35	10.3	31	10.7	9.65	782	0.77
IS-36	12.3	51	12.8	12.0	707	0.48
IS-37	13.8	30	14.3	12.7	732	0.64
IS-38	0.85	55	0.90	0.87	1218	0.31
IS-39	0.69	55	0.74	0.72	1122	0.20
IS-40	0.68	58	0.72	-	1230	0.32
IS-41	0.69	42	0.68	0.67	1265	0.26
IS-42	0.69	45	0.72	0.70	1264	0.23
IS-43	0.68	50	0.73	0.71	1247	0.32
IS-44	11.6	49	12.1	10.8	751	0.49
IS-45	0.56	54	0.74	0.74	1272	0.13
IS-78	11.7	57	12.2	10.8	773	0.57
IS-79	11.0	55	11.4	10.0	806	0.72
IS-80	12.4	62	12.5	11.6	778	0.52
IS-81	11.9	61	12.3	11.6	715	0.48
IS-82	12.4	48	12.8	11.4	719	0.62
IS-83	12.5	45	12.9	11.4	780	0.65
IS-84	10.5	52	10.7	9.92	777	0.57
IS-85	10.3	50	10.7	9.65	829	0.59
IS-86	14.5	51	15.0	14.1	710	0.37

[a]Axial gap between the alumina mandrel and end plug was 2.5 mm; radial gap between the axisymmetric mandrel and Zircaloy tube was 1.3 mm.

[b]Specimen length was 153 mm.

[c]Average heating rate for the temperature range 300-810°C.

TABLE A.12. Burst-test Results for Mandrel-constrained[a] Zircaloy-4 Cladding[b] at a Heating Rate of ~5°C/s in Steam

Test Number	Initial Pressure, MPa	Heating Rate,[c] °C/s	Maximum Pressure, MPa	Burst Pressure, MPa	Burst Temperature, °C	Maximum Circumferential Strain
IS-46	10.3	6.0	10.9	9.09	732	1.00
IS-47	11.0	5.0	11.6	10.3	675	0.91
IS-48	8.27	6.8	8.73	7.58	780	1.19
IS-49	8.27	3.2	8.68	7.44	748	1.16
IS-50	6.89	5.1	7.27	6.20	795	0.96
IS-51	6.89	5.1	8.68	7.65	775	1.13
IS-52	5.48	5.3	5.86	4.75	777	1.21
IS-53	4.13	5.3	4.46	4.27	841	0.35
IS-54	4.82	4.9	5.13	4.79	838	0.64
IS-55	4.48	5.5	4.77	4.49	849	0.50
IS-56	13.8	5.8	14.5	13.0	676	0.81
IS-57	3.45	7.6	3.76	3.64	854	0.50
IS-58	2.06	6.8	2.20	2.14	895	0.32
IS-59	1.38	5.4	1.50	1.46	942	0.31
IS-60	0.69	4.2	0.78	0.77	1030	0.14
IS-61	1.03	6.5	1.11	1.05	976	0.29
IS-62	0.68	7.4	0.76	0.75	1105	0.11
IS-63	12.4	6.1	13.5	12.3	677	0.71
IS-64	9.54	5.2	10.2	9.23	701	0.75
IS-65	10.3	5.9	11.1	10.2	700	0.72

[a]Axial gap between the alumina mandrel and end plug was 2.5 mm; radial gap between the axisymmetric mandrel and Zircaloy tube was 1.3 mm.

[b]Specimen length was 153 mm.

[c]Average heating rate for the temperature range 300-810°C.

TABLE A.13. Burst-test Results for 300-mm-long Mandrel-constrained[a] Zircaloy-4 Cladding in Steam at Heating Rates of ~5, 45, and 115°C/s

Test Number	Initial Pressure, MPa	Heating Rate,[b] °C/s	Maximum Pressure, MPa	Burst Pressure, MPa	Burst Temperature, °C	Maximum Circumferential Strain
IL-1	10.3	114	11.2	8.96	824	0.76
IL-2	8.96	118	9.72	7.86	820	0.73
IL-3	7.58	108	8.27	7.30	844	0.51
IL-4	8.27	121	8.91	6.89	814	0.55
IL-6	13.1	45	14.4	12.0	740	0.58
IL-7	10.3	42	11.2	10.1	755	0.75
IL-9	6.89	46	7.50	6.34	826	0.82
IL-10	8.27	43	9.06	7.03	817	0.89
IL-11	9.65	45	10.6	8.61	821	0.71
IL-13	8.27	45	9.04	7.92	771	0.92
IL-5	4.82	6.5	5.99	4.86	829	1.14
IL-14	10.3	7.4	1.19	1.14	693	0.84
IL-15	7.58	5.4	7.86	6.89	774	1.04
IL-16	12.4	11	12.8	11.3	691	0.69
IL-17	12.4	7.4	12.8	11.4	687	0.84
IL-18	8.27	7.1	8.48	7.30	772	0.94

[a]Axial gap between the alumina mandrel and end plug was 2.5 mm; radial gap between the axisymmetric mandrel and Zircaloy tube was 1.3 mm.
[b]Average heating rate for the temperature range 300-810°C.

Table A.14 contains the results for preoxidized mandrel-constrained tubes in a vacuum environment at a heating rate of ~115°C/s.

Isothermal stress-rupture data for Zircaloy-4 cladding in vacuum and steam environments are listed in Tables A.15 and A.16, respectively.

The burst-test results on pellet-constrained cladding with a 0.07-mm diametral-gap size are given in Tables A.17-A.19 for heating rates of ~115, 45, and 5-22°C/s, respectively, in steam. Similar results obtained with pellet-cladding diametral-gap distances of 0.5 and 0.2 mm are listed in Tables A.20 and A.21, respectively.

TABLE A.14. Burst-test Results for Preoxidized[a] Mandrel-constrained[b] Zircaloy-4 Cladding[c] in Vacuum at a Heating Rate of ~115°C/s

Test Number	Initial Pressure, MPa	Heating[d] Rate, °C/s	Maximum Pressure, MPa	Burst Pressure, MPa	Burst Temperature, °C	Maximum Circumferential Strain
CP-1	3.93	100	-	-	903	0.55
CP-2	10.4	118	10.8	9.78	798	0.43
CP-3	13.8	121	14.5	12.8	775	0.44
CP-4	8.27	108	8.34	8.06	787	0.48
CP-5	9.95	107	10.4	9.37	823	0.68
CP-6	10.7	115	11.2	10.1	826	0.67
CP-7	12.1	114	-	-	-	0.73
CP-8	12.8	113	13.4	12.1	789	0.54
CP-9	10.5	118	11.1	9.65	838	0.50
CP-10	11.0	110	11.7	10.3	780	0.57
CP-11	11.0	107	11.5	10.3	816	0.72
CP-12	12.4	116	12.9	11.4	804	0.71

[a] Specimens were preoxidized on the outer surface during heating from 25 to 800°C in steam at ~115°C/s under zero differential pressure.

[b] Axial gap between the alumina mandrel and end plug was 2.5 mm; radial gap between the axisymmetric mandrel and Zircaloy tube was 1.3 mm.

[c] Specimen length was 153 mm.

[d] Average heating rate for the temperature range 300-810°C during the burst tests in vacuum.

TABLE A.15. Isothermal Stress-rupture Data for Zircaloy-4 Cladding[a] in Vacuum

Test Number	Temperature, °C	Initial Pressure, MPa	Maximum Pressure, MPa	Burst Pressure, MPa	Time-to-Rupture, s	Maximum Circumferential Strain
SR-2[b]	750	4.13	4.07	3.72	231	1.75
SR-5[b]	750	5.17	5.14	4.95	96.5	1.79
SR-7	823	4.92	4.72	4.71	7.6	0.26
SR-9[b]	1122	2.21	1.59	1.43	0.3	1.07
SR-10[b]	1030	2.75	2.10	1.93	0.1	0.92
SR-11	831	4.82	4.82	4.82	0.6	0.23
SR-12	835	4.65	4.65	4.64	2.5	0.28
SR-13	825	4.69	4.69	4.68	2.8	0.23
SR-14	830	4.41	4.41	4.41	3.2	0.21
SR-15	827	4.17	4.17	4.16	4.6	0.24
SR-16[b]	866	3.96	3.96	3.94	0.3	0.44
SR-17	760	6.20	6.20	6.20	0.2	0.40
SR-18	714	6.89	6.89	6.89	0.4	0.29
SR-19	838	4.82	4.82	4.82	0.3	0.34
SCP-1[b,c]	750	4.13	4.17	3.72	380	2.01
SCP-2[b,c]	750	5.17	5.18	4.84	223	2.00

[a]Specimen length was 153 mm.

[b]Zircaloy tube was empty; other tubes contained an axisymmetric alumina mandrel with axial and radial gap distances of 2.5 and 1.3 mm, respectively.

[c]Specimen was preoxidized on the outer surface during heating from 25 to 800°C in steam at ∿115°C/s under zero differential pressure.

TABLE A.16. Isothermal Stress-rupture Data for Zircaloy-4 Cladding[a] in Steam

Test Number	Temperature, °C	Initial Pressure, MPa	Maximum Pressure, MPa	Burst Pressure, MPa	Time-to Rupture, s	Maximum Circumferential Strain
SS-1[b]	750	4.13	4.17	3.89	257	1.38
SS-3	808	5.10	5.13	5.07	10.1	0.55
SS-5	816	4.82	-	-	8.1	0.69
SS-7	800	4.82	4.82	4.77	8.8	0.52
SS-10	828	4.61	4.62	4.55	9.2	0.55
SS-11	1154	1.65	1.67	1.67	0.2	0.11

[a]Specimen length was 153 mm.

[b]Zircaloy tube was empty; other tubes contained an axisymmetric alumina mandrel with axial and radial gap distances of 2.5 and 1.3 mm, respectively.

TABLE A.17. Burst-test Results for Pellet-constrained[a] Zircaloy-4 Cladding[b] in Steam at a Heating Rate of ~115°C/s

Test Number	Initial Pressure, MPa	Heating Rate,[c] °C/s	Maximum Pressure, MPa	Burst Pressure, MPa	Burst[d] Temperature, °C	Maximum Circumferential Strain
IPL-16	6.89	100	7.04	6.75	800-751	0.16
IPL-17	7.58	94	7.77	7.37	747-642	0.19
IPL-18	10.3	100	10.5	9.51	838-765	0.27
IPL-19	13.8	115	14.1	12.7	780-736	0.31
IPL-20	11.7	118	11.9	11.2	737-699	0.25
IPL-21	8.96	106	9.20	8.41	779-702	0.21
IPL-23	4.82	113	4.93	4.79	903-831	0.13
IPL-24	5.51	121	5.64	5.44	870-811	0.11
IPL-25	3.45	120	3.55	3.52	950-838	0.16
IPL-26	9.65	119	9.87	9.23	804-653	0.30
IPL-28	9.44	145	9.84	8.89	820-752	0.23
IPL-43	2.75	115	2.82	2.79	920-816	0.17
IPL-44	2.06	120	2.14	2.10	921-766	0.24
IPL-45	1.38	118	1.41	1.34	979-782	0.32
IPL-46	0.69	110	0.69	0.88	1138-1070	0.22
IPL-47	1.03	104	1.08	1.03	1091-944	0.34
IPL-48	2.41	115	2.45	2.38	907-806	0.19
IPL-49	0.83	100	0.86	0.79	1175-1052	0.38

[a] Zircaloy tubes were constrained with a column of 10-mm-long alumina pellets. The axial and diametral gap distances were 2.5 and 0.07 mm, respectively.

[b] Specimen length was 300 mm.

[c] Average heating rate for the temperature range 300-810°C.

[d] Maximum temperature variation at rupture recorded from 4 or 5 thermocouples attached to the tube. The burst temperature corresponds to the maximum temperature in each test.

TABLE A.18. Burst-test Results for Pellet-constrained[a] Zircaloy-4 Cladding[b] in Steam at a Heating Rate of ~45°C/s

Test Number	Initial Pressure, MPa	Heating Rate,[c] °C/s	Maximum Pressure, MPa	Burst Pressure, MPa	Burst Temperature,[d] °C	Maximum Circumferential Strain
IPL-15	8.27	36	8.48	7.92	789-745	0.22
IPL-29	13.1	40	13.4	12.8	745-651	0.30
IPL-30	11.7	60	11.9	10.7	810-696	0.31
IPL-31	10.3	43	10.6	9.85	759-629	0.29
IPL-32	8.96	60	9.20	8.75	871-732	0.21
IPL-33	7.58	54	7.72	7.30	846-725	0.26
IPL-34	6.20	45	6.34	6.13	851-764	0.24
IPL-35	4.82	44	4.95	4.89	863-793	0.16
IPL-36	9.65	45	9.92	9.13	972-733	0.34
IPL-37	3.41	49	3.51	3.45	896-801	0.25
IPL-38	2.06	41	2.14	2.07	946-875	0.25
IPL-39	1.38	40	1.43	1.36	1032-866	0.30
IPL-40	0.69	45	0.74	0.70	1250-1147	0.14
IPL-41	1.03	41	1.07	1.03	1082-922	0.37
IPL-42	1.72	46	1.79	1.72	956-868	0.34

[a]Zircaloy tubes were constrained with a column of 10-mm-long alumina pellets. The axial and diametral gap distances were 2.5 and 0.07 mm, respectively.

[b]Specimen length was 300 mm.

[c]Average heating rate for the temperature range 300-810°C.

[d]Maximum temperature variation at rupture recorded from 4 or 5 thermocouples attached to the tube. The burst temperature corresponds to the maximum temperature in each test.

TABLE A.19. Burst-test Results for Pellet-constrained[a] Zircaloy-4 Cladding[b] in Steam at Heating Rates of ~5 and 15-22°C/s

Test Number	Initial Pressure, MPa	Heating Rate,[c] °C/s	Maximum Pressure, MPa	Burst Pressure, MPa	Burst Temperature,[d] °C	Maximum Circumferential Strain
IPL-1	8.20	5.8	8.47	7.72	785-750	0.66
IPL-2	6.75	5.7	6.89	5.99	814-790	0.74
IPL-3	10.3	5.5	10.7	-	-	-
IPL-4	8.96	4.9	9.16	8.20	723-685	0.70
IPL-5	13.0	5.0	13.0	12.6	693-725	0.73
IPL-6	6.20	5.0	6.46	5.96	802-774	0.91
IPL-7	6.06	5.0	6.28	5.82	818-800	0.88
IPL-8	4.82	5.0	5.04	4.34	848-812	0.79
IPL-9	3.45	7.0	3.59	3.48	942-916	0.21
IPL-10	2.06	8.0	2.15	2.10	918-895	0.27
IPL-11	1.38	5.0	1.48	1.41	975-932	0.32
IPL-12	11.0	5.0	11.4	9.99	728-694	0.75
IPL-13	0.69	5.0	0.77	0.75	1079-1052	0.14
IPL-14	4.13	5.0	4.33	4.01	870-848	0.26
IPL-50	7.58	5.0	7.79	6.75	757-737	0.81
IPL-51	4.82	5.8	5.02	4.48	843-815	0.54
IPL-22	9.65	15.0	9.99	9.44	688-724	0.59
IPL-27	8.27	14.0	8.47	7.79	726-788	0.48
IPL-52	9.65	15.1	9.89	8.96	750-770	0.57
IPL-53	8.96	22.3	9.23	8.34	762-857	0.43
IPL-54	8.27	14.9	8.48	7.44	771-790	0.58
IPL-55	7.58	15.2	7.79	7.03	761-812	0.49
IPS-114	13.7	20.7	14.1	14.0	-	0.31
IPS-115	11.7	22.7	11.9	11.8	731-821	0.38
IPS-116	6.21	19.3	6.59	6.51	829-783	0.43
IPS-117	5.48	15.4	5.74	5.62	823-917	0.27
IPS-118	4.83	22.4	5.10	5.04	882-931	0.26
IPS-119	4.15	15.6	4.45	4.42	821-918	0.16
IPS-120	2.76	21.5	2.93	2.92	707-845	0.16

[a]Zircaloy tubes were constrained with a column of 10-mm-long alumina pellets. The axial and diametral gap distances were 2.5 and 0.07 mm, respectively.

[b]Specimen length was 300 mm.

[c]Average heating rate for the temperature range 300-810°C.

[d]Maximum temperature variation at rupture recorded from 4 or 5 thermocouples attached to the tube. The burst temperature corresponds to the maximum temperature in each test.

TABLE A.20. Burst-test Results for Pellet-constrained[a] Zircaloy-4 Cladding,[b] with a Diametral-gap Size of 0.5 mm, in Steam at Heating Rates of ~5, 15, 45, and 115°C/s

Test Number	Initial Pressure, MPa	Heating Rate,[c] °C/s	Maximum Pressure, MPa	Burst Pressure, MPa	Burst[d] Temperature, °C	Maximum Circumferential Strain
IPL-56	12.5	7.0	13.3	11.9	722-672	0.66
IPL-57	11.1	4.2	-	-	738-692	0.70
IPL-58	10.4	8.1	10.9	9.92	702-681	0.79
IPL-59	9.55	6.5	10.1	8.68	730-690	0.68
IPL-60	8.27	4.6	8.72	7.23	759-725	0.97
IPL-61	6.89	4.5	7.25	6.27	800-751	0.72
IPL-62	5.56	4.5	5.86	4.75	825-790	0.93
IPL-70	5.51	10.0	5.82	5.27	873-824	0.59
IPL-71	8.27	9.8	8.61	7.44	803-757	0.70
IPL-72	9.68	9.4	10.1	8.82	701-659	0.57
IPL-73	9.65	10.1	10.1	9.09	811-755	0.63
IPL-76	13.8	10.2	14.6	12.6	739-691	0.72
IPL-69	6.89	20	7.30	6.82	741-831	0.55
IPL-74	11.0	20	11.6	10.7	682-708	0.41
IPL-75	12.4	14	13.0	12.0	652-749	0.38
IPL-63	6.89	51	7.24	6.61	748-652	0.30
IPL-77	9.78	54	10.2	9.26	768-688	0.60
IPL-78	12.4	41	13.0	11.7	760-683	0.56
IPL-79	11.1	50	11.5	9.51	809-722	0.45
IPL-80	9.65	47	10.1	9.03	825-744	0.37
IPL-81	8.27	47	8.68	7.79	833-725	0.52
IPL-82	6.92	46	7.23	6.61	835-754	0.40
IPL-85	9.58	50	10.1	8.68	823-744	0.49
IPL-86	10.9	51	11.6	10.4	832-752	0.48
IPL-64	6.89	93	7.22	6.55	848-722	0.29
IPL-65	9.65	133	10.1	8.68	875-766	0.52
IPL-66	11.0	132	11.6	9.71	821-696	0.52
IPL-67	12.4	130	13.0	11.2	795-664	0.33
IPL-68	13.8	139	14.5	12.1	808-701	0.26
IPL-83	8.27	95	8.68	7.51	920-824	0.29
IPL-84	9.65	94	-	-	807-711	0.56

[a]Zircaloy tubes were constrained with a column of 10-mm-long alumina pellets in which the axial-gap distance was 2.5 mm.

[b]Specimen length was 300 mm.

[c]Average heating rate for the temperature range 300-810°C.

[d]Maximum temperature variation at rupture recorded for 4 or 5 thermocouples attached to the tube. The burst temperature corresponds to the maximum temperature in each test.

TABLE A.21. Burst-test Results for Pellet-constrained[a] Zircaloy-4 Cladding,[b] with a Diametral-gap Size of 0.2 mm, in Steam at Heating Rates of ~5, 45, and 115°C/s

Test Number	Initial Pressure, MPa	Heating Rate,[c] °C/s	Maximum Pressure, MPa	Burst Pressure, MPa	Burst[d] Temperature, °C	Maximum Circumferential Strain
IPL-89	8.27	5.4	8.61	7.30	773-736	0.95
IPL-90	6.89	6.6	7.27	5.58	824-785	1.06
IPL-91	8.30	10	8.34	8.13	796-769	0.95
IPL-92	9.30	10	9.72	8.54	735-704	0.81
IPS-96	12.3	7.5	12.6	11.8	728-705	0.66
IPS-97	11.0	7.3	11.3	10.3	759-737	0.67
IPS-98	9.65	5.3	9.99	9.23	738-681	0.60
IPS-100	7.58	10	7.72	6.96	802-769	0.97
IPS-101	5.51	4.6	5.65	5.24	829-795	0.66
IPS-102	7.58	6.6	7.79	6.96	779-751	1.02
IPS-103	4.13	5.3	4.33	4.13	854-821	0.40
IPS-105	5.17	10	5.48	4.96	829-796	0.59
IPS-106	4.82	10	5.11	4.77	837-825	0.40
IPS-107	12.3	10	12.5	11.6	751-712	0.58
IPL-88	6.89	55	7.10	6.55	870-788	0.33
IPL-93	9.65	41	10.0	8.99	790-693	0.44
IPS-108	8.96	49	9.11	8.27	812-707	0.46
IPS-109	12.4	45	12.6	11.9	756-676	0.63
IPL-87	6.89	118	7.11	6.65	865-802	0.32
IPL-94	8.96	73	8.54	7.51	851-787	0.59
IPL-95	11.0	75	11.4	9.99	760-688	0.63
IPL-99	7.58	71	7.75	7.44	884-811	0.28
IPS-104	11.1	125	11.3	10.3	744-607	0.41
IPS-110	7.10	102	7.13	6.55	844-741	0.37
IPS-111	8.27	80	8.34	7.44	834-697	0.60
IPS-112	9.65	112	9.78	8.96	818-721	0.56
IPS-113	11.2	91	11.2	10.2	809-709	0.51

[a]Zircaloy tubes were constrained with a column of 10-mm-long alumina pellets in which the axial-gap distance was 2.5 mm.

[b]Specimen lengths were 153 and 300 mm for the IPS and IPL test numbers, respectively.

[c]Average heating rate for the temperature range 300-810°C.

[d]Maximum temperature variation at rupture recorded from 4 or 5 thermocouples attached to the tube. The burst temperature corresponds to the maximum temperature in each test.

APPENDIX B

Ballooning Sequences for Zircaloy Cladding in Vacuum and Steam Environments

Quantitative information on the time-dependent deformation characteristics of Zircaloy cladding in vacuum and steam environments presented here may be of use in verifying computer codes that model cladding deformation during transient heating. A detailed analysis of the ballooning sequence was made for 20 burst tests that encompass a wide range of experimental conditions, i.e., five tests on mandrel-constrained tubes and one unconstrained tube in vacuum, eight tests on mandrel-constrained tubes and three unconstrained tubes in steam, and three tests on pellet-constrained tubes in steam.

Measured values of the internal pressure, temperature, and diametral strain, and calculated values of the effective stress and strain have been tabulated for small time increments up to the moment of rupture. The temperature, internal pressure, and diametral strains were plotted as a function of time for each test, and the onset of plastic instability was noted on the diametral-strain-versus-time curve. The methods we used to determine the onset of plastic instability in the tube and the effective stress and strain during deformation were described in Secs. IV.A and IV.B, respectively.

The individual runs analyzed in detail are identified in plots of maximum circumferential strain versus burst temperature (Figs. B.1-B.4) for different experimental conditions. The time-dependent temperature, internal pressure, diametral strain, and ballooning profiles are shown in Figs. B.5-B.21 for unconstrained and mandrel-constrained tubes. Similar results for pellet-constrained tubes are given in Figs. B.22-B.27. For the unconstrained and mandrel-constrained tubes, the tabular results for the effective stress and strain, as well as other parameters, are given (Tables B.1-B.17) immediately after the graphical representation of the data.

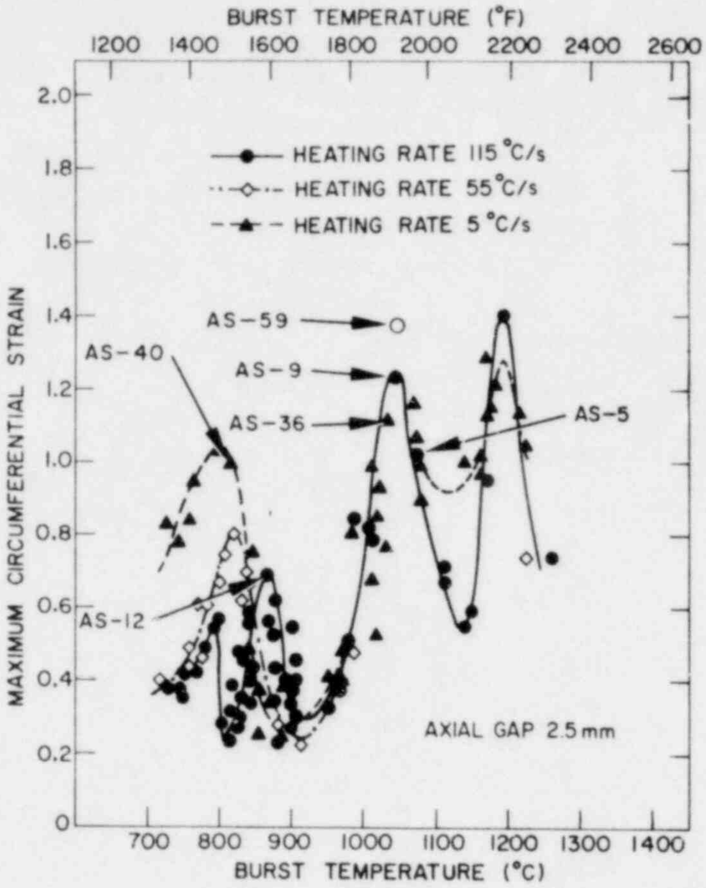

Fig. B.1

Burst Tests in Vacuum Selected for Ballooning Sequence Analysis Shown in Figs. B.5–B.10 and Tables B.1–B.6. All specimens were constrained with a mandrel, except for one unconstrained tube (AS-59). ANL Neg. No. 306-76-93 Rev.

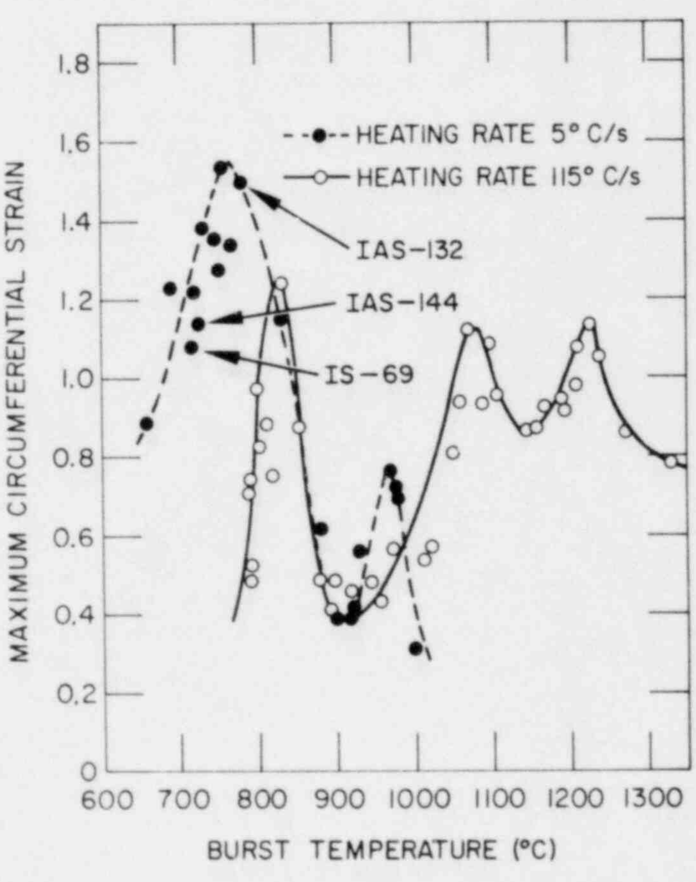

Fig. B.2

Burst Tests in Steam on Unconstrained Cladding Tubes Selected for Ballooning Sequence Analysis Shown in Figs. B.11–B.13 and Tables B.7–B.9. ANL Neg. No. 306-77-23 Rev.

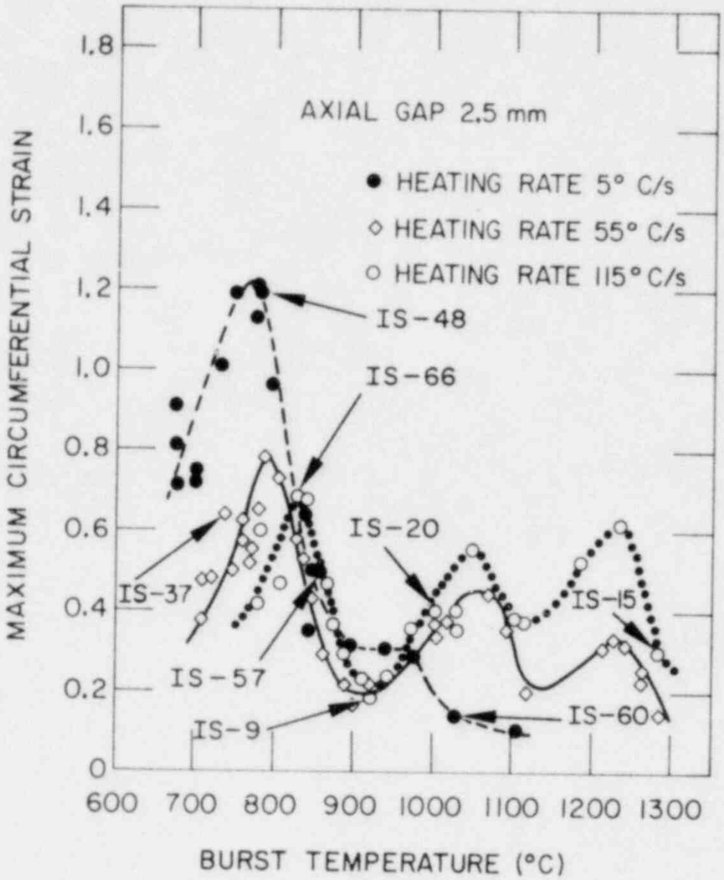

Fig. B.3

Burst Tests in Steam on Mandrel-constrained Cladding Tubes Selected for Ballooning Sequence Analysis Shown in Figs. B.14-B.21 and Tables B.10-B.17. ANL Neg. No. 306-78-414 Rev.

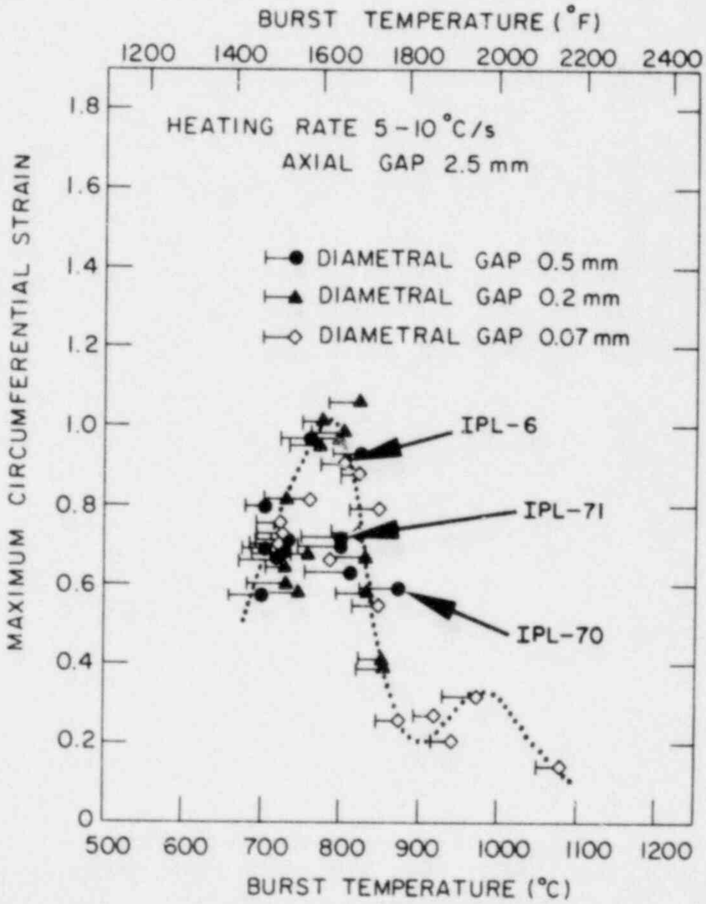

Fig. B.4

Burst Tests in Steam on Pellet-constrained Cladding Tubes Selected for Ballooning Sequence Analysis Shown in Figs. B.22-B.27. ANL Neg. No. 306-77-340 Rev.

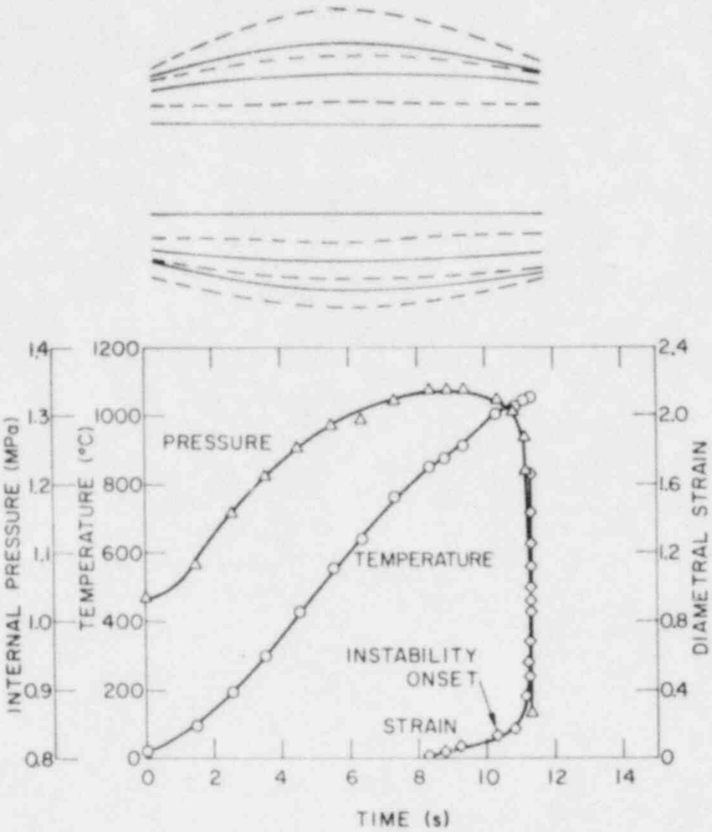

Fig. B.5

Time-dependent Temperature, Pressure, Diametral Strain, and Ballooning Profiles for Unconstrained Zircaloy-4 Tube Burst in Vacuum at Heating Rate of 120°C/s. Ballooning profiles correspond to 0, 3, 5, 10, 30, and 400 frames before rupture. Camera speed 200 frames/s. Test No. AS-59. ANL Neg. No. 306-78-413.

TABLE B.1. Effective Stress and Effective Strain as a Function of Time Obtained from the Diametral Strain and Internal Pressure during Transient Heating (120°C/s) and Rupture (1051°C) of an Unconstrained Zircaloy-4 Tube[a] in Vacuum

Time, s	Temperature, °C	Internal Pressure, MPa	Diametral Strain	Effective Strain, $\bar{\varepsilon}$	Effective Stress $\bar{\sigma}$, MPa
0	22	1.034	0	0	-
1.520	99	1.081	-	-	-
2.520	193	1.158	-	-	-
3.520	299	1.213	-	-	-
4.520	428	1.254	-	-	-
5.520	554	1.286	-	-	-
6.330	640	1.296	-	-	-
7.330	765	1.324	-	-	-
8.330	851	1.338	0.02	0.027	11.28
8.830	878	1.338	0.05	0.030	11.33
9.330	913	1.338	0.08	0.052	11.79
10.330[b]	1009[b]	1.324[b]	0.15[b]	0.172[b]	14.25[b]
10.830	1032	1.314	0.18	0.172	14.25
11.080	1044	1.269	0.24	0.274	15.99
11.180	1045	1.220	0.37	0.427	19.03
11.230	1046	1.172	0.49	0.564	21.76
11.255	1047	1.117	0.57	0.661	23.30
11.280	1049	1.089	0.69	0.796	26.36
11.300	1050	0.924	0.86	0.993	27.62
11.305	1050	0.924	0.93	1.078	29.88
11.310	1051	0.924	1.01	1.162	32.23
11.315	1051	0.910	1.12	1.292	35.50
11.320	1051	0.903	1.26	1.459	40.30
11.325	1051	0.896	1.44	1.666	46.69
11.330	1051	0.869	1.66	1.913	53.78

[a]Test No. AS-59 (Table A.1).
[b]Onset of plastic instability in the tube.

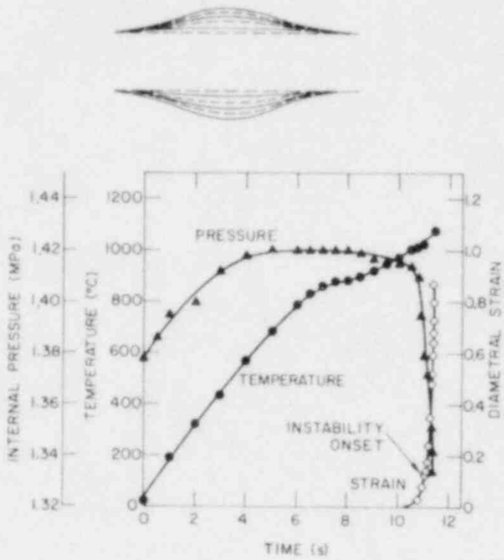

Fig. B.6

Time-dependent Temperature, Pressure, Diametral Strain, and Ballooning Profiles for Mandrel-constrained Zircaloy-4 Tube Burst in Vacuum at Heating Rate of 110°C/s. Ballooning profiles correspond to 0, 15, 40, 100, 300, and 600 frames before rupture. Camera speed 1000 frames/s. Test No. AS-5. ANL Neg. No. 306-78-405.

TABLE B.2. Effective Stress and Effective Strain as a Function of Time Obtained from the Diametral Strain and Internal Pressure during Transient Heating (110°C/s) and Rupture (1075°C) of a Mandrel-constrained Zircaloy-4 Tube[a] in Vacuum

Time, s	Temperature, °C	Internal Pressure, MPa	Diametral Strain	Effective Strain, $\bar{\varepsilon}$	Effective Stress $\bar{\sigma}$, MPa
0	23	1.378	0	0	–
1.000	195	1.395	–	–	–
2.000	321	1.400	–	–	–
3.000	437	1.412	–	–	–
4.000	570	1.418	–	–	–
5.000	685	1.420	–	–	–
6.000	790	1.420	–	–	–
6.500	832	1.420	–	–	–
7.000	862	1.420	–	–	–
7.500	880	1.420	–	–	–
8.000	885	1.420	–	–	–
8.500	900	1.419	–	–	–
9.000	922	1.417	–	–	–
9.500	945	1.416	–	–	–
10.000	977	1.415	–	–	–
10.500	1003	1.414	–	–	–
10.700	1013	1.411	–	–	–
10.799	1020	1.405	0.03	0.039	11.[illegible]
10.899	1023	1.397	0.05	0.063	12.[illegible]6
11.000	1025	1.389	0.08	0.093	13.00
11.050	1028	1.383	0.11	0.122	13.58
11.100[b]	1042[b]	1.377[b]	0.13[b]	0.151[b]	14.25[b]
11.150	1049	1.372	0.14	0.166	14.58
11.[illegible]00	1057	1.367	0.18	0.210	15.61
11.250	1062	1.362	0.24	0.283	17.41
11.300	1067	1.355	0.35	0.400	20.47
1[illegible].330	1068	1.350	0.43	0.497	23.21
11.[illegible]50	1069	1.348	0.48	0.551	24.78
11.3[illegible]0	1070	1.347	0.52	0.604	26.41
11.370	1071	1.346	0.59	0.687	29.02
11.380	1072	1.344	0.64	0.741	30.77
11.385	1073	1.343	0.68	0.785	32.24
11.390	1074	1.342	0.73	0.843	34.26
11.393	1074	1.341	0.78	0.902	36.33
11.395	1075	1.340	0.80	0.921	36.52
11.396	1075	1.339	0.81	0.941	37.22
11.397	1075	1.337	0.84	0.965	38.10
11.398	1075	1.336	0.87	1.004	39.35
11.399	1075	1.334	0.87	1.009	39.35

[a]Test No. AS-5 (Table A.3).
[b]Onset of plastic instability in the tube.

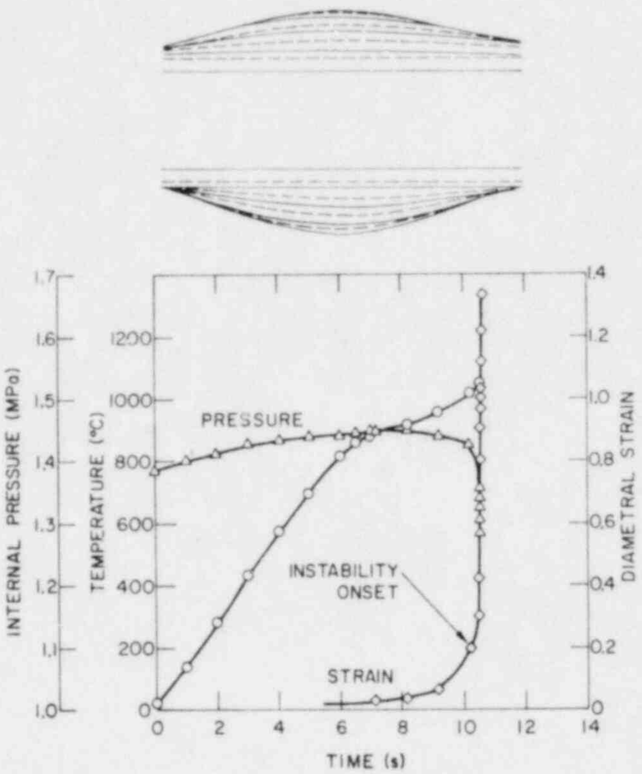

Fig. B.7

Time-dependent Temperature, Pressure, Diametral Strain, and Ballooning Profiles for Mandrel-constrained Zircaloy-4 Tube Burst in Vacuum at Heating Rate of 120°C/s. Ballooning profiles correspond to 0, 1, 2, 5, 10, 20, 50, 100, and 700 frames before rupture. Camera speed 500 frames/s. Test No. AS-9. ANL Neg. No. 306-78-399.

TABLE B.3. Effective Stress and Effective Strain as a Function of Time Obtained from the Diametral Strain and Internal Pressure during Transient Heating (120°C/s) and Rupture (1056°C) of a Mandrel-constrained Zircaloy-4 Tube[a] in Vacuum

Time, s	Temperature, °C	Internal Pressure, MPa	Diametral Strain	Effective Strain, $\bar{\varepsilon}$	Effective Stress $\bar{\sigma}$, MPa
0	21	1.386	0	0	-
1.000	141	1.401	-	-	-
2.000	286	1.413	-	-	-
3.000	434	1.428	-	-	-
4.000	575	1.431	-	-	-
5.000	698	1.438	-	-	-
6.000	814	1.440	-	-	-
6.500	862	1.443	-	-	-
7.000	874	1.449	-	-	-
7.200	895	1.448	0.04	0.041	12.44
8.200	918	1.448	0.05	0.045	12.53
9.200	960	1.441	0.07	0.086	13.39
10.200[b]	1020[b]	1.427[b]	0.20[b]	0.228[b]	16.66[b]
10.400	1040	1.407	0.30	0.344	19.43
10.500	1050	1.358	0.42	0.486	22.67
10.520	1052	1.351	0.43	0.549	24.40
10.540	1053	1.344	0.54	0.624	26.52
10.560	1054	1.331	0.69	0.800	31.84
10.570	1055	1.331	0.69	0.800	31.84
10.580	1056	1.324	0.81	0.931	36.16
10.586	1056	1.317	0.91	1.047	40.17
10.590	1056	1.310	0.97	1.125	42.92
10.592	1056	1.303	1.04	1.196	45.45
10.594	1056	1.303	1.08	1.248	47.53
10.596	1056	1.296	1.14	1.316	50.01
10.598	1056	1.289	1.23	1.424	54.29
10.600	1056	1.282	1.34	1.544	59.20

[a]Test No. AS-9 (Table A.3).
[b]Onset of plastic instability in the tube.

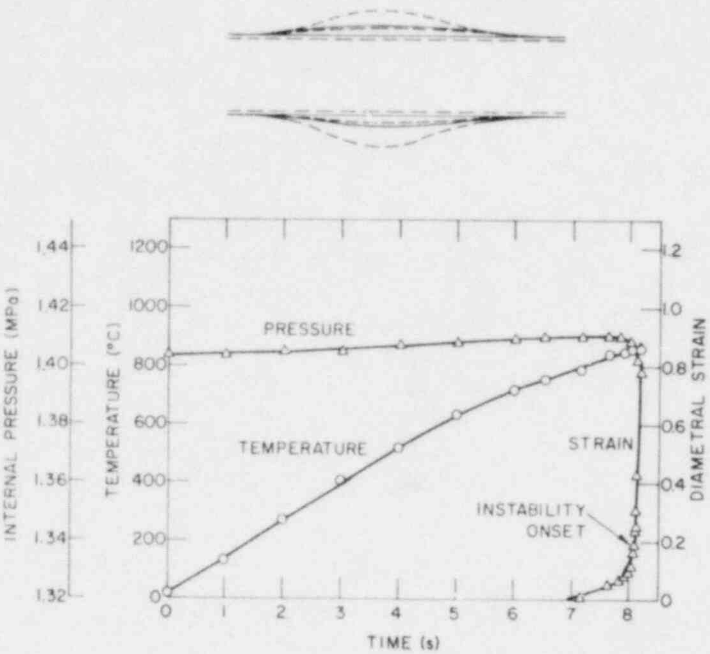

Fig. B.8

Time-dependent Temperature, Pressure, Diametral Strain, and Ballooning Profiles for Mandrel-constrained Zircaloy-4 Tube Burst in Vacuum at Heating Rate of 115°C/s. Ballooning profiles correspond to 0, 1, 2, 10, and 100 frames before rupture. Camera speed 100 frames/s. Test No. AS-12. ANL Neg. No. 306-78-412.

TABLE B.4. Effective Stress and Effective Strain as a Function of Time Obtained from the Diametral Strain and Internal Pressure during Transient Heating (115°C/s) and Rupture (865°C) of a Mandrel-constrained Zircaloy-4 Tube[a] in Vacuum

Time, s	Temperature, °C	Internal Pressure, MPa	Diametral Strain	Effective Strain, $\bar{\varepsilon}$	Effective Stress $\bar{\sigma}$, MPa
0	22	5.610	0	0	–
1.000	132	5.614	–	–	–
2.000	269	5.624	–	–	–
3.000	403	5.626	–	–	–
4.000	510	5.634	–	–	–
5.000	632	5.640	–	–	–
6.000	711	5.647	–	–	–
6.500	752	5.653	–	–	–
7.130	792	5.654	0.01	0.009	43.66
7.630	843	5.654	0.06	0.066	48.26
7.830	852	5.654	0.07	0.085	49.84
7.930	857	5.647	0.09	0.103	51.39
7.980	859	5.647	0.10	0.117	52.61
8.030	861	5.640	0.11	0.127	53.36
8.060[b]	862[b]	5.633[b]	0.17[b]	0.192[b]	59.19[b]
8.080	863	5.626	0.19	0.216	61.30
8.090	864	5.619	0.24	0.272	66.58
8.100	864	5.612	0.25	0.286	67.87
8.110	865	5.605	0.31	0.362	75.33
8.120	865	5.599	0.43	0.502	90.37
8.130	865	5.592	0.87	1.005	155.1

[a]Test No. AS-12 (Table A.3).
[b]Onset of plastic instability in the tube.

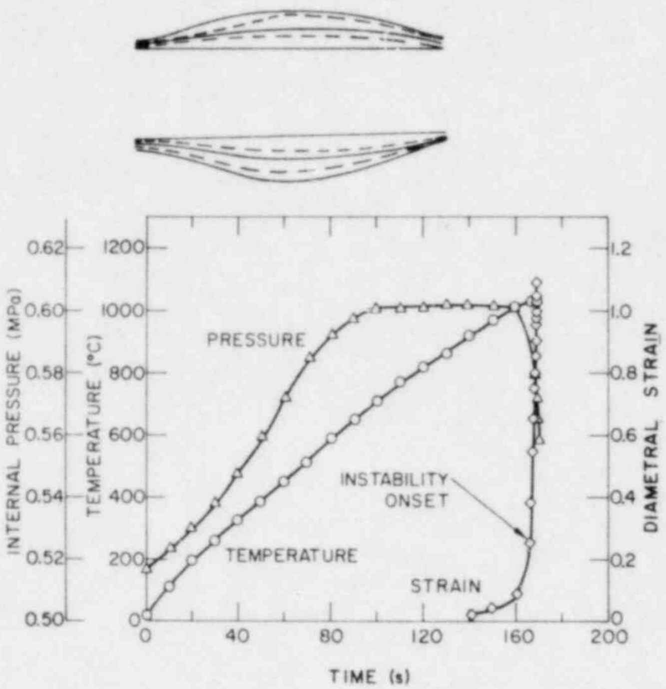

Fig. B.9

Time-dependent Temperature, Pressure, Diametral Strain, and Ballooning Profiles for Mandrel-constrained Zircaloy-4 Tube Burst in Vacuum at Heating Rate of 7°C/s. Ballooning profiles correspond to 0, 5, 30, 100, and 500 frames/s before rupture. Camera speed 50 frames/s. Test No. AS-36. ANL Neg. No. 306-78-410 Rev.

TABLE B.5. Effective Stress and Effective Strain as a Function of Time Obtained from the Diametral Strain and Internal Pressure during Transient Heating (7°C/s) and Rupture (1037°C) of a Mandrel-constrained Zircaloy-4 Tube[a] in Vacuum

Time, s	Temperature, °C	Internal Pressure, MPa	Diametral Strain	Effective Strain, $\bar{\varepsilon}$	Effective Stress $\bar{\sigma}$, MPa
0	23	0.517	0	0	-
10.000	121	0.524	-	-	-
20.000	205	0.531	-	-	-
30.000	263	0.538	-	-	-
40.000	331	0.548	-	-	-
50.000	391	0.565	-	-	-
60.000	458	0.573	-	-	-
69.420	518	0.585	-	-	-
81.420	593	0.592	-	-	-
91.420	653	0.597	-	-	-
101.420	714	0.600	-	-	-
111.420	772	0.600	-	-	-
121.420	825	0.607	-	-	-
131.420	865	0.614	-	-	-
141.420	924	0.614	0.02	0.018	5.510
151.420	977	0.614	0.04	0.041	5.737
161.420	1020	0.614	0.09	0.108	6.446
167.420[b]	1030[b]	0.586[b]	0.25[b]	0.284[b]	8.140[b]
169.420	1032	0.586	0.38	0.442	10.10
170.420	1033	0.586	0.55	0.632	12.72
170.820	1033	0.579	0.66	0.767	14.62
171.020	1033	0.579	0.75	0.866	16.20
171.120	1033	0.579	0.80	0.925	17.17
171.220	1034	0.579	0.86	0.997	18.40
171.280	1035	0.572	0.91	1.056	19.24
171.320	1035	0.565	0.96	1.110	20.00
171.340	1035	0.565	0.98	1.137	20.49
171.360	1035	0.565	1.00	1.160	20.90
171.380	1036	0.558	1.03	1.187	21.18
171.400	1037	0.558	1.04	1.196	21.35
171.420	1037	0.558	1.09	1.263	22.61

[a]Test No. AS-36 (Table A.6).

[b]Onset of plastic instability in the tube.

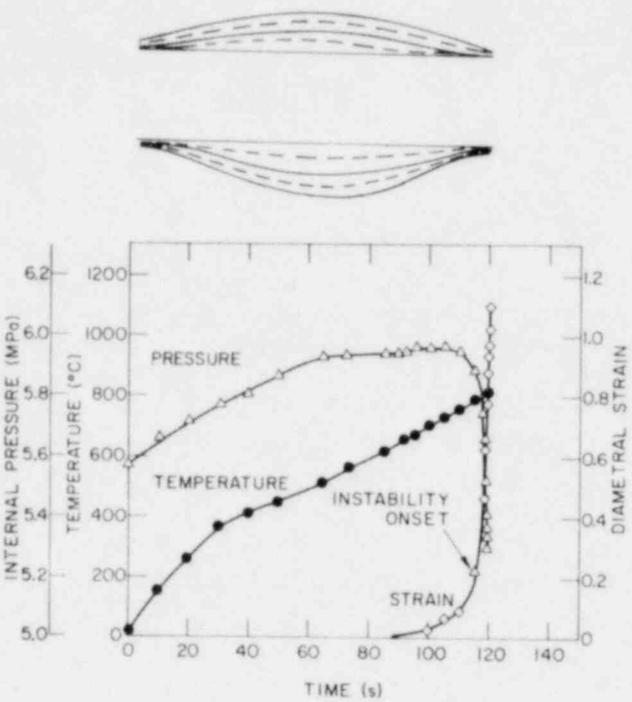

Fig. B.10

Time-dependent Temperature, Pressure, Diametral Strain, and Ballooning Profiles for Mandrel-constrained Zircaloy-4 Tube Burst in Vacuum at Heating Rate of 5.1°C/s. Ballooning profiles correspond to 0, 30, 100, 200, and 1000 frames before rupture. Camera speed 100 frames/s. Test No. AS-40. ANL Neg. No. 306-78-400.

TABLE B.6. Effective Stress and Effective Strain as a Function of Time Obtained from the Diametral Strain and Internal Pressure during Transient Heating (5.1°C/s) and Rupture (816°C) of a Mandrel-constrained Zircaloy-4 Tube[a] in Vacuum

Time, s	Temperature, °C	Internal Pressure, MPa	Diametral Strain	Effective Strain, $\bar{\varepsilon}$	Effective Stress $\bar{\sigma}$, MPa
0	21	5.554	0	0	-
10.000	159	5.661	-	-	-
20.000	265	5.720	-	-	-
30.000	366	5.770	-	-	-
40.000	417	5.801	-	-	-
50.000	451	5.871	-	-	-
65.400	518	5.938	-	-	-
73.300	578	5.939	-	-	-
85.000	627	5.940	-	-	-
90.000	654	5.941	-	-	-
92.040	668	5.943	-	-	-
95.040	675	5.957	-	-	-
100.040	713	5.964	0.03	0.038	48.45
105.040	734	5.964	0.07	0.076	51.77
110.040[b]	761[b]	5.950[b]	0.09[b]	0.103[b]	54.04[b]
115.040[b]	794	5.895[b]	0.22[b]	0.251[b]	67.62[b]
118.040	808	5.757	0.47	0.540	97.22
119.040	811	5.661	0.64	0.745	120.8
119.540	814	5.530	0.78	0.897	138.2
119.740	814	5.516	0.88	1.011	153.9
119.840	815	5.405	0.94	1.083	161.2
119.890	815	5.378	0.97	1.117	165.4
119.940	816	5.343	1.05	1.208	178.1
119.970	816	5.331	1.05	1.216	178.1
119.990	816	5.326	1.03	1.185	173.5
120.000	816	5.321	1.07	1.231	180.4
120.010	816	5.317	1.08	1.242	182.2
120.020	816	5.313	1.09	1.254	183.9
120.030	816	5.309	1.10	1.265	185.7

[a]Test No. AS-40 (Table A.6).
[b]Onset of plastic instability in the tube.

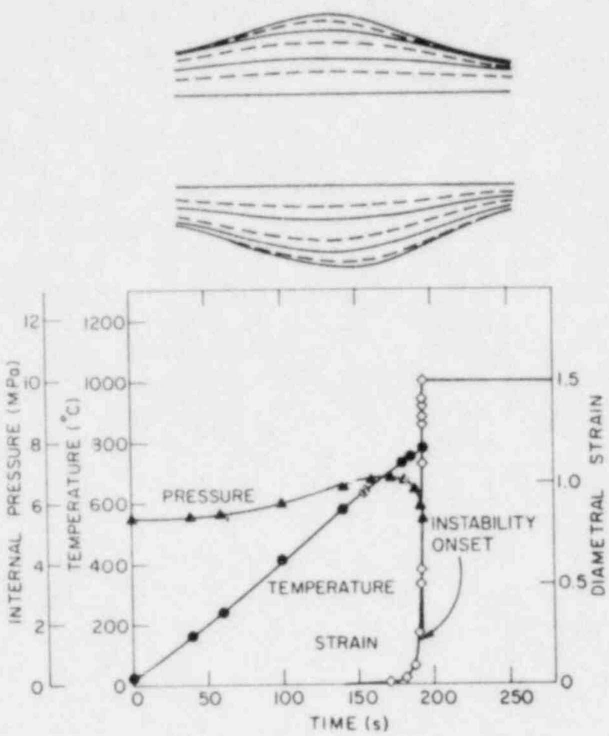

Fig. B.11

Time-dependent Temperature, Pressure, Diametral Strain, and Ballooning Profiles for Unconstrained Zircaloy-4 Tube Burst in Steam at Heating Rate of 40°C/s. Ballooning profiles correspond to 0, 3, 50, 100, 200, 400, and 1000 frames before rupture. Camera speed 200 frames/s. Test No. IAS-132. ANL Neg. No. 306-78-456.

TABLE B.7. Effective Stress and Effective Strain as a Function of Time Obtained from the Diametral Strain and Internal Pressure during Transient Heating (4.0°C/s) and Rupture (781°C) of an Unconstrained Zircaloy-4 Tube[a] in Steam

Time, s	Temperature, °C	Internal Pressure, MPa	Diametral Strain	Effective Strain, $\bar{\epsilon}$	Effective Stress $\bar{\sigma}$, MPa
0	21	5.510	0	0	-
20.000	90	5.212	-	-	-
40.000	165	5.551	-	-	-
60.000	245	5.624	-	-	-
80.000	323	5.776	-	-	-
100.000	403	5.989	-	-	-
120.000	492	6.272	-	-	-
140.000	568	6.580	-	-	-
155.000	639	6.761	-	-	-
170.000	701	6.762	-	-	-
184.300	739	6.750	0.03	0.033	54.22
187.300	761	6.419	0.09	0.102	58.14
188.050[b]	765[b]	5.936[b]	0.25[b]	0.285[b]	71.63[b]
188.800	770	5.778	0.40	0.459	88.30
189.300	772	5.695	0.48	0.551	97.56
189.800	774	5.681	0.63	0.722	118.3
190.300	775	5.667	0.97	1.125	175.5
190.450	776	5.647	1.09	1.257	195.9
190.600	777	5.626	1.20	1.391	217.8
190.650	778	5.599	1.28	1.473	231.2
190.750	780	5.585	1.33	1.532	241.2
190.775	780	5.557	1.37	1.582	249.0
190.785	781	5.516	1.40	1.621	254.4
190.800	781	5.312	1.49	1.723	268.5

[a]Test No. IAS-132 (Table A.9).
[b]Onset of plastic instability in the tube.

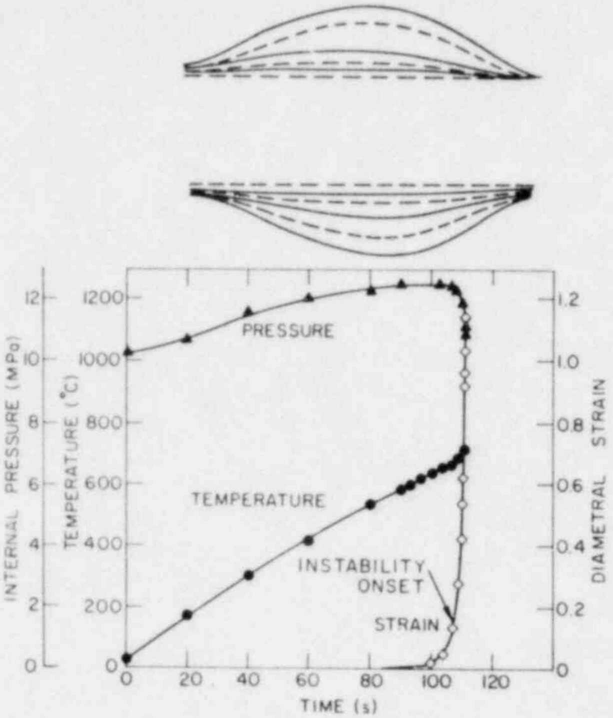

Fig. B.12

Time-dependent Temperature, Pressure, Diametral Strain, and Ballooning Profiles for Unconstrained Zircaloy-4 Tube Burst in Steam at Heating Rate of 5.3°C/s. Ballooning profiles correspond to 0, 35, 200, 400, 800, and 3520 frames before rupture. Camera speed 200 frames/s. Test No. IAS-144. ANL Neg. No. 306-78-455.

TABLE B.8. Effective Stress and Effective Strain as a Function of Time Obtained from the Diametral Strain and Internal Pressure during Transient Heating (5.3°C/s) and Rupture (708°C) of an Unconstrained Zircaloy-4 Tube[a] in Steam

Time, s	Temperature, °C	Internal Pressure, MPa	Diametral Strain	Effective Strain, $\bar{\varepsilon}$	Effective Stress $\bar{\sigma}$, MPa
0	22	10.214	0	0	–
20.000	169	10.702	–	–	–
40.000	302	11.525	–	–	–
60.000	418	12.024	–	–	–
80.000	537	12.254	–	–	–
90.000	586	12.461	–	–	–
99.700	631	12.512	0.02	0.026	99.15
103.700	657	12.564	0.05	0.060	105.6
106.700[b]	669[b]	12.383[b]	0.13[b]	0.148[b]	120.1[b]
108.700	695	12.004	0.27	0.316	150.0
109.200	701	11.728	0.42	0.486	183.9
109.700	704	11.369	0.47	0.546	191.9
110.700	705	11.369	0.54	0.623	210.1
110.450	706	11.176	0.62	0.720	230.2
110.525	707	11.080	0.84	0.976	296.3
110.625	707	11.039	0.92	1.067	321.4
110.675	708	10.983	0.98	1.127	337.5
110.685	708	10.949	1.04	1.206	360.7
110.700	708	10.894	1.12	1.297	387.5

[a]Test No. IAS-144 (Table A.9).

[b]Onset of plastic instability in the tube.

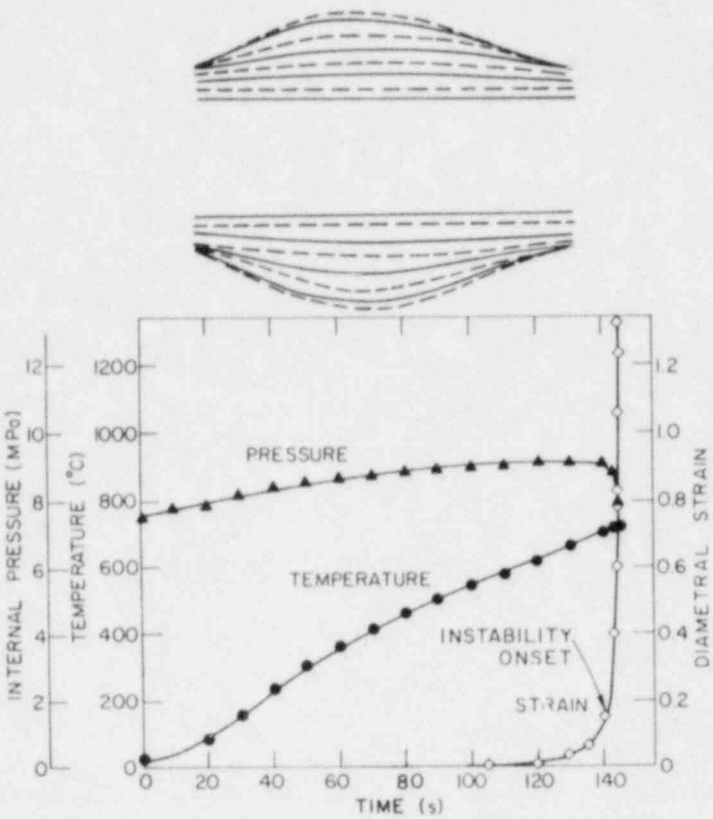

Fig. B.13

Time-dependent Temperature, Pressure, Diametral Strain, and Ballooning Profiles for Unconstrained Zircaloy-4 Tube Burst in Steam at Heating Rate of 5.0°C/s. Ballooning profiles correspond to 0, 7, 50, 100, 200, 400, 1000, and 7720 frames before rupture. Camera speed 200 frames/s. Test No. IS-69. ANL Neg. No. 306-77-472 Rev.

TABLE B.9. Effective Stress and Effective Strain as a Function of Time Obtained from the Diametral Strain and Internal Pressure during Transient Heating (5.0°C/s) and Rupture (715°C) of an Unconstrained Zircaloy-4 Tube[a] in Steam

Time, s	Temperature, °C	Internal Pressure, MPa	Diametral Strain	Effective Strain, $\bar{\varepsilon}$	Effective Stress $\bar{\sigma}$, MPa
0	20	7.572	0	0	-
20.000	86	7.887	-	-	-
40.000	239	8.411	-	-	-
60.000	362	8.673	-	-	-
80.000	464	8.824	-	-	-
100.000	548	8.990	-	-	-
120.000	621	9.100	-	-	-
129.900	661	9.156	0.04	0.047	75.07
134.900	686	9.136	0.07	0.081	79.59
139.900[b]	709[b]	9.094[b]	0.16[b]	0.180[b]	93.14[b]
142.900	711	8.880	0.40	0.460	135.0
143.900	712	8.646	0.59	0.684	171.6
144.400	714	8.294	0.82	0.951	217.3
144.650	714	8.108	1.06	1.228	273.0
144.865	715	7.943	1.24	1.431	315.8
144.900	715	7.918	1.35	1.562	347.5

[a]Test No. IS-69 (Table A.9).
[b]Onset of plastic instability in the tube.

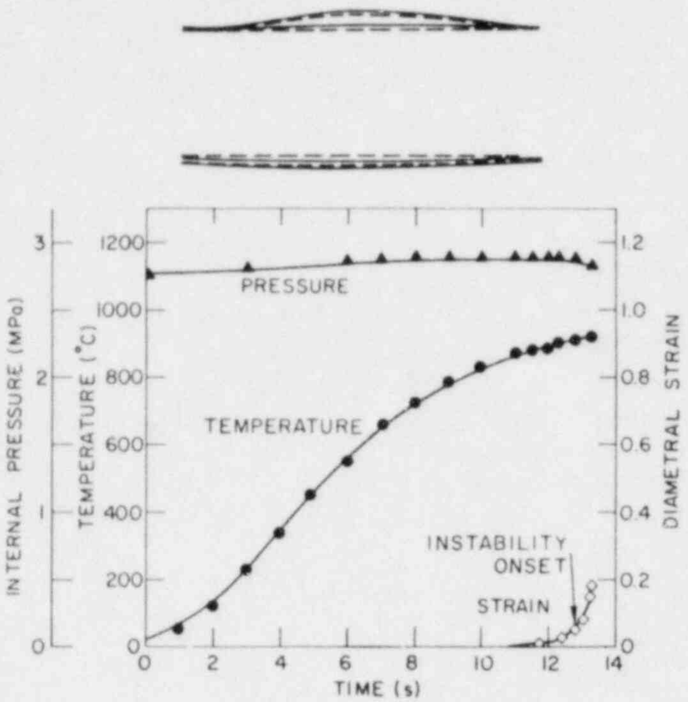

Fig. B.14

Time-dependent Temperature, Pressure, Diametral Strain, and Ballooning Profiles for Mandrel-constrained Zircaloy-4 Tube Burst in Steam at Heating Rate of 100°C/s. Ballooning profiles correspond to 1, 10, 100, and 2701 frames before rupture. Camera speed 200 frames/s. Test No. IS-9. ANL Neg. No. 306-77-473.

TABLE B.10. Effective Stress and Effective Strain as a Function of Time Obtained from the Diametral Strain and Internal Pressure during Transient Heating (100°C/s) and Rupture (920°C) of a Mandrel-constrained Zircaloy-4 Tube[a] in Steam

Time, s	Temperature, °C	Internal Pressure, MPa	Diametral Strain	Effective Strain, $\bar{\varepsilon}$	Effective Stress $\bar{\sigma}$, MPa
0	22	2.758	0	0	-
2.000	134	2.794	-	-	-
3.000	229	2.820	-	-	-
6.000	552	2.854	-	-	-
7.000	655	2.868	-	-	-
8.000	728	2.875	-	-	-
8.340	747	2.882	0.03	0.040	23.93
10.340	851	2.896	0.05	0.053	24.57
12.340	894	2.896	0.05	0.059	24.83
12.840[b]	905[b]	2.896[b]	0.06[b]	0.071[b]	25.37[b]
13.090	910	2.889	0.07	0.081	25.72
13.190	913	2.889	0.10	0.118	27.38
13.240	915	2.882	0.12	0.133	28.02
13.265	916	2.868	0.14	0.161	29.17
13.290	917	2.861	0.15	0.170	29.54
13.305	918	2.854	0.16	0.180	29.90
13.320	919	2.848	0.17	0.201	30.86
13.325	920	2.841	0.19	0.217	31.52
13.330	920	2.834	0.20	0.232	32.19
13.335	920	2.827	0.21	0.242	32.57

[a]Test No. IS-9 (Table A.10).
[b]Onset of plastic instability in the tube.

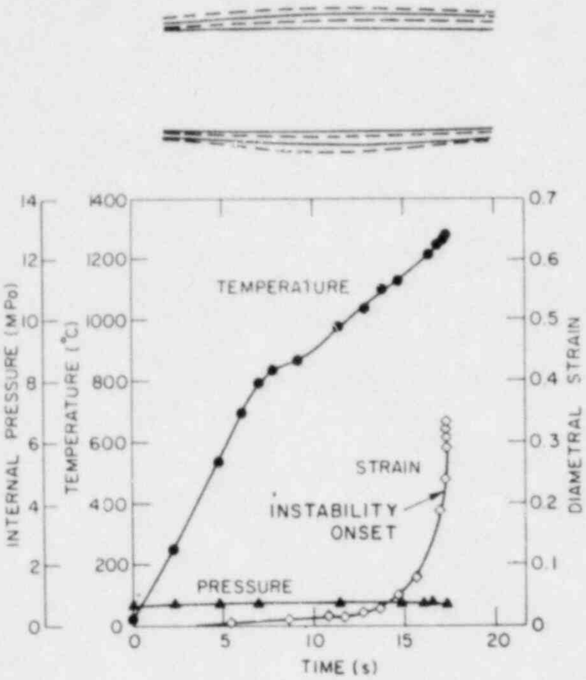

Fig. B.15

Time-dependent Temperature, Pressure, Diametral Strain, and Ballooning Profiles of Mandrel-constrained Zircaloy-4 Tube Burst in Steam at Heating Rate of 130°C/s. Ballooning profiles correspond to 0, 100, 600, and 2200 frames before rupture. Camera speed 400 frames/s. Test No. IS-15. ANL Neg. No. 306-77-462.

TABLE B.11. Effective Stress and Effective Strain as a Function of Time Obtained from the Diametral Strain and Internal Pressure during Transient Heating (130°C/s) and Rupture (1281°C) of a Mandrel-constrained Zircaloy-4 Tube[a] in Steam

Time, s	Temperature, °C	Internal Pressure, MPa	Diametral Strain	Effective Strain, $\overline{\varepsilon}$	Effective Stress $\overline{\sigma}$, MPa
0	21	0.689	0	0	-
2.000	254	0.691	-	-	-
5.000	534	0.695	-	-	-
6.000	696	0.702	-	-	-
7.000	797	0.714	-	-	-
8.000	837	0.718	-	-	-
9.000	868	0.720	-	-	-
10.000	901	0.727	-	-	-
11.730	985	0.724	0.03	0.036	6.569
12.730	1037	0.723	0.06	0.066	6.924
13.730	1105	0.721	0.07	0.084	7.142
14.730	1164	0.719	0.08	0.093	7.252
15.730	1214	0.717	0.11	0.132	7.672
16.730[b]	1255[b]	0.710[b]	0.22[b]	0.258[b]	9.249[b]
16.980	1264	0.708	0.28	0.321	10.13
17.105	1276	0.706	0.33	0.381	11.00
17.155	1278	0.705	0.34	0.417	11.54
17.180	1279	0.703	0.37	0.435	11.71
17.192	1280	0.703	0.38	0.441	11.80
17.205	1280	0.703	0.39	0.450	11.94
17.212	1281	0.703	0.39	0.456	12.03
17.217	1281	0.703	0.39	0.459	12.08
17.220	1281	0.703	0.39	0.444	11.85
17.222	1281	0.703	0.39	0.447	11.89

[a]Test No. IS-15 (Table A.10).

[b]Onset of plastic instability in the tube.

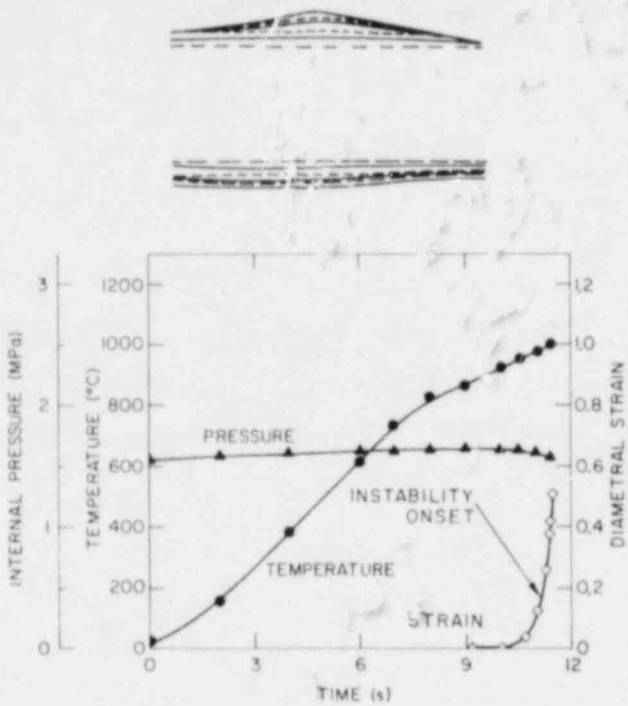

Fig. B.16

Time-dependent Temperature, Pressure, Diametral Strain, and Ballooning Profiles for Mandrel-constrained Zircaloy-4 Tube Burst in Steam at Heating Rate of 114°C/s. Ballooning profiles correspond to 1, 7, 20, 50, 200, and 4437 frames before rupture. Camera speed 400 frames/s. Test No. IS-20. ANL Neg. No. 306-77-471.

TABLE B.12. Effective Stress and Effective Strain as a Function of Time Obtained from the Diametral Strain and Internal Pressure during Transient Heating (114°C/s) and Rupture (1080°C) of a Mandrel-constrained Zircaloy-4 Tube[a] in Steam

Time, s	Temperature, °C	Internal Pressure, MPa	Diametral Strain	Effective Strain, $\overline{\varepsilon}$	Effective Stress $\overline{\sigma}$, MPa
0	23	1.552	0	0	-
2.000	158	1.563	-	-	-
4.000	383	1.584	-	-	-
6.000	614	1.601	-	-	-
7.060	788	1.606	-	-	-
8.060	877	1.613	-	-	-
9.060	908	1.620	0.05	0.052	14.10
10.060	994	1.620	0.06	0.064	14.40
11.060[b]	1046[b]	1.606[b]	0.12[b]	0.135[b]	16.08[b]
11.310	1063	1.593	0.13	0.153	16.44
11.435	1075	1.579	0.23	0.270	19.48
11.485	1078	1.565	0.25	0.291	19.93
11.510	1079	1.551	0.32	0.368	22.00
11.522	1079	1.548	0.32	0.371	19.88
11.535	1080	1.544	0.35	0.401	19.94
11.542	1080	1.541	0.40	0.466	21.47
11.547	1080	1.539	0.42	0.484	21.66
11.550	1080	1.536	0.46	0.536	22.98
11.552	1080	1.531	0.48	0.551	23.30
11.555	1080	1.528	0.53	0.616	25.01

[a]Test No. IS-20 (Table A.10).
[b]Onset of plastic instability in the tube.

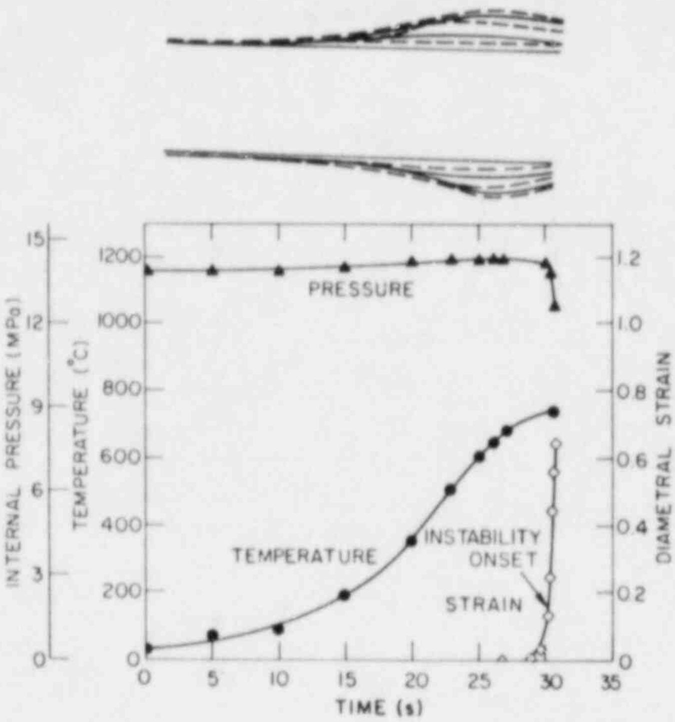

Fig. B.17

Time-dependent Temperature, Pressure, Diametral Strain, and Ballooning Profiles for Mandrel-constrained Zircaloy-4 Tube Burst in Steam at Heating Rate of 30°C/s. Ballooning profiles correspond to 2, 8, 16, 40, 80, and 3688 frames before rupture. Camera speed 200 frames/s. Test No. IS-37. ANL Neg. No. 306-77-458.

TABLE B.13. Effective Stress and Effective Strain as a Function of Time Obtained from the Diametral Strain and Internal Pressure during Transient Heating (30°C/s) and Rupture (732°C) of a Mandrel-constrained Zircaloy-4 Tube[a] in Steam

Time, s	Temperature, °C	Internal Pressure, MPa	Diametral Strain	Effective Strain, $\overline{\varepsilon}$	Effective Stress $\overline{\sigma}$, MPa
0	22	13.816	0	0	–
5.000	77	13.850	–	–	–
10.000	91	13.891	–	–	–
15.000	196	14.029	–	–	–
20.000	352	14.142	–	–	–
23.000	508	14.238	–	–	–
25.000	607	14.280	–	–	–
27.000	694	14.311	–	–	–
29.620	700	14.327	0.05	0.057	119.2
29.870	705	14.286	0.06	0.067	120.9
30.220[b]	713[b]	14.134[b]	0.16[b]	0.18[illegible][b]	144.3[b]
30.320	714	14.010	0.19	0.2[illegible]	152.9
30.420	723	13.845	0.28	0.318	173.3
30.540	726	13.286	0.50	0.579	233.0
30.580	727	12.962	0.69	0.800	290.6
30.610	732	12.686	0.88	1.018	392.6

[a]Test No. IS-37 (Table A.11).
[b]Onset of plastic instability in the tube.

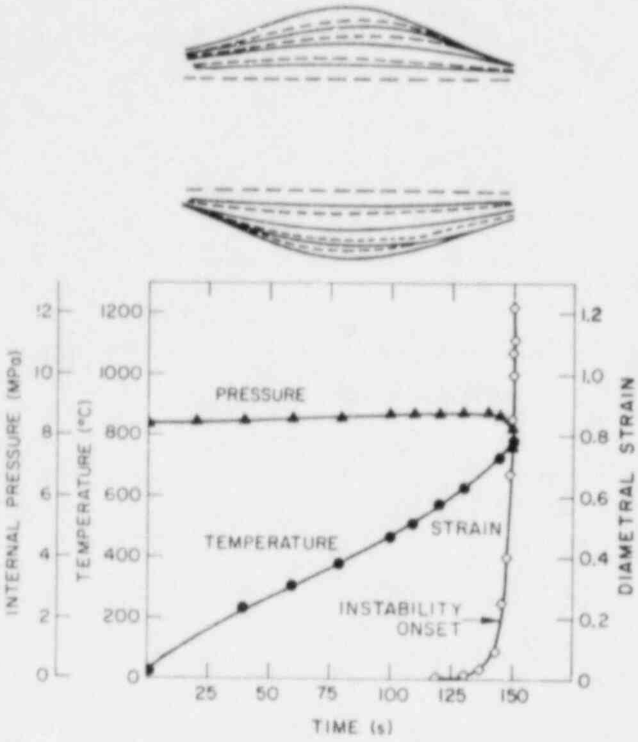

Fig. B.18

Time-dependent Temperature, Pressure, Diametral Strain, and Ballooning Profiles for Mandrel-constrained Zircaloy-4 Tube Burst in Steam at Heating Rate of 6.8°C/s. Ballooning profiles correspond to 1, 30, 50, 100, 200, 600, 1000, and 8133 frames before rupture. Camera speed 400 frames/s. Test No. IS-48. ANL Neg. No. 306-77-470 Rev.

TABLE B.14. Effective Stress and Effective Strain as a Function of Time Obtained from the Diametral Strain and Internal Pressure during Transient Heating (6.8°C/s) and Rupture (780°C) of a Mandrel-constrained Zircaloy-4 Tube[a] in Steam

Time, s	Temperature, °C	Internal Pressure, MPa	Diametral Strain	Effective Strain, $\bar{\varepsilon}$	Effective Stress $\bar{\sigma}$, MPa
0	22	8.273	0	0	-
20.000	141	8.404	-	-	-
40.000	228	8.459	-	-	-
60.000	303	8.514	-	-	-
80.000	378	8.569	-	-	-
100.000	469	8.650	-	-	-
110.000	506	8.652	-	-	-
120.000	575	8.686	-	-	-
130.000	627	8.721	-	-	-
140.000	710	8.732	0.06	0.201	85.70
144.800[b]	741[b]	8.722[b]	0.19[b]	0.225[b]	95.67
145.800	748	8.653	0.23	0.269	101.5
146.800	758	8.618	0.30	0.343	112.3
147.800	763	8.584	0.39	0.449	128.8
148.800	770	8.481	0.47	0.549	144.0
149.800	775	8.343	0.66	0.764	180.7
150.300	777	7.963	0.81	0.934	205.2
150.550	778	7.791	0.94	1.084	231.4
150.650	779	7.722	1.10	1.267	269.0
150.795	780	7.584	1.19	1.376	288.9

[a]Test No. IS-48 (Table A.12).

[b]Onset of plastic instability in the tube.

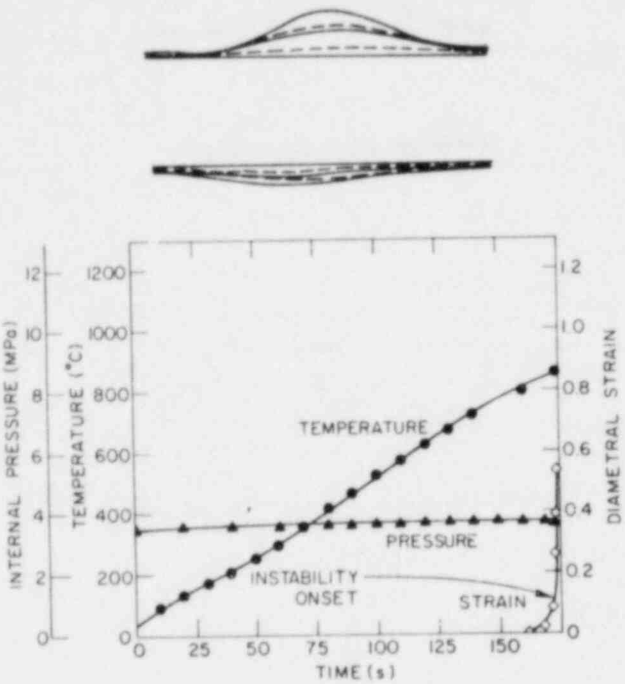

Fig. B.19

Time-dependent Temperature, Pressure, Diametral Strain, and Ballooning Profiles for Mandrel-constrained Zircaloy-4 Tube Burst in Steam at Heating Rate of 7.6°C/s. Ballooning profiles correspond to 1, 7, 15, 50, and 3040 frames before rupture. Camera speed 200 frames/s. Test No. IS-57. ANL Neg. No. 306-77-466.

TABLE B.15. Effective Stress and Effective Strain as a Function of Time Obtained from the Diametral Strain and Internal Pressure during Transient Heating (7.6°C/s) and Rupture (854°C) of a Mandrel-constrained Zircaloy-4 Tube[a] in Steam

Time, s	Temperature, °C	Internal Pressure, MPa	Diametral Strain	Effective Strain, $\bar{\epsilon}$	Effective Stress $\bar{\sigma}$, MPa
0	21	3.451	0	0	-
10.000	87	3.495	-	-	-
20.000	134	3.516	-	-	-
30.000	175	3.530	-	-	-
40.000	208	3.544	-	-	-
50.000	254	3.557	-	-	-
60.000	298	3.578	-	-	-
70.000	357	3.592	-	-	-
80.000	412	3.612	-	-	-
90.000	458	3.626	-	-	-
100.000	523	3.647	-	-	-
110.000	572	3.668	-	-	-
120.000	623	3.702	-	-	-
130.000	640	3.723	-	-	-
140.000	695	3.737	-	-	-
150.000	752	3.743	-	-	-
160.000	805	3.750	-	-	-
168.720	838	3.765	-	-	-
173.320[b]	851[b]	3.765[b]	0.03[b]	0.036[b]	30.77[b]
173.420	852	3.765	0.08	0.110	33.39
173.520	852	3.765	0.10	0.115	35.23
173.620	852	3.758	0.12	0.144	36.91
173.670	853	3.730	0.15	0.171	38.22
173.695	853	3.723	0.20	0.230	41.79
173.705	853	3.689	0.24	0.272	44.11
173.710	853	3.682	0.30	0.345	48.78
173.715	854	3.675	0.34	0.390	51.83
173.716	854	3.668	0.37	0.423	54.03
173.717	854	3.661	0.38	0.440	55.10
173.718	854	3.654	0.40	0.459	56.41
173.719	854	3.654	0.43	0.499	59.28
173.719	854	3.647	0.47	0.548	62.85
173.720	854	3.647	0.50	0.581	65.36
173.720	854	3.640	0.55	0.630	69.09

[a]Test No. IS-57 (Table A.12).
[b]Onset of plastic instability in the tube.

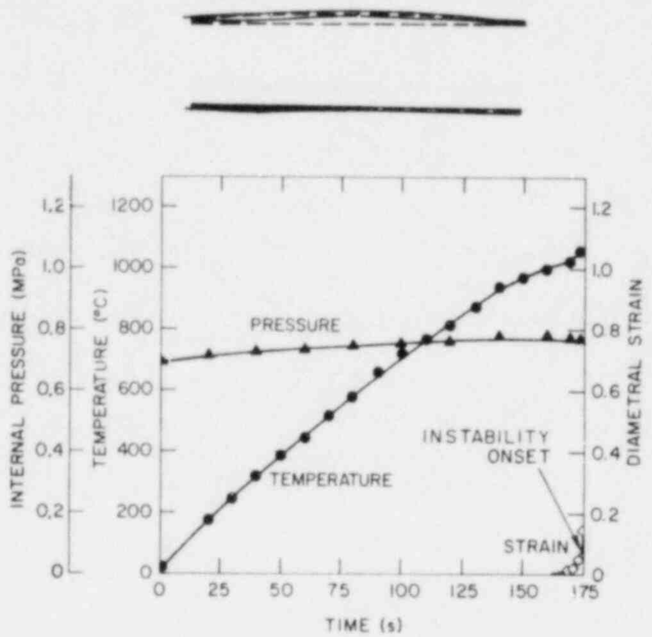

Fig. B.20

Time-dependent Temperature, Pressure, Diametral Strain, and Ballooning Profiles for Mandrel-constrained Zircaloy-4 Tube Burst in Steam at Heating Rate of 4.2°C/s. Ballooning profiles correspond to 1, 100, 1800, and 4520 frames before rupture. Camera speed 200 frames/s. Test No. IS-60. ANL Neg. No. 306-77-465.

TABLE B.16. Effective Stress and Effective Strain as a Function of Time Obtained from the Diametral Strain and Internal Pressure during Transient Heating (4.2°C/s) and Rupture (1030°C) of a Mandrel-constrained Zircaloy-4 Tube[a] in Steam

Time, s	Temperature, °C	Internal Pressure, MPa	Diametral Strain	Effective Strain, $\overline{\varepsilon}$	Effective Stress $\overline{\sigma}$, MPa
0	21	0.696	0	0	–
20.000	173	0.710	–	–	–
40.000	321	0.724	–	–	–
60.000	441	0.731	–	–	–
80.000	578	0.745	–	–	–
100.000	713	0.751	–	–	–
120.000	806	0.758	–	–	–
140.000	944	0.772	–	–	–
164.310	1003	0.779	0.02	0.104	7.150
166.310[b]	1009[b]	0.779[b]	0.05[b]	0.107[b]	7.480[b]
168.310	1013	0.779	0.08	0.110	7.730
169.310	1020	0.779	0.11	0.124	8.152
170.310	1024	0.779	0.12	0.141	8.480
171.310	1027	0.779	0.14	0.160	8.629
172.310	1028	0.779	0.15	0.172	8.806
172.810	1028	0.779	0.16	0.188	9.029
173.060	1028	0.779	0.16	0.188	9.029
173.160	1028	0.779	0.16	0.188	9.029
173.210	1029	0.779	0.17	0.195	9.119
173.235	1029	0.778	0.18	0.207	9.300
173.260	1029	0.777	0.19	0.214	9.391
173.275	1030	0.775	0.20	0.230	9.621

[a]Test No. IS-60 (Table A.12).

[b]Onset of plastic instability in the tube.

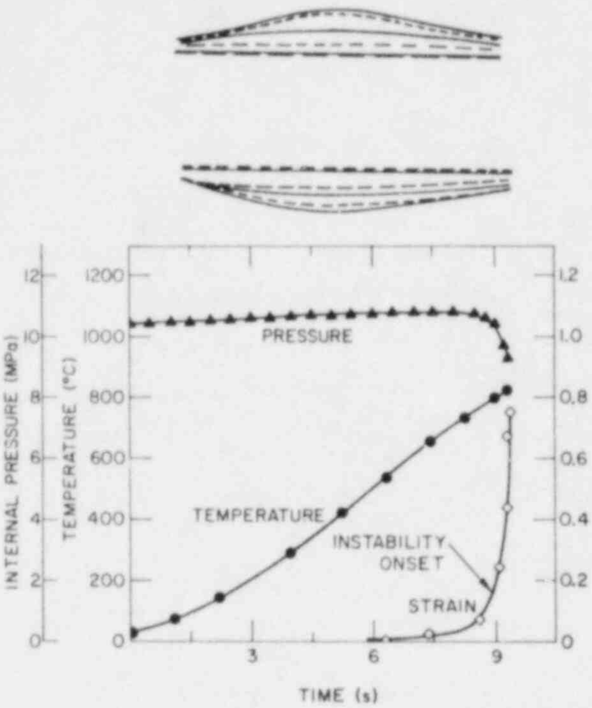

Fig. B.21

Time-dependent Temperature, Pressure, Diametral Strain, and Ballooning Profiles for Mandrel-constrained Zircaloy-4 Tube Burst in Steam at Heating Rate of 115°C/s. Ballooning profiles correspond to 1, 7, 20, 50, 400, and 1936 frames before rupture. Camera speed 200 frames/s. Test No. IS-66. ANL Neg. No. 306-77-457.

TABLE B.17. Effective Stress and Effective Strain as a Function of Time Obtained from the Diametral Strain and Internal Pressure during Transient Heating (115°C/s) and Rupture (820°C) of a Mandrel-constrained Zircaloy-4 Tube[a] in Steam

Time, s	Temperature, °C	Internal Pressure, MPa	Diametral Strain	Effective Strain, $\bar{\varepsilon}$	Effective Stress $\bar{\sigma}$, MPa
0	21	10.303	0	0	-
1.000	75	10.445	-	-	-
2.000	147	10.534	-	-	-
3.000	202	10.617	-	-	-
4.000	286	10.693	-	-	-
5.000	389	10.755	-	-	-
6.000	503	10.789	-	-	-
7.000	599	10.823	-	-	-
7.280	665	10.825	0.02	0.027	85.61
8.280	759	10.790	0.05	0.054	89.56
8.780[b]	800[b]	10.652[b]	0.14[b]	0.163[b]	106.0[b]
9.030	802	10.404	0.23	0.260	120.1
9.130	807	10.066	0.31	0.360	133.9
9.180	810	9.997	0.41	0.469	153.5
9.205	816	9.963	0.44	0.511	161.3
9.230	817	9.928	0.51	0.593	177.3
9.245	818	9.860	0.61	0.701	199.3
9.255	819	9.722	0.64	0.735	203.8
9.260	819	9.549	0.65	0.753	204.2
9.265	820	9.480	0.67	0.774	207.3
9.270	820	9.411	0.73	0.841	220.6
9.275	820	9.362	0.75	0.871	225.8

[a]Test No. IS-66 (Table A.10).
[b]Onset of plastic instability in the tube.

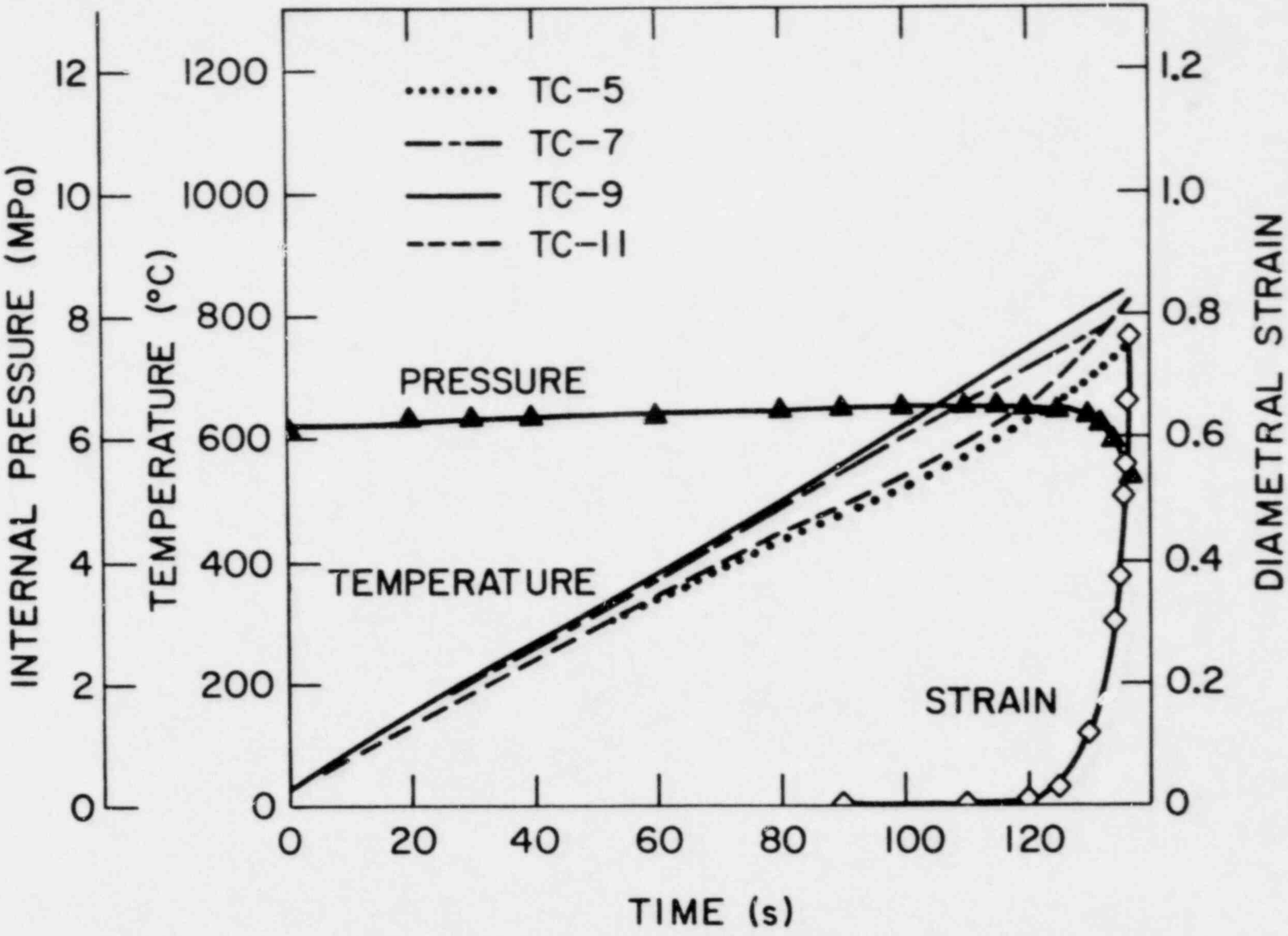

Fig. B.22. Time-dependent Temperature, Pressure, and Diametral Strain for Pellet-constrained Zircaloy-4 Tube (Pellet-cladding diametral gap 0.07 mm) Burst in Steam at Heating Rate of 5.0°C/s. Thermocouple positions are shown in Fig. B.23. Test No. IPL-6. ANL Neg. No. 306-77-467.

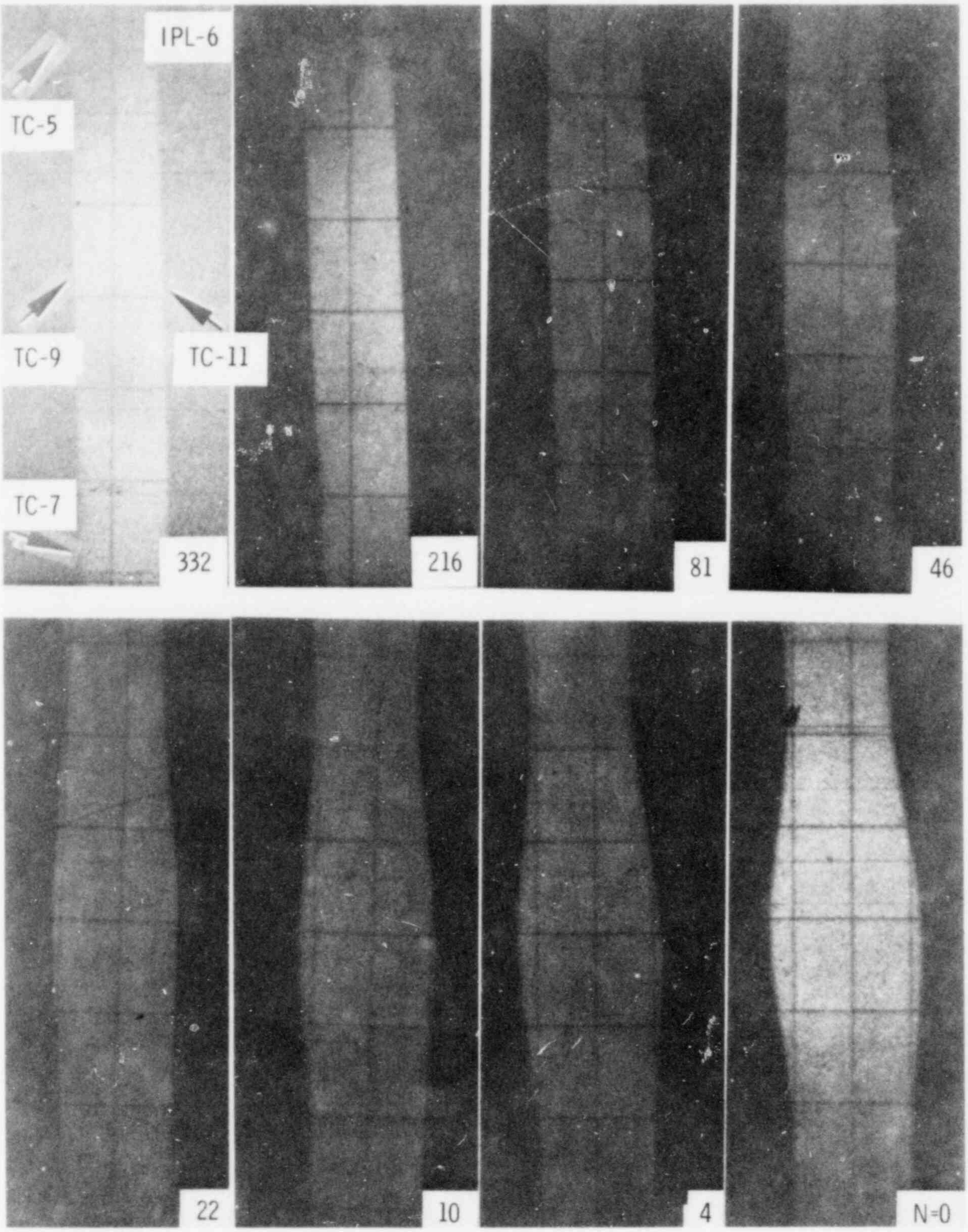

Fig. B.23. Ballooning Profiles and Surface Brightness of Zircaloy-4 Cladding Described in Fig. B.22. Photographs correspond to 0, 4, 10, 22, 46, 81, 216, and 332 frames before rupture. Camera speed 20 frames/s. ANL Neg. No. 306-77-531.

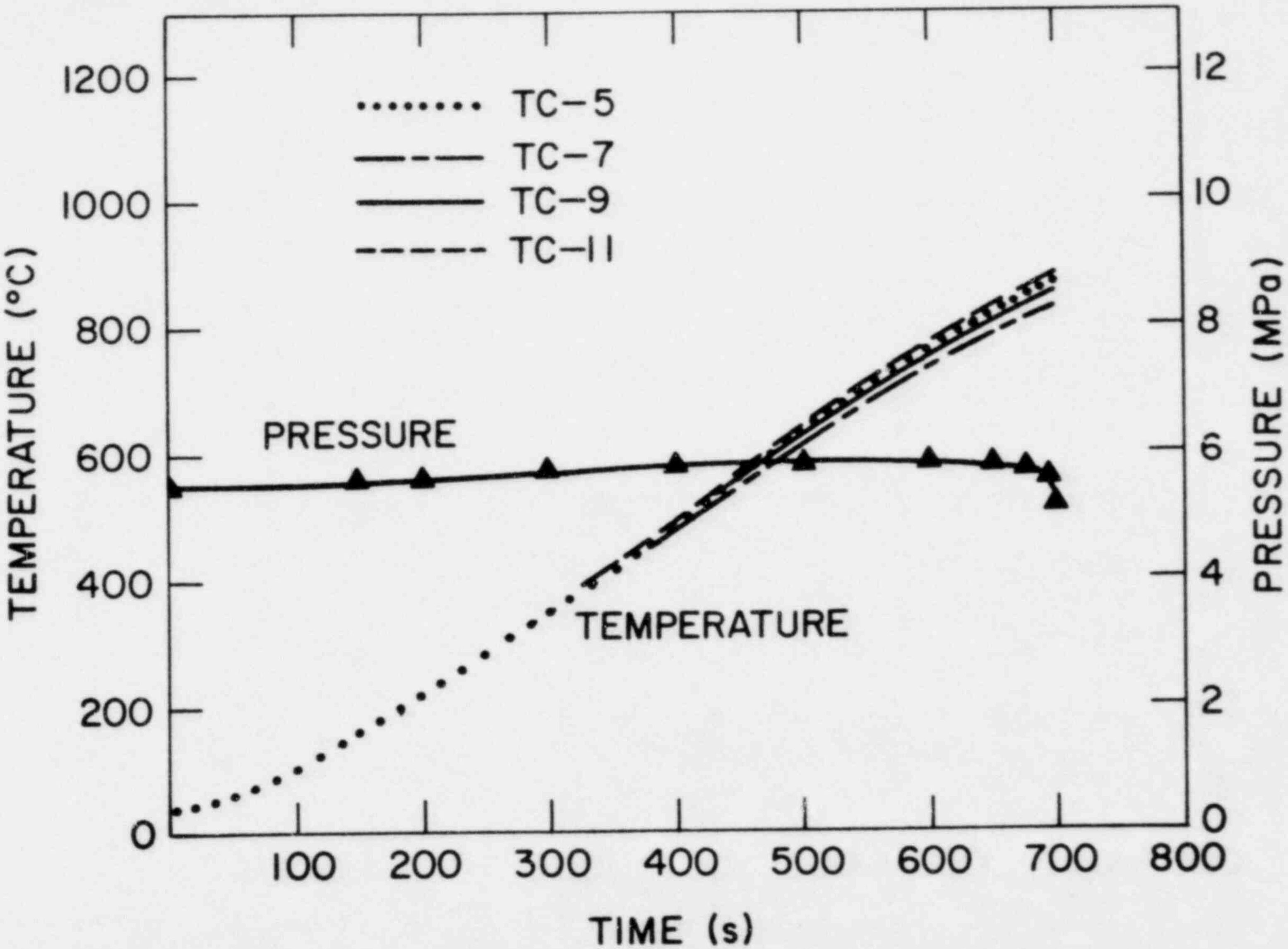

Fig. B.24. Time-dependent Temperature and Pressure for Pellet-constrained Zircaloy-4 Tube (Pellet-cladding diametral gap 0.5 mm) Burst in Steam at Heating Rate of 10°C/s. Thermocouple positions are shown in Fig. B.25. Test No. IPL-70. ANL Neg. No. 306-77-476.

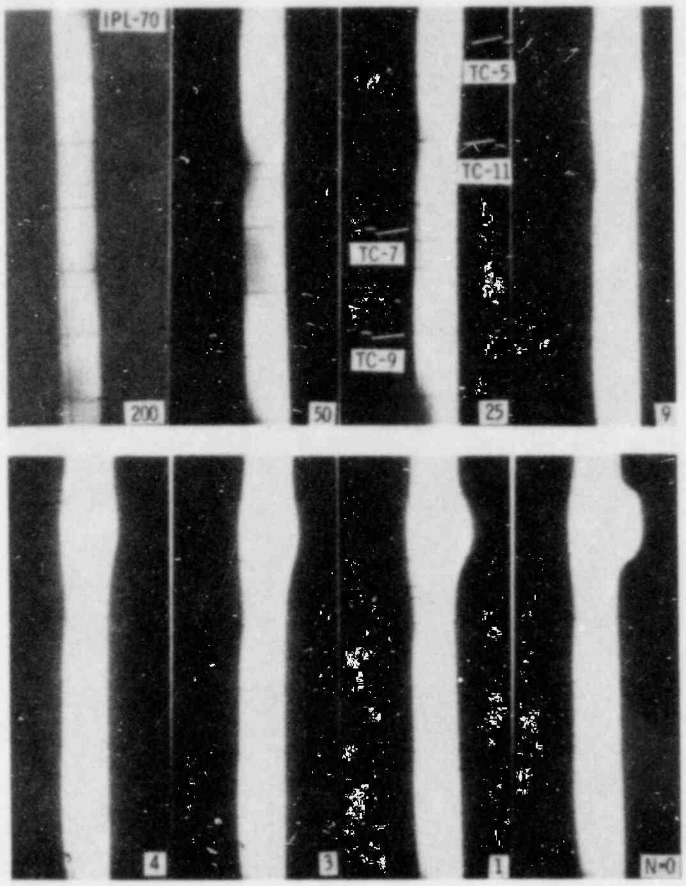

Fig. B.25

Ballooning Profiles and Surface Brightness of Zircaloy-4 Cladding Described in Fig. B.26. Photographs correspond to 0, 1, 6, 9, 20, 30, 50, and 100 frames before rupture. Camera speed 20 frames/s. ANL Neg. No. 306-77-530.

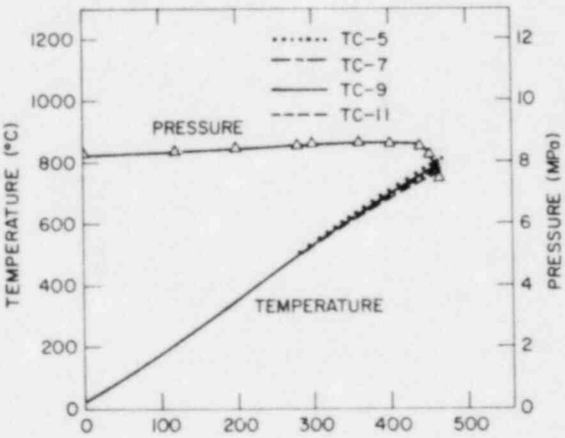

Fig. B.26

Time-dependent Temperature and Pressure for Pellet-constrained Zircaloy-4 Tube (Pellet-cladding diametral gap 0.5 mm) Burst in Steam at Heating Rate of 9.8°C/s. Thermocouple positions are shown in Fig. B.25. Test No. 1PL-71. ANL Neg. No. 306-77-464.

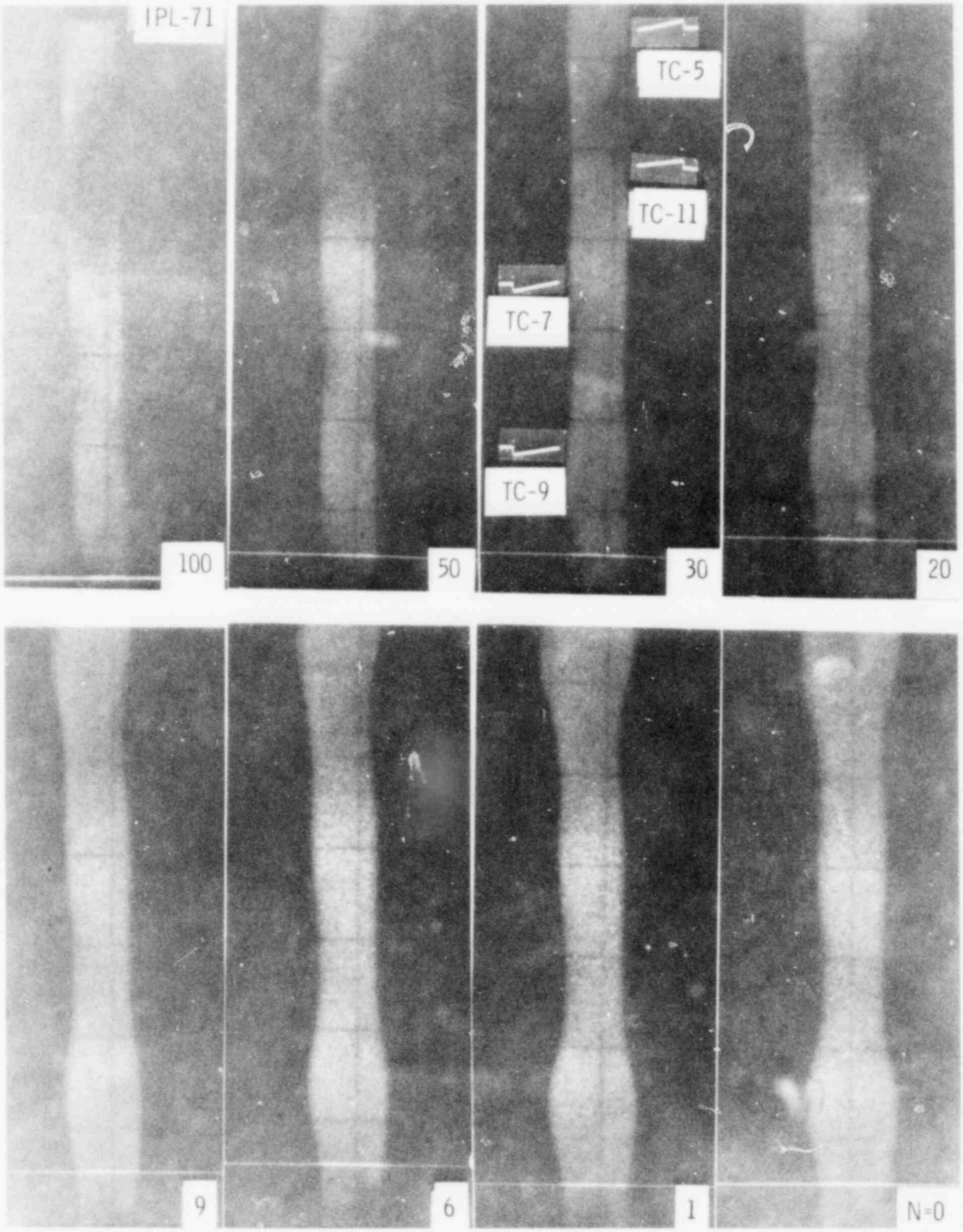

Fig. B.27. Ballooning Profiles and Surface Brightness of Zircaloy-4 Cladding Described in Fig. B.24. Photographs correspond to 0, 1, 3, 4, 9, 25, 50, and 200 frames before rupture. Camera speed 20 frames/s. ANL Neg. No. 306-77-428 Rev.

APPENDIX C

Area of Burst Opening in Zircaloy Cladding

A reliable estimate of the area of the burst opening in Zircaloy cladding may be useful in an analysis of the egress of fission products (and possibly fuel fragments) from the fuel element under LOCA situations. The area of the burst opening in pellet-constrained cladding ruptured in steam at temperatures between ~750 and 1250°C was determined by the method described in Sec. IV.D.

Figures C.1 and C.2 show the area of the burst opening as functions of burst-pressure differential and maximum recorded burst temperature, respectively. The data are also listed in Table C.1 along with the heating rate and initial internal pressure. For burst-pressure differentials ≲3.7 MPa, or for burst temperatures ≳900°C, the rupture area is quite small (≤8 mm^2) and virtually independent of temperature or pressure. For ruptures in the β- or predominantly β-phase region, the stored energy is low, and thus, the rupture opening is small (e.g., Fig. 13B). Because of steam oxidation, pinhole ruptures (e.g., Fig. 13C) are not observed, even at high temperatures, in the β-phase region.

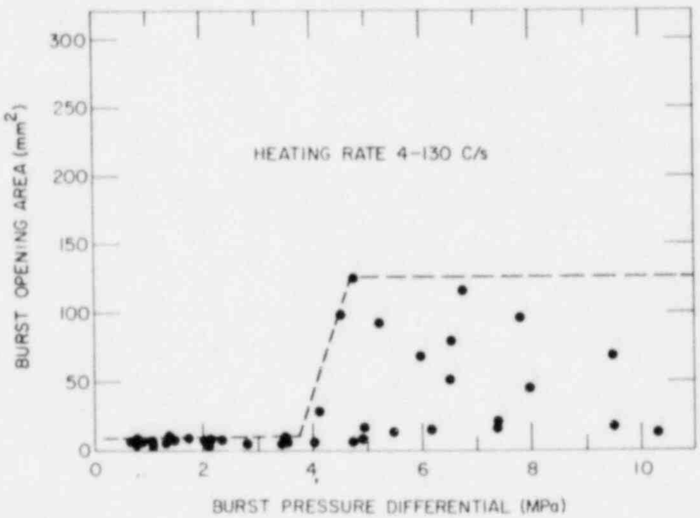

Fig. C.1

Area of Burst Opening in Pellet-constrained Tubes as a Function Burst-pressure Differential. ANL Neg. No. 306-78-403.

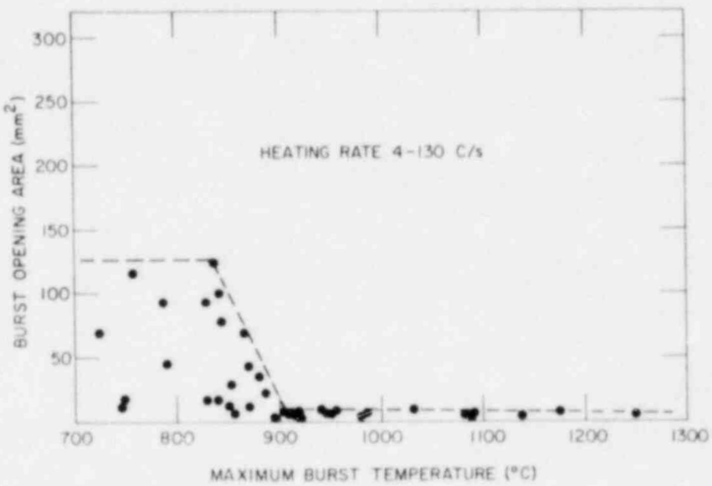

Fig. C.2

Area of Burst Opening in Pellet-constrained Tubes as a Function of Maximum Recorded Burst Temperature. ANL Neg. No. 306-78-404.

TABLE C.1. Area of the Burst Opening in Pellet-constrained Zircaloy-4 Cladding Ruptured in Steam at Heating Rates of 4-130°C/s

Test Number	Initial Pressure, MPa	Heating Rate,[a] °C/s	Burst Pressure, MPa	Maximum Burst Temperature, °C	Area of Burst Opening, mm^2
IPL-9	3.45	7.0	3.48	942	9.3
IPL-10	2.06	8.0	2.10	918	6.2
IPL-11	1.38	5.0	1.41	775	6.9
IPL-13	0.69	5.0	0.75	1079	3.1
IPL-14	4.13	5.0	4.01	870	35
IPL-15	8.27	36	7.92	789	45
IPL-17	7.58	94	7.37	747	17
IPL-18	10.3	100	9.51	838	17
IPL-22	9.65	15.0	9.44	724	69
IPL-23	4.82	113	4.79	903	6.9
IPL-24	5.51	121	5.44	870	10.4
IPL-25	3.45	120	3.52	950	6.2
IPL-27	8.27	14.0	7.79	788	93
IPL-34	6.20	45	6.13	851	12.4
IPL-35	4.82	44	4.89	863	6.2
IPL-37	3.41	49	3.45	896	4.8
IPL-38	2.06	41	2.07	946	7.6
IPL-39	1.38	40	1.36	1032	9.3
IPL-40	0.69	45	0.70	1250	5.9
IPL-41	1.03	41	1.03	1082	5.5
IPL-42	1.72	46	1.72	956	8.6
IPL-43	2.75	115	2.79	920	3.8
IPL-44	2.06	120	2.10	921	5.2
IPL-45	1.38	118	1.34	979	4.8
IPL-46	0.69	110	0.88	1138	3.5
IPL-47	1.03	104	1.03	1091	6.9
IPL-48	2.41	115	2.38	907	7.9
IPL-49	0.38	100	0.79	1175	6.9
IPL-50	7.58	5.0	6.75	757	117
IPL-51	4.82	5.8	4.48	843	100
IPL-87	6.89	118	5.96	865	69
IPL-88	6.89	55	6.55	870	41
IPS-99[b]	7.58	71	7.44	884	21
IPS-101[b]	5.51	4.6	5.24	829	93
IPS-103[b]	4.13	5.3	4.13	854	28
IPS-104[b]	11.1	125	10.3	744	12
IPS-105[b]	5.17	10	4.96	829	17
IPS-106[b]	4.82	10	4.77	837	126
IPS-110[b]	7.10	102	6.55	844	78

[a] Average heating rate for the temperature range of 300-810°C.

[b] Cladding length 153 mm, all others 300 mm.

For burst pressures ≳ 3.7, or burst temperatures ≲ 840°C, rupture areas between ~5 and 130 mm^2 were observed. In this temperature range, "fracture" -type bursts (e.g., Fig. 13A) occur because of the tube texture and the limited slip systems, with $\vec{a}$ type Burgers vectors, in α-phase Zircaloy. In this case, the burst opening is frequently quite large (≳ 40 mm^2). Occasionally, for high-heating-rate tests, "rupture" -type bursts (e.g., Fig. 73A) are observed in α- or predominantly α-phase cladding (IPL-17, IPL-18, and IPS-104 in Table C.1). In these instances, localized deformation involves pyramidal slip with $(\vec{c} + \vec{a})$-type Burgers vectors and the burst opening is small (≲ 20 mm^2). The different deformation mechanisms may account for the wide range of burst openings in the cladding at temperatures ≲ 840°C.

ACKNOWLEDGMENTS

We wish to acknowledge the contributions of L. P. Burkel and L. J. Marek in performing the experimental work. The experimental assistance of W. K. Soppet is also acknowledged. C. A. Youngdahl was most helpful in the design of the tube-burst apparatus. We are grateful to A. M. Garde and M. L. Picklesimer for helpful discussions on the physical and mechanical metallurgy of Zircaloy.

REFERENCES

1. *Light-water-reactor Safety Research Program: Quarterly Progress Report, July-September 1975*, Sec. III, "Mechanical Properties of Zircaloy Containing Oxygen," ANL-75-72.

2. *Light-water-reactor Safety Research Program: Quarterly Progress Report, October-December 1975*, Sec. III, "Mechanical Properties of Zircaloy Containing Oxygen," ANL-76-15.

3. *Light-water-reactor Safety Research Program: Quarterly Progress Report, January-March 1976*, Sec. III, "Mechanical Properties of Zircaloy Containing Oxygen," ANL-76-49.

4. *Light-water-reactor Safety Research Program: Quarterly Progress Report, April-June 1976*, Sec. III, "Mechanical Properties of Zircaloy Containing Oxygen," ANL-76-87.

5. *Light-water-reactor Safety Research Program: Quarterly Progress Report, July-September 1976*, Sec. III, "Mechanical Properties of Zircaloy Containing Oxygen," ANL-76-121.

6. *Light-water-reactor Safety Research Program: Quarterly Progress Report, October-December 1976*, Sec. III, "Mechanical Properties of Zircaloy Containing Oxygen," ANL-77-10.

7. *Light-water-reactor Safety Research Program: Quarterly Progress Report, January-March 1977*, Sec. III, "Mechanical Properties of Zircaloy Containing Oxygen," ANL-77-34.

8. *Light-water-reactor Safety Research Program: Quarterly Progress Report, April-June 1977*, Sec. III, "Mechanical Properties of Zircaloy Containing Oxygen," ANL-77-59.

9. C. C. Busby and K. B. Marsh, *High Temperature Deformation and Burst Characteristics of Recrystallized Zircaloy-4 Tubing*, WAPD-TM-900, Bettis Atomic Power Laboratory, Westinghouse Electric Corp., Pittsburgh, Pa. (Jan 1970).

10. A. D. Emery, D. B. Scott, and J. R. Stewart, *Effects of Heating Rate and Pressure on Expansion of Zircaloy Tubing During Sudden Heating Conditions*, Nucl. Tech. *11*, 474 (1971).

11. D. O. Hobson, M. F. Osborne, and G. W. Parker, *Comparison of Rupture Data From Irradiated Fuel Rods and Unirradiated Cladding*, Nucl. Tech. *11*, 479 (1971).

12. D. G. Hardy, "High Temperature Expansion and Rupture Behaviour of Zircaloy Tubing," *Topical Meeting on Water-reactor Safety*, Salt Lake City, Utah, CONF-730304, G. A. Freund, Compiler, pp. 254-273 (Mar 26-28, 1973).

13. R. H. Chapman, *Multirod Burst Test Program: Quarterly Progress Report, April-June 1977*, ORNL/NUREG/TM-135, Oak Ridge National Laboratory.

14. K. M. Rose and E. D. Hindle, "Diametral Increases in Steam Generating Heavy Water Reactor Zircaloy Cans under Loss-of-Coolant Accident Conditions," Zirconium in the Nuclear Industry, ASTM STP 633, A. L. Lowe, Jr., and G. W. Parry, Eds., American Society for Testing and Materials, pp. 24-35 (1977).

15. W. A. Fiveland, A. R. Barber, and A. L. Lowe, Jr., "Rupture Characteristics of Zircaloy-4 Cladding with Internal and External Simulation of Reactor Heating," ibid., pp. 36-49.

16. C. E. L. Hunt and D. E. Foote, "High Temperature Strain Behaviour of Zircaloy-4 and Zr-2.5 Nb Fuel Sheaths," ibid., pp. 50-65.

17. H. M. Chung, A. M. Garde, and T. F. Kassner, "Deformation and Rupture Behaviour of Zircaloy Cladding under Simulated Loss-of-Coolant Accident Conditions," ibid., pp. 82-97.

18. F. Erbacher, H. J. Neitzel, M. Reimann, and K. Wiehr, "Out-of-Pile Experiments on Ballooning in Zircaloy Fuel Rod Claddings in the Low Pressure Phase of a Loss-of-Coolant Accident," *OECD-CSNI Specialist Meeting on the Behaviour of Water Reactor Fuel Elements under Accident Conditions*, Spåtind, Norway (Sept 13-16, 1976).

19. H. G. Weidinger, G. Cheliotis, H. Watzinger, and H. Stehle, "LOCA Fuel Rod Behaviour of KWU-Pressurized Water Reactors," ibid.

20. B. D. Clay, T. Healey, and G. B. Redding, "The Deformation and Rupture of Zircaloy-2 Tubes During Transient Heating," ibid.

21. C. E. L. Hunt, D. E. Foote, and D. Grant, "The Effect of Steam Oxidation on the Strain of Fuel Sheathing at High Temperature," ibid.

22. P. Morize, H. Vidal, J. M. Frenkel, and R. Roulliay, "Zircaloy Cladding Diametral Expansion During a LOCA-EDGAR Programme," ibid.

23. D. L. Burman and C. A. Olson, "Temperature and Cladding Burst Distributions in a PWR Core During LOCA," ibid.

24. H. M. Chung, A. M. Garde, and T. F. Kassner, "High Temperature Deformation and Rupture Behaviour of Internally Pressurized Zircaloy-4 Cladding in Vacuum and Steam Environments," *Proceedings of Topical Meeting on Thermal Reactor Safety*, Sun Valley, Idaho, ANS CONF-770708, Vol. 3, pp. 60-85 (July 31-Aug 4, 1977).

25. F. Erbacher, H. J. Neitzel, M. Reimann, and K. Wiehr, "Ballooning in Zircaloy Fuel Rod Claddings in a Loss-of-Coolant Accident," ibid., Vol. 3, pp. 86-105.

26. P. Hoffman and C. Politis, "Investigations of the Influence of Oxide Fuel and Fission Products on the Mechanical Properties of Zircaloy-4 Cladding Tubes under LWR Transient Conditions," ibid., Vol. 3, pp. 43-59.

27. B. Brzoska, G. Cheliotis, A. Kunick, and G. Senski, "A New High Temperature Deformation Model for Zircaloy Clad Ballooning under Hypothetical LOCA Conditions," *Trans. 4th International Conference on Structural Mechanics in Reactor Technology*, San Francisco, T. A. Jaeger and B. A. Boley, Eds., Vol. C. (Aug 15-19, 1977).

28. E. I. H. Lin, "Analysis of the Ballooning Deformation of an Internally Pressurized Thin-Wall Tube during Fast Thermal Transients," ibid.

29. H. M. Chung, A. M. Garde, and T. F. Kassner, *Effect of Temperature Nonuniformity on the Diametral Expansion of Internally Pressurized Zircaloy-4 Cladding During Transient Heating in Steam*, Trans. Am. Nucl. Soc. *27*, 600 (1977).

30. A. Agazzi, M. Astolfi, and G. Mancini, *Probabilistic Assessment of Fuel Rod Ballooning in Large-Bundle LOCA Experiments*, Trans. Am. Nucl. Soc. *27*, 637 (1977).

31. E. Karb, "Ergebnisse von In-pile Experimenten im FR2 zum Brennstabverhalten bei Kühlmittelverluststörfällen," *Jahres Kolloquium des Projektes Nukleare Sicherheit*, Karlsruhe, Germany (Dec 1977).

32. R. H. Chapman, Compiler, *Characterization of Zircaloy-4 Tubing Procured for Fuel Cladding Reasearch Programs*, ORNL/NUREG/TM-29, Oak Ridge National Laboratory (July 1976).

33. *Light-water-reactor Safety Research Program: Quarterly Progress Report, April-June 1975*, Sec. III, "Mechanical Properties of Zircaloy Containing Oxygen," ANL-75-58.

34. H. M. Chung and T. F. Kassner, *Pseudobinary Zircaloy-Oxygen Phase Diagram Determined by Resistometric and Quenching Techniques*, to be published.

35. D. Franklin, *Theory of Plastic Instability in Thin-Wall Tubes*, Acta Met. *20*, 839 (1972).

36. A. M. Garde, H. M. Chung, and T. F. Kassner, *Uniaxial Tensile Properties of Zircaloy Containing Oxygen: Summary Report*, ANL-77-30 (June 1977).

37. E. Tenckhoff, "Operable Deformation Systems and Mechanical Behaviour of Textured Zircaloy Tubing," *Zirconium in Nuclear Applications*, ASTM STP 551, American Society for Testing and Materials, pp. 179-200 (1974).

38. K. Källström, *Closed End Burst Testing of Zircaloy Canning Tubes*, J. Nucl. Mater. *31*, 111 (1969).

39. R. L. Mehan, *Effect of Combined Stress on Yield and Fracture Behaviour of Zircaloy-2*, J. Basic Eng., Trans. ASME *83*, 499 (1961).

40. H. Maki and M. Ooyama, *Plastic Deformation and Fracture Behaviour of Zircaloy-2 Fuel Cladding Tubes Under Biaxial Stress*, J. Nucl. Sci. Tech. *12*, 423 (1975).

41. Y. Miyamoto, Y. Komatsu, T. Kakuma, and N. Nagai, *Mechanical Behaviour of Zircaloy-2 Tubing Under Biaxial Stresses*, J. Nucl. Mater. *61*, 53 (1976).

42. G. Dressler and K. H. Matucha, "Yield and Fracture of Biaxially Stressed Zircaloy-4 Cladding Tubes at Room Temperature and at 400°C," *Zirconium in the Nuclear Industry*, ASTM STP 633, A. L. Lowe, Jr., and G. W. Parry, Eds., American Society for Testing and Materials, pp. 508-522 (1977).

43. C. W. Hunter, R. L. Fish, and J. J. Holmes, *Mechanical Properties of Unirradiated Fast Reactor Cladding During Simulated Overpower Transients*, Nucl. Tech. *27*, 376 (1975).

44. J. B. Van der Sande and A. L. Bement, *An Investigation of Second Phase Particles in Zircaloy-4 Alloys*, J. Nucl. Mater. *52*, 115 (1974).

45. R. V. Southwell, *An Introduction to the Theory of Elasticity for Engineers and Physicists*, Clarendon Press, Oxford, 406 (1936).

46. C. F. Smith and W. B. Crandal, *Calculated High Temperature Elastic Constants for Zero Porosity Monoclinic Zirconia*, J. Am. Ceram. Soc. *47*, 624 (1964).

47. E. Tenckhoff, *Operation of Dislocations with ($\vec{c}$ + $\vec{a}$) Type Burgers Vector During the Deformation of Zirconium Single Crystals*, Z. Metallk. *63*, 192 (1972).

48. A. Akhtar, *Compression of Zirconium Single Crystals Parallel to the C-Axis*, J. Nucl. Mater. *47*, 79 (1973).

49. N. E. Paton and W. A. Backoffen, *Plastic Deformation of Titanium at Elevated Temperatures*, Metall. Trans. *1*, 2839 (1970).

50. J. A. Jensen and W. A. Backoffen, *Deformation and Fracture of Alpha Zirconium Alloys*, Can. Metall. Q. *11*, 39 (1972).

51. D. H. Bradhurst and P. M. Heuer, *Effect of Deformation on the High Temperature Steam Oxidation of Zircaloy-2*, J. Nucl. Mater. *55*, 311 (1975).

52. J. T. Venard, *Stress-Rupture Properties of Type 304 Stainless Steel Tubing*, ORNL-TM-535, Oak Ridge National Laboratory (June 1963).

53. T. Furuta, S. Kawasaki, M. Hashimoto, and T. Otomo, *Factors Influencing Deformation and Wall Thickness of Fuel Rods Under a Loss-of-Coolant Accident*, JAERI-M 6542, Japan Atomic Energy Research Institute (May 1976).

© U.S. GOVERNMENT PRINTING OFFICE: 1978—650-5